FACULTÉ
DES SCIENCES ET
TECHNOLOGIES

Université
de Lille

THÈSE DE DOCTORAT

Présentée par

NGO Thi Linh Dan

Pour obtenir le grade de Docteur de l'Université de Lille

École Doctorale des Sciences de la Matière, du Rayonnement et de l'Environnement

Discipline : Optique et Lasers, Physico-Chimie, Atmosphère

Characterization of soot particles and their precursors produced during the combustion of conventional and alternative fuels: an in-situ laser diagnostics and ex-situ mass spectrometry investigation

(Caractérisation des particules de suie et de leurs précurseurs produits
lors de la combustion de carburants fossiles et alternatifs:
une étude *in situ* par diagnostics laser et *ex situ* par spectrométrie de masse)

Soutenue le 10 Octobre 2019 devant la commission d'examen

Rapporteurs:	Thomas Dreier Barbara D'Anna	Professeur, Universität Duisburg-Essen, Allemagne Directrice de Recherche, CNRS, LCE, Marseille
Président du jury:	Cristian Focsa	Professeur, Université de Lille
Examinateurs:	Patrizia Minutolo Francois-Xavier Ouf Xavier Mercier	Chargé de Recherche, IRC-CNR, Napoli, Italie Ingénieur - Chercheur, IRSN, Gif-sur-Yvette Chargé de Recherche, CNRS, PC2A, Villeneuve d'Ascq
Directeur de thèse:	Eric Therssen	Professeur, Université de Lille
Co-encadrant:	Yvain Carpentier	Maître de Conférences, Université de Lille
Membre invité:	Cornelia Irimiea	Ingénieur, ONERA, Palaiseau

Laboratoire de Physique des Lasers, Atomes et Molécules
&
Laboratoire de PhysicoChimie des Processus de Combustion et de l'Atmosphère

Acknowledgements

I would like to express my appreciation to the Université de Lille and Labex CaPPA who finance this PhD project and give such an opportunity to me during three years.

I would like to say thank you to Prof. Eric Therssen, Dr. Yvain Carpentier, Dr. Xavier Mercier. I'm very honor to be one of their PhD students. I appreciate all of their contribution of time, of ideas and their direction to this work. Without their dedication and support, this work could have never been done.

Special thanks to Prof. Cristian Focsa and Dr. Pascale Desgroux for their precious advises, for all the scientific discussions and for all of their support during three years.

Big thanks to Prof. Laurent Gasnot for all the help concerning to the administrative procedures, and for all the useful advises.

Many thanks are dedicated to Cornelia, Alessandro, Marin and Dumitru, for their helps with the data interpretation and the instruments, for their willingness to help me any time I get problem in the lab.

Thanks to Nicolas for teaching me how to work with ToF-SIMS device during the first year and for accompanying me whenever I have SIMS measurement campaign.

Thanks to Sylvie, Olivier, Sébastien(s) (yes both of you), Valérie, Benjamin, Bénédicte, Marc, Luc-Sy for helping me so many times. They never get annoyed even when I asked for so many things (or maybe I'm not annoying enough).

I'd like to thank all the people in the laboratory PC2A, PhLAM and CERLA. Without them I could never finish this work.

Thanks to all my friends in the laboratories: Morgane, Siveen, Carla, Junteng, Quan, Lucia, Carolina, Jinane, Lise for all good time spent together.

Last but not least, thanks to my family Ba, Má, cu Hề, Nội, Ngoại for their support not only during these three years but for my whole life. Thanks to my closest friends Con Chó và Uno hội. Thanks to my love, Bruno, for always being beside me and giving me the strength I need.

Abstract

Interest in biofuels has increased significantly in recent years as they could reduce dependence on fossil fuels and contribute to carbon-neutral growth. The influence of using biofuels on their exhaust emissions ($\mathrm{CO}, \mathrm{CO_2}, \mathrm{NO}_x, \mathrm{HC}$, etc.) has been studied widely. However, the effects of the nature of these alternative fuels on the physical and chemical properties of the particles and aromatic species produced are not fully understood. As part of this thesis work, we aim to study the emissions of soot particles and polycyclic aromatic hydrocarbons (PAHs) during the combustion of conventional and alternative fuels (biofuels) relevant to the automotive and aerospace sectors, while trying to highlight their influence on the formation of such pollutants. To achieve this goal, two laboratory combustors, a swirled turbulent jet burner and a Combustion Aerosol STandard (CAST), were used as soot generators. In addition, we have combined various complementary *in-situ* laser techniques, laser-induced incandescence and fluorescence (LII/LIF), and *ex-situ* two-step laser mass spectrometry (L2MS) and secondary ion mass spectrometry (SIMS). In a swirled turbulent jet flame for five fuels (Diesel, *n*-butanol, 50/50 Diesel/*n*-butanol mixture, Jet A-1 and Synthetic Paraffinic Kerosene SPK), the LII and LIF profiles and properties of soot particles and their precursors with the height in the flame as well as their chemical composition were studied. Strong correlations between the results obtained with *in-situ* and *ex-situ* techniques have been demonstrated which allowed us to characterize these species spectrally and chemically. In addition, a new calibration method has been developed to directly deduce the soot volume fraction from the LII signal using the absolute radiance emitted from a light source having black body behavior. In parallel, experiments using the CAST device were conducted with aeronautical fuels (Jet A-1 and SPK). In addition to the influence of the alternative fuel, the effects of a catalytic stripper (CS) on soot particles and volatile species were examined.

Keywords: Combustion, biofuels, soot particles, polycyclic aromatic hydrocarbons, laser diagnostics, laser-induced incandescence, laser-induced fluorescence, soot volume fraction, mass spectrometry, principal component analysis.

Résumé

L'intérêt pour les biocarburants s’est considérablement accru ces dernières années car ceux-ci pourraient permettre de diminuer la dépendance aux combustibles fossiles et contribuer à une croissance neutre en carbone. L’influence de l’utilisation de biocarburants sur les émissions de polluants ($\mathrm{CO}, \mathrm{CO_2}, \mathrm{NO}_x, \mathrm{HC}$, etc.) a fait l’objet de nombreux travaux, cependant les effets de la nature de ces carburants alternatifs sur les propriétés physico-chimiques des particules et des espèces aromatiques produites sont encore peu étudiés. Dans le cadre de ce travail de thèse, nous visons à caractériser les émissions de particules de suie et d'hydrocarbures aromatiques polycycliques (HAP) lors de la combustion de carburants conventionnels et alternatifs (biocarburants) pertinents pour les secteurs de l'automobile et de l'aéronautique, tout en essayant de mettre en lumière leurs influence sur les mécanismes de formation de ces polluants. Pour atteindre cet objectif, deux réacteurs de laboratoire, un bruleur turbulent swirlé et un Combustion Aerosol STandard (CAST), ont été utilisés comme générateurs de suie. De plus, nous avons combiné différentes techniques laser complémentaires *in situ*, les incandescence et fluorescence induites par laser (LII/LIF), et *ex situ*, la spectrométrie de masse après désorption et ionisation laser (L2MS) et la spectrométrie de masse des ions secondaires (SIMS). Dans une flamme turbulente swirlée pour cinq carburants (Diesel, *n*-butanol, mélange 50/50 Diesel/*n*-butanol, Jet A-1 et Synthetic Paraffinic Kerosene SPK), les profils LII et LIF et les propriétés des particules de suie et de leurs précurseurs en fonction de la hauteur dans la flamme ainsi que leur composition chimique ont été étudiés. De fortes corrélations entre les résultats obtenus avec les techniques *in situ* et *ex situ* ont été mises en évidence permettant de caractériser spectralement et chimiquement ces espèces. En outre, une nouvelle méthode d'étalonnage a été développée pour déduire directement la fraction volumique de suie à partir du signal LII en utilisant la luminance énergétique absolue émise par une source ayant un rayonnement de corps noir. En parallèle, les expériences utilisant le dispositif CAST ont été menées avec les carburants aéronautiques (Jet A-1 et SPK). Outre l'influence du carburant de substitution, les effets d’un stripper catalytique (CS) sur les particules de suie et les espèces volatiles ont été examinés.

Mots-clés: Combustion, biocarburants, particules de suie, hydrocarbures aromatiques polycycliques, diagnostics laser, incandescence induite par laser, fluorescence induite par laser, fraction volumique de suie, spectrométrie de masse, analyse en composantes principales.

List of acronyms

CAST : combustion aerosol standard
CS : catalytic stripper
FT : Fischer-Tropsch
GFF : glass fiber filter
GHG : greenhouse gases
HAB : height above the burner
HACA : H abstraction C_2H_2 addition
HCA : hierarchical clustering analysis
HEFA : hydroprocessed esters and fatty acids
ICCD : intensifier charged coupled device
IR : infrared
L2MS : two-step laser mass spectrometry
LD : laser desorption
LHV : lower heating value
LI : laser ionization
LIF : laser induced fluorescence
MFC : mass flow controller
MVA : multivariate analysis
NSP : nascent soot particles
nvPM : non-volatile particulate matter
OC/TC : organic carbon to total carbon
PAH : polycyclic aromatic hydrocarbon
PC : principal component
PCA : principal component analysis
PIC : partial ion counts
PM : particulate matter
PMT : photomultiplier tube
QFF : quartz fiber filter
R2PI : resonant two photons ionization
SIMS : secondary ion mass spectrometry
SPK : synthetic paraffinic kerosene
TF : transfer function
TIC : total ion counts
ToF : time-of-flight
UV : ultraviolet
Vis : visible

Contents

List of figure

List of tables

Chapter 1.

Introduction

1. Introduction

1.1. General

More than 90% of primary consumption of energy in the world is used in the combustion (Tissot 2003). The demand of worldwide energy, especially fossil energy, has been increased with the development of technology and civilization. Petroleum fuels – a type of fossil combustibles – are actually being used in important quantity in transport system. However, there are two big problems caused by the utilization of fossil fuels: (1) the shortage of their stocks because they are not renewable and (2) the increase of the concentration of carbon dioxide in the atmosphere due to their combustion. In lately decades, the extreme increase of greenhouse gas provokes the climate change all around the planet, leading to the more frequent extreme climatic phenomena.

Biofuels appears as an interesting and promising solution that is able to solve both problems: decrease the dependence of human on fossil fuels and reduce the negative impact on environment. Biofuels are considered as a renewable energy and could be produced from alimental or non-alimental biomass stocks. The utilization of biofuels as a source of energy would not increase the total concentration of CO_2 in the atmosphere because biomass uses the carbon containing in CO_2 for their growth due to the photosynthetic process.

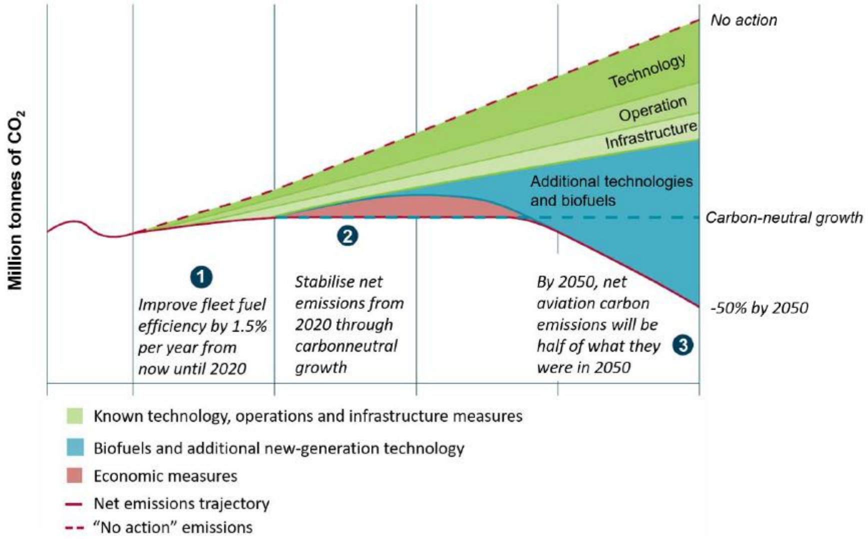

Figure 1.1.1. Aircraft CO_2 emissions from International Aviation, 2005 to 2050 (ICAO Environmental Report 2016 - Aviation and Climate Change 2017)

Figure 1.1.1 shows the estimated scenario of CO_2 emissions in aviation sector from 2020 – 2050 with different options. It can be seen from the figure that biofuels take an important role to achieve the goal of carbon-neutral growth in 2050. In other words, the carbon-neutral growth cannot be without the use of biofuels.

However, care must be taken in using biofuels for the combustion. Since the engines have been always designed to use fossil fuels, any modification of fuels could influence many aspects as technical problems (density, viscosity, filtration, volatility,…) or fuel consumption (concerning to calorific values), or the exhaust emissions as CO, hydrocarbons (HC), particulate matter (PM), NO_x,… Most of studies reported that the use of biofuels reduces the emissions of CO_2, CO, soot particles, but increases NO_x emissions (Schumacher et al. 1996; Bünger et al. 2000; Kooter et al. 2011; Krahl et al. 2002; Dorado 2003). However, some scholars reported that there is an increase of benzene, aldehydes and ozone precursors in the exhaust of biofuels (Geyer, Jacobus, and Lestz 1984; Krahl et al. 2001; Krahl et al. 2002; Turrio-Baldassarri et al. 2004). Jaramillo et al. (2018) stated that the differences in fuels and combustion conditions affect strongly the physicochemical properties of emitted particles. And with these differences, the biological/toxicological responses could be affected. There is inconsistency of this problematic among the studies. A lower mutagenic potency is found due to the lower content of PAHs in exhaust of biodiesel compared to diesel as in the studies of (Bünger et al. 2000; Krahl et al. 2002). Whereas in other studies, a strong increase of cytotoxicity, mutagenicity and genotoxicity of emissions from biofuels (compared to conventional fossil fuels) is reported (Topinka et al. 2012; Kooter et al. 2011; Bünger et al. 2007).

Among different types of species in the exhaust emissions of the combustion, we are interested mostly in soot emissions and polycyclic aromatic compounds. These unwanted byproducts are the result of incomplete combustion. These emissions classify as negative role players in the climate and environment. In the atmosphere, these particles can play as condensation nuclei forming cloud, which have a cooling effect on Earth's atmosphere or they can absorb sun radiation and produce the greenhouse effect. This particulate matter could be the second largest contributor to global warming (Jacobson 2001; Ramanathan and Carmichael 2008). The deposition of them on snow is considered as a major source for arctic sea ice retreat and melting glaciers (de_Richter and Caillol 2011). The size of particles covers many orders of magnitude. They are classified in function of their aerodynamic diameter as PM_{10} (< 10 µm), $\mathrm{PM}_{2.5}$, PM_1 and UFP (ultra-fine PM, < 100 nm). The smallest particles are the most dangerous ones because they are considered to exacerbate respiratory, cardiovascular, and allergic diseases due to their small respirable size, large surface area, surface reactivity and potential toxicity (Shiraiwa, Selzle, and Pöschl 2012; Libalova et al. 2016; Zhang and Balasubramanian 2017). The PAHs carried along with soot particles in exhaust emissions of combustion have been reported to cause impaired lung function in asthmatics and thrombotic effects in short-term. In long term, several PAHs are identified as highly toxic, mutagenic and/or carcinogenic to microorganisms as well as higher systems including humans (Kim et al. 2013; Abdel-Shafy and Mansour 2016; Shiraiwa, Selzle, and Pöschl 2012). Therefore it is necessary to investigate soot and PAH emissions in the exhaust of different fuels.

Soot is the terms used for particulate matter resulting from incomplete combustion of organic materials. In literature, there are many other terms used as Black Carbon (BC), Black carbon (CB), Refractory Black Carbon (rBC), Equivalent Black Carbon (eBC), Total Carbon (TC), Brown Carbon (BrC), Light Absorbing Carbon (LAC), Elemental Carbon (EC), Organic Carbon (OC), etc.

These terms are used related to specific material properties and/or techniques used to investigate them. This combustion by-product is not a pure compound. It mainly contains C and a significant amount of H as well as O, N and metals, etc. depending on its origin. Soot is present everywhere around us, from natural sources as interstellar dust or biomass burning, to anthropogenic sources as transportation, industrial activities or domestic activities. Soot formation is a complex process containing series of mechanisms. The formation starts after the fuel pyrolysis, which produces a significant amount of acetylene (C_2H_2) in the incipient zone of a flame. The addition of C_2H_2 to molecular precursors states under the name of HACA mechanism (H abstraction C_2H_2 addition). This mechanism was first introduced by (Frenklach and Wang 1991). It describes a repetitive reaction pathway involving acetylene molecules in the formation of the first aromatic ring up to large molecules. The nucleation process – which is the initiation of soot particles has not been well understood (Desgroux, Mercier, and Thomson 2013). There are few pathways for this step proposed by scholars. (Homann 1998) suggested a pathway stating the formation of fullerene-like structures by the bimolecular reactions produced between two PAHs, involving coordinate detachment of H or so-called zipper mechanism. (Frenklach 2002) proposed another pathway which involves the coagulation of PAHs on compact clusters through collisions, due to Van der Waals interactions, forming PAH dimers, trimmers, tetramers and so on. They assumed that the formation of dimers marks the emergence of the "solid" particle phase. Another mechanism states that the formation of the first nuclei is due to the chemical coalescence of PAHs through $C-C$ bonds which results in a tridimensional structure (Richter and Howard 2000). After the first nuclei are formed, the surface of soot particles increases by two processes: the condensation of PAHs onto the soot carbon matrix, and heterogeneous reactions between soot carbonaceous matrix and the surrounding gaseous precursors with HACA mechanism (Frenklach and Wang 1991; Balthasar 2000). The newly formed soot particles are called nascent soot particles. During the particle coagulation process, sticking collisions between particles during the mass growth process significantly increases particles size and decreases particle number without changing the total mass of soot present. This process is accompanied by a progressive reduction of the number of hydrogen and a rearrangement of the internal structure of soot particles which give them the spherical shape. After coagulation, particles can undergo a number of surface reactions having as consequence the aggregation of the particles. During the collision process, mature soot is not coagulating anymore, but particles can merge. At the final step of the process, oxidation of PAHs and soot particles takes place. It decreases the mass of PAHs and soot materials through the formation of CO and CO_2 (Richter and Howard 2000).

1.2. *N*-butanol as alternative for diesel fuel

Transport is Europe's biggest source of carbon emissions, contributing 27% to the EU's total CO_2 emission. Transport is the only sector in which emissions have grown since 1990, contributing to the increase in the EU's overall emissions in 2015 (Todts 2018). Among different fossil fuels that are responsible for the production of greenhouse gases (GHG), diesel is responsible for more than 90% of PM emission according to the study of (Minjares, Wagner, and Akbar 2014). Diesel accounts for more than 40% of global on-road energy consumption and is the main fuel of heavy-duty trucks (at about 90% of fuel consumption) and buses (at more than 75%) (Miller and Jin 2018). In last few decades, alcohols, vegetable oils, their derived biodiesels, liquefied petroleum gas (LPG), compressed natural gas (CNG), etc. have been proposed as alternative fuels to replace partly or completely conventional diesel fuel (Geng et al. 2017; Rajesh Kumar and Saravanan 2016; Shah et al. 2011; Wei and Geng 2016). However, it is not an easy duty to choose the best suited alternative fuel for diesel engine due to the technical problems (density, viscosity, pressure vapor, etc.), energy efficiency (calorific density, fuel consumption, etc.) or other characteristics (cetane number, flash point, etc.) and economic problems (raw materials, production process, etc.).

The main disadvantages of vegetable oils, as replacement of diesel fuels, are associated with their highly increased viscosity, 10-20 times greater than the normal diesel fuel. To overcome this problem, few options can be used: blending only a small portion of vegetable oils in diesel fuel, micro-emulsification with methanol or ethanol, cracking, and conversion into biodiesels mainly through the transesterification process. Similarly to vegetable oils, disadvantages of their derived biodiesels include high viscosity and pour point, low calorific value and volatility, low oxidation stability and hygroscopic tendency. For all reasons above, it can only be blended to maximum 20% of biodiesels or vegetable oils in diesel fuel to use in diesel engines without any modification (Rakopoulos et al. 2011).

Generally, alcohols show a better tendency to decrease internal combustion engine emissions. There are many studies performed to observe engine performance and exhaust emissions by alcohol fuels blended with diesel. Most of them concern the use of methanol and ethanol (Valentino et al. 2012). Methanol can be produced from coal or petrol based fuels with low cost production, but it has a restrictive solubility in the diesel fuel (Rakopoulos et al. 2010). Ethanol can be produced easily from biomass by fermentation but its properties are more suitable to be alternative for gasoline fuel. Ethanol possesses low viscosity and adding ethanol to diesel fuel reduces lubricity and creates potential wear problems in sensitive fuel pump designs (Yao et al. 2010; Rakopoulos et al. 2010; Valentino et al. 2012). In this context, butanol becomes a promising renewable fuel due to its many properties close to fossil-based fuels. With higher number of carbons in the molecule, butanol has higher heating value. Furthermore, this alcohol is less hydrophilic, has higher cetane number, lower vapor pressure and higher miscibility than ethanol and methanol, making it preferable for blending with diesel fuel (Rakopoulos et al. 2010; Yao et al. 2010; Doğan 2011).

	Density at 15°C, kg/m^3	**Flash point,** °C	**LHV,** MJ/kg	**Viscosity at 40°C,** cSt	**Cetane number**
Diesel[1]	845 ≥ x ≥ 820	≥ 55	43	4.5 ≥ x ≥ 2	≥ 51
***N*-butanol**[2]	810	35	33.1	2	15.92[5]
Vegetable oils[6]	903 - 960	150 - 277	37[7]	30 - 45[3]	38 - 45
Biodiesels[2]	881 – 891[4]	101	37.2	4.1 – 4.9[4]	48 - 65
Ethanol[2]	794	8	26.8	1.08	5 - 8
Methanol[2]	800	12	20	0.59	0-3

[1] EN590 Diesel fuel requirements in the EU
[2] (Tran 2013)
[3] (Esteban et al. 2012)
[4] (Kanaveli, Atzemi, and Lois 2017)
[5] (Lapuerta et al. 2017)
[6] (Blin et al. 2013)
[7] (Mehta and Anand 2009)

Table 1.2.1. Properties of diesel and certain potential biofuels

Butanol is a four-carbon alcohol with chemical formula of C_4H_9OH. It exists in four structural isomers (and five isomeric structures) as *n*-butanol, i-butanol, sec-butanol and t-butanol as shown in Figure 1.2.1. All four isomers contain about the same energy. However their manufacturing methods are very different. Tert-butanol is a petrochemical product and there is no known biological process that can produce it, whereas sec-butanol (2.33 cSt at 40°C) and iso-butanol (2.5 cSt at 40°C) have significantly higher viscosity compared to *n*-butanol (Bravo-Sánchez et al. 2010). With all above reasons, in this study, we choose *n*-butanol to study because of their excellent properties compared to others.

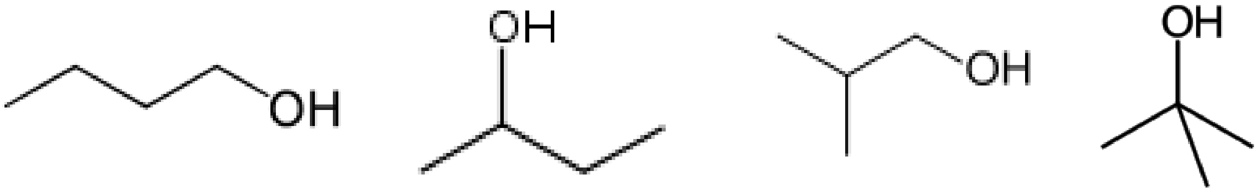

n-butanol sec-butanol iso-butanol tert-butanol

Figure 1.2.1. Structural isomers of butanol

1.2.1. Bio-butanol production

N-butanol is produced through petrochemical pathways as well as through biological mechanisms (Valentino et al. 2012). Indeed, bio-butanol can be produced from the same feedstocks as ethanol including corn, sugar beets, and other biomass feedstocks containing cellulose as barley, straw, bagasse, corn core, etc. The production of bio-butanol via fermentation has been used since the early 1900s. A clostridium acetobutylicum organism was found to be capable of converting large amounts of sugars into a mixture of acetone-butanol-ethanol (so called ABE process) (Chen et al. 2014; Nigam and Singh 2011). Later in 1950s, ABE fermentation lost their trend due to the increase of biomass feedstock cost. Almost all butanol was produced via petrochemical routes because petroleum derived solvents became more effective at that time. Until 2000s, the interest in bio-butanol was renewed, some research groups and biotechnology companies have been developing new process to increase the butanol yield of fermentation product (Chen et al. 2014). All the research efforts have brought bio-butanol close to large-scale commercialization as liquid alternative fuel.

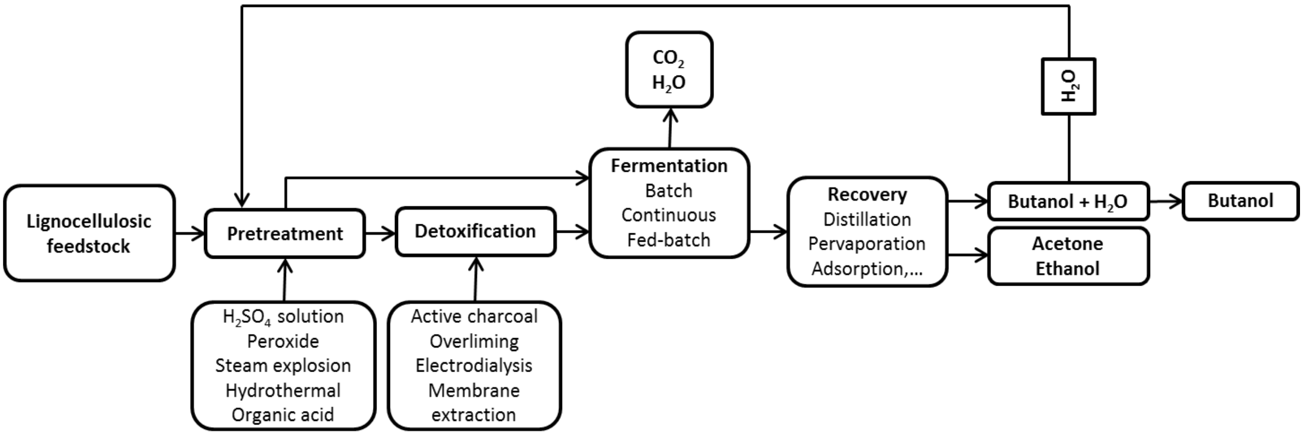

Figure 1.2.2. Schematic of biobutanol production process. Adapted from (Trindade and Santos 2017)

Figure 1.2.2 shows the production process of biobutanol. The process includes these following steps (Trindade and Santos 2017):

- Biomass containing lignocellulosics is pretreated using sulfuric acid, proxide, steam, hydrothermal or others, depending on the available material.
- Then inhibitors are removed through detoxification process by using activated charcoal, overliming, electrodialysis or others.
- Materials after the detoxification are now fermented using different methods.
- After the fermentation, the product is recovered and purified. Acetone, ethanol and butanol are separated based on their different boiling points.

1.2.2. Studies of soot emissions from *n*-butanol combustion in literature

Reference	Reactor	Fuel	Analysis techniques
(Rakopoulos et al. 2010)	High-speed direct-injection diesel engine	Diesel blended with 8%, 16%, 24% of *n*-butanol	Gas analyzer, Smoke meter, Non-dispersive infrared analyzer, Chemiluminescent analyzer, Flame-ionization detector
(Yao et al. 2010)	Heavy-duty direct-injection diesel engine	5%, 10%, 15% of *n*-butanol blended in diesel	Smoke meter, Exhaust analyzer
(Doğan 2011)	Single-cylinder direct-injection diesel engine	5%, 10%, 15%, 20% of *n*-butanol blended in diesel	Exhaust gas analyzer, Opacimeter
(Rakopoulos et al. 2011)	Six-cylinder heavy-duty direct-injection diesel engine	Blends of diesel and *n*-butanol (8%, 16%)	Gas analyzer, Smoke meter

(Valentino et al. 2012)	Common rail injection diesel engine	Diesel blended with 20% and 40% of *n*-butanol	Gas analyzer, Smoke meter
(Chen et al. 2014)	Single-cylinder heavy-duty diesel engine	40% of *n*-butanol blended with diesel	Exhaust analyzer, Smoke meter
(Choi and Jiang 2015)	Four-cylinder common rail direct-injection diesel engine	Blends of diesel and 5%, 10%, 20% of *n*-butanol	Differential mobility analysis, Condensation particle counter, Scanning mobility particle sizer, Transmission electron microscopy, Fourier transform infrared spectroscopy
(Jia et al. 2015)	Premixed laminar burner	Blend of 16.8% *n*-butanol in toluene reference fuel	Laser-induced incandescence
(Saxena and Maurya 2016)	Four-stroke, single-cylinder, direct-injection diesel engine	Diesel blended with 10%, 20%, 30% of *n*-butanol	Opacity meter, Particle spectrometer
(Yilmaz and Davis 2016)	four-cylinder direct-injection diesel engine	Blends of diesel and 10% or 15% of *n*-butanol	Thermogravimetric analysis, Fourier transform infrared spectroscopy, X-ray diffraction spectroscopy, Raman spectroscopy, Transmission electron microscopy
(Kumar et al. 2015)	Four-stroke, single-cylinder, direct-injection diesel engine	Blends of diesel and 10%, 20% or 30% of *n*-butanol	Gas analyzer, Smoke meter
(Viteri et al. 2017)	Tubular flow reactor	*n*-butanol	Gas chromatography-Mass spectrometry
(Chen et al. 2017)	Co-flow partially-premixed burner	20% and 40% of *n*-butanol blended in the mixture of toluene and *n*-heptane	Laser-induced fluorescence and Laser-induced incandescence
(Yan et al. 2017)	Premixed-combustio*n*-preheated constant volume combustion chamber	Blend of diesel and 30% of *n*-butanol	Transmission electron microscopy
(Cadrazco et al. 2017)	four-cylinder direct-injection diesel engine	Blend of diesel and 10% of *n*-butanol	Soluble organic material extraction and cell viability, Comet assay

(Ying and Liu 2017)	Inverse diffusion burner and Normal diffusion burner	Blend of 15% of *n*-butanol in ethylene	High resolution transmission electron spectroscopy, Raman spectroscopy, Thermogravimetric analyzer, Surface area and porosimetry analyzer, Elemental analyzer.
(Fushui Liu et al. 2018)	Partially premixed burner	16.8% and 20% of *n*-butanol blended in the mixture of toluene and *n*-heptane	Laser-induced fluorescence and Two-color laser-induced incandescence
(Xinling Li et al. 2019)	four-cylinder direct-injection diesel engine	20% of *n*-butanol blended in diesel	Gas analyzer, Scanning mobility particle sizer, OC/EC analyzer
(Verma et al. 2019)	Six-cylinder common rail diesel engine	Diesel blended with 20% and 30% of *n*-butanol	Transmission electron microscopy
(Huang, Li, et al. 2019)	Four-cylinder common rail diesel engine	Blend of diesel and 30% of *n*-butanol	Emission analyzer, Smoke meter
(Damyanov 2019)	Modified four-cylinder diesel engine	Blends of diesel and 10%, 20% of *n*-butanol	Standard exhaust gas measurement, Micro soot sensor, Particle counter, Smoke meter
(Lapuerta et al. 2019)	Euro6 diesel engine	10%, 20% of *n*-butanol blended in diesel	X-ray diffraction, Raman spectroscopy, Transmission electron microscopy, Surface area analysis, X-ray photoelectron spectroscopy, Fourier transform infrared spectroscopy, Thermogravimetric analysis and Differential scanning calorimetry
(Huang, Zhu, et al. 2019)	Four-cylinder diesel engine	20% of *n*-butanol blended in diesel	Exhaust analyzer
(Zhang et al. 2019)	High-pressure high-temperature constant volume combustion chamber		Backlight illumination, Laser extinction diagnostics

Table 1.2.2. Literature review on soot emissions of combustion involving *n*-butanol

The investigation of particulate emissions from *n*-butanol has caught more attention lately. Table 1.2.2 shows a review on studies of soot emissions from the combustion of *n*-butanol and blends of diesel-*n*-butanol. Most of studies focused on the emissions from blends of *n*-butanol from 5% to 40% in volume in conventional diesel or surrogates of diesel in diesel engine. In general, majority of scholars claimed that the addition of *n*-butanol in diesel reduces significantly soot emissions in the exhaust but increases unburned HC emissions (Rakopoulos et al. 2010; Yao et al. 2010; Doğan 2011; Saxena and Maurya 2016; Chen et al. 2017; Damyanov 2019; Huang, Zhu, et al. 2019). Some scholars explained that the addition of *n*-butanol in fuel prolongs the ignition delay, leading to a better mixing rate before the combustion starts, thus improving the particulate matter emissions (Valentino et al. 2012; Huang, Li, et al. 2019; Xinling Li et al. 2019). On the other hand, (Kumar et al. 2015) and (Zhang et al. 2019) concluded that the addition of butanol reduces the formation of soot rather due to the increase of oxygen content. (Zhang et al. 2019) also claimed that lower stoichiometric A/F ratio and higher latent heat of vaporization caused by the adding of alcohol in fuel might be additional reasons for soot reduction of *n*-butanol.

In 2015, (Jia et al. 2015) investigated experimentally and theoretically the influence of different alcohols, including *n*-butanol, on the formation of benzene, naphthalene and PAHs in premixed laminar toluene-reference-fuel flame. Their results show that the concentration of soot and the mole fractions of the PAHs are reduced with the addition of alcohols. They claimed that this reduction is mainly due to the dilution of toluene in the fuel blends by alcohol, thus reducing the formation of benzene. The presence of alcohols in fuel blends also increases the mole fractions of OH and O, which oxidize the PAHs produced in the flame. This might also be an additional reason of the reduction of PAHs.

Later in 2018, (Haifeng Liu et al. 2018) studied the process of soot and PAHs evolutions in a partially-premixed laminar flame at atmospheric pressure using LII and LIF techniques. Instead of using other conventional fossil fuels, blends of *n*-heptane and toluene were used as surrogate of diesel fuel. *N*-butanol and 2.5-dimethylfuran (DMF) were added to the base fuel. Similar as (Jia et al. 2015), they also concluded that the reduction of toluene content in blends due to the addition of oxygenated fuels is the main factor for the reduction of soot. *N*-butanol was found to be more efficient in reducing PM emissions due to its straight and low carbon chain structure. As DMF leads to much formation of $\mathrm{C_5H_5}$ radicals, which enhances the formation of PAHs and subsequent soot, *n*-butanol can only form PAHs through the production of small hydrocarbons like $\mathrm{C_2H_2}$ or $\mathrm{C_3H_3}$, etc. Additionally, particle size was also investigated in this study. The authors claimed that the addition of oxygenated fuels can shrink the size distribution of soot. The main reason might be that the smaller and larger sizes of soot are oxidized by the oxygenated fuel.

There are few works studying also the structure and morphology of soot particles produced from the combustion of blends with *n*-butanol. (Yan et al. 2017) are in agreement with other scholars that the blending of *n*-butanol in diesel reduces soot formation. Besides number and mass concentration, soot internal structure, geometry, and morphology are also changed by the presence of *n*-butanol in the blend. The aggregate particle and primary particle from *n*-butanol blend combustion were reported to slightly decrease, and the aggregation extent increased. The primary particle diameter of diesel-*n*-butanol blend was smaller, while average primary diameter number per aggregate N was bigger because the blend produces more PAH intermediate product than pure diesel.

In the study of (Lapuerta et al. 2019), the increase of reactivity of soot with the addition of *n*-butanol in diesel was reported. Besides that, the degree of order of soot nanostructure decreases and soot nanostructure becomes more disorganized with the addition of less than 10% of *n*-butanol. However, adding more than 10% of *n*-butanol in diesel, soot nanostructure becomes more organized. The increase of oxygenated functional groups on soot surface with the increase of *n*-butanol was reported. The consistency was found between soot oxygen functional groups and fuel components, thus these groups were claimed to come from fuel decomposition rather than being produced during the combustion process.

(Yilmaz and Davis 2016) had different conclusion since they claimed that soot nanostructure and morphology were not affected by the addition of butanol in diesel fuel. The content of -OH and aliphatic radical groups were found different for all samples. The authors also concluded that soot produced by dual-fuel with alcohol is more reactive to oxidation.

In 2019, (Verma et al. 2019) used TEM technique to investigate soot produced from blends of *n*-butanol and diesel in diesel engine. They concluded that the addition of butanol had significant impact on the aerodynamic behavior of soot, leading to different lung deposition patterns and different toxicity. An addition of 20% and 30% of *n*-butanol to diesel could refine particle size but increase specific surface area of soot. The scholars stated clearly that engine operating parameter had strong impact on the morphology and nanostructure characteristics of soot particles.

Differently to other research groups, (Ying and Liu 2017) compared soot samples produced in blend of ethylene and 15% of *n*-butanol in inverse diffusion flame (IDF) and normal diffusion flame (NDF). The addition of butanol enhances the growth of soot samples and reduces the degree of crystallization of soot compared to the one of pure ethylene flames. Soot from *n*-butanol addition in IDF showed the most amorphous carbon, whereas soot samples from NDF were aggregated by several tens or hundreds nearly rounded particles. The addition of butanol in IDF increases the soot reactivity with respect to NDF, because IDF had more disordered carbon, which was more accessible to oxygen.

Some studies showed that the use of *n*-butanol in conventional fossil fuels must be considered with more caution. (Choi and Jiang 2015) reported that the number of small particles (< 50 nm) was reduced when adding 5 – 10% of *n*-butanol. But this number increased when the addition was 20%. They warned that the addition of *n*-butanol in diesel should be less than 10% to reduce the PM mass. From a toxicological point of view, (Cadrazco et al. 2017) claimed that PM produced with *n*-butanol blends causes more DNA damage and more genotoxic than original diesel alone.

In conclusion, research on particulate matter emitted from *n*-butanol combustion has been getting more and more attention. However, the majority of studies were carried out in the engine, whose operating parameters interfere very much in the PAHs and soot formation as injection strategy, ignition delay, exhaust gas recirculation (EGR) rate, etc. Furthermore, scholars so far focused mainly on the PM concentration emitted with smoke meter. Only few of them went further with structure, morphology of soot using TEM, and PAHs variation with LIF technique. To better understand the formation of soot in *n*-butanol and the interference of it with diesel in the blend, it is necessary to investigate the combustion of these fuels in an actual flame without the influence of technique parameters from engine. The temperature - a very important parameter in combustion - of flame, evolution of soot and PAHs with reaction time, chemical information of soot surface are needed to be studied.

Thus in this work, a swirled jet burner is used to be able to burn *n*-butanol and its blend with diesel at atmospheric pressure and compare with diesel fuel. In-situ techniques as laser-induced incandescence/fluorescence (LII/LIF) are applied to obtain the evolution of soot and PAHs along the height of the flame – which equals to the variation of reaction time. Additional ex-situ techniques as two-step laser mass spectrometry (L2MS), secondary ion mass spectrometry (SIMS) are used to get chemical information of PAHs exhaust in gas phase and PAHs adsorbed on the soot surface. Temperature of flame could be obtained using thermocouple and two-color thermometry calculation. Other aspects as variation of particle size along the flame, soot temperature, soot volume fraction will be also discussed.

1.3. HEFA-Synthesized Paraffinic Kerosene as alternative fuel for aviation

In 2016, aviation took account for around 4% of the total greenhouse gas emissions and more than 13% of the emissions from transport in Europe (Greenhouse Gases Reviewer 2018). This makes aviation the second most important source of transport greenhouse gases emissions after road traffic. The contribution of air traffic may seem to be minor but it is expected to strongly increase in next years while other industries move to lower carbon options. This is the reason that aeronautics sector was included in the European Union Greenhouse Gas Emission Trading Scheme from 2012 (Starck et al. 2016). Aviation is also an important source of other air pollutants as nitrogen oxides (NO_x) and soot particles. Figure 1.3.1 shows pollutants emitted from a typical two-engine jet aircraft during 1-hour flight with 150 passengers. It should be noted that emissions reduction from aeronautics sector is more difficult to achieved than other sectors of the economy due to the relatively long lifespan of aircraft, which could remain in operation for 25 years or even more (European Aviation Environmental Report 2019). Furthermore, aircraft cruise emissions are the only direct source of anthropogenic soot particles at altitudes above the tropopause. These particles play as ice nucleation sites and cloud activators, which contribute to climate forcing indirectly (Abrahamson et al. 2016). Over past decades, much effort has been put in technological developments, except for the fossil-based fuel used by aircraft, which has remained relatively unchanged. Unlike road sector that has electrification as a promising strategy for decarbonizing, alternative clean propulsion technologies, such as electric-powered aircraft or cryogenic hydrogen fuel, are still under development and are unlikely to be commercially ready before 2030 (European Aviation Environmental Report 2019). Thus aviation sector will likely remain reliant on liquid fuels largely through 2050, particularly for long-haul flight (Pavlenko, Searle, and Christensen 2019). The International Air Transport Association (IATA) has identified the development of renewable fuel as the most promising strategy to reduce the environmental impact of the aviation sector (Gutiérrez-Antonio et al. 2017).

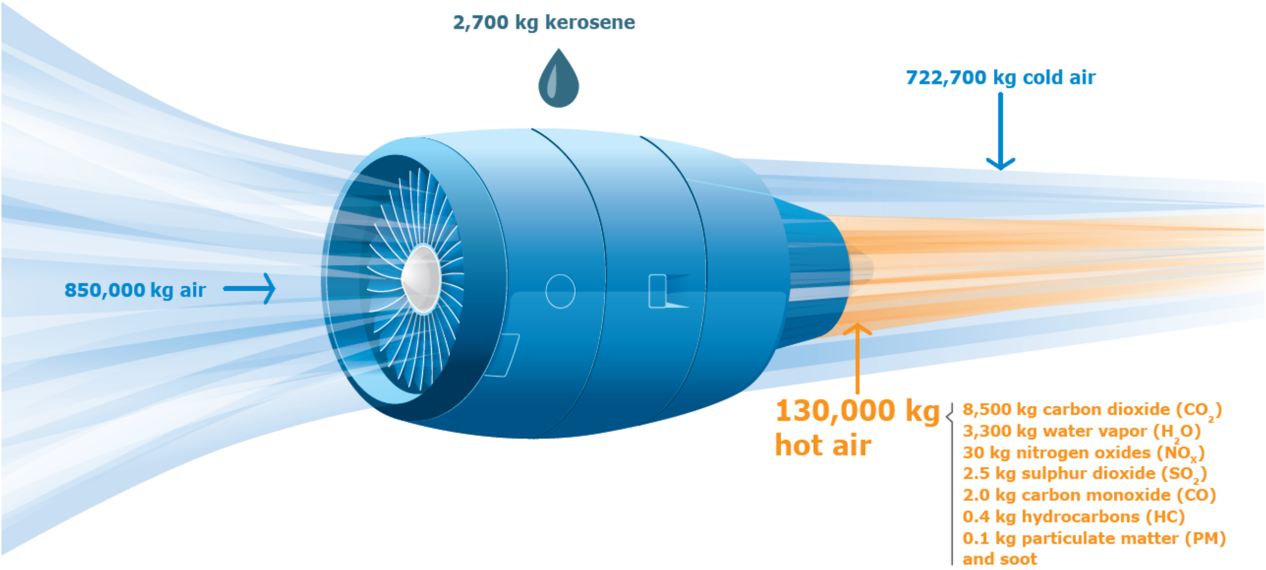

Figure 1.3.1. Emissions from a typical two-engine jet aircraft during 1-hour flight with 150 passengers (ICAO Environmental Report 2016 - Aviation and Climate Change 2017)

Bio-based aviation fuels are obtained from sources other than petroleum, such as woody biomass, hydrogenated fats and oils, recycled waste or other renewable sources (European Aviation Environmental Report 2019). There are many issues to be considered when evaluating the potential of a specific alternative fuel. These include, but are not limited to, the economic cost of fuel production, the technical feasibility of fuel, the impact of using the fuel on the atmosphere in terms of global climate change and air quality, and the efficient usage of resources (Hileman and Stratton 2014). There are three main governing ASTM standards with regards to aviation fuel certification and deployment, namely, ASTM D1655 (Aviation Turbine Fuels), D7566 (Aviation Turbine Fuel Containing Synthesized Hydrocarbons) and D4054 (Evaluation of New Aviation Turbine Fuels and Fuel Additives). While D1655 is the protocol for petroleum-based fuels, D7566 is used for alternative ones. However, all candidate for alternative jet fuels need to be evaluated through an approval process D4054, which is composed of four main tiers of testing: (i) fuel specification properties, (ii) fit-for-purpose properties, (iii) component tests and (iv) engine test (Vozka et al. 2019). Five pathways for alternative jet fuel production already certified as drop-in-fuels by ASTM are presented in Table 1.3.1.

Annex	Conversion Process	Abbreviation	Possible Feedstocks	Blending ratio by Volume	Commercialization Proposals
1	Fischer-Tropsch hydroprocessed synthesized paraffinic kerosene	FT-SPK	Coal, natural gas, biomass	50%	Fulcrum Bioenergy, Red Roc Biofuels, SG Preston, Kaidi, Sasol, Shell, Syntroleum

2	Synthesized paraffinic kerosene produced from hydroprocessed esters and fatty acids	HEFA-SPK	Bio-oils, animal fat, recycled oils	50%	AltAir Fuels, Honeywell UOP, Neste Oil, Synamic Fuels, EERC
3	Synthesized iso-paraffins produced from hydroprocessed fermented sugars	SIP-HFS	Biomass used for sugar production	10%	Amyrics, Total
4	Synthesized kerosene with aromatics derived by alkylation of light aromatics from non-petroleum sources	SPK/A	Coal, natural gas, biomass	50%	Sasol
5	Alcohol-to-jet synthetic paraffinic kerosene	ATJ-SPK	Biomass used for starch and sugar production and cellulosic biomass for isobutanol production	30%	Gevo, Cobalt, Honeywell UOP, Lanzatech, Swedish Biofuels, Byogy

Table 1.3.1. Conversion processes approved as annexes to ATSM D7566 (Status of Technical Certification of Aviation Alternative Fuels 2017)

Fischer-Tropsch hydroprocessed synthesized paraffinic kerosene (FT-SPK) was certified as the first nonpetroleum-originated synthetic blending component for civil jet fuels in 2009. This fuel conversion pathway includes the gasification of feedstock into synthesis gas – a mix of CO and H_2. This syn-gas is then combined with a catalyst in a reactor to generate a mix of hydrocarbons, which can be refined into various liquid fuels (Pavlenko, Searle, and Christensen 2019). The maximum blend ratio that can be used for FT-SPK is 50%v/v with conventional jet fuel. However, current commercial plants that produce FT-SPK have not used biomass as feedstocks, but only coal and natural gas. Thus FT technology does not really reduce the carbon footprint of air transportation (Vozka et al. 2019).

Synthesized paraffinic kerosene from hydroprocessed esters and fatty acids (HEFA) is the second nonpetroleum blending component approved by ASTM in 2011. Any vegetable oils, animal fats, or used cooking oil can be used as an HEFA feedstock. During the complex process of turning biomass into fuel, plant oils and animal fats are turned into a paraffin wax that is later submitted to FT process. Hence, HEFA-SPK properties are almost identical to the FT fuels (Baena-Zambrana et al. 2013). Maximum volume of HEFA-SPK which can be blended into conventional jet fuel is up to 50%v/v. HEFA fuels have reported lifecycle greenhouse gas emissions 60% lower than petroleum-based fuels (Pearlson, Wollersheim, and Hileman 2013). This is also the alternative jet fuel being studied in this work. Thus, details of this fuel production process will be presented in next subchapter.

Synthesized iso-paraffins (SIP) – which are also called direct sugars-to-hydrocarbons (DSHC) – are the third one getting approved in 2014. This fuel conversion pathway converts sugary feedstocks through fermentation into farnesene ($C_{15}H_{24}$), followed by upgrading into farnesane ($C_{15}H_{32}$), which can be used as drop-in fuel (Pavlenko, Searle, and Christensen 2019). The volume limited of SIP in jet fuels is up to 10%.

The fourth component, synthesized paraffinic kerosene with aromatic (FT-SPK/A) was appoved in 2015. It is a variation of FT-SPK, where alkylation of light aromatics creates a hydrocarbon blend that includes aromatic compounds. Maximum blend ratio of this fuel in conventional jet fuels is 50%.

Alcohol-to-jet synthesized paraffinic kerosene (ATJ-SPK) is the fifth component approved by ASTM in 2016. This fuel conversion pathway uses fermentation to convert sugars, starches, or hydrolyzed cellulose into an intermediate alcohol, either iso-butanol or ethanol, which is then further processed and upgraded into a mix of hydrocarbons. The maximum blend ratio allowed for this fuel is 30%v/v.

1.3.1. HEFA-SPK production

In this work, HEFA-SPK is chosen to be investigated in comparison with Jet A-1 fuel. While the cost of FT fuels is three times the cost of petroleum based jet fuels (Li, Mupondwa, and Tabil 2018), HEFA process has been described as low capital processes for producing high quality renewable jet fuel, showing the potential of substituting conventional jet fuels with low cost and environmentally beneficial biofuels. The HEFA hydrocarbon mixtures are primarily composed of saturated *n*-paraffins and iso-paraffins and do not contain any aromatics (Vozka, Šimáček, and Kilaz 2018). As mentioned earlier, any kind of vegetable oils or animal fats can be used as feedstock for this process. The main components of fats and oils are triglycerides, which are tri-esters comprising three fatty acid hydrocarbon chains and a glycerol backbone. The degree of unsaturation of the fatty acid chains varies according to the nature of oil or fat (Starck et al. 2016).

The hydrogenation process generally composes of few steps (Pearlson, Wollersheim, and Hileman 2013; Starck et al. 2016; Li, Mupondwa, and Tabil 2018) including:

- Catalytic hydrogenation, which is a treatment involving hydrogen, using noble metal catalysts or metal sulfide catalysts. Propane is then cleaved from the molecules, thereby producing three moles of free fatty acids.
- Deoxygenation, which consists of oxygen removal. The oxygen removal could be obtained via two pathways: (i) decarboxylation that produces a paraffin chain and CO_x or

(ii) hydrodeoxygenation which produces H_2O and a paraffin chain through the addition of hydrogen. After this step, oxygen is completely removed from the started material and a pure paraffinic product is obtained. This product has a very high cetane, but poor cold flow properties. Moreover, it also has a carbon-number composition very similar to the fatty acid carbon-number distribution of fat/oil feedstock. Although the carbon-number is in the diesel fuel range, it is still too heavy for jet fuel. Thus to improve these problems, it is necessary to treat the product with the next steps.

- Hydro-isomerization, which converts linear paraffins into iso-paraffins using a bifunctional catalyst comprising a hydrogenation function and an acid function.
- Hydrocracking, which is composed of catalytic cracking and hydrogenation. This step reduces the chain length within a carbon-chain distribution of approximately C8-C15 and produces more molecules from methane to liquefied petroleum gas (LPG).
- Separation, which includes certain distillation steps. Besides bio-based jet fuel, LPG, Naphtha and biodiesel are also obtained as by-products.

A HEFA production process is presented in Figure 1.3.2.

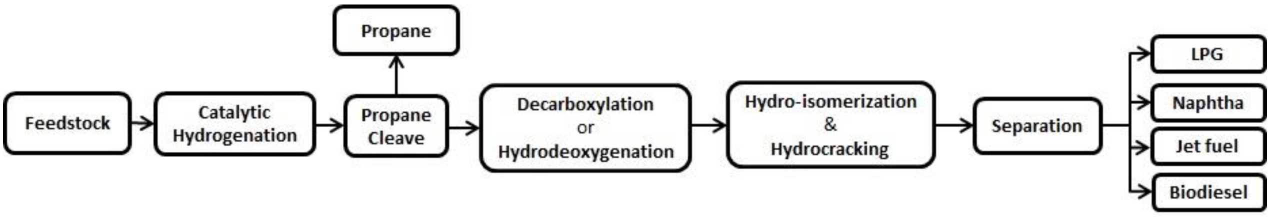

Figure 1.3.2. Schematic diagram of the HEFA process

1.3.2. Studies on soot emissions of HEFA-SPK in literature

Reference	Reactor	Fuel	Analysis techniques
Corporan et al 2011	T63-A-700 turboshaft engine	Hydroprocessed renewable jet fuels (HRJ) from Syntrolem and UOP, FT-SPK from Sasol, Shell and Rentech, JP-8	Condensation particle counter, Scanning mobility particle sizer, Nano-differential mobility analyzer, Tapered element oscillating microbalance, Fourier transform infrared based analyzer
Corporan et al. 2012	7 turbine engines	JP-8, 4 different FT-SPK and 3 different HEFA fuels	Condensation particle counter, Scanning mobility particle sizer, Nano-differential mobility analyzer
Lobo et al. 2015	Aircraft auxiliary power unit (APU)	Blends of Jet A-1 and used-cooking-oil HEFA with various blend ratios (from 2 to 95%w/w)	AVL advanced particle counter, Artium laser-induced incandescence LII-300, AVL micro-soot sensor, Cambustion DMS500 Fast particle analyzer
Christie et al.	GTCP85-129	Jet A-1 and blend of used-	Smoke meter, AVL advanced

2016	gas turbine engine (as an APU on Boeing 737 aircraft)	cooking-oil HEFA in Jet A-1 at different ratios (from 2 to 95%w/w)	particle counter, Artium LII, AVL micro-soot sensor, Cambustion DMS500
Moore et al. 2017	Four wing-mounted CFM56-2-C1 engines aircraft	Jet A-1 and a blend of Jet A-1 and 50%v/v Camelina-based HEFA	Condensation particle counters, Scanning mobility particle sizers, Radiance research particle soot absorption photometer
Xue et al. 2017	Non-premixed counterflow burner	JetA, JP-8, JP-5, FT-SPK, Camelina-based HEFA, and ATJ	Laser-induced incandescence, Light Extinction
Elser et al. 2018	Engine test cell at Zurich Airport	Blends of Jet A-1 and HEFA fuel at percentage 0, 5, 10, 32%v/v	Aerosol analyzer, Photo-acoustic extinctiometer, Scanning mobility particle sizer, Micro-soot sensor
Chan et al. 2018	General Electric CF-700-2D-2 turbo fan engine	SKA (synthetic kerosene with aromatic), FT fuel, mixture of 50% Jet A-1 and 50% Camelina-based HEFA	Engine exhaust particle sizer, Microaethalometer, Gaseous analyzer, Artinum LII,
Okai et al. 2018	Single concentric lean-burn burner for an aero-engine	Kerosene and HEFA	Flame ionization detetor, Photo acoustic soot sensor
Xue et al. 2018	Counterflow flame burner	Blends of Jet A-1 and three alternative jet fuels: camelina-based HEFA, FT-SPK, ATJ	Laser-induced incandescence, Light Extinction
Zheng et al. 2018	Tay combustor research rig	Different blends of Jet A-1 and bio jet fuels including a 80%/20% blend of HEFA and *n*-dodecane	Cambustion DMS500
Sundararaj et al. 2019	High enthalpy rig with combustor	7 different fuel blends. HEFA fuels are derived from Jatropha and Camelina	Artium LII 300
Liati et al. 2019	CFM 56-7B26 hi-bypass turbofan engine	Jet A-1, a blend of Jet A-1 and 32% HEFA	Scanning transmission X-ray microscopy coupled to near edge X-ray absorption fin structure spectroscopy

Table 1.3.2. Literature review on soot emissions of combustion involving HEFA-SPK

The influence of alternative jet fuels on their emissions, especially particulate matter emissions has been caught attention from researchers lately. Table 1.3.2 shows a summary of studies with HEFA-SPK up to date. All of reviewed studies concluded that fuel blends with HEFA-SPK and neat HEFA-SPK reduce significantly soot formation compared to conventional jet fuels in various conditions. This phenomenon is mainly explained by the fuel composition. HEFA contains lower (or no) aromatic compounds and higher *n*-paraffins compared to kerosene (Xue et al. 2017; Christie et al. 2017; Chan et al. 2015). Some authors preferred to use hydrogen content in fuel to explain the reduction of particulate matter emissions of HEFA since it showed better correlation (Lobo et al. 2015; Xue et al. 2017; Chen et al. 2014). In the study of (Corporan et al. 2011), they also mentioned that combustion temperature had strong impact on the production of soot from alternative jet fuels. This was explained that at lower combustion temperature, the rate of molecular soot growth and subsequent particle nucleation with the aromatic-free fuels is relatively low compared to conventional jet fuels, thus they produced significantly lower soot. However, at high combustion temperature, this reduction decreases because the relative role of aromatics on fuel soot formation is reduced as the chemical rates of soot production from paraffinic compounds increase. The theory was re-confirmed by the same research group in next year (Corporan et al. 2012). (Xue et al. 2017) mentioned in their study that the soot reduction of HEFA blends is not linear to the percentage of this alternative fuel in the blend. They explained that the high concentration of *n*-paraffins in HEFA leads to different production rates of small soot precursors (as C_2H_2, C_3H_3, etc.). That is why other alternative fuels (as ATJ, FT, etc.) containing more iso-paraffins show a linear correlation with soot reduction. Additionally, the presence of HEFA in fuel blends also decreases the particle size (up to 35%) as evidenced in studies of (Lobo et al. 2015; Corporan et al. 2012; Moore et al. 2017; Corporan et al. 2011). Whereas (Sundararaj et al. 2019) did not have the same opinion since they said soot particle size did not vary with the change in blend composition. Reactivity of produced soot is impacted with the presence of HEFA in fuel. However, the influence depends on conditions of engines. In the study of (Liati et al. 2019), soot reactivity of HEFA blend decreases slightly at ground idle conditions. But at climb-out conditions, the blend shows higher reactivity.

To sum up, previous works have paid more attention to the impact of HEFA-SPK fuel in soot emissions, however, most of studies focused on the particulate number and particle size. Soot optical properties and chemical composition of PAHs emitted along with the exhaust particles and gas has been studied scarcely. In addition, most of studies were carried on turbo engine – which includes many other factors influencing to soot formation as thrust, combustion temperature, etc. Furthermore, these experiments required a lot of time, effort and were expensive. Thus to simplify the parameters impacting to PM emissions, we propose an experiment carried on a modified CAST instrument – which can be used with liquid fuels as Jet A-1 of HEFA-SPK. The instrument is successfully developed by ONERA France and experiments were carried out in collaboration with three laboratories: ONERA, PC2A and PhLAM. Details of the modified liquid CAST will be presented in subchapter 2.1.3. The study on soot and PAHs produced from liquid CAST with LII and L2MS, ToF-SIMS will be shown in detail in chapter 5.

1.4. General objectives of the thesis

This thesis is performed in collaboration between the Combustion group from Physicochimie des Processus de Combustion et de l'Atmosphère (PC2A) laboratory and the ANATRAC group from Physique des Lasers, Atomes et Molécules (PhLAM) laboratory in the framework of the CERLA (Centre d'Études et de Recherches Lasers et Applications) at the University of Lille, Faculty of Sciences and Technologies. By following all achievements from previous works (Mihesan 2007; Faccinetto 2009; Bejaoui 2012; Irimiea 2017), the coupling between in-situ and ex-situ laser-based techniques is obtained to study the combustion products. The Combustion group of PC2A laboratory is well known with optical diagnostics as Laser-induced incandescence/fluorescence or Cavity ring-down spectroscopy, etc. applied on laboratory flames or industrial combustor. ANATRAC group from PhLAM has developed highly-sensitive and selective laser-based mass spectrometry techniques to analyze chemical composition of different types of samples. The collaboration between these two approaches can contribute to a better understanding of complex mechanisms leading to soot formation. Previous works at this platform were focused on the combustion of conventional fossil fuels as kerosene, diesel, etc. This dissertation is the first work investigating soot and PAH formation in the combustion of pure renewable fuels in these laboratories. Thus, this thesis has a general objective including the following main points:

(1) Develop a new method to separate non-volatile particulate matter and volatile particulate matter produced during the combustion. The front/back filter is tested with a CAST instrument at different set points with help from the CORIA laboratory (Rouen, France).
(2) Design and develop a new burner that allows us to burn different types of liquid fuels, including fossil fuels and alternative fuels, at atmospheric pressure without the intervention of other pilot flames. In order of that, a swirl generator is designed and developed into the burner to stabilize the combustion.
(3) Using in-situ LII/LIF techniques at different excitation wavelengths to detect and locate PAH and soot evolution along the home-made flame. Combustion products are then collected with front/back filter system and mass analyzed using two different ex-situ mass spectrometry techniques. The correlation between in-situ and ex-situ techniques is then exploited.
(4) A part of the thesis is in collaboration with ONERA laboratory to study the emissions of conventional and alternative aviation fuels. This work is carried on a liquid CAST instrument (developed at ONERA Palaiseau). Optical properties of soot and chemical composition of combustion products are obtained.

This work is composed of six chapters. The first chapter gives the practical and scientific context of the thesis. A review of biofuels using on road transportation as well as air transportation with bibliographic study on soot formation is presented. The second chapter describes in detail all experimental techniques and set-ups employed in this work. Furthermore, the theory of optical diagnostics and the description of statistical analysis used in this work are also reported. Chapter

3 focuses on our work of defining a new method to separate non-volatile particulate matter (nvPM) and gaseous PAHs using the so-called front and back filters approach. Chapter 4 includes in-situ and ex-situ experimental results obtained from our swirled flames with five different fuels. The chapter presents separately results from different techniques, and it shows the comparison between techniques and the comparison inter-fuels. The fifth chapter is dedicated to the study on aeronautic fuels with the liquid CAST instrument. LII results accompanied with the surface chemical analysis of soot particles are presented. The last chapter summarizes the main results of the thesis, and proposes some general conclusions with perspectives opened by this work.

Chapter 2.

Experimental techniques

2. Experimental techniques

2.1. Laboratory soot generators

2.1.1. Swirled jet flames

The swirled jet flames in this study are generated in a home-made burner at atmospheric pressure presented in Figure 2.1.1. The burner is equipped with a direct injection high efficient nebulizer (DIHEN-170-AA). The nebulizer consists of a capillary of 104 µm in diameter, surrounded with an annular space of 15 µm of thickness, as presented in Figure 2.1.2. This type of injector requires a gas flow supply with high speed as the driving force for liquid atomization. This nebulizer allows us to transform liquid fuel into very small droplets which are able to vaporize quickly.

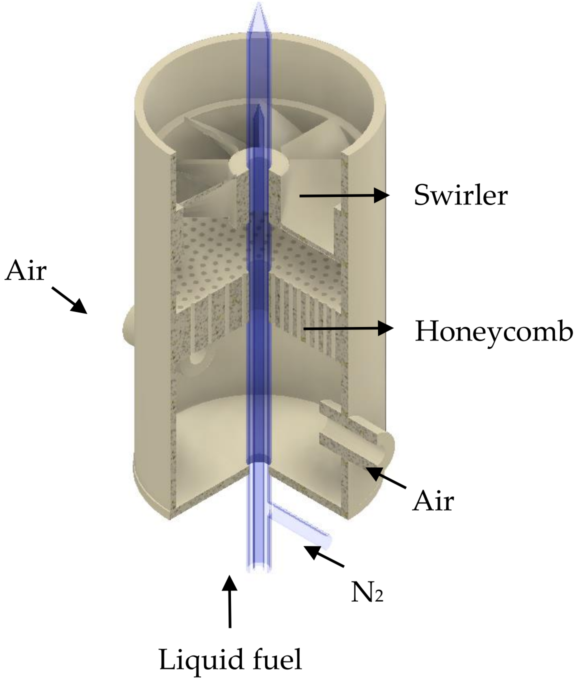

Figure 2.1.1. Sketch of the burner generating swirled jet flame in this study.

In this work, nitrogen is used as nebulization gas, which is regulated by a MFC Bronkhorst F-201CV. Oxidation air flow is regulated with a MFC Tylan FC-2920. MFC for gas is calibrated with DryCal Definer 220 device. Liquid fuel rate is regulated with a liquid MFC from Bronkhorst, model M13V14I.

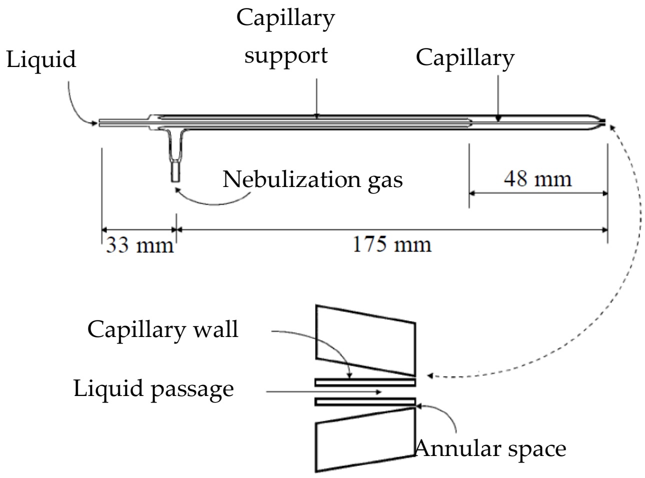

Nebulizer DIHEN 170-AA	
Material	Borosilicate
Inner diameter of the capillary D_c	$1{,}04.10^{-4}$ m
Thickness of the capillary e_c	$1{,}50.10^{-5}$ m
Outside diameter of gas passage section D_g	$1{,}73.10^{-4}$ m
Capillary section A_c	$8{,}49.10^{-9}$ m^2
Section of the annular space A_{ea}	$9{,}40.10^{-9}$ m^2

Figure 2.1.2. Specifications of nebulizer DIHEN 170-AA (PhD thesis Lemaire, 2012)

Air flows enter the burner from two symmetrized sides and are homogenized with the help of a honeycomb before getting swirled by a swirl generator. These two pieces are customized with Autodesk® Inventor® (Figure 2.1.3) and printed by 3D printer at PhLAM laboratory.

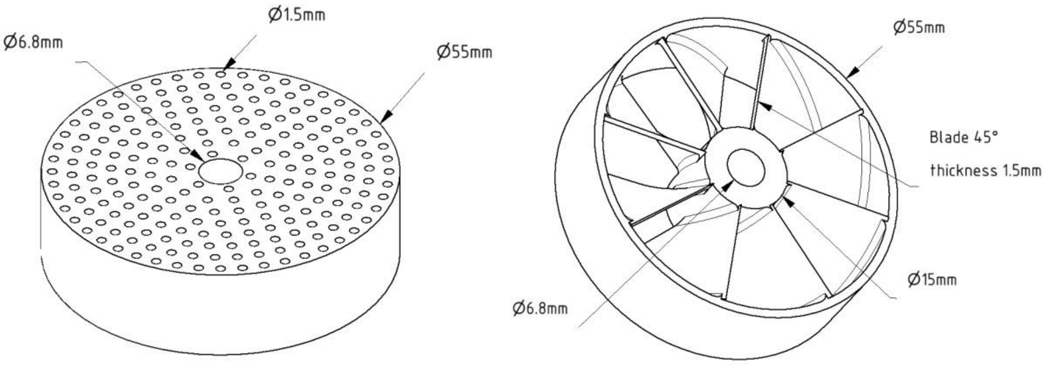

Figure 2.1.3. Sketch design of honeycomb and swirler

Twirler is used in this burner in order to improve the stability and efficiency of combustion. The flame is then able to burn by itself without the presence of pilot flame. The swirl number (S_{ng}) of the swirler is 1.193. The swirl number S_{ng} can be calculated using the following formula (PhD thesis Merlo, 2015):

$$S_{ng} = \frac{1}{2} \cdot \frac{1}{1-\varphi} \cdot \frac{1-\left(\frac{R_{tube}}{R_b}\right)^4}{1-\left(\frac{R_{tube}}{R_b}\right)^2} tan\alpha_o \qquad \text{(eq.1)}$$

where R_{tube} is the outside radius of the central tube, R_b is the radius of the coaxial tube, α_o is the angle of the blade to the outside border of the swirler and φ is the coefficient of block which can be calculated as below:

$$\varphi = \frac{z.s}{2\pi.R_h.cos\alpha_o} \qquad \text{(eq.2)}$$

where z is the number of blades, s is the thickness of the blades and $R_h = R_{tube}$.

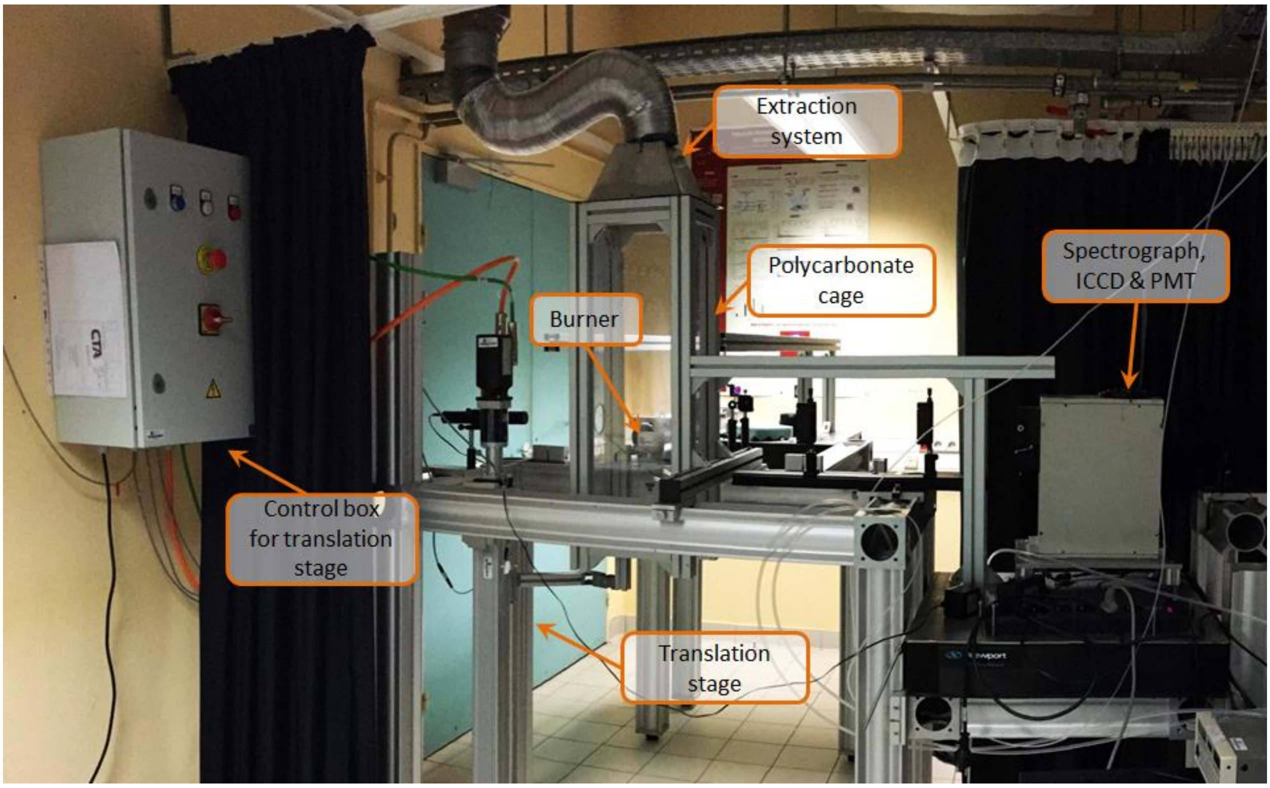

Figure 2.1.4. Picture of burner system endorsed in a polycarbonate cage, and mounted on a translation stage, below the extraction system and the detector. This experimental configuration is used for LII/LIF measurement

The burner is surrounded by a polycarbonate cage equipped with an extraction system as presented in Figure 2.1.4. The burner is mounted on a vertical translation stage consisting of a MTV 65 linear unit from Unimotion, coupled with a BMD 65 servomotor from Bonfiglioli. The translation stage system is supplied by CTA - France. The burner position can be modified on vertical axis with 1 μm precision and it can move on the vertical axis 65 cm.

In this work, four different fuels (diesel, *n*-butanol, Jet A-1 and SPK) will be studied in five flames as presented in Table 2.1.1. As heating values of *n*-butanol and diesel are different as presented in Table 1.2.1, flow rates of diesel, *n*-butanol and mixture, as well as the oxidation air are adjusted to produce the same heating energy. Jet A-1 and SPK flames have the same fuel flow rate as their lower heating values (LHV) values are similar. The information of flow rates used for five flames is presented as below.

Flame	Fuel, g/h	Oxidation air, sLm	Nebulization N_2, sLm
Diesel	109.06	22.24	0.264
N-butanol	142.1	21.95	0.264
Mixture	125.58	22.09	0.264
Jet A-1	109.06	22.24	0.264
SPK	109.06	22.24	0.264

Table 2.1.1. Flow rates of fuels, nebulization nitrogen and oxidation air in five swirled flames

2.1.2. Gaseous CAST soot generator

A miniature Combustion Aerosol Standard (MiniCAST, model 5201 C) was used in this work as a source of soot particles to develop and test a separation technique of condensable gas phase and particulate-bounded PAHs with Front Filter (FF) and Back Filter (BF). The MiniCAST device used in this study belongs to INSA laboratory (CORIA, Rouen University)(Yon et al. 2015; Bescond et al. 2016).

MiniCAST has a co-flow laminar diffusion flame of propane as presented in Figure 2.1.5. The burner consists of an inner tube with a diameter of 10 mm to provide propane fuel gas and nitrogen diluent, an outer tube with diameter of 30 mm to provide the combustion air. There is a nitrogen stream quenching the tip of the flame with the aim of freezing the combustion and preventing the oxidation of soot particles at the region near the front of the flame. The quenched combustion products are then diluted with air to inhibit the coagulation of particles.

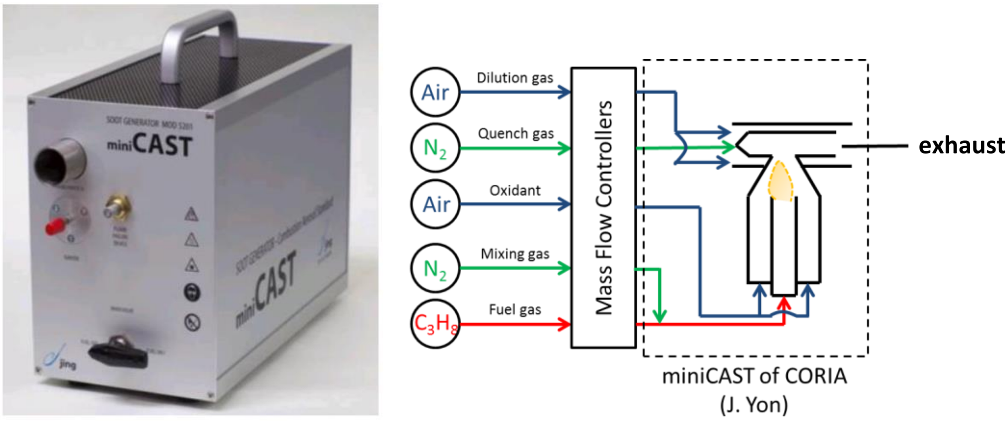

Figure 2.1.5. Photo (left) and schematic (right)f of MiniCAST burner (model 5201 C)

Different global fuel-air equivalence ratios are obtained by regulating the flow rates of fuel, fuel diluent, combustion air, dilution air and quench gas.

2.1.3. Liquid JING CAST soot generator

The liquid CAST soot generator is implemented by ONERA laboratory and its configuration is based on the previously presented MiniCAST. The device is mostly similar to the gas MiniCAST but contains an integrated mass flow controller which is able to measure precisely the liquid fuel flow consumed for the combustion (105 μL/min). The liquid fuel entering the instrument is vaporized by a pilot flame. The laminar diffusion flame is ignited by the propane (C_3H_8) pilot flame, and stabilized by an air shield. The fuel flow rate is maintained constant with a liquid MFC at 105 μL/min. The oxidation air flow N_2 and dilution air flows are maintained constant at 7 L/min and 30 L/min, respectively. The particles escaping from the flame are quenched with a nitrogen flow in order to prevent further combustion processes. Afterwards, the combustion flow is diluted with compressed air to avoid the coagulation of particulates before being sent to on-line analysis or deposited on filters. The photo and schematic of the device are presented in Figure 2.1.6.

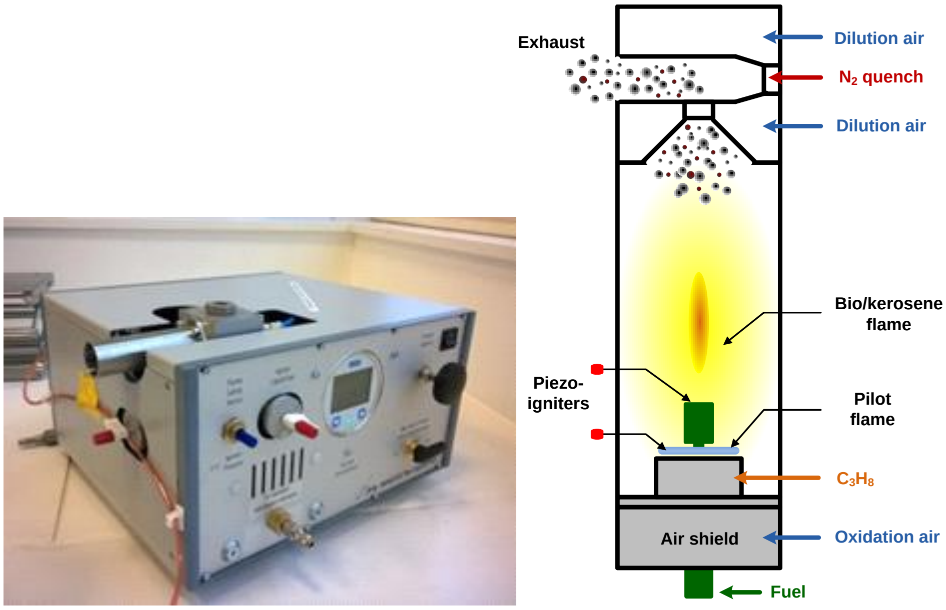

Figure 2.1.6. Photo and schematic of Liquid JING CAST (Private communication, Irimiea, 2019)

2.2. Thermocouple

Temperature in the non-sooting zone of five swirled jet flames is measured with an Inconel thermocouple type K model 406-534 purchased from TCdirect. This thermocouple is covered with semi-rigid metallic sheath. It is able to measure temperature in the range between -100°C and 800°C. The device is 300 mm long with 0.5 mm of diameter.

2.3. Soot sampling system

Combustion products are extracted from the flame with a sampling system, illustrated in Figure 2.3.1, containing a ceramic probe with inner diameter of 0.5 mm.

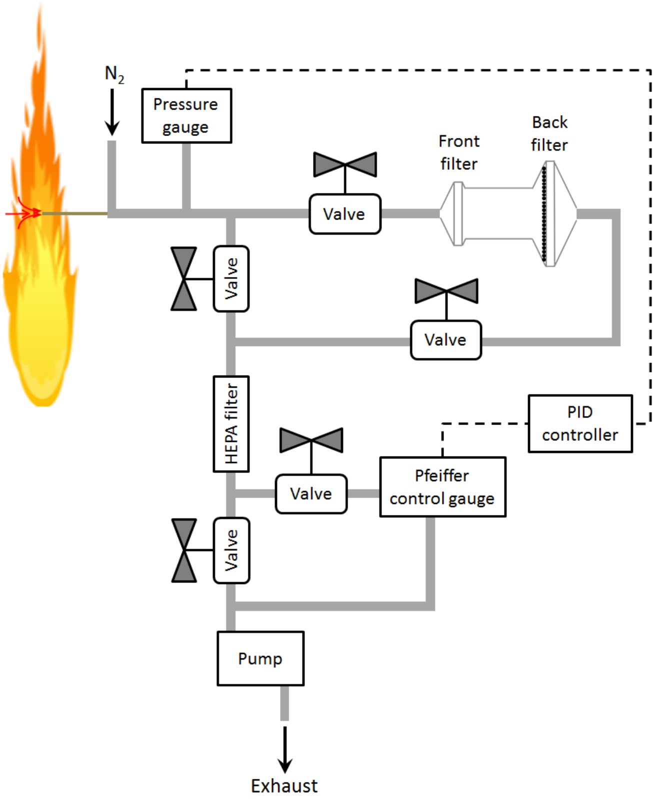

Figure 2.3.1. Scheme of extraction system

The probe is introduced radially in the swirled jet flames. A nitrogen flow coming from a side tube and controlled by a MFC Bronkhorst F-201CV with the flow rate of 4 L:min allows the dilution of soot and gas in order to reduce the condensation phenomena and quench the chemical reactions still occurring at the sampling time. Soot and gas enter the ceramic probe thanks to the pressure difference between upstream and downstream. The differential pressure is regulated by the reference pressure gauge which is located not far from the probe, a Pfeiffer control gauge (EVR 116) with a proportional-integral-derivative (PID) controller (Pfeiffer RVC 300). In order to not damage the Pfeiffer control gauge, the exhaust stream needs to pass through a TSI HEPA filter before entering the regulation system. In our study with swirled jet flame, all samples were collected with differential pressure of 10 mbar during 2 minutes.

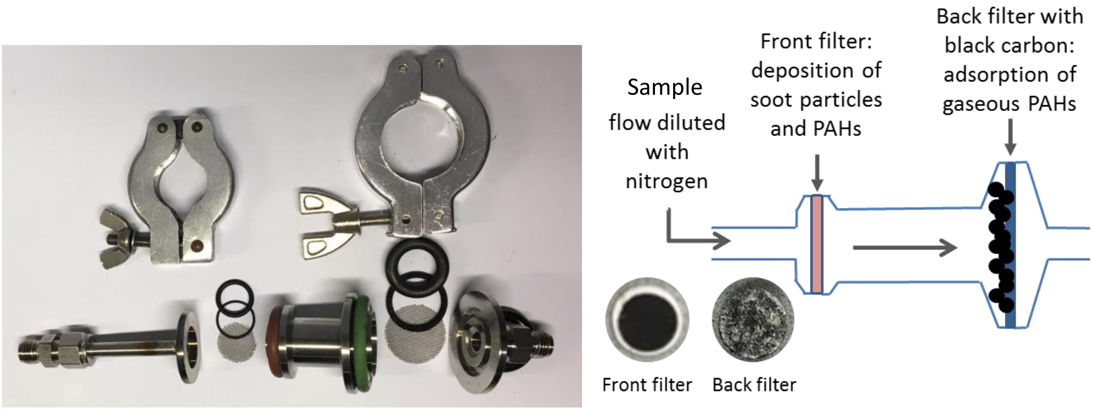

Figure 2.3.2. Sampling system of Front/Back filters

A bypass line is set in order to maintain the flow constant during the sampling procedure and to assist changing the deposition substrate. After entering the sampling line, gas and particles are deposited on the Front/Back filter system as shown in Figure 2.3.2. The sample-holder is a home-made piece consisting of an ISO-KF 16/25 fitting, Swagelok – KF fittings, sealing o-rings. The sample-holder is designed to hold a series of two substrates. In our case, Whatman glass fiber filters (grade GF/F with pore size of 0.7 µm) or quartz fiber filters (Pall Tissuquartz QAT-UP 2500) are used. The flow of soot particles and PAHs enters the system and deposes on the first substrate – called Front filter. The second substrate – Back filter, made of glass fiber filter with the deposition of a thin layer of black carbon, is used to adsorb gaseous PAHs passing through the Front filter. The Black carbon is previously activated in oven at 150^{o}C for at least one night. This technique allows us to separate condensable gas phase – which deposes on Back filter, and particulate phase – which deposes on Front filters. The collected samples are then analyzed using ex-situ MS techniques, described in following subchapters. The probe is fixed but the burner is mounted on a vertical translation stage – which allows us to easily collect the sample at different heights above the burner (HABs) in the selected flame.

2.4. In-situ experimental techniques LII/LIF

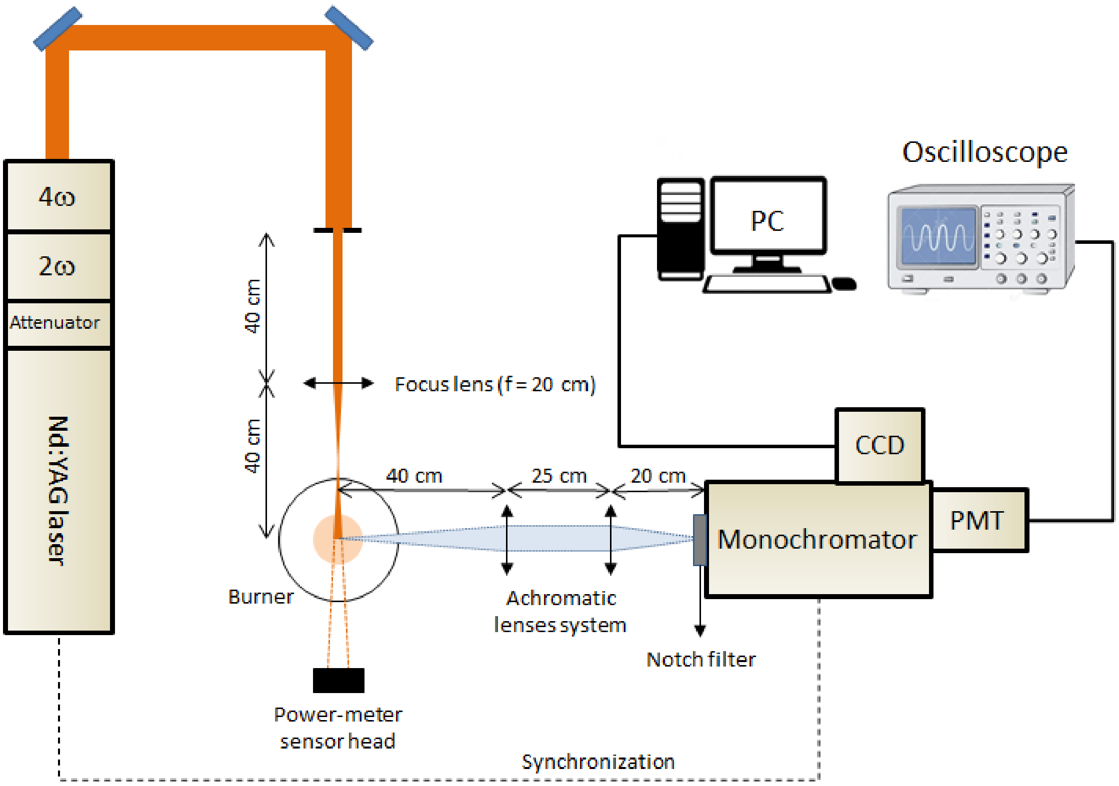

Figure 2.4.1. Scheme of the experimental setup used for LII/LIF measurements.

The setup used for laser induced incandescence/fluorescence (LII/LIF) measurements is illustrated in Figure 2.4.1. LII/LIF are in-situ techniques that use certain excitation wavelengths to detect particulate matter and gaseous species in flames. In this subchapter, principle and main parts of LII/LIF techniques such as excitation source, the detection system and calibration procedure are described.

2.4.1. Laser Induced Fluorescence (LIF) working principle

Laser induced fluorescence is a subsequent isotropic and non-coherent emission following the adsorption radiation by molecules. The technique was first evidenced by George Stokes in 1852. Certain molecules are able to absorb light at one frequency and subsequently emit light at different frequencies. The multitude of photo-physical processes taking place after the absorption of light can be described using the Perrin-Jablonski diagram, as showed in Figure 2.4.2 adapted from (Valeur 2005). This diagram is only applicable for organic molecules, but not for radicals as OH, CH, etc. S_0 stands for singlet ground states and S_i (i = 1, 2) for singlet excited states, grouped in the intermediary ro-vibrational energy levels (from 0 to 4). The triplet state (T_1) is the electronic state with parallel spins.

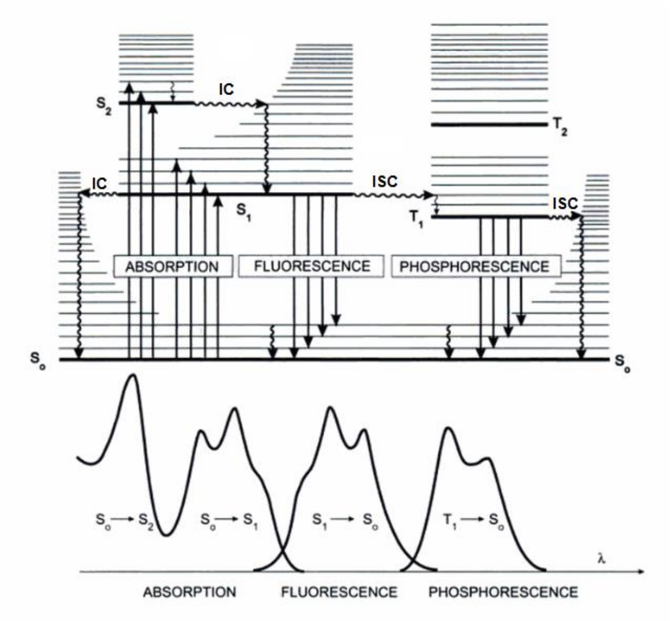

Figure 2.4.2. Perrin-Jablonski diagram representing energy levels and spectra (Valeur 2005). ISC is intersystem crossing. IC is internal conversion

The photophysical transitions can occur by radiative or non-radiative ways. The radiative transitions are intrinsic properties of excited species. However, the non-radiative processes are very sensitive to the change of temperature, pressure or concentration of excited molecules. These transitions have shorter lifetime than fluorescence, thus they can be dominant with respect to radiative processes.

a. Radiative transitions:

   i. Absorption: is the transition from the ground state S_0 to an excited state (S_1 and/or S_2) of the same multiplicity. This process accounts for a lifetime with the order of 10^{-15} s. This process can only occur if the photon has the energy equal to the transition energy of the electrons involved in the chemical bond.

   ii. Fluorescence: is a spontaneous emission of a photon due to the radiative relaxation from an excited electronic state to the ground state of the same multiplicity. It is well known as Kasha's rule, named after Michael Kasha who proposed it in 1950 (Kasha 1950). This process occurs in very short time. Indeed, a molecule can only stay at an excited state from 10^{-10} to 10^{-7} s before emitting a photon or being de-excited by other ways. Due to the loss of energy by the vibrational relaxation, fluorescence emission occurs with lower energy than absorption. This phenomenon is called "Stoke displacement". The loss of energy might be due to internal and intersystem conversions.

   iii. Phosphorescence: is a radiative relaxation from an excited state T_1 to the ground state S_0. Due to the difference of multiplicity of these states, this process occurs very slowly compared to other relaxation processes (10^{-6} to 1 s).

b. Non-radiative transitions:

i. Intersystem crossing: is a non-radiative transition between two vibrational levels belonging to electronic states with different multiplicity. This process is carried out by a coupling between the excited state S1 and the isoenergetic vibrational state of a triplet state T_1, then by vibrational relaxation until the zero vibration state of T_1. This relaxation is considerably fast with lifetime of 10^{-10} to 10^{-7} s.
ii. Internal conversion: a molecule can also be de-excited by evacuating through internal coupling or by colliding with other molecules. Lifetime of this conversion is from 10^{-14} to 10^{-10}s.
iii. Vibrational relaxation: is as energy transfer between vibrational levels in the same electronic state by internal or intramolecular collision. This process redistributes energy in each vibrational state and maintains a constant molecular internal energy. Lifetime of this relaxation is shorter than fluorescence (10^{-15} to 10^{-12} s).

An important property of fluorescence is its lifetime – the decay of fluorescence, shown in (eq.3). The population of the excited molecules [M*], which is generated at the moment of excitation t = 0 (at the end of the laser pulse), starts to decrease exponentially through the radiative (k_r), non-radiative (k_{nr}) and relaxation rate by collision (k_{coll})

$$\frac{d[M^*]}{dt} = -(k_r + k_{nr} + k_{coll})[M^*] \qquad \text{(eq.3)}$$

Then the population of the excited molecules can be obtained as (eq.4)

$$[M^*](t) = [M_0^*]exp(k_r + k_{nr} + k_{coll})t \qquad \text{(eq.4)}$$

where $[M^*]$ is the population of the excited level at t = 0. In the case of linear excitation regime, the population density on the excited state $[M_0^*]$ is related to the population density of the ground state M_0 through

$$[M_0^*] = M_0 \frac{K_{abs}(\lambda)}{(k_r + k_{nr} + k_{coll})} U_\lambda \qquad \text{(eq.5)}$$

where $K_{abs}(\lambda)$ is the absorption cross section at the corresponding excitation wavelength and U_λ is the spectral energy density per surface. From (eq.4) and (eq.5), one can obtain the population density of the excited level, in function of time. We can assume that the effective fluorescence lifetime is defined as:

$$\tau_{eff} = \frac{1}{(k_r + k_{nr} + k_{coll})} \qquad \text{(eq.6)}$$

The flux of emitted photons from a probing volume in a Ω solid angle corresponds to the fluorescence signal as:

$$\Phi_{LIF}(t, \lambda) = g_o k_{LIF} [M^*](t) \frac{\Omega}{4\pi} V \qquad \text{(eq.7)}$$

where g_o is the optical gain from the collection system, k_{LIF} is the fluorescence radiative rate and V is the fluorescence collection volume. By combining (eq.5) and (eq.7), the fluorescence signal can be written as:

$$\Phi_{LIF}(t,\lambda) = g_o k_{LIF} M_0 \frac{K_{abs}(\lambda)}{(k_r + k_{nr} + k_{coll})} U_\lambda \frac{\Omega}{4\pi} V exp\left(-\frac{\tau_r}{\tau_{eff}}\right) \qquad \text{(eq.8)}$$

where τ_r is the radiative lifetime.

The LIF technique has been developed and applied in several fields. In combustion, laser induced fluorescence is used to provide qualitative and quantitative measurements of fluorescent species such as diatomic molecules NO and OH or aromatic species as PAHs or to measure the temperature (Petarca and Marconi 1989; Desgroux et al. 1995; Nguyen et al. 1996; van Gessel et al. 2013, etc.). At PC2A laboratory, LIF technique has been applied widely in combustion domain in previous theses (Lemaire 2008; Wartel 2011; Bejaoui 2012; Mouton 2014; Irimiea 2017). In this study, the LIF technique is involved in the detection and localization of soot precursors.

2.4.2. Laser Induced Incandescence (LII) working principle

Laser induced incandescence is a technique relying on the heating of soot particles with a high powered laser to very high temperature, that is generally in the range of 2500-4000 K characterized by a blackbody emission, according to the Planck law. During and after the absorption of radiation, other processes can also occur as conduction, oxidation, annealing, sublimation and thermionic emission.

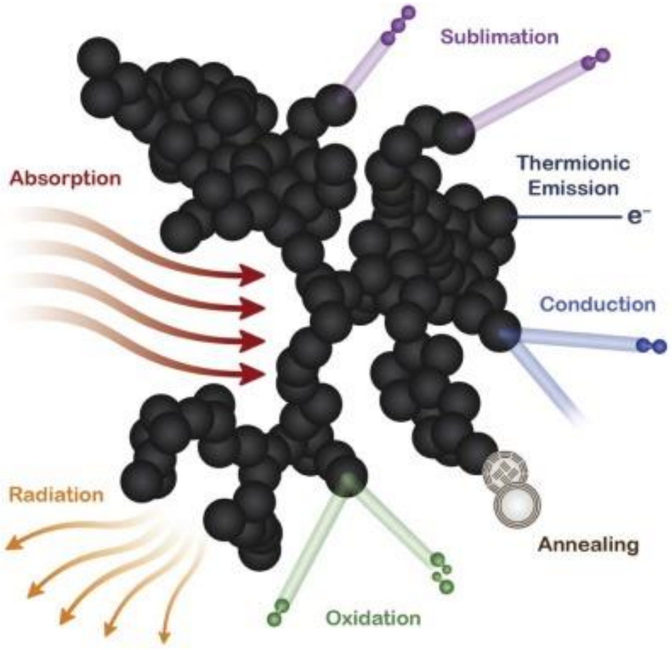

Figure 2.4.3. Illustration of processes influencing the temperature and mass of a particle during LII-signal collection (Michelsen et al. 2015).

Figure 2.4.3 illustrates the processes that influence the temperature and mass of a particle during LII-signal collection. Particles are first heated by absorption of laser radiation. The oxidation and annealing also contribute to the heating processes but this contribution is negligible. Afterwards, particles are cooled down by conduction to surrounding environment, sublimation, thermionic emission and radiative emission. Particle mass changes are through sublimation and oxidation processes. LII signal is derived from particle radiative emission (Michelsen et al. 2015). The emitted radiation is recorded with a fast photon detector or a CCD camera, at the start of the laser pulse or immediately after the laser pulse. Temporal or spatial LII signal can be measured depending on the detection system. Temporal LII signal is used to deduce the evolution of particle size by measuring decay time during cooling process (Michelsen et al. 2007), but this typically requires more sophisticated procedures with LII model comparisons (Olofsson et al. 2015). Spatial LII signal is used to determine soot volume fraction or to characterize the optical and physical properties of these particles (Therssen et al. 2007). However, quantitative volume-fraction measurements using LII technique require calibration with other techniques such as laser extinction (Michelsen 2017) or gravimetric sampling (Vander Wal, Zhou, and Choi 1996). In 2005, (Snelling et al. 2005) proposed a new technique to calibrate soot volume fraction in flame from absolute light intensity and blackbody temperature derived from the two-color LII (2C-LII) technique. This technique has the advantage to be independent of another source of particles with a known soot volume fraction. In this study, we also propose a new "direct technique" that is able to deduce the soot volume fraction from absolute LII signal calibrated with a known light source. The detail will be presented in subchapter 4.1.6.

All processes which occur during and after the absorption of radiation by the particle are described in detail below, adapted from the work of (Michelsen et al. 2015):

a. Energy and mass balance equation

The energy-balance equation of the particle can be described as:

$$\frac{dU_{int}}{dt} = \dot{Q}_{abs} + \dot{Q}_{raq} + \dot{Q}_{cond} + \dot{Q}_{sub} + \dot{Q}_{oxi} + \dot{Q}_{ann} + \dot{Q}_{therm} \qquad \text{(eq.9)}$$

where U_{int} is the internal energy of the particle, t is time, $\dot{Q}_{abs}$ is the absorptive-heating rate for a single primary particle, $\dot{Q}_{raq}$ is the radiative-cooling rate, $\dot{Q}_{cond}$ is the conductive-cooling rate, $\dot{Q}_{sub}$ is the evaporative-cooling rate, $\dot{Q}_{oxi}$ is the oxidative-heating rate, $\dot{Q}_{ann}$ is the heating rate from annealing, $\dot{Q}_{therm}$ is the thermionic-cooling rate. The rate of change of the internal energy of the particle can also expressed as:

$$\frac{dU_{int}}{dt} = Mc_s\frac{dT}{dt} = \rho_s c_s \frac{\pi d_p^3}{6}\frac{dT}{dt} \qquad \text{(eq.10)}$$

where M is the particle mass, c_s is the particle specific heat, T is the particle temperature, ρ_s is the particle density, d_p is the primary-particle diameter.

The mass loss is expressed as:

$$\frac{dM}{dt} = \left(\frac{dM}{dt}\right)_{sub} + \left(\frac{dM}{dt}\right)_{ox} \qquad \text{(eq.11)}$$

It is related to the particle diameter as:

$$d_p = \left(\frac{6M}{\pi\rho_s}\right)^{1/3} \qquad \text{(eq.12)}$$

b. Absorption of laser radiation

According to the Kirchhoff's law, the emissivity $\varepsilon(\lambda, T)$ is equal to the absorption coefficient $\alpha(\lambda, T)$ for the same couple of λ and T values, whereas T is the temperature of the considered soot particle.

In the Rayleigh approximation, where $d_p \ll \lambda$

$$\alpha(\lambda, T) = \frac{4\pi d_p E(m)}{\lambda} \qquad \text{(eq.13)}$$

where m is the complex index of refraction and $E(m)$ is the refractive index function for absorption. $E(m)$ is dependent of wavelength, and based on Kirchhoff's law, describes both absorption and emission properties of a particle.

The heating rate by absorption represents the energy transferred by the laser pulse to the soot particle. This property depends on the laser fluence and soot absorption efficiency as:

$$\dot{Q}_{abs} = \frac{\pi d_p^3 E(m)}{\lambda} E_e(t) \qquad \text{(eq.14)}$$

with $E_e(t)$ the time dependent fluence of incident beam.

c. Thermal radiation

The radiative-cooling rate can be calculated using the Plank function integrated over all wavelengths. If there is no wavelength dependence to $E(m)$, the radiative-cooling rate can be described as:

$$\dot{Q}_{rad} = -8\Gamma(5)\zeta(5)\frac{\pi^3 d_p^3 (k_B T)^5 E(m)}{h(hc)^3} \qquad \text{(eq.15)}$$

where k_B is the Boltzmann constant, the value of the gamma function of 5, $\Gamma(5) = (5-1)! = 24$, and the value of the Riemann zeta function of 5, $\zeta(5) = \sum_{n=1}^{\infty}\frac{1}{n^5} = 1.0363$. Thus:

$$\dot{Q}_{rad} = -\frac{198.97\pi^3 d_p^3 (k_B T)^5 E(m)}{h(hc)^3} \qquad \text{(eq.16)}$$

Normally, the radiative-cooling rate is significantly smaller than other cooling rates at atmospheric pressure and at high laser fluence. However, under vacuum condition and at low laser fluence, this process is dominant compared to others.

d. Heat conduction

Conductive cooling is considered to be the most important process for heat loss by particle at atmospheric pressure. The (McCoy and Cha 1974) expression assumes a transition regime between the free-molecular regime and the continuum regime and is presented as:

$$\dot{Q}_{con} = -\frac{2\kappa_a \pi d_p^2}{d_p + GL}(T - T_0) \qquad \text{(eq.17)}$$

where κ_a is the thermal conductivity of the bath gas, L is the mean free path, and G is a function of the heat-capacity ratio ($\gamma = C_p/C_v$ where C_p is the molar heat capacity of air at constant pressure, C_v is the molar heat capacity of air at constant volume), given by:

$$G = \frac{2(9\gamma - 5)}{\alpha_{\mathrm{T}}(\gamma + 1)} \qquad \text{(eq.18)}$$

where α_{T} is the thermal accommodation coefficient. This coefficient represents the heat fraction transferred by the surrounding gas from soot particles after collision and it depends on the gas nature and the soot surface.

e. Sublimation and other vaporization mechanisms

Evaporative-heat loss is the most important cooling mechanism at high laser fluence. And due to the significant mass loss from the particle body, this process leads to a rapid decrease of LII signal. The evaporative-cooling rate can be explained by:

$$\dot{Q}_{sub} = \frac{\Delta H_V}{W_V}\left(\frac{dM}{dt}\right)_{sub} \qquad \text{(eq.19)}$$

with ΔH_V is the enthalpy of formation of the sublimated carbon clusters, and W_V is the average molecular weight of the sublimated carbon clusters. The mass-loss rate attributable to the sublimation is given by:

$$\left(\frac{dM}{dt}\right)_{sub} = \frac{-\pi d_p^2 W_V \alpha_M p_V}{RT}\left(\frac{RT}{2\pi W_V}\right)^K \qquad \text{(eq.20)}$$

where α_M is the mass-accommodation coefficient, p_V is the average saturation partial pressure of the sublimed carbon clusters, and K is a constant that is typically equal to 0.5.

f. Oxidation

The oxidation mechanism can lead to both particle heating and mass loss. However, at high laser fluence, this process is much slower and less important than laser heating and evaporative-mass loss. The oxidative-heating can be expressed as:

$$\dot{Q}_{ox} = \frac{\left(\Delta H_{ox} + \alpha_T C_p^{CO} T\right)}{W_1}\left(\frac{dM}{dt}\right)_{ox} \qquad \text{(eq.21)}$$

where ΔH_{ox} is the enthalpy of the formation of CO, α_T is the thermal accommodation coefficient, C_p^{CO} is the heat capacity of CO, and W_1 is the molecular weight of a carbon atom. The rate of mass loss through oxidation can be described as:

$$\left(\frac{dM}{dt}\right)_{ox} = \frac{-\pi d_p^2 W_1 2 k_{ox}}{N_A} \qquad \text{(eq.22)}$$

with N_A is the Avogadro constant, and k_{ox} is the rate constant for CO formation reaction.

g. Annealing

This process is expected to be exothermic and leads to the heating of the particle. It could affect the other processes due to the change of physical structure in the particle. The heating rate for this mechanism can be expressed as:

$$\dot{Q}_{ann} = \frac{-\Delta H_{ann} k_{ann} N_d}{N_A} \qquad \text{(eq.23)}$$

where ΔH_{ann} is the enthalpy for annealing, k_{ann} is the rate constant for annealing and N_d is the number of defect sites in the particle.

h. Thermionic emission

Thermionic emission has a relatively small influence on the particle-cooling rate. However, it is also included in order to understand and predict the charging of the particle caused by laser heating. The cooling rate for this process can be expressed by:

$$\dot{Q}_{therm} = -\frac{4\phi m_e(\pi d_p k_B T)^2}{h^3}\exp\left(\frac{-\phi}{k_B T}\right) \quad \text{(eq.24)}$$

where ϕ is the work function, and m_e is the electron mass.

i. LII signal

The LII signal is thermal emission of black body radiation, that can be expressed by:

$$E(T,\lambda) = \int_{\lambda_1}^{\lambda_2} \frac{2\pi hc^2}{\lambda^5}\frac{1}{exp\left(\frac{hc}{\lambda k_B T}\right) - 1} d\lambda \quad \text{(eq.25)}$$

where E is the emissivity, T is the temperature, h is the Plank constant and c is the speed of light. The soot emission spectrum on a defined spectral range, depends on the value of its emissivity Q_{em}, and is derived from:

$$S_{LII}(T,\lambda) = \int_{\lambda_1}^{\lambda_2} Q_{em}\frac{2\pi hc^2}{\lambda^5}\frac{1}{exp\left(\frac{hc}{\lambda k_B T}\right) - 1} d\lambda \quad \text{(eq.26)}$$

Taking account to Kirchhoff's law, it is possible to make the approximation that heated soot particles are in thermodynamic equilibrium with the encountered radiation. Thus, soot particles emissivity is considered being equal with the absorption efficiency (eq.11). In consequence, the LII signal can be expressed as:

$$S_{LII}(T,\lambda) = \int_{\lambda_1}^{\lambda_2} N_p\frac{8\pi hc^2 E_m(\lambda) d_p^3}{\lambda^6}\frac{1}{exp\left(\frac{hc}{\lambda k_B T}\right) - 1} d\lambda \quad \text{(eq.27)}$$

Considering the soot volume fraction – defined as $f_v = N_p\frac{\pi d^3}{6}$ (with N_p the number of soot particles), the LII signal can be expressed by:

$$S_{LII}(T,\lambda) = \int_{\lambda_1}^{\lambda_2} \frac{48\pi^2 hc^2 E_m(\lambda)}{\lambda^6}\frac{1}{exp\left(\frac{hc}{\lambda k_B T}\right) - 1} d\lambda\, f_v \quad \text{(eq.28)}$$

2.4.3. Excitation sources

The excitation source is a Quantel Brilliant B laser with 6 ns pulse width and 10 Hz repetition rate. The device is equipped with a frequency doubling (2ω) and a quadrupling module (4ω) so it is able to generate 1064 nm, 532 n and 266 nm wavelengths. The energy of the laser beam is adjusted with an energy attenuator module – which consists of a half wave plate and a Glan prism. In our work, 1064 nm wavelength is used for LII, while 266 nm and 532 nm wavelengths are used to excite the fluorescence.

Mirrors are used to direct the beam through a circle pinhole (Φ = 1 mm). The laser beam is relayed at the center of the burner using a focus lens of 20 cm of focal length. The lens is placed at two times the distance of the focal length between the pinhole and the burner in order to avoid the diffraction patterns of the laser spot (Irimiea 2017). The profile of the laser beam is measured with a Gentec (Beamage) beam profiler. Each time the alignment is changed, the spatial profile of the laser spot is imaged at the center of the burner. The spatial profile or 1064 nm and 532 nm laser beams are presented in Figure 2.4.4 and Figure 2.4.5. Similar profile is also obtained for 266 nm laser irradiation. The laser beam energy is measured using a laser pyroelectric energy sensor OPHIR PE25-C placed after the burner as showed in Figure 2.4.1. The mirrors used to direct the laser beam are chosen according to the laser wavelength.

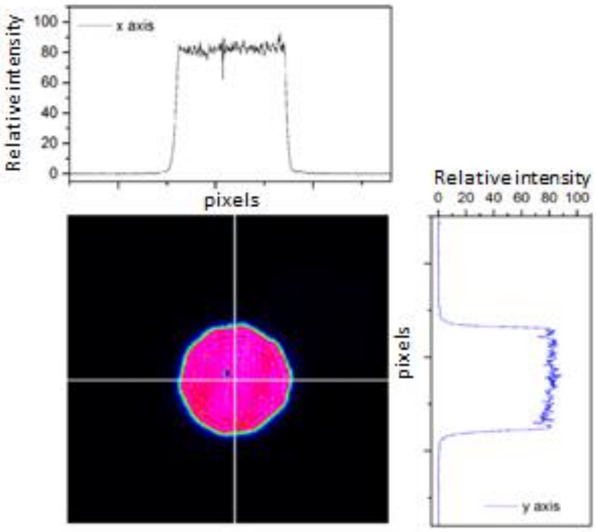

Figure 2.4.4. Top-hat spatial profile for 1064 nm laser irradiation (1127.5 µm x 1105.5 µm, ellipticity 98.0%)

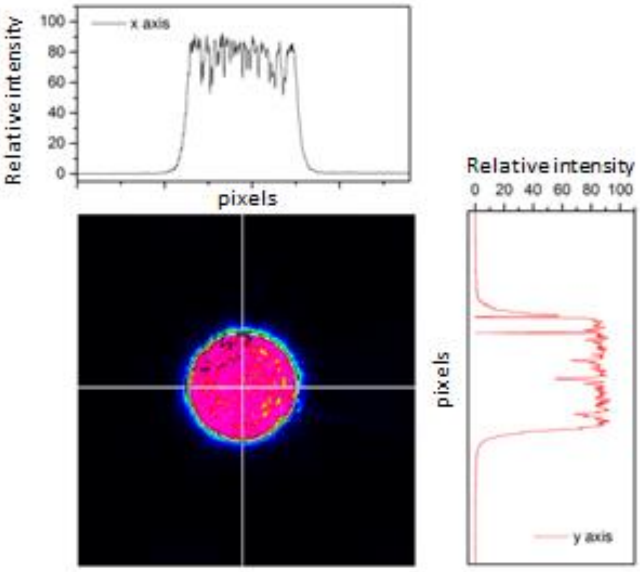

Figure 2.4.5. Top-hat spatial profile for 532 nm laser irradiation (1265 µm x 1248 µm, ellipticity 97.7%)

Incandescence or fluorescence emission from the flame is collected through the slit of a spectrograph using two achromatic lenses (f_1 = 40 cm and f_2 = 20 cm) setting a magnification factor of 0.5. A Notch filter is used for removing part of 532 nm laser irradiation in order to limit the undesired signal produced by the excitation wavelength due to the Rayleigh scattering.

2.4.4. Detection system

2.4.4.1. *Spectrograph*

The emission signal is collected with an Acton SP300i (with a focal distance of 30 cm) spectrograph. The entrance slit is adjustable between 12.5 and 2000 µm. In our study, the entrance slit is set at 1000 µm. Two diffraction gratings are used: 150 groves/mm, blazed at 300 nm (high transmission in UV) and 150 groves/mm, blazed at 800 nm (high transmission in near IR). The diffraction gratings are rolled around a rotating mount. This allows us to select the desired wavelength for the detection according to the emission spectral range. The spectral width covered by these diffraction gratings is almost 260 nm. The spectral calibration of the spectrograph is carried out using an Ar-Hg pencil calibration lamp – which emits known emission lines. The spectrograph has two outputs provided to collect the signal either by a photomultiplier tube (PMT) or by an ICCD camera. The output connected to the PMT is equipped with an adjustable slit. The PMT enables the recording of the temporal LIF signal while the camera provides 1D spectral images of the collected photons as explained in the following.

2.4.4.2. *Photomultiplier tube (PMT)*

The temporal profile of the LII signal is recorded using a photomultiplier tube placed after the spectrograph. A PMT contains a photocathode, several dynodes, and an anode. All of the materials are constructed in evacuated glass housing like vacuum tube. An incident photon of few eV arrives on the photocathode of the PMT and ejects an electron from the surface as a consequence of the photoelectric effect. This electron is accelerated by the electric field, and then multiplied by emitting surfaces. The output is an electrical signal which is proportional to the number of incident photons as illustrated in Figure 2.4.6. The PMTs are extremely sensitive to light, with a short rising time. It allows us to detect photons with a very low incident flux.

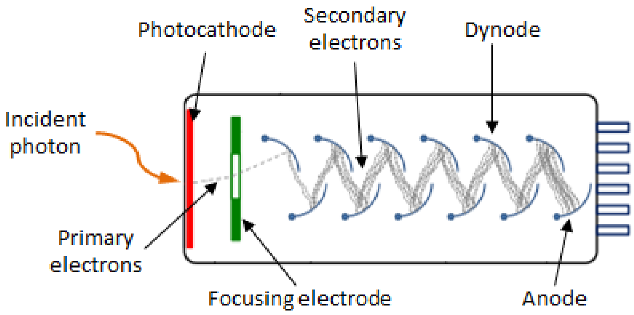

Figure 2.4.6. Working principle of a photomultiplier tube

Thanks to the spectrograph, the optical signal corresponding to a selected wavelength is send to the first exit with an adjustable slit set at 300 µm. In our case, a Philips XP2020Q PMT supplied by a Hamamatsu C7169 high voltage power supply is employed. This PMT is characterized by a rising time of 1.5 ns and an optimal spectral response between 400-800 nm. The temporal profiles are recorded using a Lecroy WaveSurfer oscilloscope of 500 MHz. The signal is triggered with a photodiode detector (Thorlabs DET 210) and averaged over 1000 laser shots.

2.4.4.3. *Intensifier charged-coupled device (ICCD) camera*

An ICCD camera consists of two main parts: the intensifier and the CCD detector. The intensifier contains a photocathode, a micro channel plate (MCP) and a phosphor screen as presented in Figure 2.4.7. When an incident photon enters in the window of the intensifier, the photocathode converts it into photoelectrons, which are then accelerated by an electrical field towards the MCP – which is a mosaic of plates containing very thin channels that are made from semiconductor glass. Once enter the MCP, electrons are accelerated in these tubes and collide with glass channel walls which in turn multiplies them. After that, the phosphor screen converts back the electrons into photons. The formed image is transferred to the focal plan of the CCD through optical fibers of 4 – 6 μm diameter. Each fiber transports a portion of signal and then by combining several fibers, it forms the signal for each pixel. The image is then detected by the CCD array, digitized and transferred to computer.

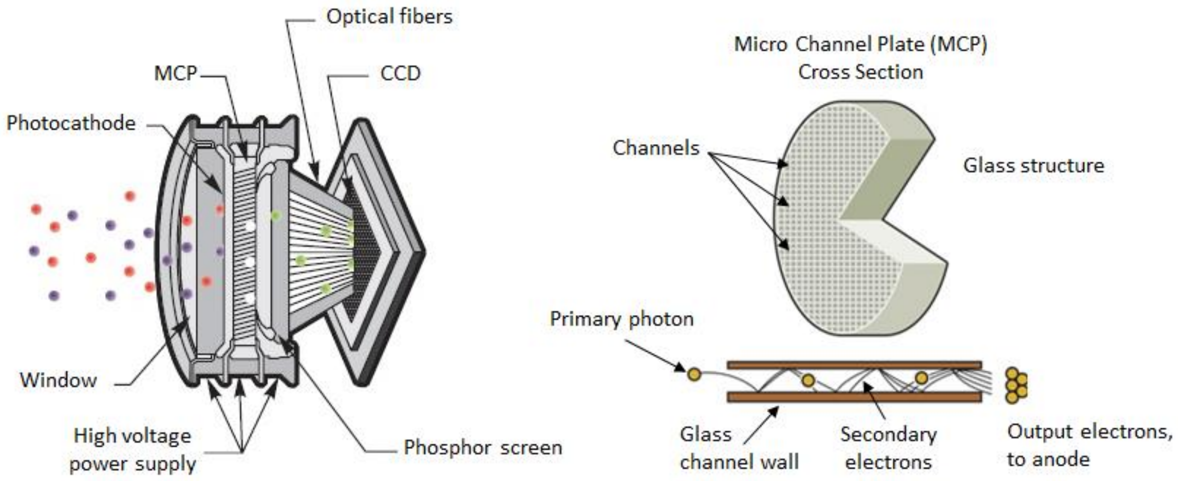

Figure 2.4.7. Scheme of working principle of an ICCD intensifier

In our study, a Princeton Instrument PI MAX detector (equipped with an HB Gen III intensifier) is used to record the collected light from the flame redirected by the achromatic lenses. Its optimal quantum efficiency range is between 280 and 700 nm. It includes a 512 x 512 pixels array. Each pixel has a size of 23 μm. If we take into account the magnification imposed by the two achromatic lenses (0.5), the spatial resolution of the collection system is 46 μm per pixel in the flame. The obtained image represents the sum of all the intensities emitted along the radial profile of the flame on irradiated volume. Full CCD image, also called 1D-spectral image is recorded in order to obtain the emission spectra for the chosen wavelength domain or to obtain the flame emission profile, depending on binning methods. The ICCD is synchronized with the laser pulse. An electric impulse from the Q-switch is sent out of the laser to the camera controller in order to open and close the ICCD gate between two consecutive laser pulses.

2.4.5. Transfer function calibration

An optical chain has its own optical response called optical transfer function (TF). To interpret correctly the results, it is necessary to determine the optical response of the measurement system on selected wavelength range. To do that, we used an integration sphere from SphereOptics CSTM-LR-6-M, placed at the same position as the burner, with the same optical path. The sphere consists of a lamp located inside of a cavity, which is covered by white Lambertian substrate ($BaSO_4$). It emits a black body type radiation with a tunable temperature between 2000 and 3300 K by adjusting the voltage of the external power supply module. An optical fiber connected with the sphere directs the light to another calibrated spectrograph, which provides spectra as reference. The configuration used to obtain the optical response by using the sphere is shown in Figure 2.4.8.

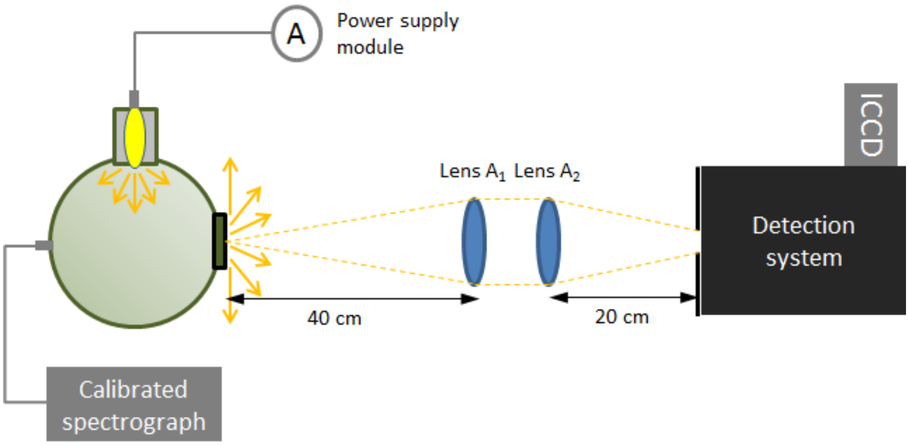

Figure 2.4.8. Set up used to determine the optical response of measurement system

Parameters used in LII/LIF measurements (as settings of ICCD detector, slit height, optical path) are kept constant while measuring the spectrum of the Sphere radiance. The transfer function of the collection system is calculated as the ratio between the two spectra, the spectrum recorded with the ICCD and the reference spectrum from the calibrated spectrograph. The TF is important to calculate soot particles temperature using Planck law, which will be presented later in subchapter 4.1.6.1.

2.5. Ex-situ experimental techniques

2.5.1. Two-step Laser Mass Spectrometry (L2MS)

Two-step Laser Mass Spectrometry is an ex-situ technique which consists of three stages: laser desorption (LD), laser ionization (LI) and time-of-flight mass spectrometry (ToF-MS). This technique was developed in our group well before 2009 and can be especially sensitive and selective to the analysis of PAHs desorbed from soot (Mihesan et al. 2006; Bouvier et al. 2007; Thomson et al. 2007; Faccinetto et al. 2008; Ziskind et al. 2009; Faccinetto 2009; Faccinetto et al.

2011; Faccinetto et al. 2015; Irimiea 2017). The principle of the technique is described in Figure 2.5.1. During a L2MS analysis, the surface of the solid sample is irradiated by a first nanosecond laser pulse – laser desorption. Neutral species are then desorbed from the sample as a consequence of the induced local heating. A second nanosecond laser pulse – laser ionization – irradiates, after a delay (in this case 100 µs), the expanding plume of ejecta to produce the ions to be mass analyzed.

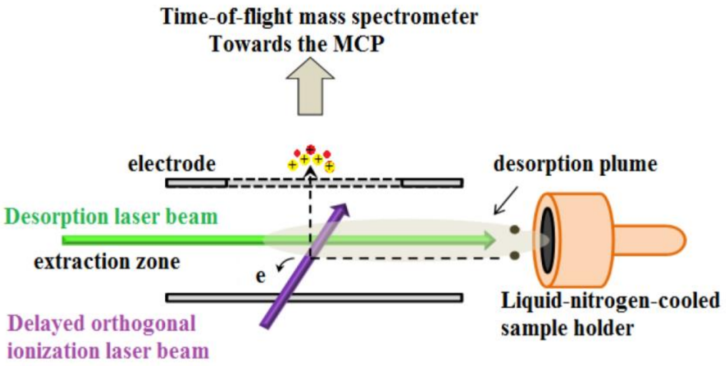

Figure 2.5.1. Scheme of working principle of L2MS technique (Irimiea 2017).

In the whole process, the sample is cooled down to -100°C to avoid the sublimation of volatile compounds in vacuum. The sample is introduced in a preliminary chamber, which is equipped with a holding arm to assist the sample holder (as presented in Figure 2.5.2). The core of the arm is insulated with regard to the atmosphere using an empty layer pumped at a preliminary vacuum pressure (10^{-2} Torr). Liquid nitrogen incorporated in this core starts circulating since the pressure of the preliminary chamber goes down to 10^{-2} Torr by using a primary pump (Agilent TS300). After that, a secondary turbo pump (Agilent TV301 NAV) takes place to decrease the pressure until high-vacuum. As soon as the pressure of preliminary chamber reaches 10^{-7} Torr, the gate valve is opened and the sample is introduced into the analysis chamber at very high vacuum with residual pressure of 10^{-9} Torr.

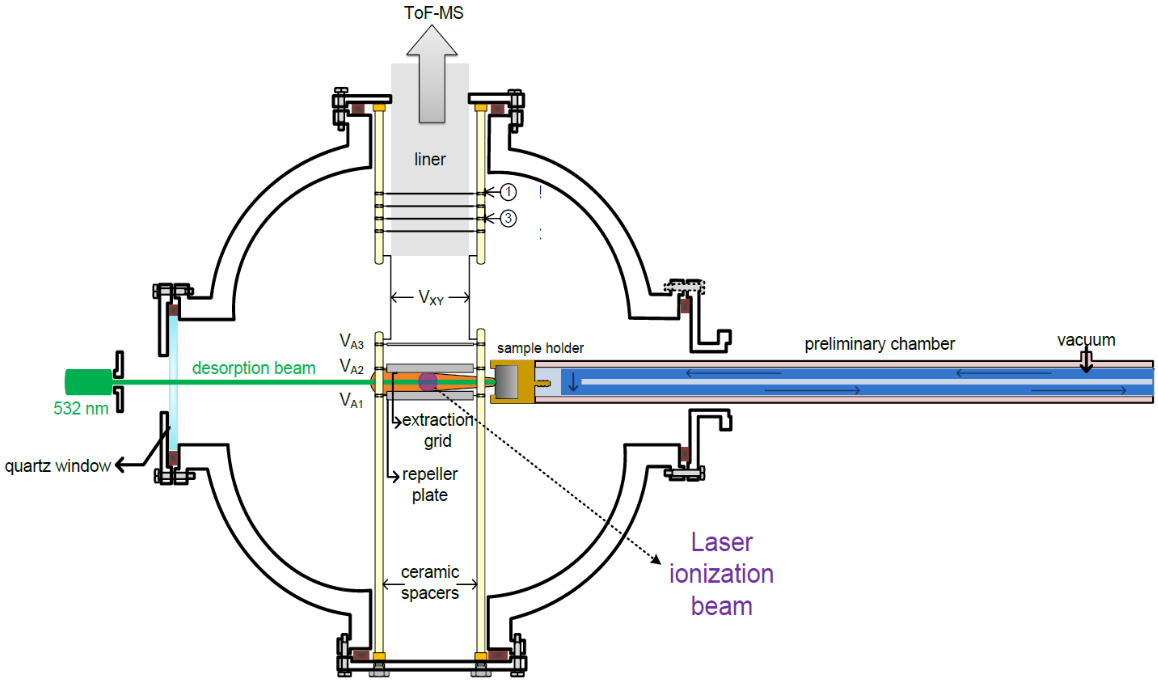

Figure 2.5.2. Cross section of analysis chamber, top view (Irimiea 2017).

2.5.1.1. *Laser desorption*

After entering the analysis chamber, the sample is irradiated at normal incidence by the laser desorption pulses - 2nd harmonic (532 nm) of a Nd:YAG laser (Continuum Minilite II, 3-5 ns pulse duration, 10 Hz repetition rate).

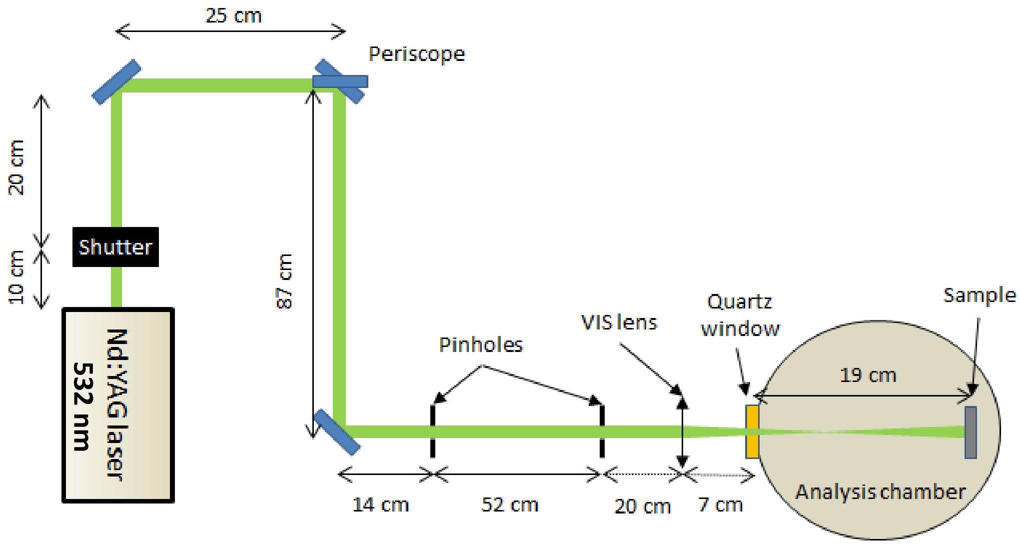

Figure 2.5.3. Optical pathway of the laser desorption beam.

In this stage, the energy transfer involves both the carbonaceous matrix and the adsorbed substances, in consequence, inducing a desorption of neutral species from the sample surface (Faccinetto 2009). Since this is a soft desorption process, only a fraction of the first monolayer is removed from the sample surface (Faccinetto et al. 2015).

The optical pathway of the laser desorption beam is illustrated in Figure 2.5.3. The shutter placed on the pathway of the laser is able to permit a defined number of laser pulses to irradiate the sample surface each time. In this study, 200 laser pulses are used for all L2MS analyze. The distance between the VIS lens and the quartz window is adjustable to adapt the size of the laser beam for each sample. Laser fluence is also adjusted from one sample to another to have good signal to noise ratio and to optimize the signal.

2.5.1.2. *Laser ionization*

Due to the desorption step, the species ejected from the samples surface (forming the so-called desorption plume) expand with velocities of hundreds of m/s (Mihesan 2007) in between the ToF-MS repeller and the extraction grid. The plume is now irradiated by a quadrupled Nd:YAG laser (Continuum Powerlite 8010, 6ns, 10 Hz repetition rate) with 266 nm wavelength. The optical pathway of the ionization laser beam is shown in Figure 2.5.4.

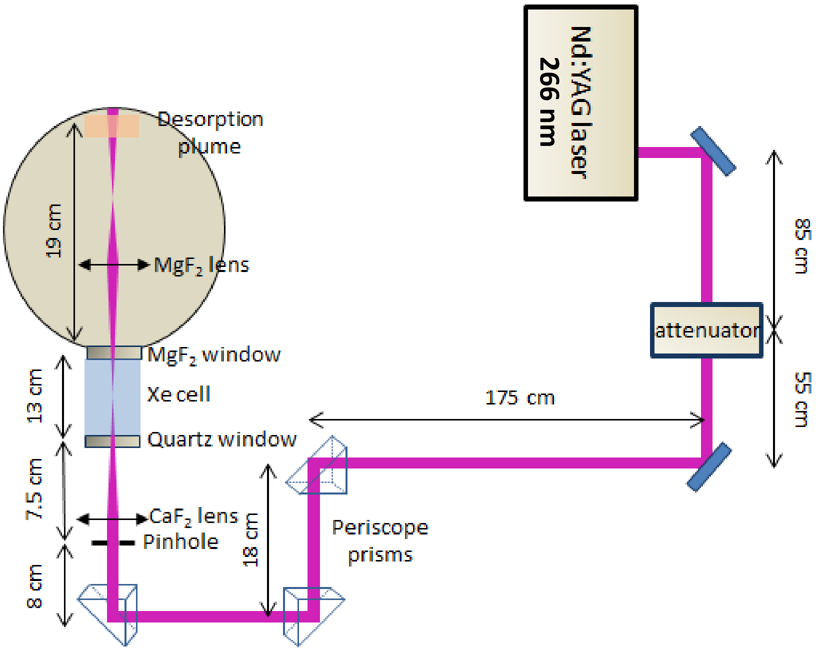

Figure 2.5.4. Optical pathway of the ionization laser beam.

The laser energy is set to maximum output in order to obtain a stabilized beam. An attenuator (Altechna S/N 6ATT693D) is placed on the optical pathway to adjust the fluence. From one sample to another the fluence is optimized to get the maximum and fragment-free signal.

In this study, we are especially interested in PAHs due to their important role in the soot particle formation. As illustrated in Figure 2.5.5, these molecules have ionization energies below 8.2 eV. Most of these species have electronic absorption features around 250 nm. This makes the utilization of 266 nm excitation wavelength as ionization source sensitive and selective to polyaromatic compounds in a resonance-enhanced 2-photon ionization (R2PI) process (Carpentier, Pino, and Bréchignac 2013).

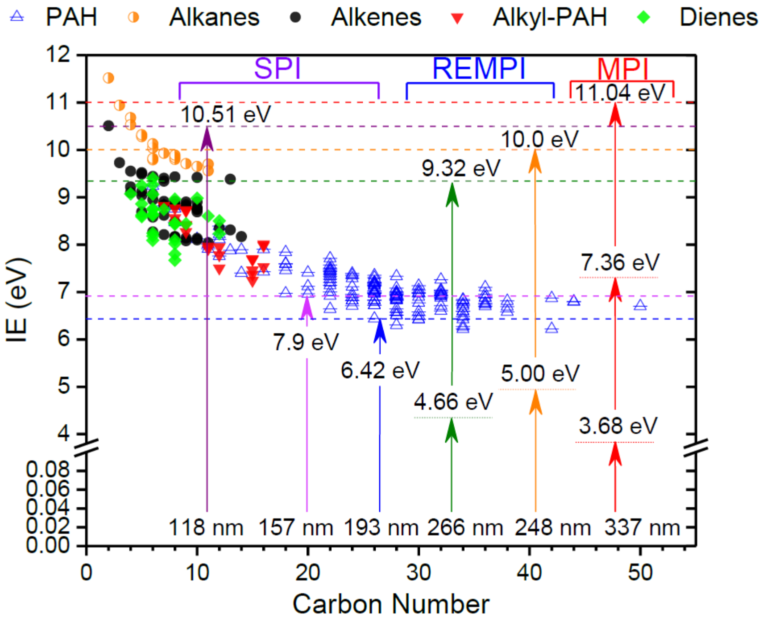

Figure 2.5.5. Photo ionization mechanisms for molecular species commonly involved in combustion chemistry (Desgroux, Mercier, and Thomson 2013)

The distance between the sample surface and the ionization beam is ≈30 mm. As the velocity of the desorption plume is hundreds of m/s in this condition of working, it needs a delay of time from tens to hundreds of µs for the desorbed species to reach the ionization beam. In this study, the time delay is set to 100 µs in order to get the maximum of signal for all the analytes. The timing of desorption and ionization pulses is controlled using a digital four channel delay/pulse generator (Stanford Research System, Inc. model DG-535).

2.5.1.3. *Time-of-Flight Mass Spectrometer*

The ion packets formed after the ionization stage between the repeller plate V_{A1} (2299 V) and the extraction grid V_{A2} (1878 V) are then mass-analyzed in a Time-of-Flight Mass Spectrometer (Jordan TOF Products, Inc.). The ion path in the ToF-MS is presented in Figure 2.5.6. The ToF direction is perpendicular to the propagation axis of the sampled plume (orthogonal extraction). As $V_{A1}>V_{A2}$, the ion packets accelerate toward the direction of V_{A2}, passing through V_{A3} (grounded), the Einzel lens, between the deflection plate V_{XY} (75 V) before entering the drift region. When ion packets arriving at the end of the drift region, an ion mirror (two-stage reflectron, V_{R1} = 1321 V, V_{R2} = 2308 V) changes the direction of the ions, by slowing them down and then reflecting them back towards the micro channel plates. The mass separation is achieved by the different time-of-flight required to ions having different mass to fly through the field-free tube before reaching the MCP.

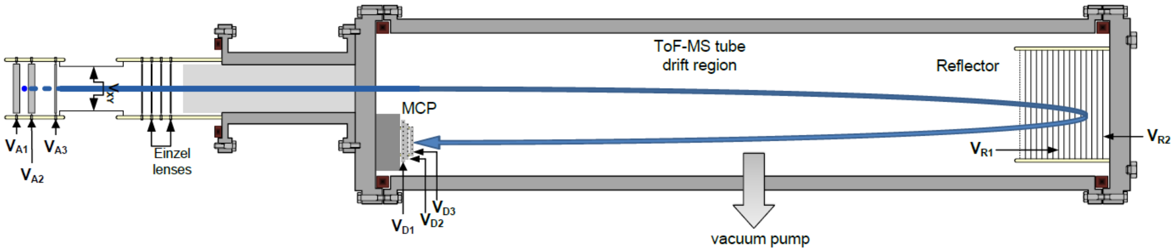

Figure 2.5.6. Ion path in the ToF-MS, from the generation of the ion packets in the analysis chamber to their detection by the micro channel plate detector (Irimiea 2017).

When the ions arrive at the detector, they impact the first microchannel plate V_{D3}, leading to the delivery of approximately ≈10^3 electrons for one impacting ion onto the face of the second plate V_{D2}. Each of these electrons continues generating other ≈10^3 electrons in the second plate. These electrons exit the bottom of the plate V_{D1} and accelerate towards the final anode which is at ground potential. The generated current is recorded using a 2 GHz oscilloscope Lecroy Waverunner 6200A. Obtained mass spectra are then transferred to a PC to further treatment. The typical mass resolution ($m/\Delta m$) obtained with this instrument is approximately 800 (at 202 m/z).

2.5.2. Time-of-flight Secondary Ions Mass Spectrometry

Time-of-Flight Secondary Ion Mass Spectrometry is a very sensitive surface analytical technique, well established for industrial and research applications. In this study, ToF-SIMS analysis is carried on a TOF.SIMS5 instrument from ION-TOF GmbH available at the Regional Platform of Surface Analysis in University of Lille. The device (as presented in Figure 2.5.7) is a compact and well integrated system used for various applications, such as self-assembly monolayer characterization, solid-electrolyte interphase analysis, single cell chemical imaging and environmental related particle investigation (Huang et al. 2017).

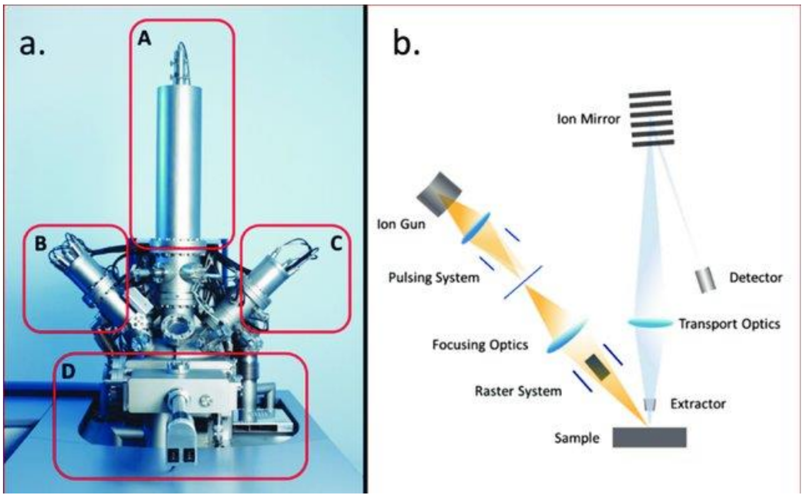

Figure 2.5.7. (a) A ToF-SIMS instrument with component labeled, including (A) the ToF-MS, (B, C) ion sources for sputtering and analysis, and (D) load lock for introducing samples. (b) Schematic presentation of some of the internal components of a ToF-SIMS instrument. The primary ions are represented in yellow, while secondary ions are represented with blue (Cushman et al. 2018)

SIMS can be operated in two working modes: static and dynamic. The static mode is used for the surface analysis (first mono-layers) while the dynamic mode is used for the in-depth distribution analysis of trace elements (from few nm to few μm depth). We use static mode which provides positive and negative mass spectra in our case. Due to our main interest of the organic content in combustion samples, Bi_3^+ is the appropriate primary particle source to be used because it is highly efficient for organic compounds. The energy of the primary ions is 25 keV with a current intensity of 0.3 pA.

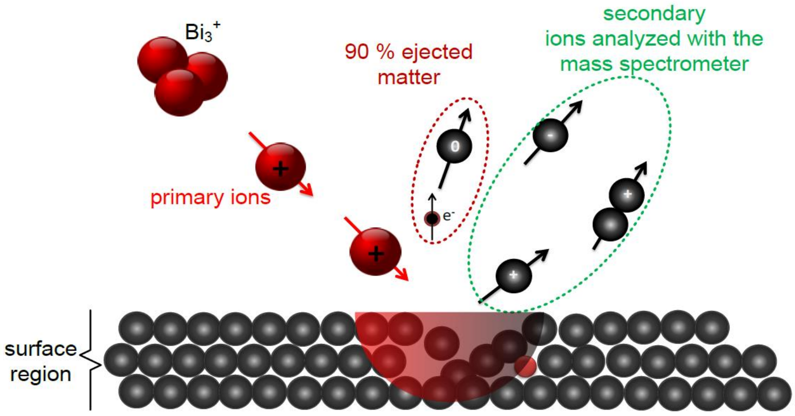

Figure 2.5.8. Scheme of working principle of SIMS.

The primary ions bombard the selected surface; the particle energy is transferred to the atoms of the solid by a "billiard-ball-type" collisional process which is showed in Figure 2.5.8. A cascade of collisions occurs between the atoms in the solid followed by the emission of atoms and molecules via sputtering. A small percentage of them exists in ionized state. The formed beam is called secondary ion beam. Ions from the sputtered region are then extracted/accelerated using ion optics and sent into the ToF-MS tube before striking the detector.

The spectrum is converted from time-to-flight scale to mass scale via mass calibration using Surface Lab Software with at least five ions. For this technique, the mass resolution is critically dependent on the roughness of the sample surface (Irimiea et al. 2018). Since glass fiber filters are used for our sampling procedure, mass resolution obtained with ToF-SIMS is approximately 2500 (at 202 m/z).

2.5.3. Multivariate analysis applied to mass spectrometry data

Mass spectra obtained from L2MS and SIMS contains a significant amount of chemical information about the composition of the analyzed samples. The challenge is to determine which mass peaks are related to each other, and how they relate the chemical differences present on the surface. This difficulty is then exacerbated by the fact that a given data set typically contains multiple spectra from multiple samples, which can result in a large data matrix to be analyzed (Graham and Castner 2012). Multivariate analysis (MVA) is one of many tools that are able to help in the processing of large data sets and in the determination of differences between samples. MVA includes several different methods as principal components analysis (PCA), hierarchical clustering analysis (HCA), discriminant analysis (DA), partial least squares (PLS), multivariate curve resolution (MCR) and maximum autocorrelation factors (MCF). In this study, PCA is mainly applied to the interpretation of L2MS and SIMS mass spectra. Theoretically, PCA is an orthogonal transformation that projects a set of observations onto linearly uncorrected variables denoted as principal components, allowing one to highlight similarities and differences within the dataset (Pei et al. 2008).

In PCA, a data set is defined as a matrix where the rows contain samples and the columns contain variables. In our case, for L2MS and SIMS data, samples are mass spectra and variables are integrated peak areas. From the covariance matrix of this data set, PCA "rotates" the axis to define a new set of axes – called principal components (PC). With three new matrices generated from PCA including scores, loadings and residuals, we can see the relationship between the spectra and which peaks are responsible for those separations (Graham and Castner 2012). To properly perform PCA, it is necessary to follow certain steps as described below. These steps are adapted from the tutorial of (Graham 2013) and the work of (Tanaka 1988).

a. Data collection: know what to expect from measuring setup before analyzing a sample. Because PCA is a statistically based method, it's necessary to have at least three mass spectra per sample.
b. Data calibration: it is important that all spectra within the sample set are calibrated properly and in the same way. The calibration including a large range of mass from low *m/z* to high *m/z* can increase the accuracy of identifying peaks. All mass spectra of the data set should be overlay to assure the consistency.
c. Peak selection: since the peak list can definitely affect PCA results, peak selection becomes an essential step. It's recommended to start with selecting all the peaks within a given set of criteria. If later in the analysis, it is determined that some peaks are not necessary, they can always be removed from the data matrix.
d. Data scaling: data preprocessing includes normalization, mean centering, scaling and transformation. Purpose of this step is to remove variance from the matrix that is not due to chemical differences between the samples.
    i. Normalization is done by dividing each variable in the matrix by a scalar value. Many different methods of normalization are commonly used as total intensity, sum of selected peaks, highest peak in spectrum, etc. Each method brings with it a set of assumptions. No matter which method is used, normalization removes information from the data set.
    ii. Mean centering subtracts the average of each variable from the data set. This allows the data to be compared across a common mean of zero.
    iii. Scaling divides each variable by a factor – the scaling factor. The goal of this step is to adjust the differences in fold changes between the variables by converting the data into differences in concentration relative to the scaling factor (van den Berg et al. 2006).

iv. Transformation is used to correct for heteroscedasticity, to convert multiplicative relations into additive relations, and to make skewed distribution more symmetric (van den Berg et al. 2006).

As been said earlier, there is no standard method of data preprocessing in PCA. It is adapted uniquely for each data set depending on what we expect. Table 2.5.1 adapted from the work of (van den Berg et al. 2006) summarizes some scaling methods used widely.

Table 2.5.1. Overview of widely-used PCA scaling method. The mean is calculated as $\bar{x}_i = \frac{1}{J}\sum_{j=1}^{J} x_{ij}$ and the standard deviation is calculated as $s_i = \sqrt{\frac{\sum_{j=1}^{J}(x_{ij}-\bar{x}_i)^2}{J-1}}$

Method	Formula	Goal	Advantages	Disadvantages
Auto-scaling	$\tilde{x}_{ij} = \frac{x_{ij} - \bar{x}_i}{s_i}$	Compare variables based on correlations	All variables become equally important	Inflation of the measurement errors
Range scaling	$\tilde{x}_{ij} = \frac{x_{ij} - \bar{x}_i}{(x_{imax} - x_{imin})}$	Compare variables relative to the chemical response range	All variables become equally important	Inflation of the measurement errors and sensitive to outliers
Pareto scaling	$\tilde{x}_{ij} = \frac{x_{ij} - \bar{x}_i}{\sqrt{s_i}}$	Reduce the relative importance of large value, but keep data structure partially intact	Stay closer to the original measurement than autoscaling	Sensitive to large fold changes
Vast scaling	$\tilde{x}_{ij} = \frac{(x_{ij} - \bar{x}_i)}{s_i} \cdot \frac{\bar{x}_i}{s_i}$	Focus on the variables that show small fluctuations	Aims for robustness, can use prior group knowledge	Not suited for large induced variation without group structure
Level scaling	$\tilde{x}_{ij} = \frac{x_{ij} - \bar{x}_i}{\bar{x}_i}$	Focus on relative response	Suited for identification of e.g biomarkers	Inflation of the measurement errors

e. Interpretation of PCA results: needs to be done using the scores and loadings plots together because two plots contain complimentary information and either one without the other is incomplete. Samples with positive scores on a given PC axis are positively correlated with variables with positive loadings on the same PC axis. Samples with negative scores are positively correlated with variables with negative loadings. By looking at the scores plot, we can deduce the relationship between samples and also the reproducibility or homogeneity of the spectra within a given sample group.

2.6. Conclusion

In this study, different combustors are used as soot generators. The swirled jet burner allows us to conduct the combustion of diesel and its alternative fuel – *n*-butanol with stability. The liquid

CAST device is used for the combustion of Jet A-1 and its alternative fuel – SPK. In-situ laser diagnostics LII/LIF are able to detect and locate soot particles and their precursors along the flames. Whereas ex-situ L2MS/SIMS techniques are used to exploit the chemical information of particulate matter and gas-phase exhaust, which are collected on QFF or GFF by using a two-filter separation method. Multivariate analysis is used to analyze the data obtained and derive the link between in-situ and ex-situ techniques.

Chapter 3.

Application of gas phase/ particle-bounded PAHs separation technique on CAST soot

3. Application of gas phase/particle-bound PAHs separation technique on CAST soot

This chapter is dedicated to a novel method developed to separate gas phase and particle-bound PAHs called two-filter system. The two-filter system is tested and applied to soot and gas phase PAHs produced from a miniCAST device.

3.1. Experimental configuration

The experiment was carried out in collaboration between CORIA (COmplexe de Recherche Interprofessionnel en Aerothermochimie UMR 6614, Rouen), PhLAM and PC2A laboratories, in the continuation of the MERMOSE national project (2012-2015, national funding DGAC – Direction Générale de l'Aviation Civile). The CAST burner was lent to PC2A laboratory for one week measuring campaign to investigate optical properties of soot produced from this soot generator. As the CAST burner is a widely known soot generator and has been studied by several research groups, it is a good opportunity for us to test and validate the separation performance of the front and back filter system.

The CAST burner and the two-filter system were described in detail in the subchapter 2.1.2 and subchapter 2.3, respectively. For all four set points used in this study, the flow rates of propane, nitrogen quench gas and dilution air are held constant, whereas the flow rates of oxidant air and nitrogen mixing gas are changed. Values of these different configurations are summarized in Table 3.1.1.

Table 3.1.1. Experimental conditions corresponding to the four studied set points

Sample	Fuel gas C_3H_8, sLm	Mixing gas N_2, sLm	Oxidant Air, sLm	Dilution gas Air, sLm	Quench gas N_2, sLm	Sampling time, min	OC/TC (Bescond et al. 2016)	OC/TC (Yon, Bescond, and Ouf 2015)
Reference	0.06	0	1.55	20	7	2	-	-
SP1	0.06	0	1.55	20	7	20	4.1	16.2
SP2	0.06	0	1.15	20	7	20	40	58.3
SP3	0.06	0	1.00	20	7	20	87	87
SP4	0.06	0.2	1.20	20	7	20	22.1	22

Particle phase of exhausted gas is first collected in a front filter made of quartz fiber. The gas phase passing through the first filter is then collected with a back filter also made of quartz fiber but with a layer of black carbon (Pureblack 100 Carbon, Columbian Chemicals Company, specific surface 80 – 150 m^2g^{-1}) added on top of it in our laboratory. Quartz fiber filters are supplied by Pall Tissuquartz Filter, QUAT-UP from Sigma Aldrich. The QFF are commonly used in soot collection due to their high efficiency in capturing combustion emissions and to their stable penetration curve in comparison with the other filters (Zíková, Ondráček, and Ždímal 2015). It is complicated to determine the collection coefficient of QFF for particles with only the particle size, since the collection process includes five mechanisms as (Lindsley 2016) described in their study. These mechanisms are:

(i) Interception: occurs when a particle moving with the flow contacts the filter material. The mechanism is valid for particles bigger and also smaller than the filter pores. However, it is likely more efficient for the particles with larger size.
(ii) Impaction: occurs when the flow changes its direction suddenly, causing the collision of the particle and the filter materials due to the particle's inertia. The impaction is usually more important for larger particles due to their greater inertia, however, it is also dependent on the density and velocity of the particle.
(iii) Diffusion: is caused by Brownian motion that leads the particle to move randomly and disperse within the flow, then it may deposit on the filter if it collides with the filter material.
(iv) Electrostatic attraction: occurs when filters carry an electrostatic charge, which can attract the charged particles.
(v) Sedimentation: occurs due to the gravitational forces, which lead particles fall onto filter material.

There are many factors affecting the effectiveness and the relative importance of these mechanisms. A diagram illustrating the collection efficiencies due to each mechanism as a function of particle size by (Lindsley 2016) is shown in Figure 3.1.1. This diagram is calculated for a fibrous filter 1-mm thick with 2µm fibers and an air velocity of 10 cm/s. As it can be seen from the figure, interception, impaction and sedimentation are enhanced with the increase of particle size, whereas diffusion has a reverse tendency. The filter is placed horizontal in this case, with air flowing downward into it, which increases the importance of sedimentation mechanism.

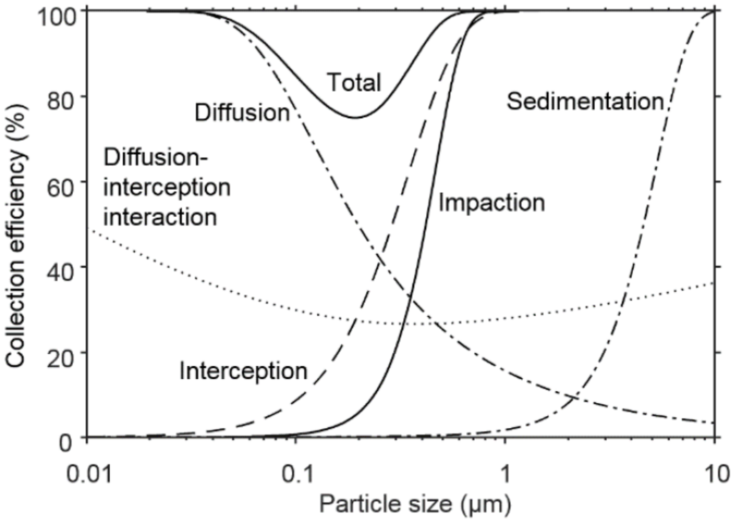

Figure 3.1.1. Theoretical collection efficiencies of particles collection mechanisms for a fibrous filter 1mm thick with 2µm fibers and an air velocity of 10 cm/s. Total shows the collection efficiency of the filter due to all mechanisms combined (Lindsley 2016).

Two reference samples including front and back samples are also collected. These samples are achieved by running the SP1 regime during two minutes. These samples represent pre-stabilized condition of the CAST equipment. Reference samples are used to ensure that other samples collected during 20 minutes are not impacted by the early combustion phase. With much lower sampling time, the coverage on these samples is much lower compared to others as presented in Figure 3.1.2.

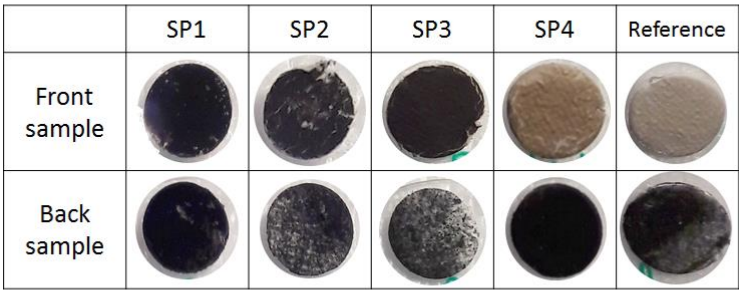

Figure 3.1.2. Photos of CAST front and back samples

3.2. L2MS results

The chemical composition of CAST samples is first mass-analyzed using the L2MS technique. The configuration of analysis is the same for all samples with laser desorption (532 nm, 12.9 mJ/cm^2) and laser ionization (266 nm, 48.5 mJ/cm^2). During the experiment, the pressure in the analysis chamber is maintained at 9.10^{-8} Torr while the temperature is kept at -90^{o}C. Overall mass resolution $m/\Delta m$ achieved for this sample set is around 1300. L2MS mass spectra of CAST front and back samples are displayed in Figure 3.2.1.

The spectrum of SP4 back sample shows more peaks at higher masses than the others. This might be due to the particular condition of this operation set point compared to the others. SP4 is the only working set point with the presence of N$_2$ dilution in the fuel flow. There is more ion signal detected on back filters of SP2 and SP3 than the other regimes.

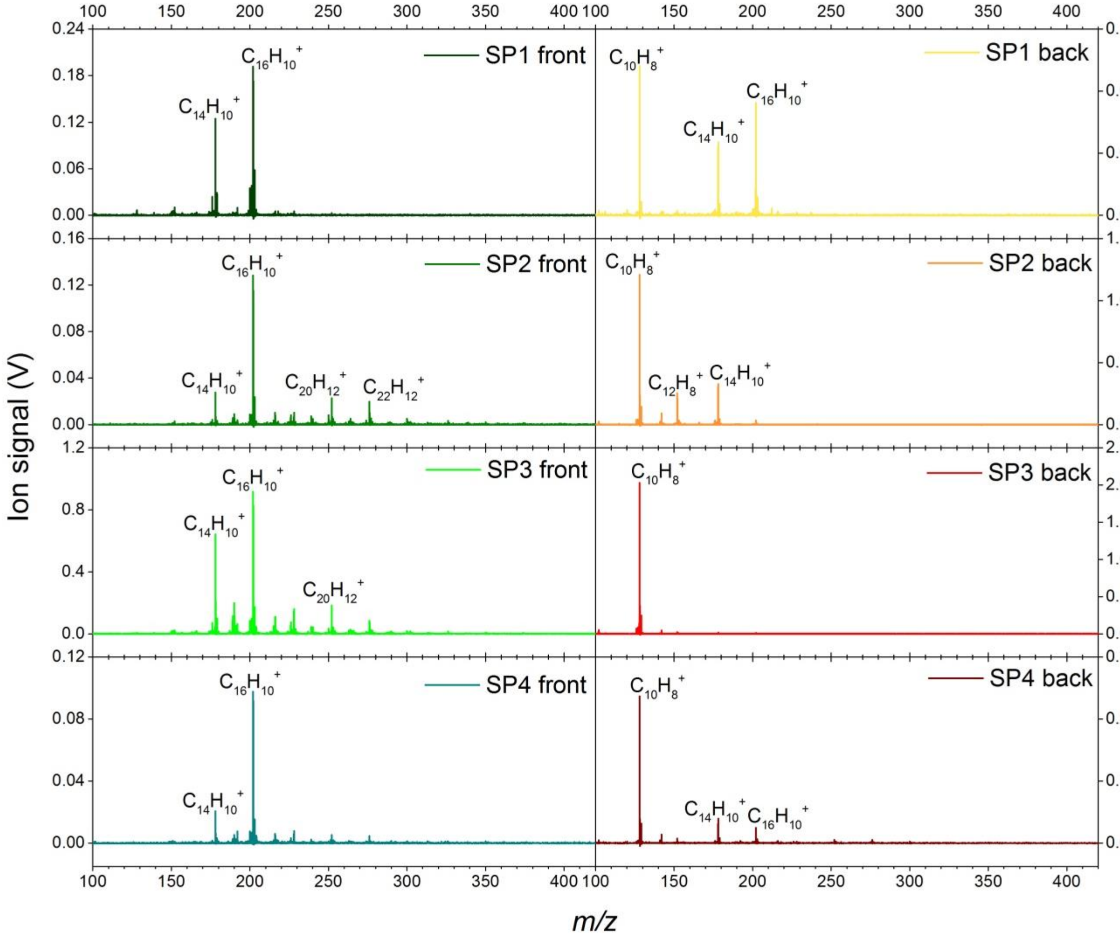

Figure 3.2.1. L2MS mass spectra of CAST samples

Overall, mass spectra are rich in peaks associated to PAH compounds. There are low signals coming from species as $C_3H_3^+$, $C_4H_3^+$, $C_5H_3^+$, etc. corresponding to aromatic fragments (McLafferty and Tureček 1993). Mass spectra of front samples are dominated by $C_{14}H_{10}^+$ (*m/z* 178) and $C_{16}H_{10}^+$ (*m/z* 202) peaks. The highest mass peaks are m/z 276 for SP1 front sample, m/z 398 for SP2 front sample and m/z 448 for SP3 and SP4 front samples. $C_{10}H_8^+$ (*m/z* 128) is the base peak of mass spectra of back samples. The lightest aromatic compound that could be found in these mass spectra is $C_6H_6^+$- which corresponds to benzene. Compounds consisting of one and two aromatic rings are present mostly on the back samples. This happened due to the deposition of black carbon on the back filters before the sampling procedure. PAHs of m/z 176-242 are found on both kinds of samples, while those of m/z > 252 are only on front samples. Similar categories were obtained in the work of (Bari et al. 2010). They classified aromatic compounds into three groups based on the number of aromatic rings. Two aromatic rings compounds are classified as volatile species, those with three and four rings are considered as semi-volatile compounds, and PAHs with more than four rings are in the group of non-volatile PAHs. Slightly different classes are defined in some other studies (Sun et al. 2006; Elghawi et al. 2010; An et al. 2016) as presented in Table 3.2.1.

Study	Gas phase PAHs	Exist in both phases	Particle-bound PAHs
(Sun et al. 2006)	Fluorene Phenanthrene	Fluoranthene Pyrene	Benz[a]anthracene Triphenylene Chrysene Benzo[b]fluoranthene Benzo[k]fluoranthene Benzo[e]pyrene Benzo[a]pyrene Indenol[1,2,3-cd]pyrene Benzo[ghi]perylene
(Elghawi et al. 2010)	Naphthalene Acenaphthylene Acenaphthene Fluorene Anthanracene Phenanthrene Fluoranthene	Pyrene	Benz[a]anthracene Chrysene Benzo[b]fluoranthene Benzo[k]fluoranthene Benzo[a]pyrene
(An et al. 2016)	Napthalene Acenaphthylene Acenaphthene Fluorene Phenanthrene Anthracene	Fluoranthene Pyrene	Benz[a]anthracene Chrysene Benzo[b]fluoranthene Benzo[k]fluoranthene Benzo[a]pyrene Dibenz[a,h]anthracene Indenol[1,2,3-cd]pyrene Benzo[ghi]perylene

Table 3.2.1. List of PAHs present in gas phase and particle-bound phase in some studies.

To better understand and discriminate between mass spectra corresponding (i) to front and back samples and (ii) to four CAST set points of sample set, PCA is applied with 96 attributed peaks. The first two principal components are presented in the score plot of Figure 3.2.2 with their loadings in Figure 3.2.3.

These two PCs represent more than 75% of the variance. A remarkable discrimination between front and back samples is permitted by PC1. This principal component is composed of high mass aromatic species (≥ *m/z* 178), especially $C_{14}H_{10}^{+}$ and $C_{16}H_{10}^{+}$, with its positive coefficients. Negative loadings of PC1 are attributed to volatile PAHs as $C_{10}H_{8}^{+}$, $C_{12}H_{8}^{+}$. The result from PC1 shows a good separation between gas phase and particulate-bound PAHs by using the two-filter technique. PC2 (representing 14.68% of the variance) is composed of high mass PAHs (≥ *m/z* 216) with positive coefficients, and of lower mass PAHs (≤ *m/z* 202) with negative coefficients. This principal component separates SP1 front samples from the others. The regime of SP1 consists of the highest oxidant flow, allowing a better combustion process among all, leading to a lower organic content in the exhaust. Previous studies (Yon, Bescond, and Ouf 2015; Bescond et al. 2016) confirm this result according to their OC/TC ratios as presented in Table 3.1.1.

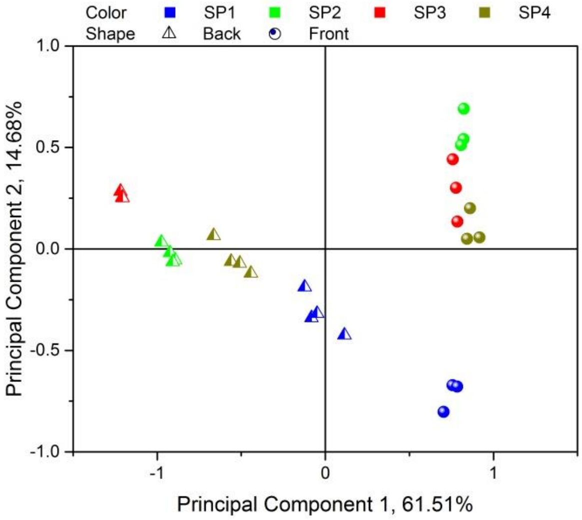

Figure 3.2.2. Score plot of PC1 and PC2 from PCA analyses applied of L2MS mass spectra of CAST samples

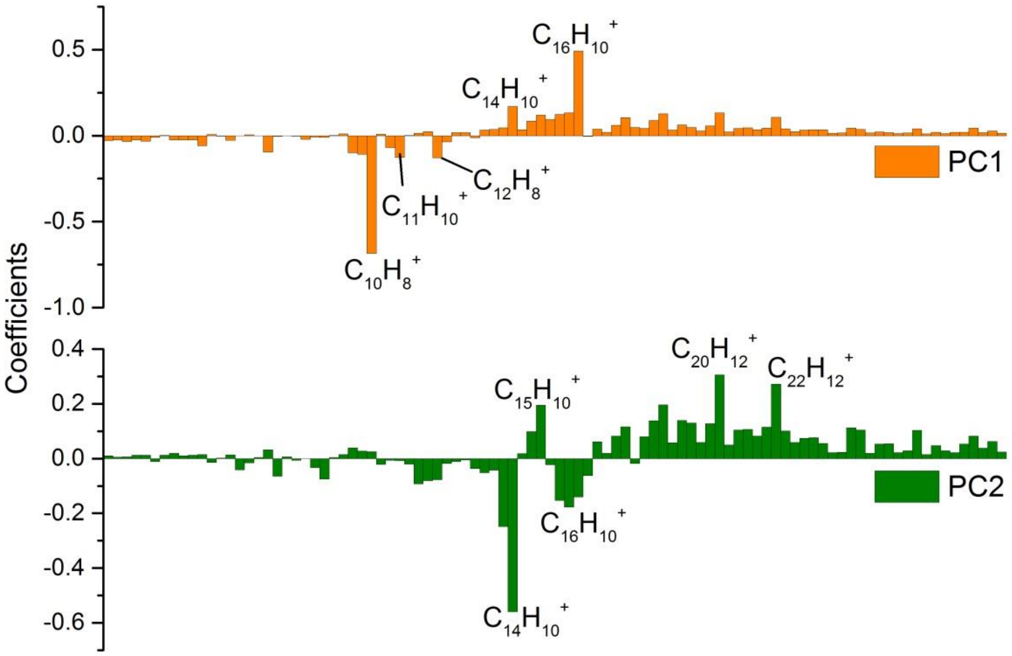

Figure 3.2.3. Loadings corresponding to PC1 and PC2 presented in Figure 3.2.2

3.3. SIMS results

CAST front and back samples are analyzed using the ToF-SIMS technique. Positive and negative SIMS mass spectra are shown in Figure 3.3.1 and Figure 3.3.5, respectively. Positive mass spectra consist of hundreds of peaks – which can be divided into two main groups, one with low mass fragments (*m*/*z* < 150) and the other with higher masses corresponding to PAHs or other compounds. In agreement with the L2MS results, mass spectrum of SP1 front sample shows a shorter PAHs sequence compared to the other front samples. Mass spectra of SP2, SP3 and SP4 front samples have $\mathrm{C_{19}H_{11}^{+}}$ peak as the most intense PAH peak, whereas it is $\mathrm{C_{16}H_{10}^{+}}$ in the case of SP1 front sample. In overall, spectrum of SP3 front sample is the richest in PAHs, followed by SP2 and SP4 front samples, while SP1 front sample has the lowest content of PAH. In terms of total PAH content, positive SIMS spectra of back samples show an inverse behavior to those of front samples. SP4 back sample has the highest PAH content, whereas SP2 and SP3 back samples, which are very similar to each other, show an insignificant signal of PAHs. Spectrum of SP1 back sample is very close to the one of SP1 front sample.

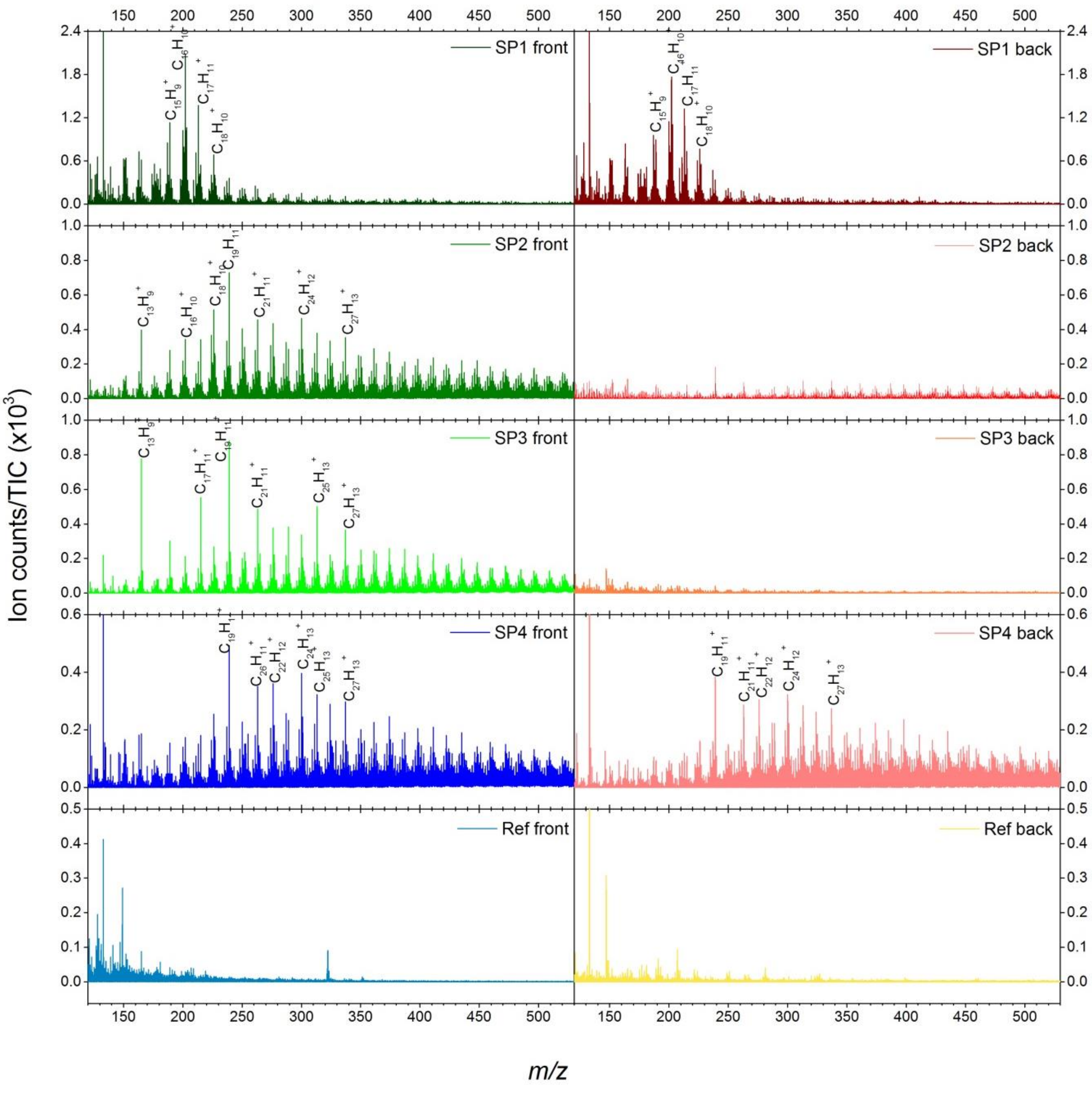

Figure 3.3.1. Positive SIMS mass spectra of CAST samples

The proportion of total PAH content is shown in Figure 3.3.2 for all 10 front and back samples including the reference ones. The organic carbon to total carbon ratio (OC/TC) determined by using thermo-optical analysis from previous studies (Yon, Bescond, and Ouf 2015; Bescond et al. 2016) is also shown as grey and red scatter. As it can be noticed from the figure, the total PAH content in SIMS mass spectra of front samples shows similar trend to OC/TC ratio. This trend can probably be linked to the difference in oxidation air flow between regimes. SP1 has the highest oxidation air flow in all, allowing a better combustion process, leading to more graphitization of soot particles and less organic compounds covering soot. Back samples show a much lower content in PAHs compared to front ones, except in the case of SP4. The difference in color of SP4 front and back samples could explain it well. This regime is the only one having nitrogen flow mixing with fuel. This particular condition compared to the others might be the cause of the behavior of front and back samples. In the PhD thesis of (Irimiea 2017), there is no LII signal collected in the case of SP4, suggesting that the particulate matter from SP4 regime are different to the other working set points. Another study on soot produced from CAST equipment from (Malmborg et al. 2019) works on different set points with N_2 dilution in fuel flow – similar to the condition of SP4 regime. The particulate matter produced in those conditions is called fullerene carbons with high refractory property. With these particular conditions, large molecules produced from SP4 regime might not be condensed on the particles at the outlet of the burner, but still in the gas phase. These condensable gas phase products might be able to pass through the first filter and to be then collected on the second filter covered with black carbon.

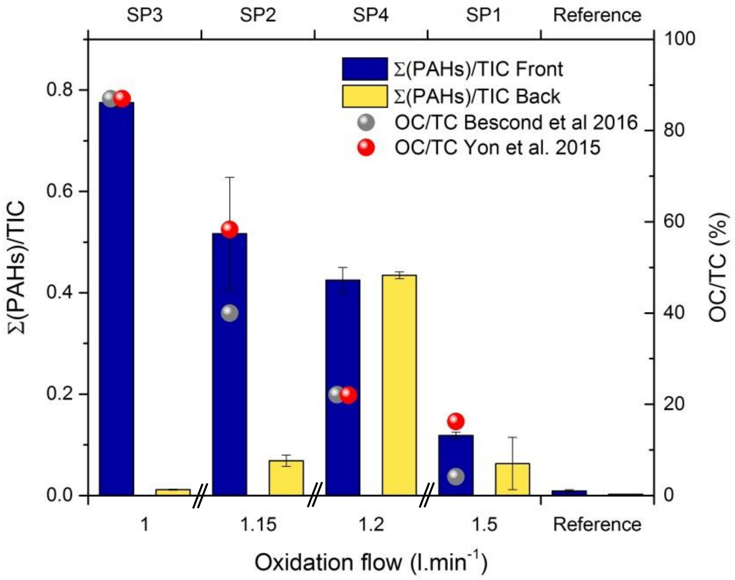

Figure 3.3.2. Total PAH content detected with SIMS on CAST front and back samples. Red and grey dots represent OC/TC ratios measured in previous studies on the same set points of CAST.

PCA is applied to the positive SIMS mass spectra of CAST samples. 155 peaks associated to all hydrogenated carbon fragments and the most representative peaks for PAHs are chosen for the analysis. Score plot and loadings of PC1 and PC2 is shown in Figure 3.3.3 and Figure 3.3.4, respectively. The first two principal components represent more than 85% of the variance. The first principal component PC1 is composed of peaks associated with PAHs heavier than $C_{13}H_9^+$ with positive coefficients and to fragment ions with negative coefficients. The majority of back samples are located at the negative side of PC1, whereas front samples and SP4 back sample exhibit positive PC1 scores due to their high PAH contents. SP1 front and back samples are present almost at the same position due to their low organic material content. This result agrees well with what is displayed in Figure 3.3.2. PC2 separates mainly SP1 samples and the others. Low-hydrogenated fragments and some light PAHs are associated to positive coefficients of PC2, whereas other compounds are associated to negative loadings of this principal component. This can be explained if one considers that the SP1 regime produces more mature soot than the others, leading to a low organic content. This also might lead to the low-hydrogenated organic materials on the samples.

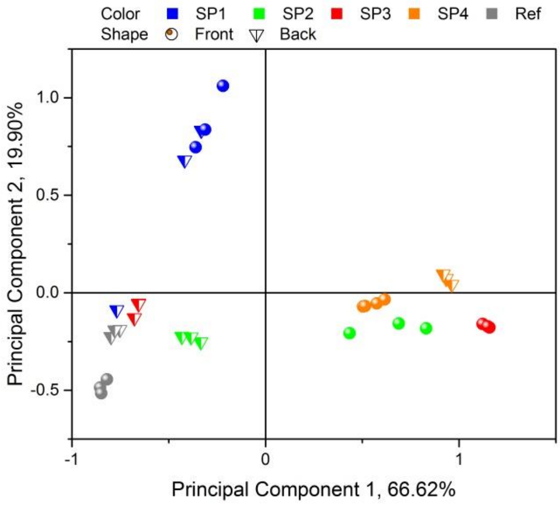

Figure 3.3.3. Score plot of PCA applied on positive SIMS spectra of CAST samples

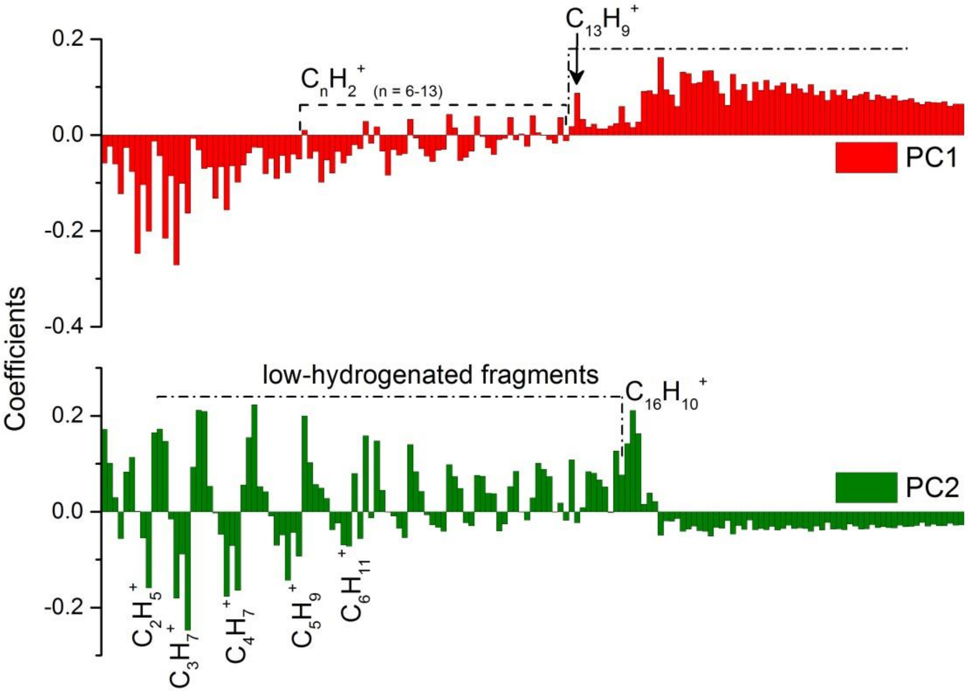

Figure 3.3.4. Loadings corresponding to PC1 and PC2 components in the PCA of positive polarity SIMS spectra of CAST samples

Negative SIMS mass spectra of CAST samples are shown in Figure 3.3.5. In general, all mass spectra are dominated by C_n^- and C_nH^- clusters (n = 1 – 16). SP2 and SP3 back samples exhibit a similar behavior to reference samples with O^- dominating their mass spectra. A remarkable feature of C_nH^- (where n is an even number of carbon atoms) is found in SP2, SP3 and SP4 front and back samples. The intensity of these peaks decreases with increasing mass.

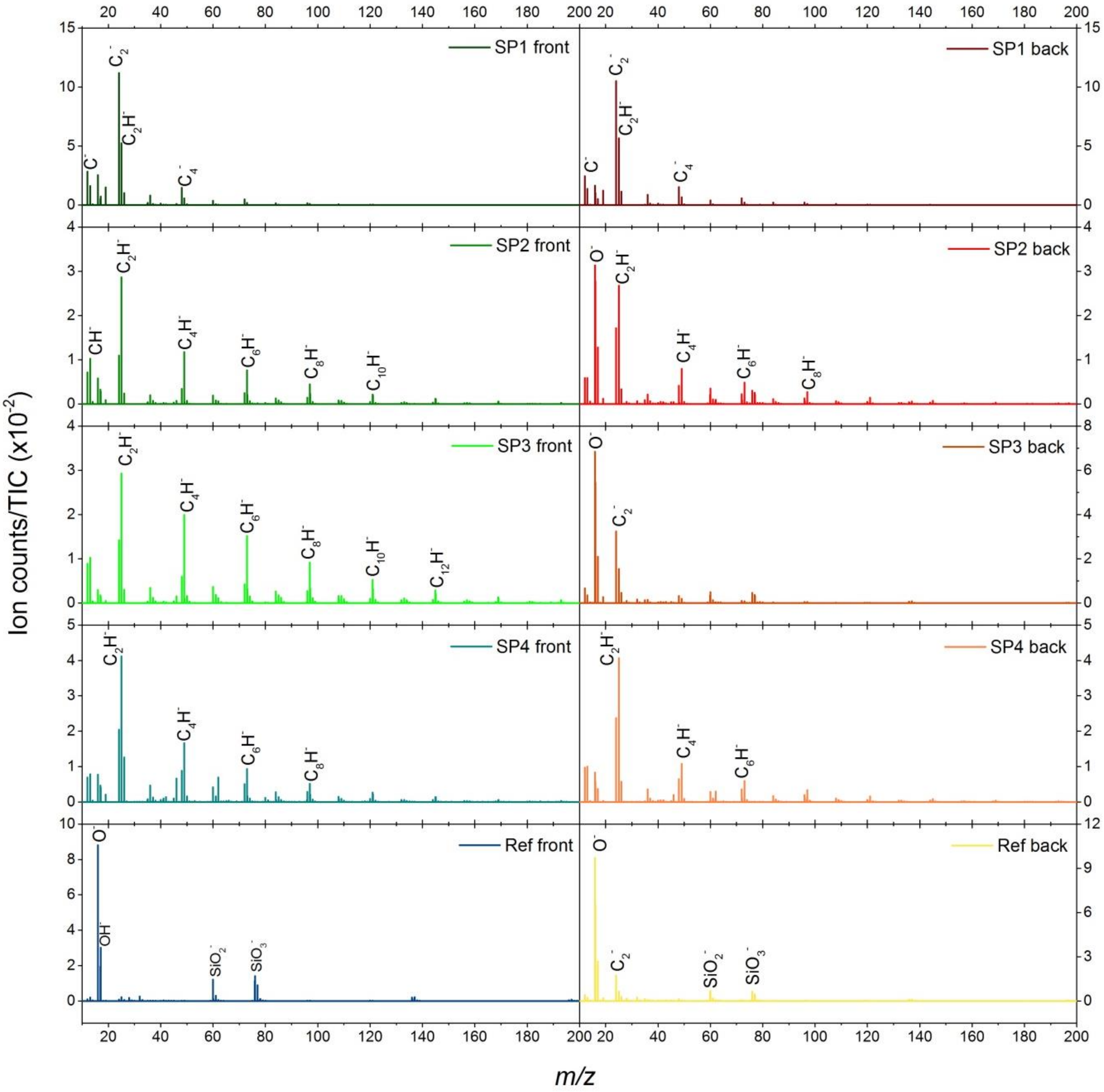

Figure 3.3.5. Negative SIMS mass spectra of CAST samples

To better understand the difference between the mass spectra, PCA is applied to negative SIMS spectra of CAST sample with 223 assigned peaks. The score plot of PC1 and PC2 with their loadings are displayed in Figure 3.3.6 and Figure 3.3.7, respectively. PC1 (representing 64.45% of the variance) discriminates samples with low and high material contents, corresponding to negative and positive coefficients, respectively. Negative coefficients of this principal component are associated with peaks detected on the reference samples as O^-, OH^- and series of $Si_xO_y^-$. Other peaks as C_n^-, $C_nH_x^-$ clusters are associated with positive loadings of PC1. Except SP1 and

SP4 back samples, other back samples and reference samples present negative scores of PC1. The second principal component (accounting for 25.79% of the variance) is composed of C_nH^- clusters (n even) with positive coefficients, and of C_n^- carbon clusters, especially C_2^-, with negative coefficients. The separation with PC2 discriminates samples with their PAH content. This is found to be similar to PC1 in PCA applied on positive SIMS spectra in previous part. Regarding the trend, C_nH^- clusters might be associated to the organic material content on samples, and C_2^- might be associated to the elemental carbon content of the sample.

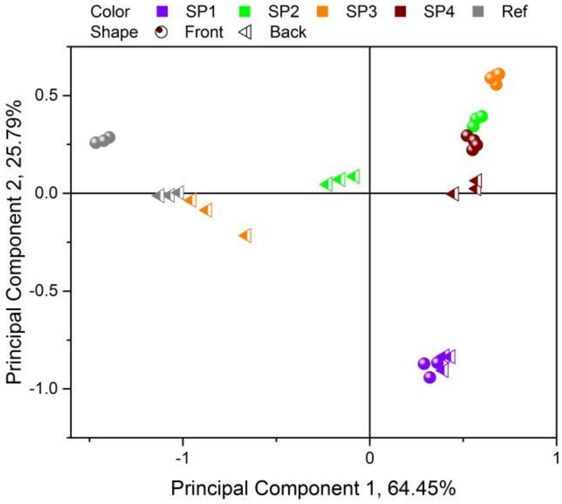

Figure 3.3.6. Score plot of PCA applied on negative SIMS spectra of CAST front and back samples

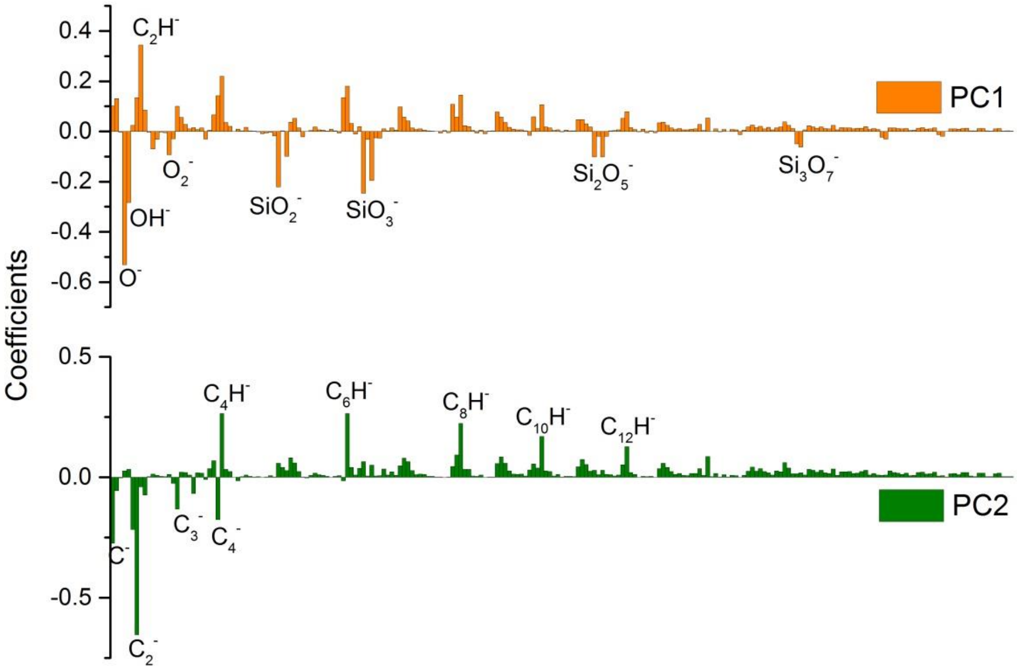

Figure 3.3.7. Loadings corresponding to PC1 and PC2 presented in Figure 3.3.6

The relative contribution of various hydrocarbon clusters (C_nH^- with n = 4, 6, 8) is computed and the variations between the samples is shown in Figure 3.3.8. The left figure shows the sum of C_4H^-, C_6H^-, and C_8H^- peaks area after being normalized to total icon counts. The trend for these ions is identical to the one obtained with the total PAH signal in positive SIMS mass spectra shown in Figure 3.3.2. Right figure displays C_2^- cluster after being normalized to total ion counts. A reverse trend on front samples is achieved compared to the left one. The content of black carbon on back samples can explain why the C_2^-/TIC is almost similar for all back samples. It can be suggested that the sum of C_4H^-, C_6H^-, and C_8H^- could be a good indicator for organic material content on soot samples, whereas C_2^- could be used as a marker for elemental carbon. This suggestion is in agreement with (Mayama et al. 2013) and (Popovicheva et al. 2017). However, other authors have different opinions. (Pagels et al. 2013) suggested that C_2H^-, C_3H^-, and C_4H^- are markers for elemental carbons, whereas (Kirchner et al. 2003) claimed that C_5H^-, C_6H^-, and C_7H^- are indicators of fragments from soot core.

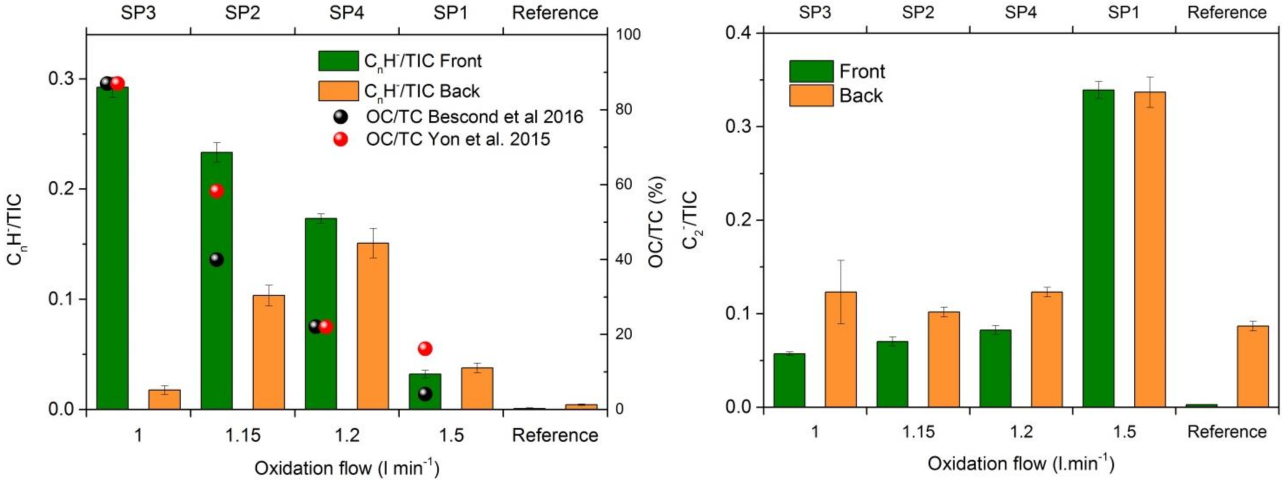

Figure 3.3.8. Variation of the content of various markers, derived from negative SIMS mass spectra

3.4. Conclusion

Combustion products from a miniCAST soot generator are collected by using a two-filter system. These filters are then mass analyzed using L2MS and ToF-SIMS. Aromatic compounds are found in all mass spectra. The PAH distribution across front and back samples are able to be classified as the work of (Bari et al. 2010) with volatile PAHs (1-2 aromatic rings), semi-volatile PAHs (3-4 rings) and non-volatile PAHs (> 4 rings). Particulate matter is collected on front filters, whereas back filters capture volatile PAHs and a part of semi-volatile PAHs. The two-filter system is found to make a good separation between the two phases. C_nH^- clusters in negative SIMS mass spectra, with $n \geq 4$ (even number of carbons), are found to be a good indicator of organic material content in soot samples. On the other hand, C_2^- is found as a good marker of elemental carbon content in soot samples.

Chapter 4.

Characterization of soot and soot precursors produced in swirled jet flames by in-situ and ex-situ techniques

4. Characterization of soot and soot precursors produced in swirled jet flames by in-situ and ex-situ techniques

This chapter is dedicated to the characterization of soot particles and their precursors in swirled jet flames of different fuels. The chapter is written with four main parts. The first part presents systematically the laser diagnostic results on five flames: diesel, *n*-butanol, mixture 50% diesel-50% *n*-butanol, Jet A-1 and SPK in the order UV-LIF, Vis-LIF, Vis-LII and IR-LII. The second part shows results obtained with ex-situ mass spectrometry techniques applied on samples from the three flames with automobile fuels. In the next two parts of the chapter, the discussion is focused on the correlation between in-situ and ex-situ techniques, and on the different behaviors of fuels. The last part will summarize our conclusions of this chapter.

4.1. In-situ detection of soot particles and their precursors produced in swirled jet flames

Care must be taken to the laser fluence used for the experiment while working with LII/LIF technique with any excitation. In general, it is necessary to avoid the interference from LII whenever doing LIF measurement by using laser fluence not higher than the detection threshold of LII signal. Similarly, for LII measurement, it is necessary to use a laser fluence not higher than the sublimation threshold of soot particles. To figure out the laser fluence needed to be used in different cases, the evolution of LII signal in function of laser fluence taken in sooting zone needs to be exploited. An example for the diesel flame is given in Figure 4.1.1.

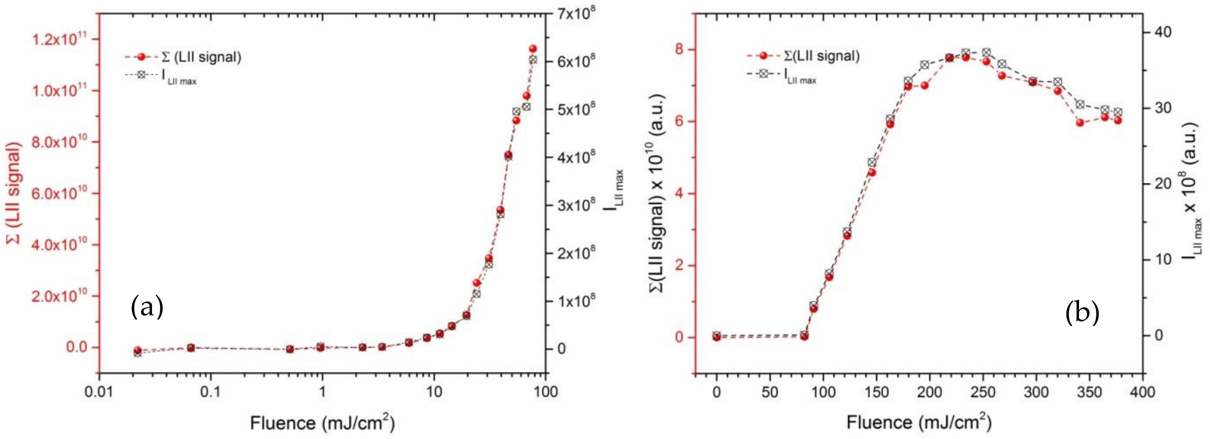

Figure 4.1.1. Fluence curves obtained at 152 cm HAB in the diesel flame with (a) 266 nm and (b) 532 nm excitation wavelength. Detection wavelength ranges are 700-892 nm and 700-800 nm, respectively.

According to the fluence curve taken with 266 nm excitation wavelength, LII signal starts with the fluence higher than 6 mJ/cm². Therefore, laser fluence chosen for UV-LIF measurement is 1.46 mJ/cm². For 532 nm excitation wavelength, the LII signal starts approximately at 80 mJ/cm². Then the incandescence emission increases sharply with the rise of laser fluence until 220 mJ/cm² where the sublimation threshold is reached. After that, the LII signal decreases with the increase of the laser fluence. Therefore, a laser fluence at 6.3 mJ/cm² is chosen to carry out the Vis-LIF measurement and a laser fluence at 180.6 mJ/cm^2, which is below the sublimation threshold, is used for the LII measurements. Table 4.1.1 sums up the configuration used for LII and LIF measurements of five swirled flames in this chapter.

Flame	Measurement	Diffraction grating	Laser fluence used, mJ/cm^2	Gate width, ns
Diesel	UV-LIF	150 groves/mm, blazed at 300 nm	1.5	50
	Vis-LIF	150 groves/mm, blazed at 300 nm	6.3	50
	Vis-LII	150 groves/mm , blazed at 800nm	180.6	50
	IR-LII	150 groves/mm , blazed at 800nm	338.1	50
N-butanol	UV-LIF	150 groves/mm, blazed at 300 nm	1.5	50
	Vis-LIF	150 groves/mm, blazed at 300 nm	42.1	50
	IR-LII	150 groves/mm , blazed at 800nm	439.2	50
Mixture	UV-LIF	150 groves/mm, blazed at 300 nm	1.1	50
	Vis-LIF	150 groves/mm, blazed at 300 nm	6.3	50
	Vis-LII	150 groves/mm , blazed at 800nm	179.8	50
	IR-LII	150 groves/mm , blazed at 800nm	340.1	50
Jet A-1	UV-LIF	150 groves/mm, blazed at 300 nm	1.4	50
	Vis-LIF	150 groves/mm, blazed at 300 nm	5.8	50
	Vis-LII	150 groves/mm , blazed at 800nm	183.1	50
SPK	UV-LIF	150 groves/mm, blazed at 300 nm	1.5	50
	Vis-LIF	150 groves/mm, blazed at 300 nm	5.8	50
	Vis-LII	150 groves/mm , blazed at 800nm	180.6	50

UV-LIF: Laser induced fluorescence with 266 nm excitation
Vis-LIF: Laser induced fluorescence with 532 nm excitation
Vis-LII: Laser induced incandescence with 532 nm excitation
IR-LII: Laser induced incandescence with 1064 nm excitation

Table 4.1.1. Configuration of LII/LIF measurements carried out on five swirled flames.

4.1.1.Diesel flame

Diesel is one of the most common fuels used on-road, especially for heavy-duty trucks andbuses (Miller and Jin 2018). This fuel is responsible for most of the particulate matters emitted by the transport sector (Minjares, Wagner, and Akbar 2014). To reduce PM emissions from the use of diesel fuel, as well as compare the soot formation in the combustion of diesel to the one of other alternative fuels, it is necessary to understand the mechanisms for soot formation and the properties of soot. There are many of scholars investigating particulate matter emitted by diesel, from premixed to diffusion combustion, from low pressure to high pressure, from burners to engines. In this study, we propose an experiment with diesel fuel, carried out on our home-made swirled jet burner. The advantage of using this burner is that we are able to investigate the influence of fuel composition on soot formation without the interference of other properties as chamber pressure, delay of ignition as in engines, or the interference of flat flame as in McKenna burner, etc.

Diesel flame obtained with our home-made swirled burner is approximately 260 mm tall by using 109.6 g/h of diesel, 264 ml/min of nitrogen for nebulization and 22.24 L/min of air. The flame is characterized with LII/LIF techniques and their combustion pollutants samples are chemically analyzed with L2MS and SIMS. Multi-wavelength excitations as 266 nm, 532 nm, 1064 nm are used for LII and LIF measurement. The UV-Vis excitations are used to excite PAHs, while Vis-IR excitations are employed to detect soot particles.

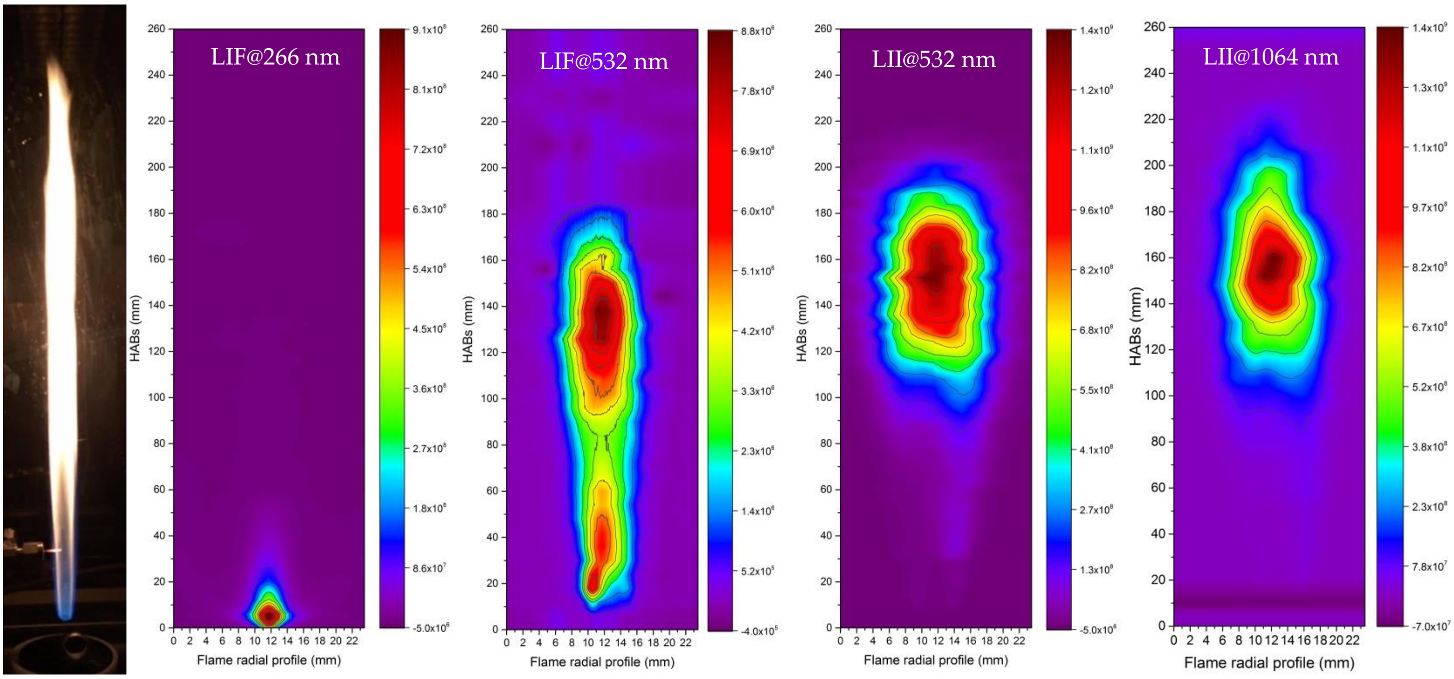

Figure 4.1.2. Photo of diesel swirled jet flame and its 2D plots of soot and soot precursor obtained by coupling of LII and LIF at 266, 532 and 1064 nm excitation.

Figure 4.1.2 shows the photo of the diesel flame and the corresponding LII, LIF images taken with different excitation sources. As it can be seen in the figure, the fluorescence at 266 nm excitation starts very early in the flame and fade out quickly, whereas fluorescence signal excited by 532 nm excitation takes place a short time later and goes along until 180 mm HAB. The Vis-LIF signal starts intensely at 20 mm HAB and reduces its intensity until 80 mm HAB. At 100 mm HAB, Vis-LIF signal re-increases and reach its maximum at 140 mm HAB. Incandescence signals obtained with 532 nm and 1064 nm excitations show a good coherence between LII measurements and also a good repeatability of the flame. The maximum of these LII signals locates at around 150 – 160 mm HAB in the flame.

4.1.1.1. *Fluorescence induced by 266 nm wavelength*

Figure 4.1.3 shows the evolution of LIF signal obtained with 266 nm excitation at different HABs at the centerline of diesel flame and the spectra corresponding to each HAB. From these two graphs, we can see that fluorescence signal is obtained at very early position in the flame, even at 0 mm HAB – which locates right at the outlet of the nebulizer. This is due to the presence of petrogenic PAHs in diesel fuel.

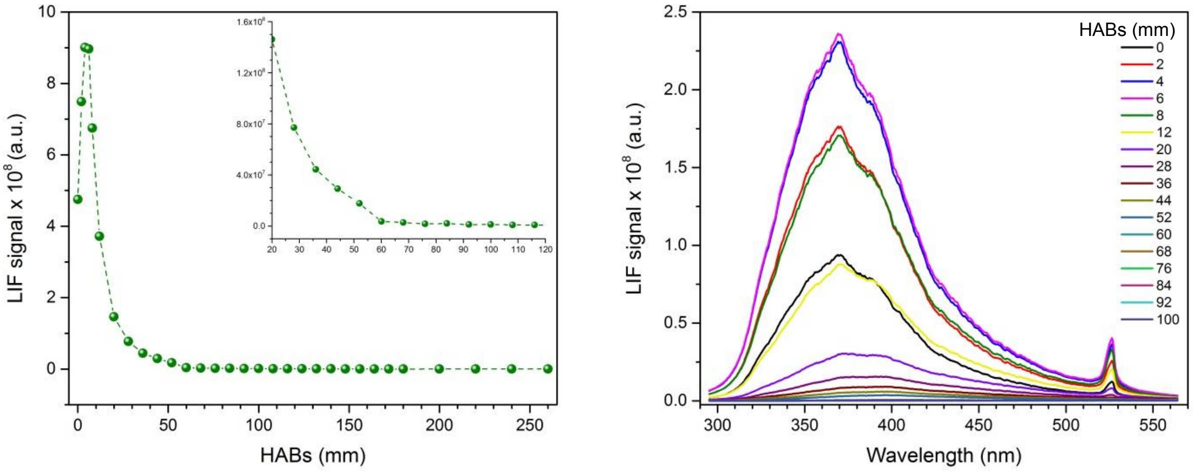

Figure 4.1.3. Left: LIF profile obtained at the centerline of diesel flame with 266 nm excitation. Right: LIF spectra with 266 nm excitation at different HABs in diesel flame (obtained at the centerline). Laser fluence used is 1.5 mJ/cm². Detection wavelength range is 295-564 nm.

Indeed, the spectra obtained from 0 – 8 mm HAB are similar to the fluorescence spectrum of pure diesel placed in a quartz-cuvette as shown in Figure 4.1.4. The LIF signal increases from 0 mm and reaches its maximum at 4 mm HAB. This is the consequence of the atomization and vaporization of fuel droplets and expansion of diesel jet with the increase of height. After this HAB, the intensity of the emission decreases gradually. The fluorescent compounds in diesel fuel are then pyrolyzed and consumed due to occurring combustion process. The fluorescence signal fades out at HABs higher than 60 mm in the flame. The small peaks which appear at 532 nm wavelength in the spectra come from the second diffraction order of the grating induced by the excitation source. This signal cannot be avoided due to the diffusion of laser excitation at 266 nm from fuel droplets.

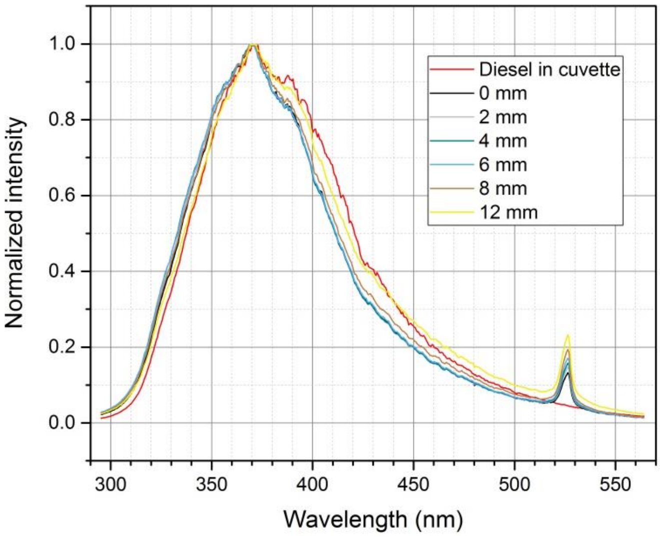

Figure 4.1.4. Comparison of normalized LIF spectra obtained with pure diesel in quartz cuvette and LIF spectra of several HABs in diesel flame, measured with 266 nm excitation.

LIF spectra obtained at the centerline of the diesel flame at different HABs are normalized and shown in Figure 4.1.5. The global shape of the LIF spectra measured from 0 – 8 mm HAB do not show any change. All these spectra are characterized by a broadband structure in the 300 – 500 nm range, peaking around 370 nm. At higher HAB in the flame, the fluorescence spectra become wider and the maximum signal is red shifted. In the studies of (Ciajolo et al. 2001) or (Bejaoui 2012) on diesel spray flame, they obtained similar fluorescence emission with 266 nm excitation in cold spray of diesel. The shape and the maximum of the LIF spectrum is a fingerprint of the molecular species being involved in the LIF process. Hence, a change of these LIF spectra indicates a change of the fluorescence species. Thus at HABs below 6 mm, we do not notice any change yet, or only a minor change which happens for the fuel during the combustion process. The minor change might be blurred by the major presence of petrogenic PAHs in the fuel.

The significant expansion of spectral fluorescence towards IR starting with 8 mm HAB is attributed to the appearance of new species. This shift is correlated to LIF results achieved with 532 nm excitation, which will be discussed in the next part of the subchapter. The red shift of spectra is more significant at higher HABs in the flame. In the studies of (Ciajolo et al. 2001) and (Bejaoui 2012), the shift of fluorescence emission to IR wavelength is also noticed. However, these authors claimed that the visible emission could come from high molecular weight PAHs formed in the flame. In their recent study, (Mercier et al. 2019) proposed that dimers of moderate-size PAHs might be responsible for this emission signals.

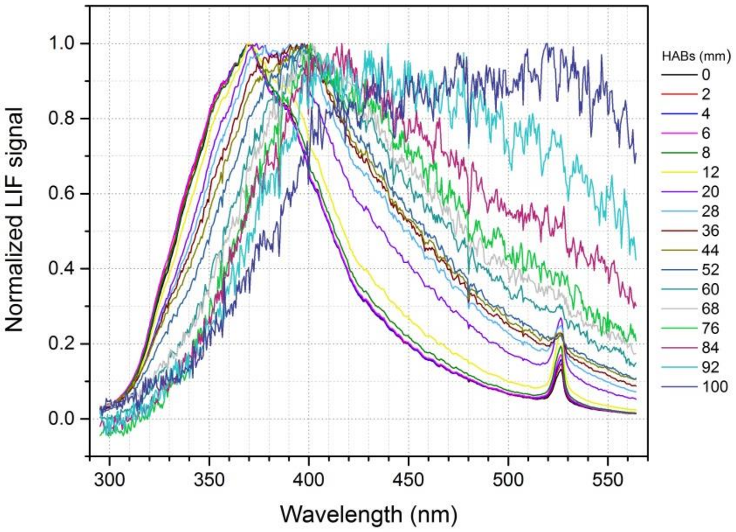

Figure 4.1.5. Normalized LIF spectra obtained at the centerline of diesel flame with 266 nm excitation.

Where the UV-LIF spectra start to deform and become broader, at 100 mm HAB, the second peak of Vis-LIF also starts being formed. This is discussed in the next subchapter.

4.1.1.2. *Fluorescence induced by 532 nm wavelength*

Figure 4.1.6 shows the evolution of the LIF signals obtained with 532 nm excitation at different HABs at the centerline of the diesel flame and the spectra corresponding to each HAB. In particular, a bimodal profile is obtained in the diesel flame using 532 nm excitation wavelength. The first peak of the signal is located at around 40 mm HAB whereas the second peak is identified at 140 mm HAB. The first peak might correspond to a first class of petrogenic fluorescent species whereas the second peak might come from a second class of pyrogenic species.

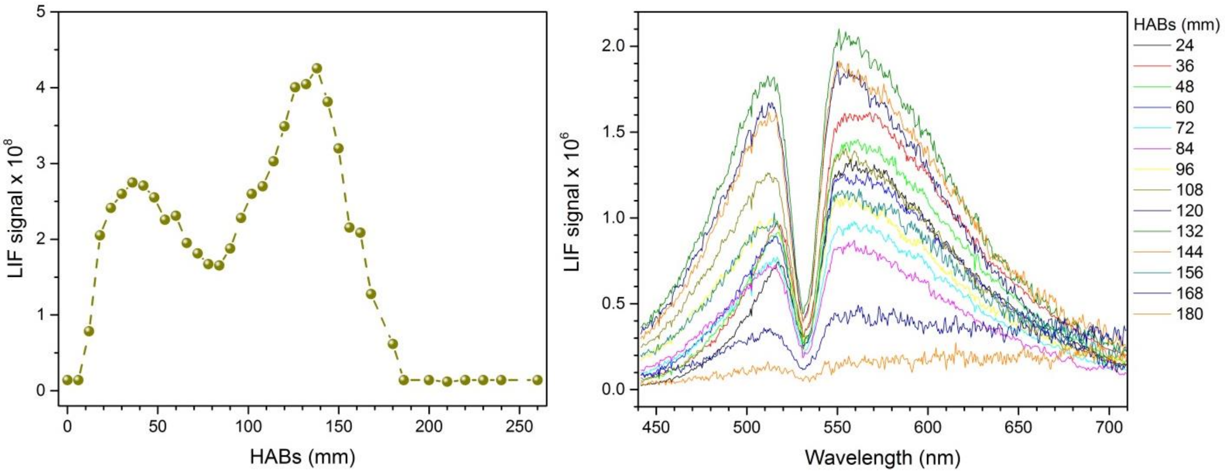

Figure 4.1.6. Left: LIF profile obtained at the centerline of the diesel flame with 532 nm excitation. Right: LIF spectra with 532 nm excitation at different HABs in the diesel flame (obtained at the centerline). Laser fluence used is 6.3 mJ/cm²

The UV-LIF spectra become broader toward infrared wavelength from 100 mm HAB indicating the formation of new species. We make this hypothesis because the first peak starts very early in the flame and the signal of LII from soot particles starts at the second peak. This is the first time that a bimodal of LIF profile is obtained in diesel flame as far as we know. (Bejaoui 2012) also studied on diesel spray flame, however they obtained unimodal LIF profile at 532 nm excitation wavelength. It is necessary to take into account the difference between the two spray burners used in these different studies. In the case of (Bejaoui 2012), a flat flame of methane is used to ignite and stabilize the diesel flame whereas in this work, the flame stabilizes itself with the help of a swirl generator. The presence of the methane flat flame probably induces the combustion procedure of the diesel droplets precluding the appearance of the first petrogenic LIF peak.

The obtained fluorescence emission spectrum starts at 400 nm and fades out at 700 nm. Both Stokes and anti-Stokes components are observed from both sides of the excitation wavelength on the emission spectrum, as usually observed with visible excitation wavelengths in flames.

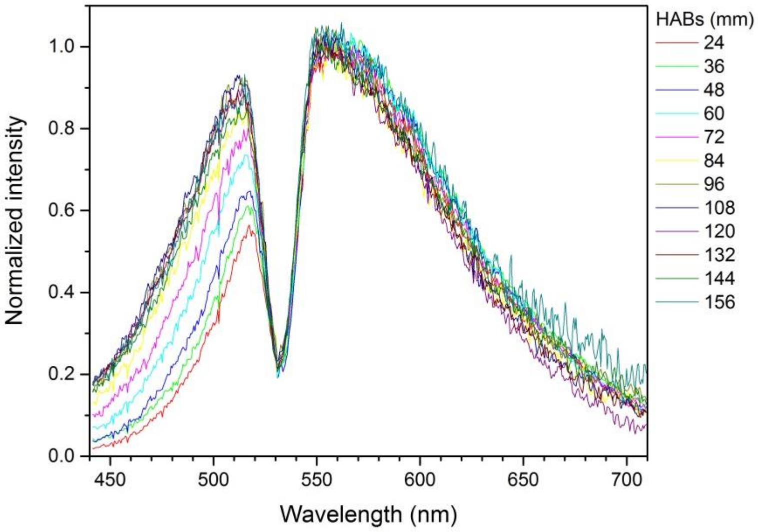

Figure 4.1.7. Normalized LIF spectra obtained at the centerline of the diesel flame with 532 nm excitation.

Figure 4.1.7 represents LIF spectra normalized to the maximum signal with 532 nm excitation. We note a remarkable evolution of the fluorescence emission spectra with the increase of HAB from 24 to 84 mm HAB. This zone corresponds to the zone of appearance of the first peak of visible fluorescence observed in Figure 4.1.6. This evolution might be due to the change of species during the combustion process. At HABs higher than 84 mm, there is no change in the form of the fluorescence spectra, therefore indicating that the pool of fluorescent species does not evolve anymore. However, the interpretation of such spectra is still subject to debate.

Many studies claimed that the fluorescence emission formed with visible excitation in the flame associates to PAHs containing more than five aromatic rings (Bejaoui et al. 2014; Smyth 1997; Goulay et al. 2013). However, according to (Karcher et al. 1985), there is no PAH up to coronene possessing strong enough absorption bands above 450 nm. In the recent work of (Mercier et al. 2019), they stated that no PAH can be excited at 532 nm excitation but only dimers of PAHs, as dimers of benzo(a)pyrene and perylene, which are formed slightly after the formation of PAHs and reach a maximum at the position corresponding to the beginning of the soot inception region. Note that in the previous work of (Salma Bejaoui et al. 2014), the flat flame of CH_4 quickly heats the diesel fuel, thus no such distinction was observed in the fluorescence spectra according to the flame height.

4.1.1.3. *Incandescence induced by 532 nm wavelength*

The LII profile obtained at the centerline of the diesel flame with 532 nm excitation is shown in Figure 4.1.8. The incandescence emission from particles starts at around 90 mm HAB in the flame. This height corresponds to the appearance of the second peak of fluorescence emission obtained with 532 nm excitation wavelength. Then the incandescence emission reaches its maximum at 150 mm HAB. After this height, the LII signal decreases with the increase of HAB. The decrease of the LII signal is due to the decrease of the volume fraction of soot particles because of the oxidation processes.

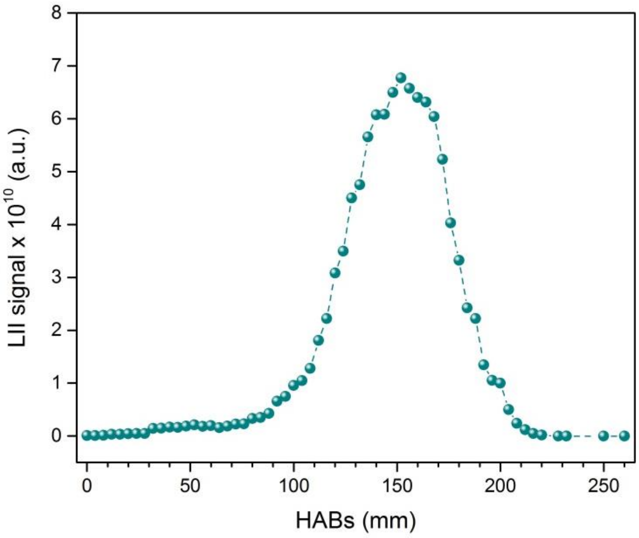

Figure 4.1.8. LII profile obtained at the centerline of diesel flame with 532 nm laser excitation. The measurement is conducted with a laser fluence of 180.6 mJ/cm². Detection wavelength range is 750-882 nm.

We also measure the decay time of LII signal with the PMT at the same laser fluence. The decay time of LII signal is affected by the primary particle size. The LII signal-decay rates depend predominantly on the conductive-cooling rates at laser fluences at which particles do not reach the sublimation point. But at higher fluences (over the sublimation threshold), the signal-decay rate is dominated by mass loss and cooling by sublimation (Migliorini, Thomson, and Smallwood 2011). A typical LII signal decay time at atmospheric pressure can be up to 1.5 µs, depending on the particle size (Irimiea 2017). The primary particle size can be determined by analyzing the decay rate of LII signal and soot temperature through detection of time-resolved LII signal coupled with modeling (Yon, Bescond, and Ouf 2015).

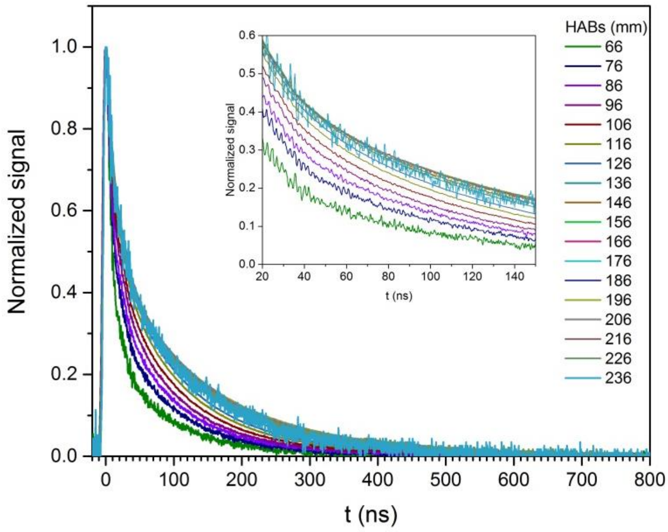

Figure 4.1.9. LII temporal profile obtained at different HABs with 532 nm laser excitation. The decay curves are averaged over 1000 laser pulses. The detection wavelength is centered at 900 nm with a width range of 6 nm.

Figure 4.1.9 presents the LII temporal profile obtained at 20 different HABs in the diesel flame with 532 nm excitation. To facilitate the determination of differences between decay curves, the term time constant τ is used in order to represent the evolution of soot and it is expressed as:

$$\tau = \frac{t}{-ln(S_{LII})} \quad \text{(eq.29)}$$

The interval between 85 and 285 ns is chosen to determine the time constant as shown in Figure 4.1.10. This method is helpful to distinguish the difference between decay curves. However, it is impossible to determine the absolute value of the particle size without a LII model. We can only qualitatively state on the increase or decrease of the diameter of the primary soot particles. Time constant τ obtained from the temporal LII profile in diesel flame with 532 nm excitation is shown in Figure 4.1.11. From the figure, we can conclude that the soot particle size increases from 66 mm up to 186 mm HAB. After this height, their size is reduced dramatically with increasing HAB because the particles are oxidized as they move toward the tip of the flame.

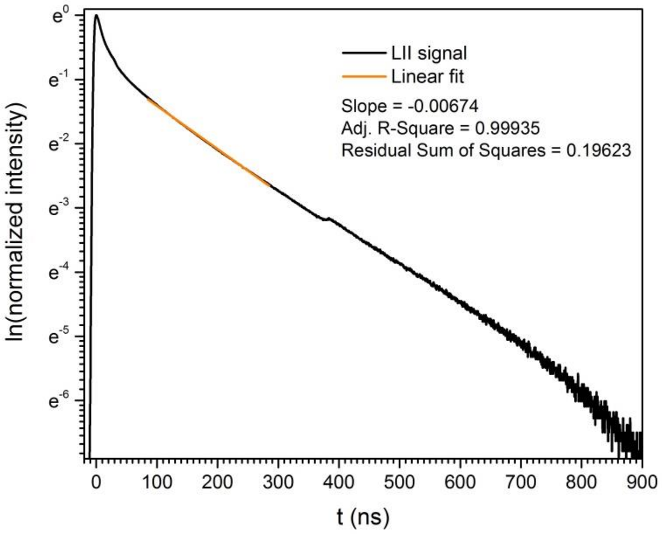

Figure 4.1.10. Normalized LII signal at 186 mm HAB in the diesel flame

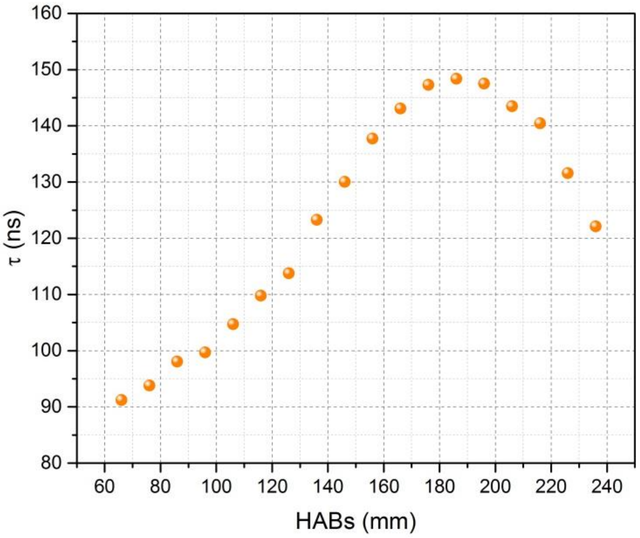

Figure 4.1.11. Time constant obtained from the temporal LII profile in Figure 4.1.9

4.1.1.4. *Incandescence induced by 1064 nm wavelength*

Incandescence emission is collected from the diesel flame at each 8 mm HAB. The LII profile obtained at the centerline of the flame is presented in Figure 4.1.12. The result observed with 1064 nm excitation is consistent with the one from 532 nm excitation, which is presented in the previous chapter. The emitted incandescence from soot particles starts at around 110 mm HAB, then increases steeply to reach its maximum around 150 mm HAB, followed by a quick decrease.

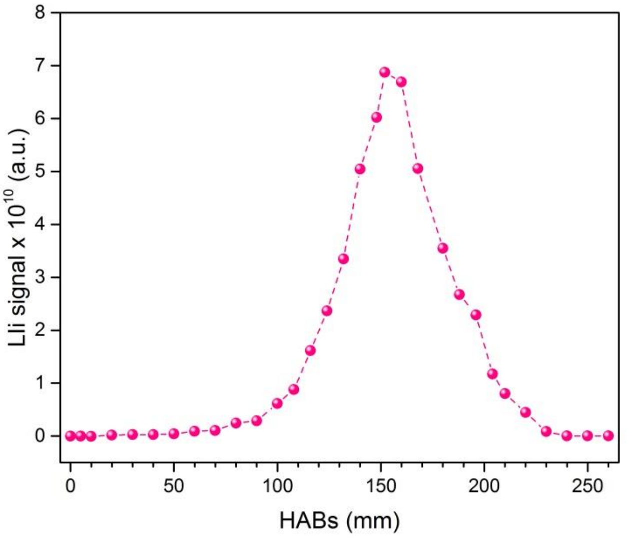

Figure 4.1.12. LII profile obtained at the centerline of the diesel flame with 1064 nm laser excitation. The detection wavelength is 535-803 nm.

Figure 4.1.13 shows the LII temporal profile obtained from 66 to 236 mm HAB in diesel flame with 1064 nm excitation. The evolution of the decay time, which is related to the evolution of primary particle size, at different HABs can be observed from the figure. Time constant τ is calculated from these decay curves to provide a better view of this evolution and is presented in Figure 4.1.14.

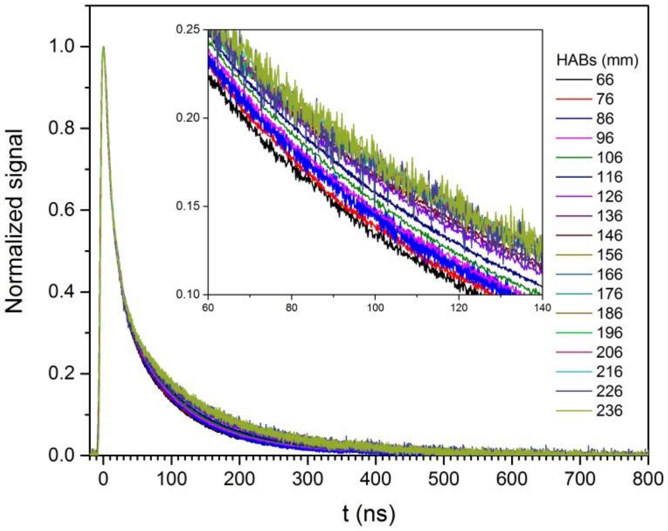

Figure 4.1.13. LII temporal profile obtained at different HABs with 1064 nm laser excitation. The decay curves are averaged over 1000 laser pulses.

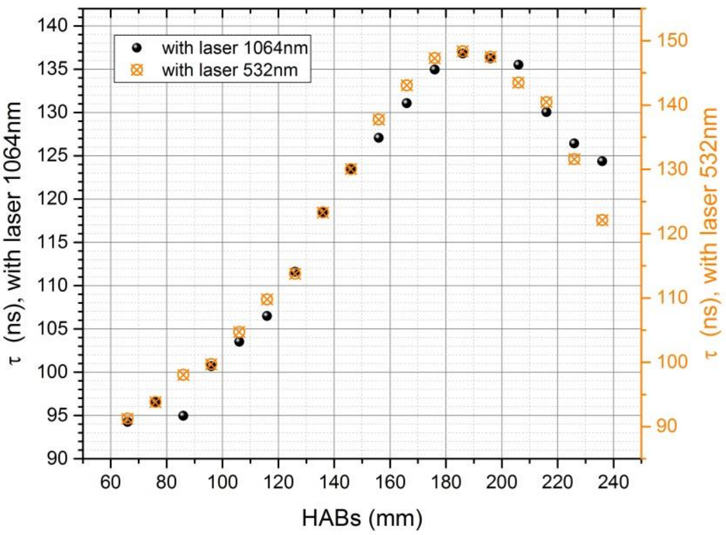

Figure 4.1.14. Time constant corresponding to the LII signal presented in Figure 4.1.13 (1064 nm excitation), compared with time constant obtained with 532 nm excitation

There is consistence between time constants obtained with 1064 nm and 532 nm excitations. The soot diameters increase gradually from 66 mm HAB up to 186 mm HAB. Then we observe a dramatic decrease of the time constant after this HAB indicating a reduction of the particle diameter in this region. The LII measurement at 532 and 1064 nm using the same detection range (900 ± 6 nm) validates the possibility to use 532 nm excitation for LII measurement and the absence of interfering LIF signals above 700 nm.

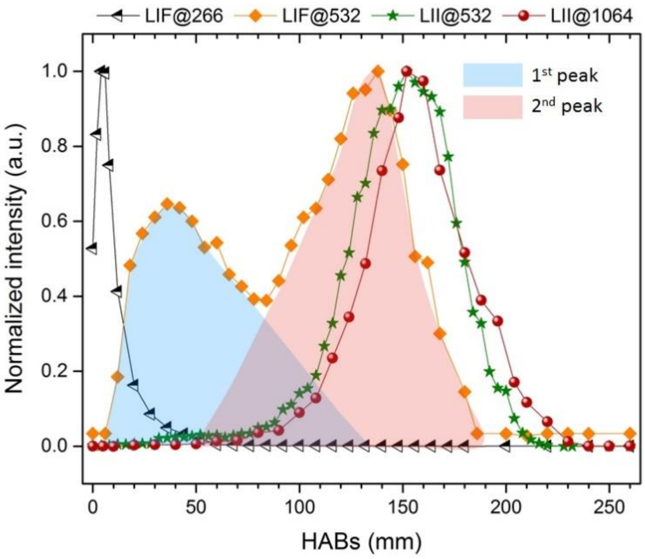

Figure 4.1.15. Variation of soot particles and their precursors in the centerline of the diesel flame. Blue and pink areas show the potential zones of two different classes of species, which correspond to the 1st and 2nd peaks of Vis-LIF profile obtained with 532 nm excitation wavelength.

Figure 4.1.15 displays an overview of the detected classes of compounds in the centerline of the diesel flame. The UV-LIF signal starts at 0 mm HAB due to the presence of petrogenic species present in the fuel and increases strongly up to 4 mm HAB due to the expansion of the liquid jet before decreasing sharply and reaching the minimum at 60 mm HAB. The maximum of UV-LIF signal corresponds to the appearance of Vis-LIF signal at 4 mm. The consumption of fuel leads to the decrease of UV-LIF and the increase of new species, which are fluorescent with 532 nm excitation. The species reach a first maximum at 40 mm HAB and are then consumed along with the combustion process, before re-increasing in the flame to reach the second peak at 140 mm HAB. In the figure, there are two areas marked in blue and pink showing the potential zone of two different classes of fluorescent species with visible excitation, according to the bimodal profile of Vis-LIF signal. The soot particles start to form above 90 mm HAB. The maximum LII signal measured with the two wavelengths (532 and 1064 nm) is located around 150 mm HAB. After this height, the signal decreases due to the oxidation process and disappears at 230 mm HAB.

4.1.2. *N*-butanol flame

N-butanol is a promising candidate to replace partly or totally diesel fuel, thus it has caught more and more attention among worldwide research groups. The investigation on particulate matter emitted from combustion of *n*-butanol in diesel blends has been carried on different types of combustors, especially engines (Choi and Jiang 2015; Jia et al. 2015; Saxena and Maurya 2016; Yan et al. 2017; Xinling Li et al. 2019; Verma et al. 2019; Lapuerta et al. 2019). In this study, we conduct the combustion of *n*-butanol on our home-made swirled jet burner in order to avoid the interference of operating parameters as in engine on the PAH and soot formation.

The experimental configuration for the study with *n*-butanol is similar to the diesel one. However, the flow rates of fuel and air are modified in order to obtain an equal heating value for the two flames. The *n*-butanol flame produced in our home-made swirled jet burner is approximately 260 mm tall, similar to the diesel flame, using 142.1 g/h of *n*-butanol, 264 mL/min of nebulization nitrogen and 21.946 L/min of air.

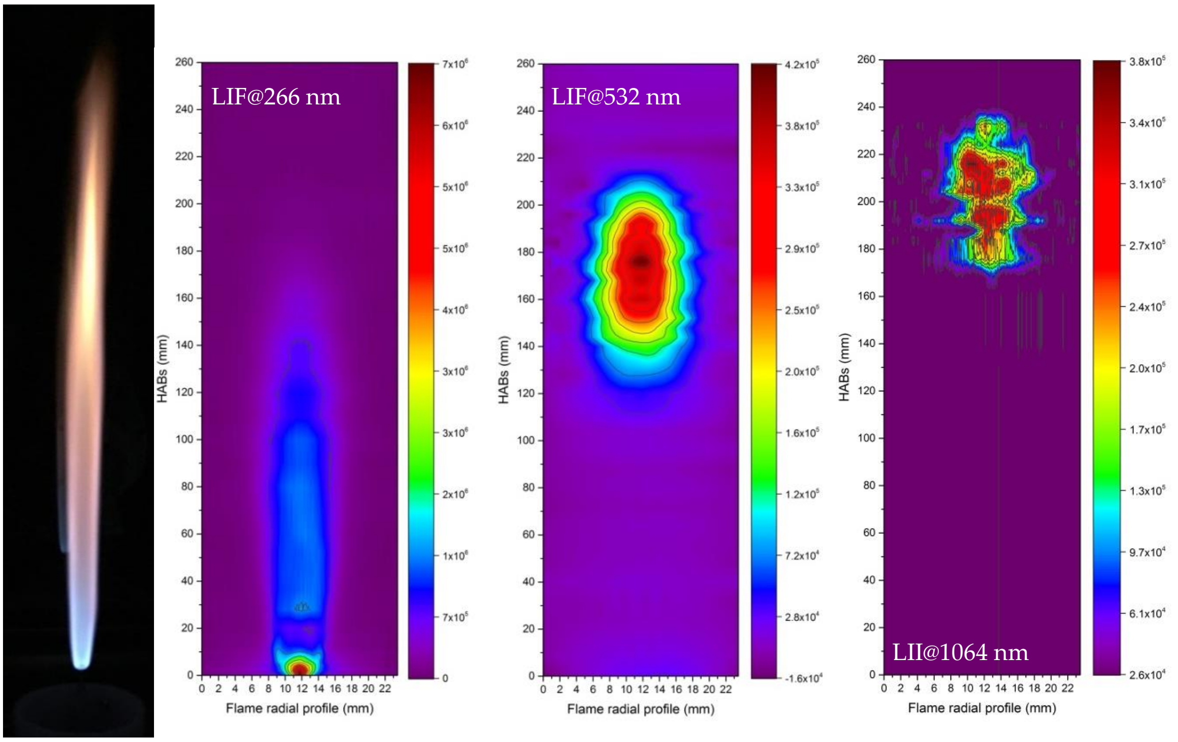

Figure 4.1.16. Photo of *n*-butanol swirled jet flame and its 2D plots of soot and soot precursor obtained by coupling of LII and LIF at 266, 532 and 1064 nm excitation.

The picture of the *n*-butanol flame and 2D plots of soot and soot precursors are represented in Figure 4.1.16. As it can be seen in the figure, the fluorescence signal from 266 nm excitation starts very early in the flame. LIF emission from 532 nm excitation starts later at 130 mm HAB, and fades out around 210 mm. In comparison with the diesel flame, this LIF emission in the *n*-butanol flame does not appear with bimodal structure. LII signal from soot particles starts later in the flame around 170 mm HAB which corresponds to the maximum of the LIF signal from 532 nm wavelength and fades out at 240 mm HAB.

4.1.2.1. *Fluorescence induced by 266 nm excitation*

As discussed in previous subchapters, it is necessary to determine the laser fluence value to use for LII and LIF measurement. Comparatively with the diesel flame, only a very small amount of particles are formed in the *n*-butanol flame, close to the LII sensitivity threshold, which precludes the recording of LII fluence curves at 266 nm. Therefore, we first choose to use the same laser fluence (1.46 mJ/cm^2) used for the diesel LIF experiments to carry out the LIF measurements in this flame. However, this fluence was too low to allow the measurement of any LIF signals in the *n*-butanol flame.

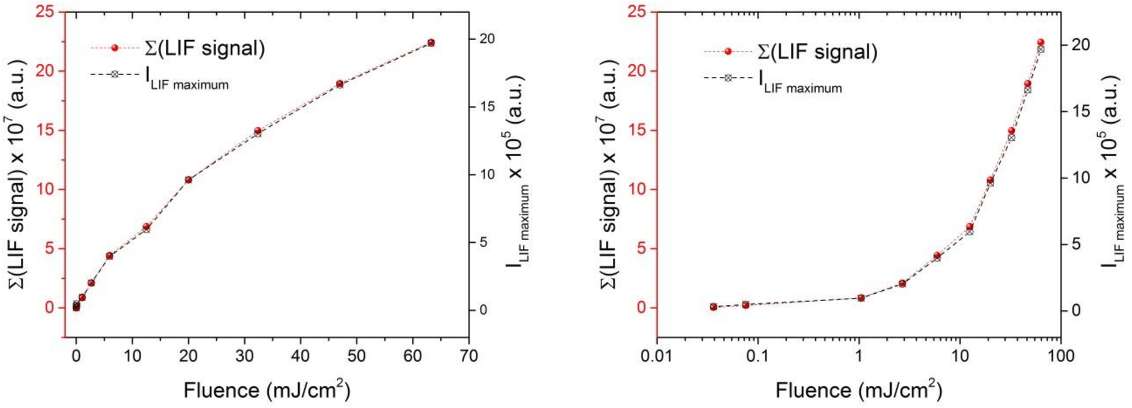

Figure 4.1.17. LIF fluence curve (in linear-log (left) and linear-log (right) graphs) obtained with 266 nm wavelength excitation at 70 mm HAB in *n*-butanol flame. Emitted light is collected in the spectral range 295 - 470 nm.

The evolution of the fluorescence signal recorded as a function of the laser fluence at 70 mm HAB in *n*-butanol flame is shown in Figure 4.1.17. The emitted light is collected in the range 295 – 470 nm. Left figure represents the data with linear mode, while right figure shows them with a fluence logarithm scale. From the figures, LIF signal increases with the rise of laser fluence. From this last figure, the fluorescence signal emitted by the *n*-butanol flame appears to only start at around 2 mJ/cm^2, and increase sharply with laser fluence higher than 11 mJ/cm^2. In order to have sufficient LIF signal without any incandescence emission, we choose a laser fluence of 42.1 mJ/cm^2 for the LIF measurement in this flame.

The optical configuration used for the LIF measurement with 266 nm excitation for the *n*-butanol flame is similar to the one used for the diesel flame. A diffraction grating equipped with a 150 groves/mm blazed at 300 nm, centered at 430 nm wavelength is used. Each spectrum is averaged over 800 laser pulses with a gate width of 50 ns. Fluorescence emission profile taken at the center of the *n*-butanol flame and emission spectra at different HABs are shown in Figure 4.1.18. There is a significant involvement of the second order of diffraction at 532 nm due to the laser excitation wavelength. The presence of this signal is more intense at low HABs due to the existence of fuel droplets at these heights. To avoid overestimating the fluorescence signal at these HABs, only wavelengths in the range of 295 – 410 nm are integrated to build the LIF image. However, this way will underestimate the fluorescence emission at higher HABs where there is no existence of droplets since the scattering signal disappears and the LIF spectra shift to the red.

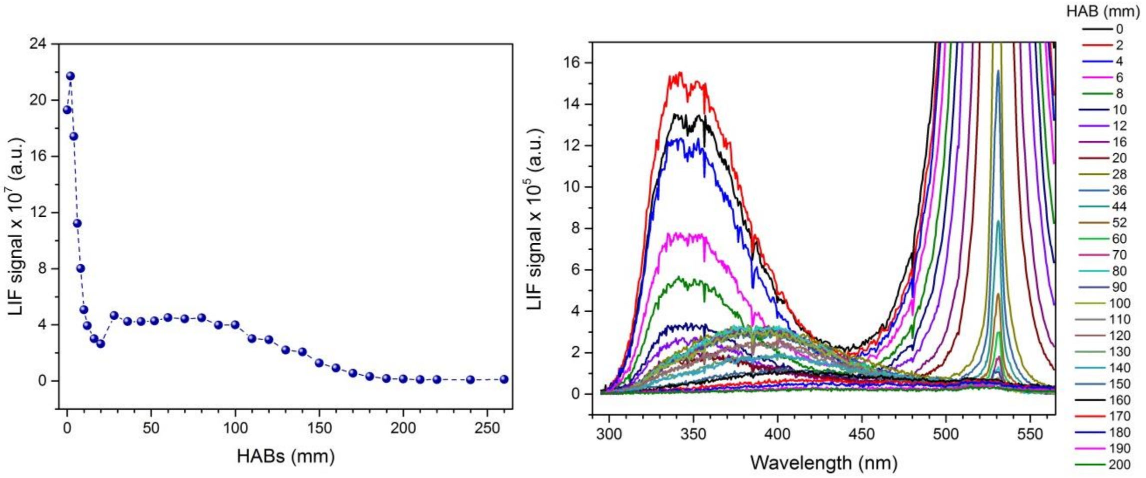

Figure 4.1.18. Left: LIF profile obtained at the centerline of *n*-butanol flame with 266 nm excitation. Right: LIF spectra with 266 nm excitation at different HABs in *n*-butanol flame (obtained at the centerline). Laser fluence used is 42.13 mJ/cm^2.

As it can be seen in Figure 4.1.18, the fluorescence signal is the most intense at low HABs. This phenomenon is similar to what was obtained with the diesel flame. However, there were aromatic species present in the diesel fuel, which is not the case with *n*-butanol. To deepen this study, a fluorescence spectrum of cold droplets of *n*-butanol is reported as in Figure 4.1.19.

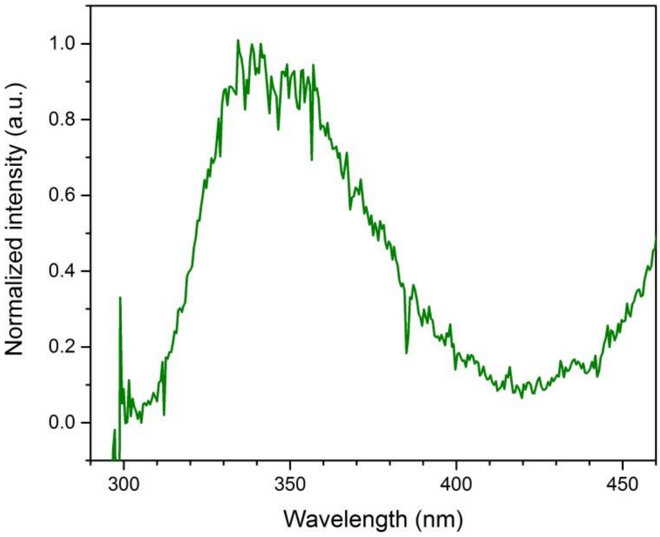

Figure 4.1.19. Normalized fluorescence emissions of *n*-butanol cold droplets, obtained with 266 nm excitation

The results show that *n*-butanol droplets absorb very well UV light, in this case at 266 nm, and emit a broadband spectrum from 300 nm to 400 nm. The second order of diffraction of the laser is still visible here due to the obvious presence of *n*-butanol droplets. In the study of (Xu et al. 2018), they reported that *n*-butanol absorbs efficiently UV light in the range 190 – 250 nm and the fluorescence emitted is detected only in the UV range 210 – 250 nm. We did not find any other studies reporting visible fluorescence emission of *n*-butanol as we found.

The LIF signal increases slightly from 0 mm to 2 mm HAB, this might be due to the effect of atomization and vaporization of *n*-butanol droplets. After this height, the fluorescence decreases sharply until 20 mm HAB due to the consumption of *n*-butanol fuel in the combustion process. The LIF signal re-increases from 20 mm HAB and the intensity of the signal stays the same until 100 mm HAB before gradually diminishing and fading out after 200 mm HAB.

In order to better analyze these signals, we normalize the LIF spectra to their maximum value as shown in Figure 4.1.20. The emission spectra from 0 mm to 8 mm HAB are very similar with a maximum signal located around 335 – 355 nm, meaning that at these heights in the flame, there might be no or very minor change of the formed species. We then observe a first red shift of the spectra from 8 to 28 mm HAB. These spectra do not evolve from 28 to 110 mm, characterized by a broadband structure centered around 380 – 400 nm. Furthermore, at these HABs, the intensity of the LIF emission remains constant. Above 110 mm HAB, the spectra change again and shift to the red until 160 mm HAB. The very last LIF spectra obtained from 170 to 200 mm HAB have poor signal to noise. Peaks of these spectra are located in the range of 410 – 470 mm HAB.

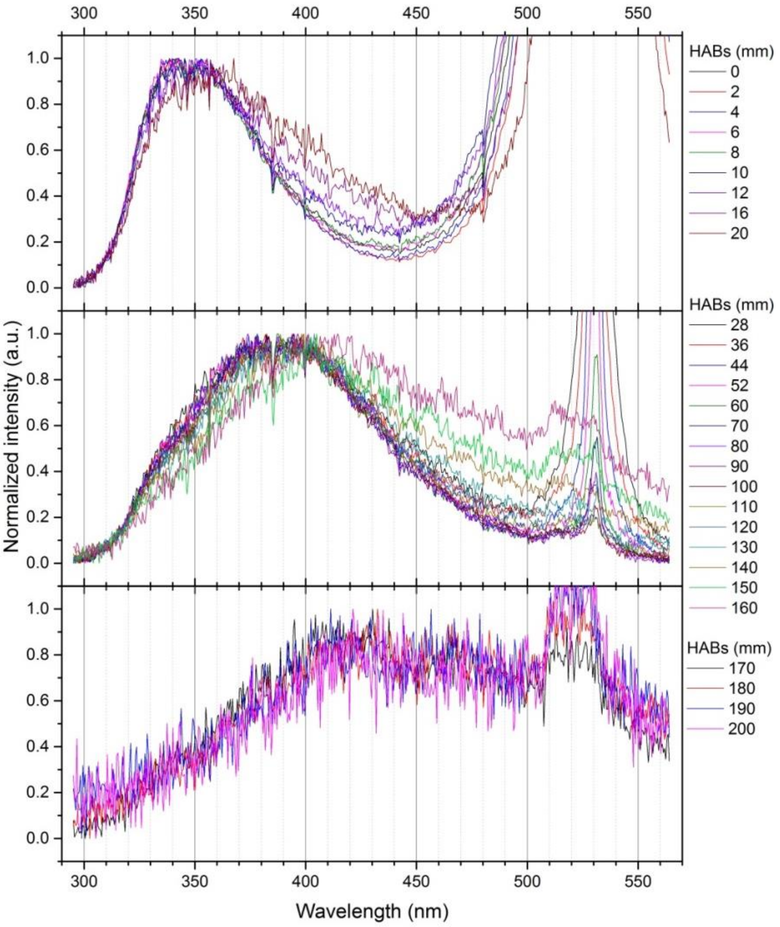

Figure 4.1.20. Normalized LIF spectra obtained at the centerline of *n*-butanol flame with 266 nm excitation.

4.1.2.2. Fluorescence induced by 532 nm excitation

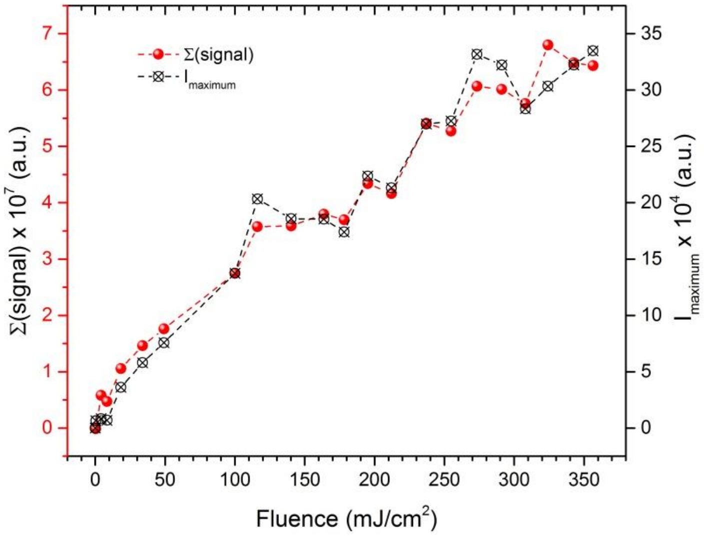

Figure 4.1.21. Laser induced incandescence (LII) fluence curve obtained with 266 nm wavelength excitation at 185 mm HAB in *n*-butanol flame. Emitted light is collected in the spectral range 800 - 900 nm.

As for the diesel flame, we also use the 532 nm excitation wavelength for LIF measurement in the *n*-butanol flame. The optical configuration was similar to the one used for the study of the diesel flame. The fluence curve obtained with this wavelength in the *n*-butanol flame is shown in Figure 4.1.21. Emitted light is collected in the spectral range 800 – 900 nm. In contrast with the diesel flame, we could not reach the sublimation threshold of soot particles in *n*-butanol flame. The emission collected is roughly linear to the laser fluence. Therefore, for this LIF measurement, a laser fluence at 10.7 mJ/cm^2 – which is similar to the laser fluence employed in the diesel flame – is used. As it can be seen from the figure, there is very poor LII signal observed with 532 nm excitation wavelength in the *n*-butanol flame.

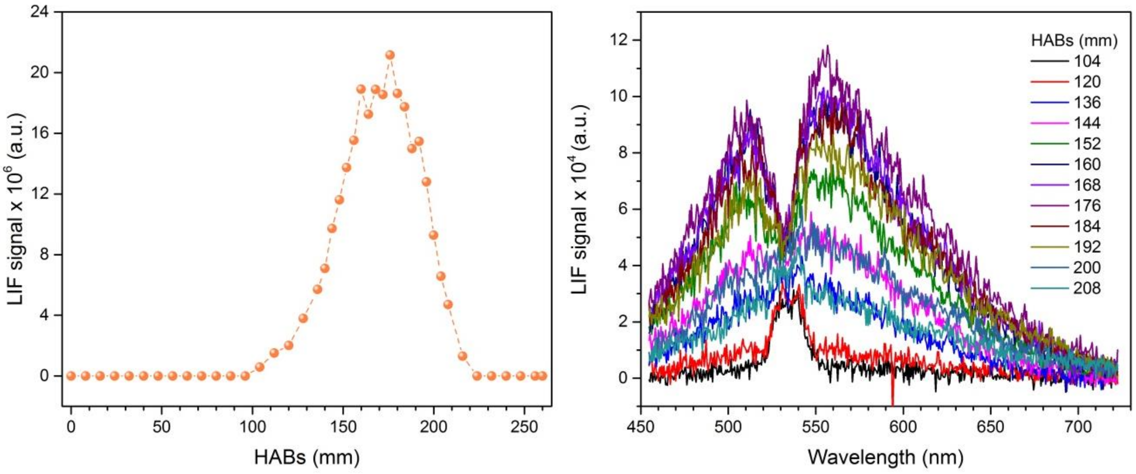

Figure 4.1.22. Left: LIF profile obtained at the centerline of *n*-butanol flame with 532 nm excitation. Right: LIF spectra with 532 nm excitation at different HABs in *n*-butanol flame (obtained at the centerline). Laser fluence used is 10.73 mJ/cm²

The measurements have been done every 8 mm along the height of the flame. Each spectra is averaged over 800 laser pulses with a gate width of 50 ns. We used a 150 groves/mm blazed at 300 nm diffraction grating. The grating is centered at 570 nm. The obtained LIF profile and corresponding spectra are represented in Figure 4.1.22. As it can be seen from the figure, the fluorescence signal starts at 110 mm HAB. The LIF signal increases and reaches its peak at 176 mm HAB. After this height, fluorescence signal diminishes and completely fades out at 220 mm HAB. This result corresponds well to the LIF measurement done with UV excitation in the previous subchapter.

Normalized fluorescence emission spectra are reported in Figure 4.1.23. There is no significant evolution of spectral shape. This might indicate that the pool of fluorescent species does not evolve very much.

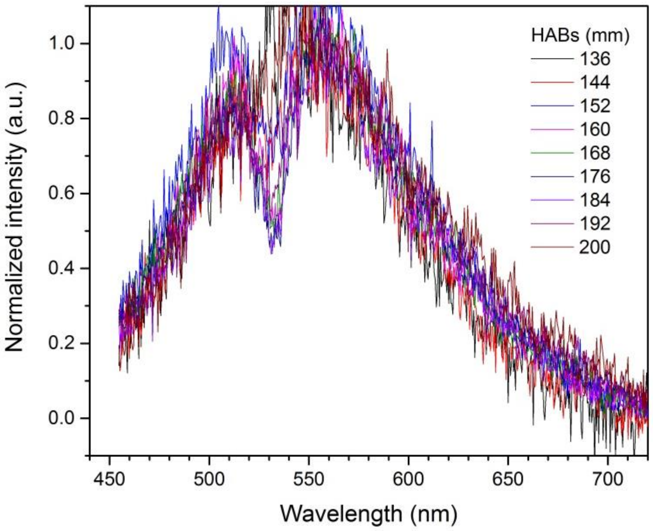

Figure 4.1.23. Normalized LIF spectra obtained at the centerline of *n*-butanol flame with 532 nm excitation

It is not possible to detect soot particles in the *n*-butanol flame with 532 nm excitation because of very low amount of formed soot particles in this flame. Therefore we present directly the LII measurement obtained in this flame with 1064 nm excitation in the next subchapter.

4.1.2.3. Incandescence induced by 1064 nm excitation

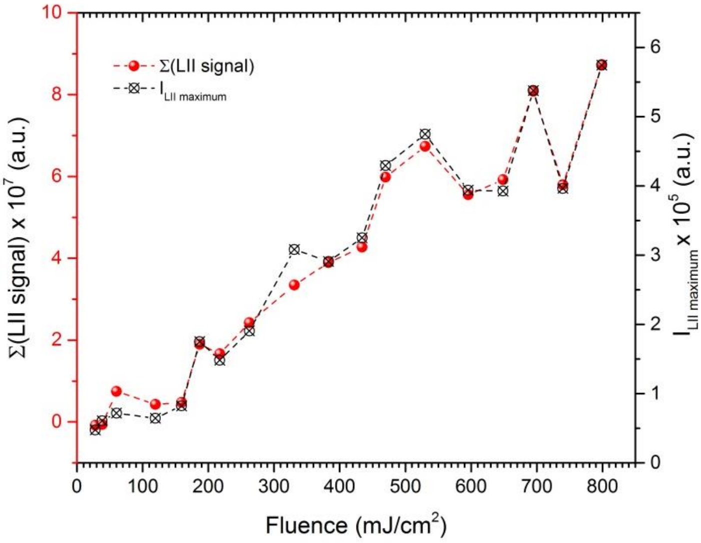

Figure 4.1.24. LII fluence curve obtained with 1064 nm wavelength excitation at 196 mm HAB in *n*-butanol flame. Emitted light is collected in the spectral range 700 - 800 nm.

The optical configuration is similar to the one used with diesel flame. Incandescence emission is collected with a 150 groves/mm grating, blazed at 800 nm. Each spectrum obtained is averaged over 1000 laser pulses with 50 ns gate width. Fluence curve obtained with 1064 nm excitation at 196 mm HAB in the *n*-butanol flame is presented in Figure 4.1.24. Similarly to the case of 532 nm, the fluence curve shows a linear relationship between the LII emissions observed from the soot and the laser fluence. There is no sublimation threshold found in this case. The laser fluence at 439.2 mJ/cm^2 is used for LII measurement in *n*-butanol. The laser fluence used in this case is higher than the one used in the diesel flame due to the very low incandescence signal that can be obtained with *n*-butanol.

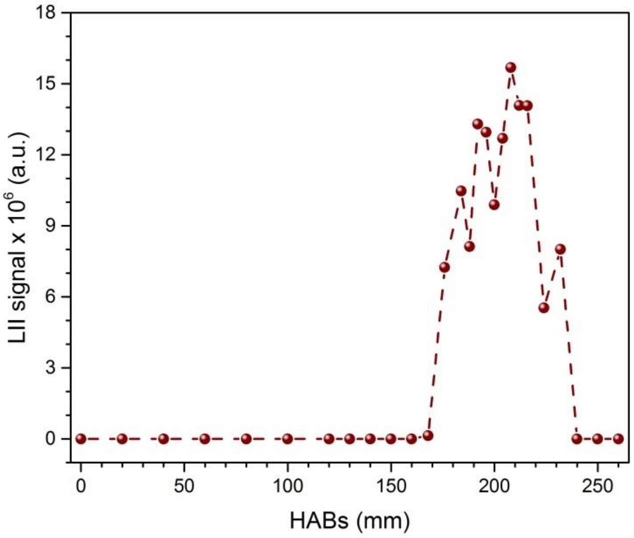

Figure 4.1.25. LII profile obtained at the centerline of *n*-butanol flame with 1064 nm laser excitation. Laser fluence is used at 439.2 mJ/cm^2

The profile of incandescence signal obtained at the centerline of *n*-butanol flame with 1064 nm laser excitation is shown in Figure 4.1.25. This profile is noisy due the low concentration of soot in the flame. However, it is still possible to see that the soot particles start forming at 170 mm up to 240 mm HAB. The most intense LII signal is located at 210 mm HAB.

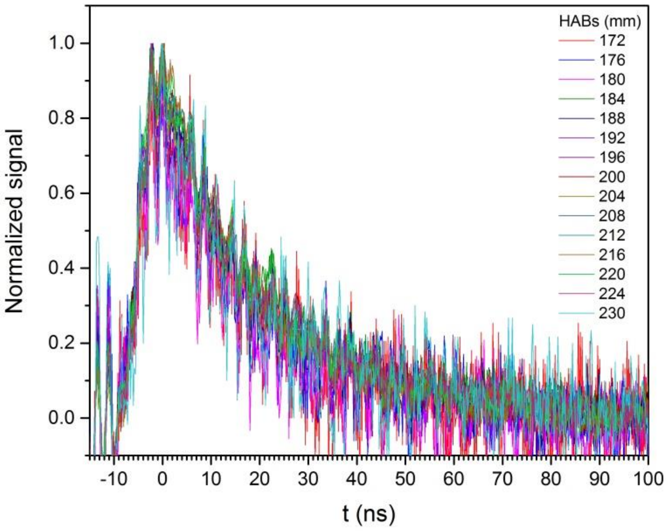

Figure 4.1.26. LII temporal profile obtained at different HABs in *n*-butanol flame with 1064 nm laser excitation. The decay curves are averaged over 1000 laser pulses. Laser fluence is 344.23 mJ/cm^2.

The corresponding incandescence temporal decay curves have been also measured with a PMT in the *n*-butanol flame and reported in Figure 4.1.26. The curves are measured with the 1064 nm excitation wavelength, a fluence of 344.23 mJ/cm^2 and are averaged over 1000 laser pulses. The temporal LII result shows that the LII signal associated with the soot particles in the *n*-butanol flame have similar decay times at different HABs from 172 mm to 230 mm. The decay time of the signal is approximately 90 ns, much shorter than what was achieved in the diesel flame (about 500 ns). This result is very similar to the previous measurements reported in the study of (Betrancourt et al. 2017) in a nucleation flame of butane, of (Desgroux et al. 2017) and (Mouton et al. 2013) in low pressure methane flames. Their LII signals decay very rapidly and are almost the same for the measurement at different heights, meaning that soot particles formed in this flame do not undergo growth processes. Moreover, the atypical shape of the fluence curve is very similar to the ones measured in the different "nucleation" flames (Mouton et al. 2013; Betrancourt et al. 2017). All these statements seem to indicate that soot produced in n-butanol flame in this study is very similar to the nascent soot particles (NSP) in "nucleation" flames.

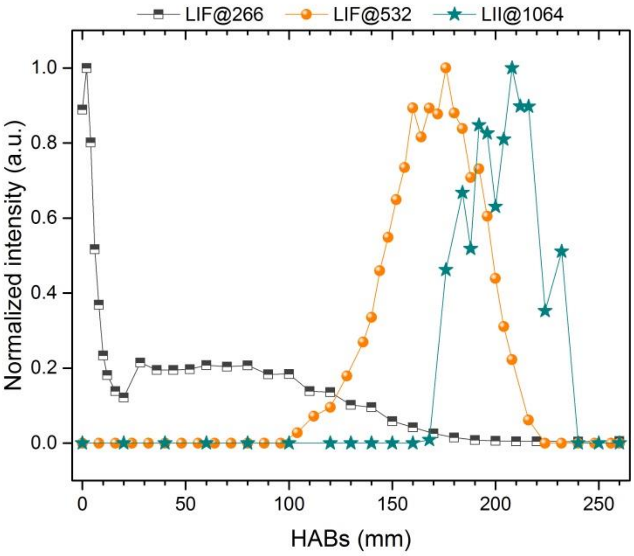

Figure 4.1.27. Variation of soot particles and their precursors in the centerline of *n*-butanol flame

An overview of the detected classes of compounds in the *n*-butanol flame is reported in Figure 4.1.27. The UV-LIF signal starts at maximum intensity at the beginning of the flame due to the strong fluorescence from *n*-butanol molecules. The signal is then diminished sharply because of the consumption of *n*-butanol in the combustion process until 20 mm HAB. After this height, the UV-LIF signal re-increases slightly due to the formation of other fluorescent species. The concentration of these species is stable until 100 mm HAB before decreasing and completely fading out at 200 mm HAB. The Vis-LIF signal is active at the height where UV-LIF signal started diminishing – 110 mm. The consumption of UV-LIF species leads to the formation and increase of Vis-LIF species to reach the maximum at 176 mm HAB. At this height, the LII signal is active. The start of LII signal corresponds accurately to the maximum Vis-LIF signal. Then the Vis-LIF profile continuously decreases while the soot profile increases until 210 mm HAB. Finally the LII signal characterizing soot particles is not observed anymore above.

4.1.3. Mixture flame

In the previous subchapter, the neat *n*-butanol flame shows very little LII signal compared to the diesel flame. This subchapter is dedicated to the LII and LIF measurements on a flame of mixture of 50%v/v *n*-butanol blended in diesel in order to determine if there are any interactions or synergistic effects between these two fuels.

To obtain similar heating value as for the diesel and *n*-butanol flames, the fuel flow rate of 125.58 g/h, nebulization nitrogen flow rate of 264 mL/min and air flow of 22.09 L/min are used. The obtained flame is approximately 260 mm height with luminous yellow color in the top half and transparent blue color in the bottom half.

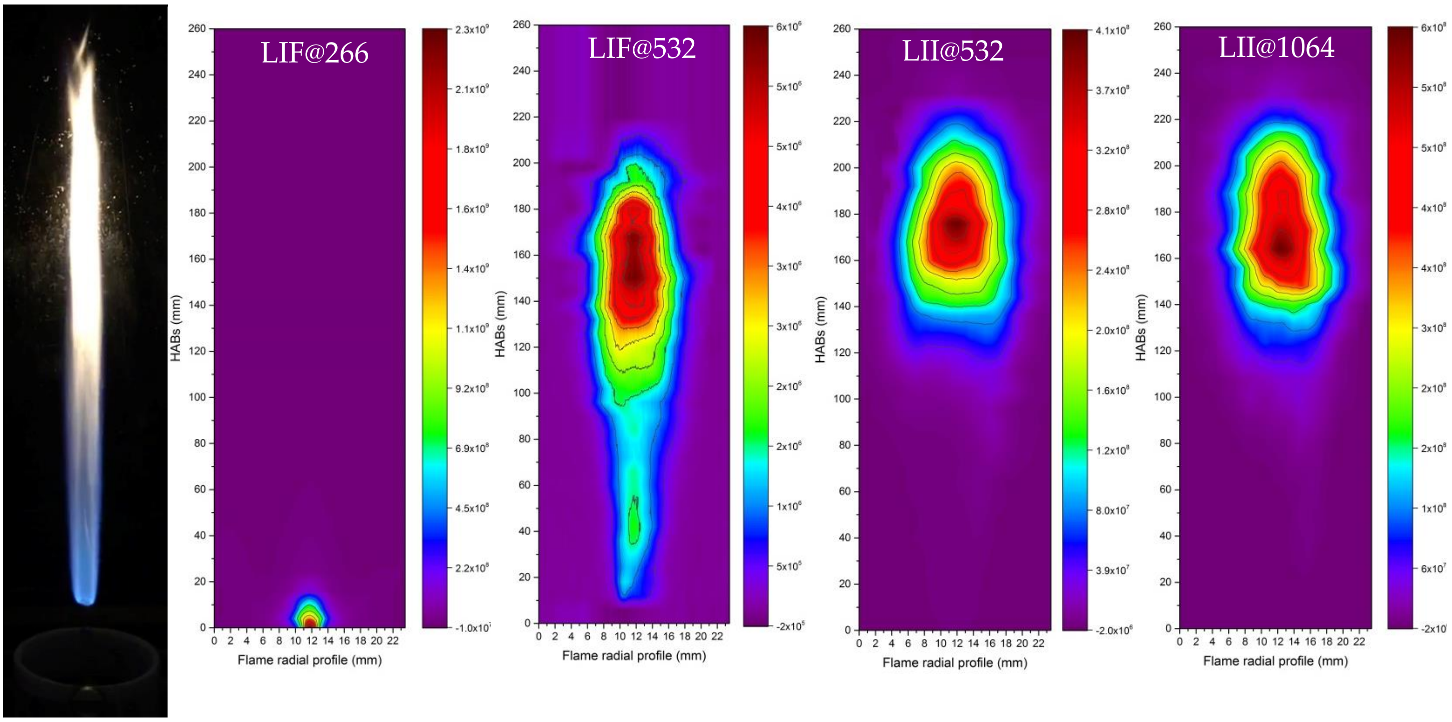

Figure 4.1.28. Photo of mixture swirled jet flame and its 2D plots of soot and soot precursor obtained by coupling of LII and LIF at 266, 532 and 1064 nm excitation.

The photo and 2D images of soot and soot precursors detected by LII/LIF techniques are presented in Figure 4.1.28. Similarly as for diesel and *n*-butanol flames, the UV-LIF signal from the mixture flame is very intense at the outlet of the nebulizer. This signal disappears quickly at 20 mm HAB. The Vis-LIF emission starts very early at 10 mm HAB due to the early formation of petrogenic species in the flame. After 45 mm HAB, Vis fluorescence signal decreases and re-increases above 100 mm up to the maximum value at 150 mm HAB. The Vis-LIF completely disappears at 210 mm HAB. The bimodal shape of the Vis-LIF signal in mixture flame is similar to what was obtained with the diesel flame but less intense. LII signals with Vis and IR excitation show a good agreement. Particulate matter starts forming at 120 mm HAB and fades out at 210 mm HAB. However, the positions of the maxima of the LII intensity according to the different excitation wavelengths exhibit a slight difference. In the case of 532 nm excitation, the maximum of soot is located around 175 mm HAB, whereas with 1064 nm excitation, the soot peak is at 165 mm HAB.

4.1.3.1. *Fluorescence induced by 266 nm excitation*

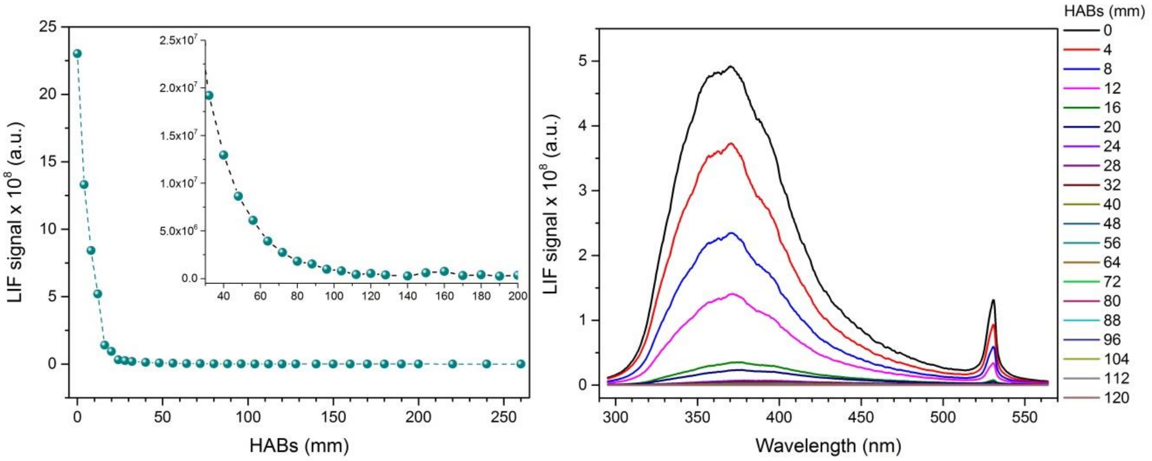

Figure 4.1.29. Left: LIF profile obtained at the centerline of the mixture flame with 266 nm excitation. Right: LIF spectra with 266 nm excitation at different HABs in the mixture flame (obtained at the centerline). Laser fluence used is 1.1 mJ/cm^2.

The LIF profile obtained along the centerline of the flame and the corresponding spectra at different HABs are shown in Figure 4.1.29. As shown in the spectra, there is a small peak at 532 nm corresponding to the second order of diffraction of the laser beam at low HABs – where the fuel droplets still exist. The profile of UV-LIF signal is recorded in the wavelength range of 295 – 510 nm to avoid the interferences due to the diffraction signal. The maximum of the fluorescence signal is located at the tip of the nebulizer (0 mm HAB). As presented in subchapters 4.1.1.1 and 4.1.2.1, both diesel and *n*-butanol absorb strongly UV excitation wavelengths and fluoresce in the wavelength range of 350 – 390 nm. Therefore the LIF signal emitted at low HABs in the mixture flame originates from the fuel. Figure 4.1.30 compares the spectra obtained for several HABs in the flame with the fluorescence emission spectrum recorded in the cold droplets of the mixture fuel. No significant difference between these spectra is observed, therefore meaning that the spectra recorded in the flame are more representative of petrogenic species at these HABs

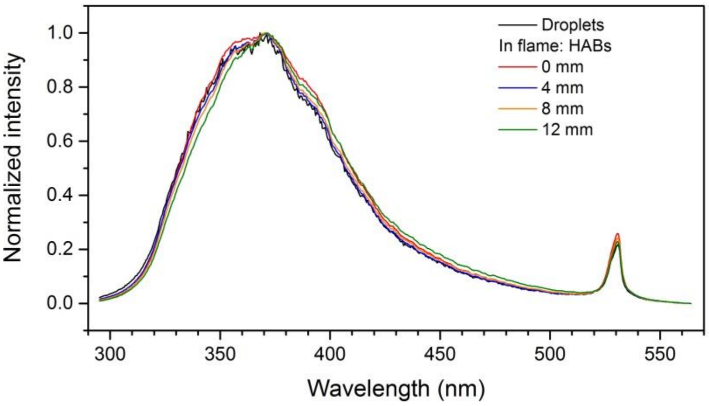

Figure 4.1.30. Comparison of LIF spectra obtained at certain HABs in the mixture flame and on cold droplets of mixture fuel

As it can be seen in the Figure 4.1.29, the LIF signal decreases sharply from 0 mm HAB due to the consumption of fuel during the combustion process. The fluorescence of the fuel is so intense that it dominates the LIF signal emitted by pyrogenic species. The fluorescence emission completely fades out at 120 mm HAB.

Fluorescence emission spectra normalized to their maximum value are shown in Figure 4.1.31. Above 12 mm HAB, the spectra start shifting to higher wavelength revealing change in the pool of the fluorescence species. The maximum intensity of these spectra varies from 370 nm to 410 nm wavelength. At higher HAB, from 104 mm, the spectra are broadened and become noisier. The 104 nm HAB corresponds to the beginning of the second peak of the Vis-LIF signal, which will be discussed in the next subchapter.

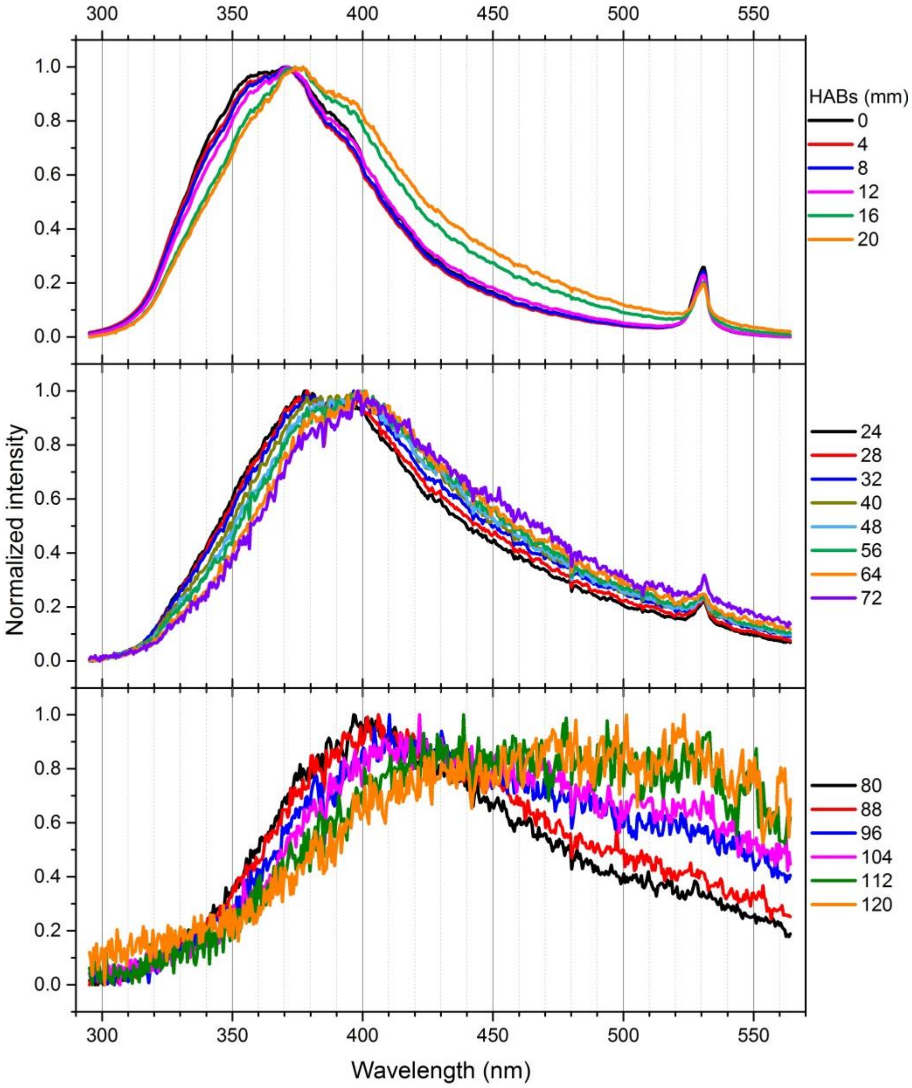

Figure 4.1.31. Normalized LIF spectra obtained at the centerline of mixture flame with 266 nm excitation.

4.1.3.2. Fluorescence induced by 532 nm excitation

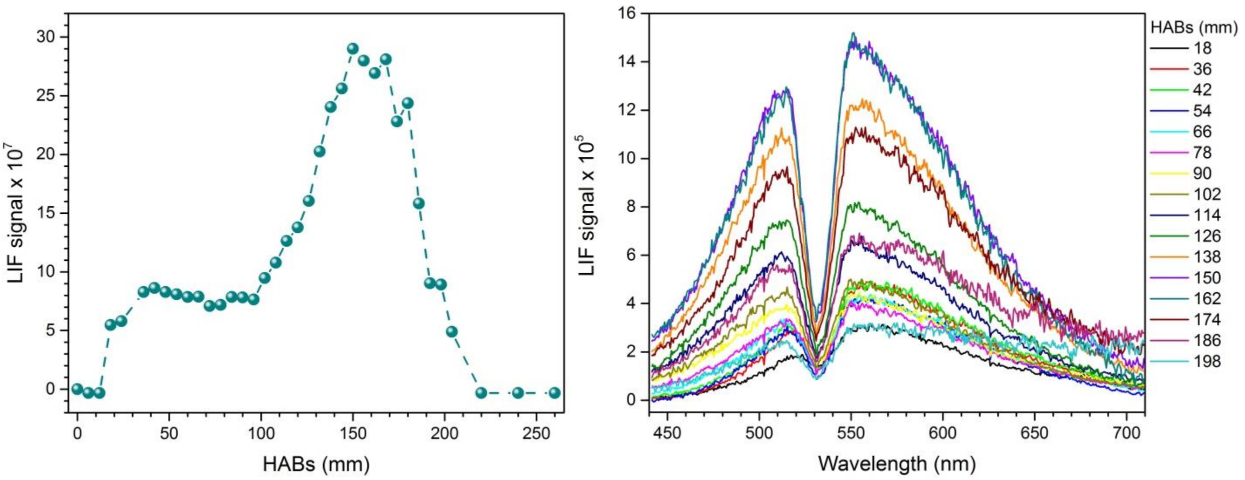

Figure 4.1.32. Left: LIF profile obtained at the centerline of the mixture flame with 532 nm excitation. Right: LIF spectra with 532 nm excitation at different HABs in the mixture flame (obtained at the centerline). Laser fluence used is 6.3 mJ/cm^2.

The profile of the Vis-LIF signal obtained in the mixture flame with 532 nm excitation and the corresponding LIF spectra measured for the different HABs are presented in Figure 4.1.32. The Vis-LIF profile again highlights a bimodal structure, similarly to what was observed in the diesel flame. A noticeable difference compared to the diesel flame is that in this case, the pyrogenic peak is less intense than for the diesel one. The first peak is located at 40 mm HAB. After this height, the LIF slightly decreases until 80 mm HAB, and re-increases again until a second peak is reached at 150 mm HAB.

The corresponding spectra are normalized to the maximum signal and shown in Figure 4.1.33. As already observed for the diesel flame, we also note an evolution of the shape of the fluorescence spectra characterized by a shift of the overall structure of the spectrum from red to blue from 18 to 78 mm HAB. Above this height, the global shape of the spectra remains identical. This evolution is similar to the observation made in the diesel flame, very likely indicates an evolution of the pool of the fluorescent species in the zone 18 – 78 mm.

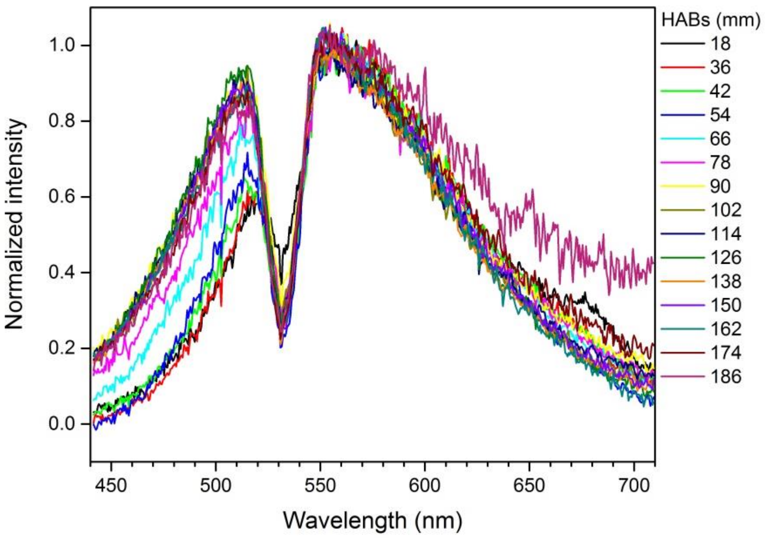

Figure 4.1.33. Normalized LIF spectra obtained at the centerline of the mixture flame with 532 nm excitation.

4.1.3.3. Incandescence induced by 532 nm excitation

The incandescence profile obtained at the centerline of the mixture flame is presented in Figure 4.1.34.

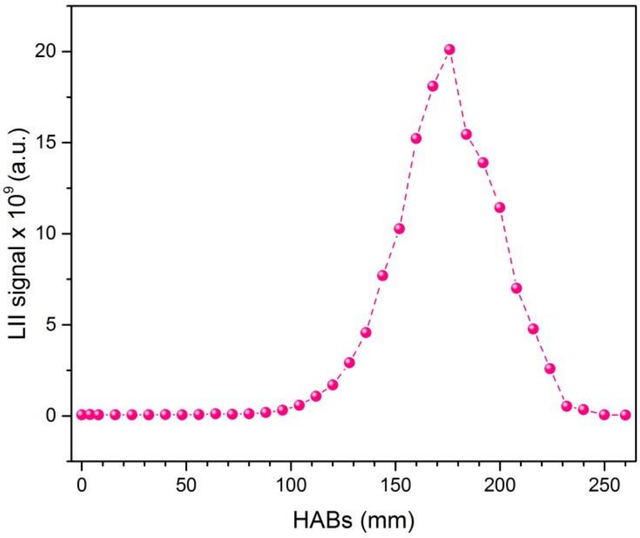

Figure 4.1.34. LII profile obtained at the centerline of the mixture flame with 532 nm laser excitation. Laser fluence is used at 179.8 mJ/cm^2

The LII signal starts being active at around 100 mm HAB, near the second Vis-LIF peak, as also observed in the diesel flame. Above 100 mm HAB, soot particles form quickly until 175 mm HAB. After this height, the LII signal decreases gradually due to the decrease of the soot volume fraction. The incandescence emission finally fades out above 240 mm HAB.

A photomultiplier tube (PMT) is used to measure the time decay of incandescence signal in the sooting zone. The normalized decay curves are shown in Figure 4.1.35.

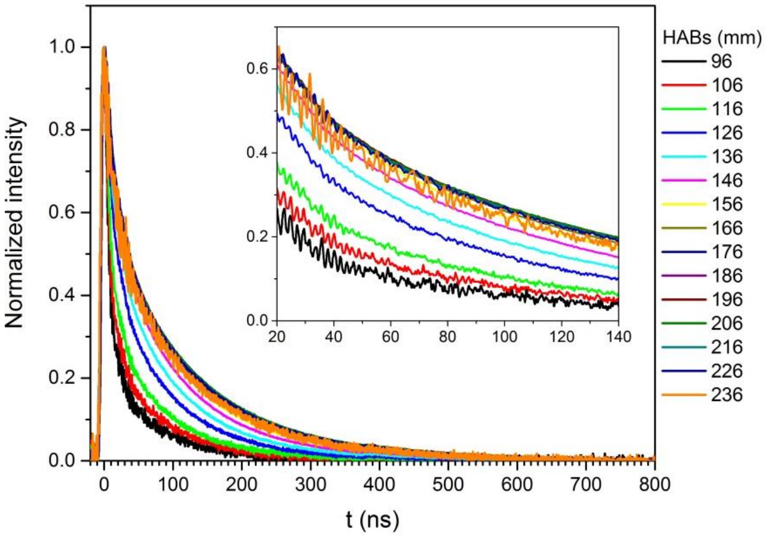

Figure 4.1.35. LII temporal profile obtained at different HABs with 532 nm laser excitation. The decay curves are averaged over 1000 laser pulses.

According to the graph, it suggests that the size of particles increases from 96 mm to 206 mm HAB. After that height, the particle diameter reduces. To facilitate the discrimination between the temporal profiles, the time constant is calculated from the decay curves and presented in Figure 4.1.36.

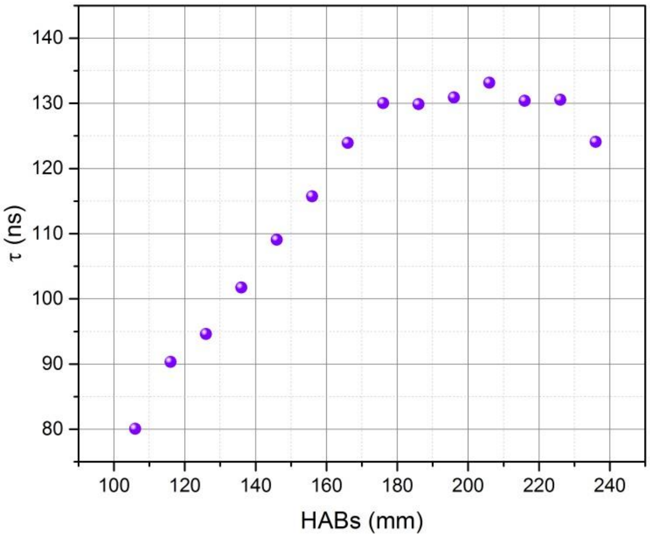

Figure 4.1.36. Evolution of LII time constant (obtained from the temporal profiles in Figure 4.1.35) with the HAB

Similarly as in the case of the diesel flame, an interval between 85 and 295 ns is chosen to calculate the time constant. From the figure, it can be concluded that the particles grow up in size until 206 mm HAB. After this height, the particles reduce their size through oxidation or other processes.

4.1.3.4. Incandescence induced by 1064 nm excitation

The LII signal is collected every 8 mm HAB in the mixture flame using a similar configuration as in the previous subchapter. Figure 4.1.37 presents the LII profile taken at the centerline of the mixture flame with 1064 nm excitation.

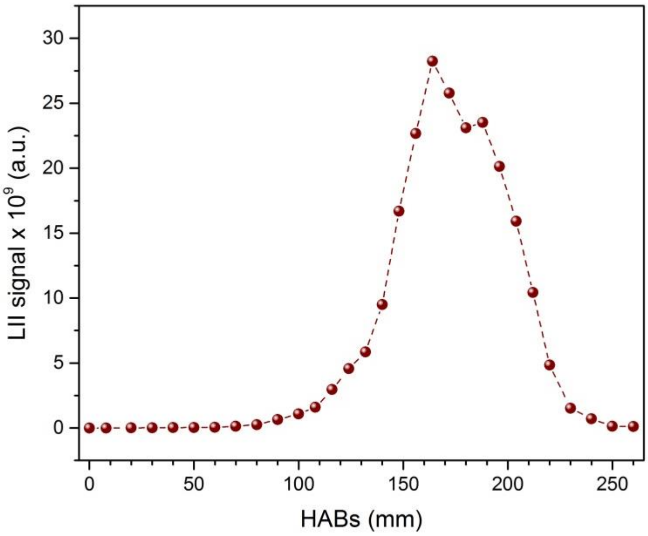

Figure 4.1.37. LII profile obtained at the centerline of the mixture flame with 1064 nm laser excitation. Laser fluence is 340.1 mJ/cm²

The profile is in good agreement with the LII measurements done with 532 nm excitation. The LII signal is activated at around 100 mm HAB and increases sharply up to 165 mm HAB before decreasing and fading out at 240 mm HAB.

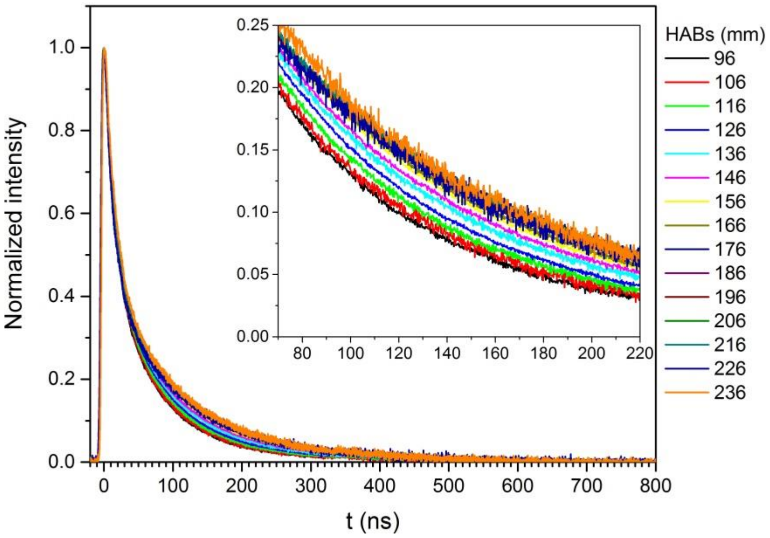

Figure 4.1.38. LII temporal profile obtained at different HABs in the mixture flame with 1064 nm laser excitation. The decay curves are averaged over 1000 laser pulses.

Temporal profiles of LII emissions obtained at different HABs in the mixture flame are shown in Figure 4.1.38. LII decay curves are decreasing over 600 ns. Time constants deduced from the temporal profile are presented in Figure 4.1.39 to better distinguish between the decay curves. The figure also compares the time constant obtained with 532 nm and 1064 nm excitation wavelengths. The result shows that there is no distinct difference between the two measurements. They both show the growth of soot particles up to 206 mm HAB. After this height, the soot particle size decreases towards the upstream of the flame.

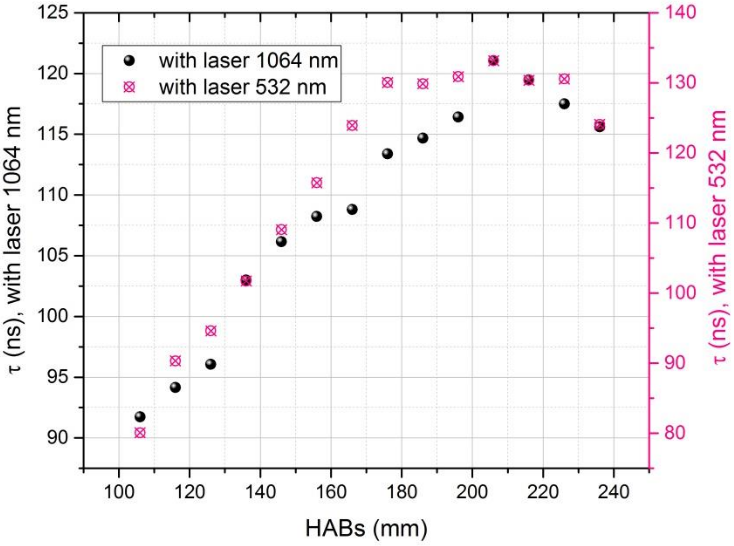

Figure 4.1.39. Time constant corresponding to the LII signal presented in Figure 4.1.38 (1064 nm excitation), compared with time constant obtained with 532 nm excitation

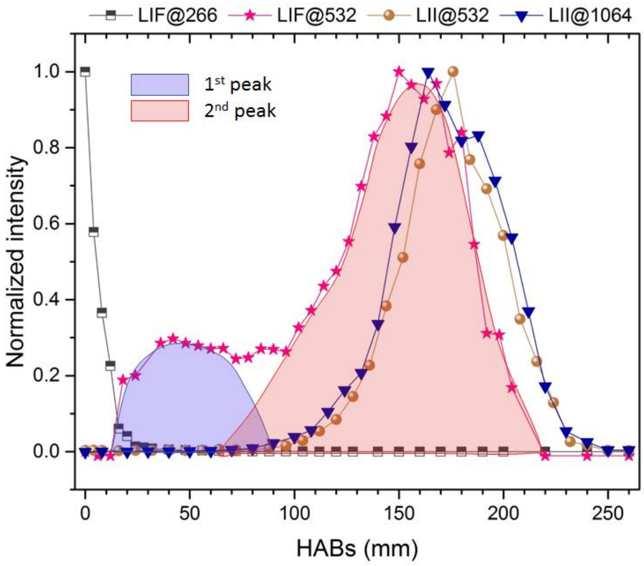

Figure 4.1.40. Variation of soot particles and their precursors in the centerline of the mixture flame. Blue and pink areas show the potential zones of two different classes of species corresponding to the Vis-LIF profile obtained with 532 nm excitation wavelength.

Figure 4.1.40 sums up the variation of soot particles and their precursors in the centerline of the mixture flame, detected by LII/LIF techniques at different wavelengths. The intense UV-LIF signal starts at the nebulizer exit due to the high ability to fluoresce of diesel and *n*-butanol in the mixture. The decrease of the UV-LIF signal reveals the fast consumption of the fuel during the combustion process. Vis-LIF signal is activated at the end of the decrease of UV-LIF. We attribute the first Vis-LIF peak around 40 mm HAB. Then the Vis-LIF signal decreases slightly while the second Vis-LIF peak begins to appear and reach its maximum around 150 mm HAB. The Vis-LIF signal disappears completely at 220 mm HAB. The LII signal starts around 100 mm HAB and reaches its peak value at 165 – 175 mm HAB before decreasing towards the upstream of the flame.

4.1.4. Jet A-1 flame

Jet A-1 fuel is used in swirled jet flame with the fuel flow rate at 109.06 g/h, nebulization nitrogen flow rate at 264 mL/min and oxidant air flow rate at 22.24 L/min at atmospheric pressure. The flame is approximately 260 mm height with luminous yellow color. Figure 4.1.41 presents 2D images of soot and soot precursors in Jet A-1 flame obtained by LIF and LII techniques with different excitation wavelengths.

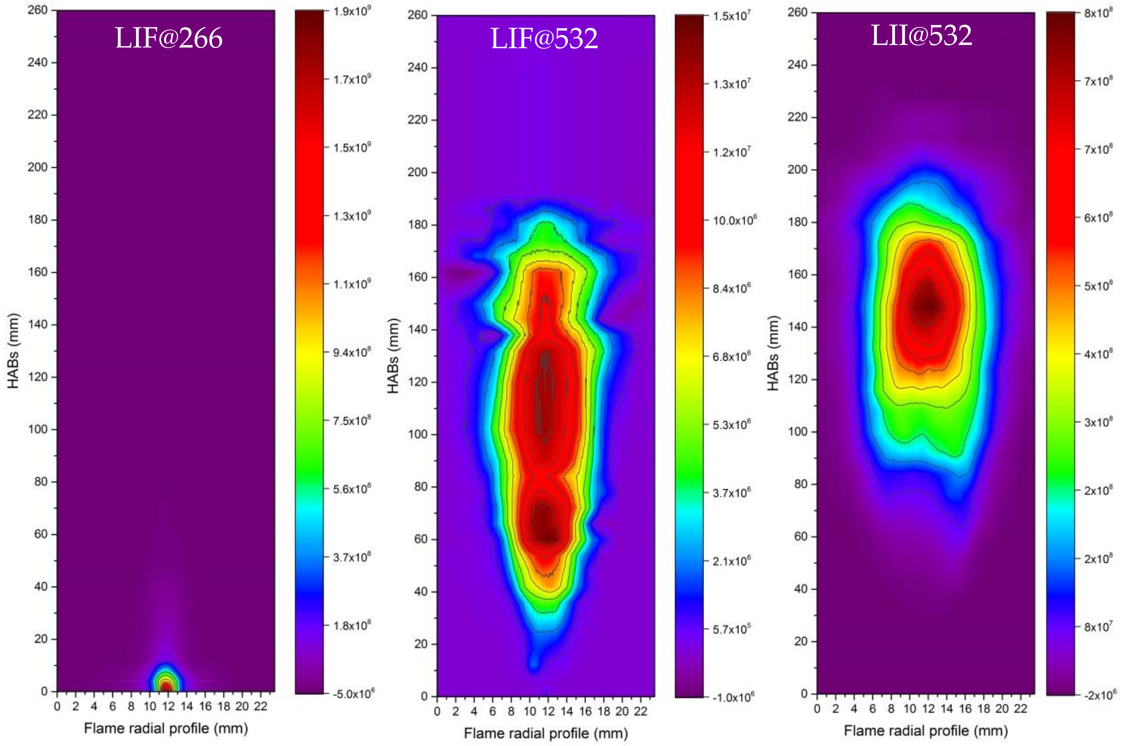

Figure 4.1.41. 2D plots of soot and soot precursors obtained by coupling of LII and LIF at 266 and 532 nm excitation taken in Jet A-1 swirled jet flame.

Similarly to other flames, UV-LIF signal starts very early in the flame due to the presence of fluorescent species in the fuel at 266 nm excitation, and diminishes quickly at 10 mm HAB due to the consumption of fuel in the combustion process. The end of UV-LIF signal is concomitant with the beginning of the Vis-LIF signal. As observed in the diesel flame, the Vis-LIF signal in the Jet flame shows a bimodal profile. The first most intense signal is located at 60 mm HAB and the second intense signal is at 120 mm HAB. Fluorescence emission from visible excitation fades out completely at 190 mm HAB. Incandescence signal from soot particles begins with the second peak of Vis-LIF, at 80 mm HAB. The most intense LII signal detected is at 150 mm HAB and it decreases until 200 mm HAB before completely fading out.

4.1.4.1. *Fluorescence induced by 266 nm excitation*

Profile of fluorescence emission taken at the centerline of Jet A-1 flame and the spectra corresponding to each HAB are shown in Figure 4.1.42.

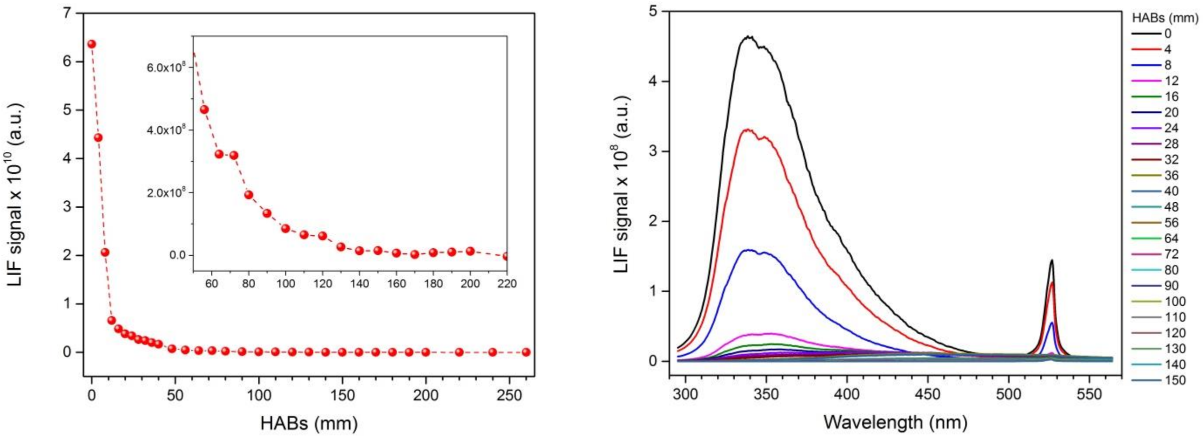

Figure 4.1.42. Left: LIF profile obtained at the centerline of Jet A-1 flame with 266 nm excitation. Right: LIF spectra with 266 nm excitation at different HABs in Jet A-1 flame (obtained at the centerline). Laser fluence used is 1.4 mJ/cm^2.

As can be seen in the figure, the most intense signal is measured at the output of nebulizer, 0 mm HAB. The signal decreases strongly afterwards. By comparing the signal from 0, 4, 8 mm HAB and the fluorescence emission from cold fuel droplets as in Figure 4.1.43, we can state as previously that there is almost no or very minor change of the fluorescence species occurring at these height in the flames.

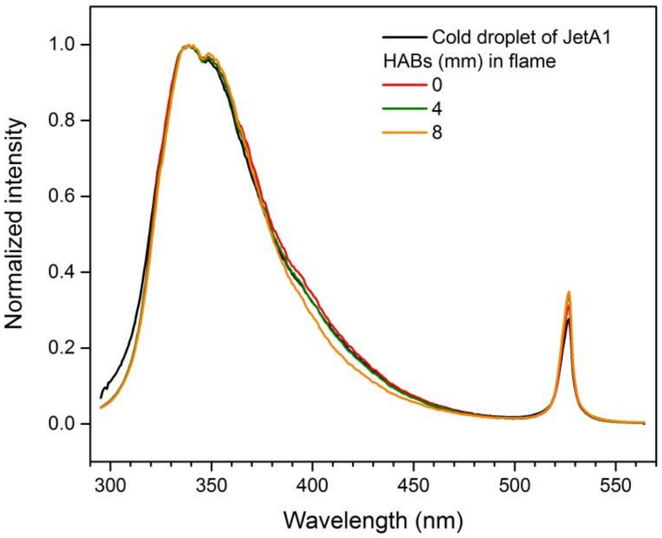

Figure 4.1.43. Comparison of LIF spectra taken at several HABs and cold droplets of Jet A-1 fuel, with 266 nm excitation

After 8 mm HAB, the UV-LIF signal decreases gradually and completely disappears above 150 mm HAB. At 0, 4, 8 mm HAB, the fluorescence emission must come from the Jet A-1 fuel. (Orain et al. 2014) studied the fluorescence emission of kerosene vapor at different temperatures and pressures with UV excitations. Their fluorescence spectra obtained with 266 nm excitation include two bands at 290 nm and 320-340 nm wavelength. The spectra obtained at 0 – 8 mm HAB in this study is similar to the second band at 320 – 340 nm, which is attributed to di-aromatics, in their study. However, the first band – that is contributed by mono-aromatics is not present in this study. (Orain et al. 2014) claimed that the first band in their study is sensitive to temperature as it deforms and disappears quickly once the temperature increases. This might explain the absence of this band in our study. (Allouis et al. 2003) measured LIF emissions at different HABs in kerosene flame with 266 nm excitation. Their spectrum obtained with cold spray of kerosene is similar with what is obtained in this study with the peak located in the range 320 – 340 nm.

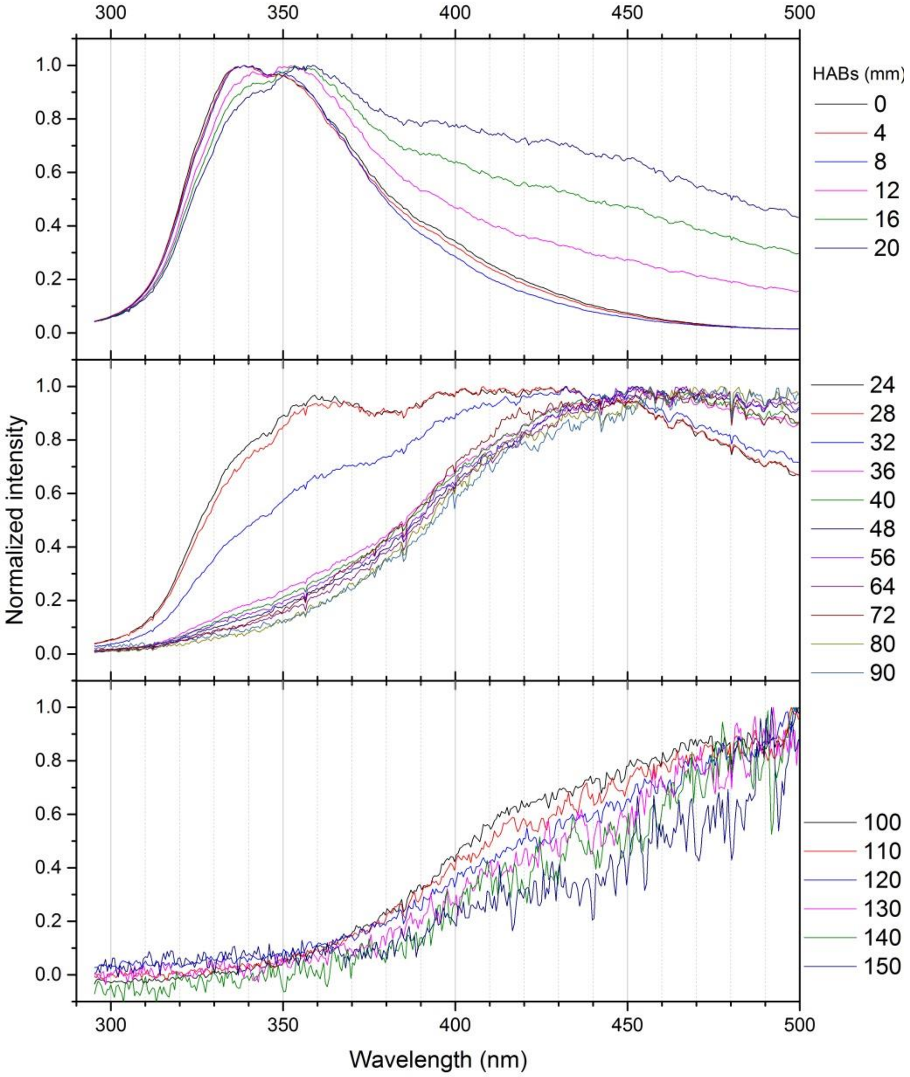

Figure 4.1.44. Normalized LIF spectra obtained at the centerline of Jet A-1 flame, with 266 nm excitation

LIF spectra obtained from 0 to 150 mm HAB are normalized to their relative maximum intensity. The normalized spectra are shown in Figure 4.1.44. The first three HABs – 0, 4, 8 mm – show the same structure of spectra. As discussed previously, these spectra are ascribable to unburned fuel components. From 12 mm HAB, a broad fluorescence emission appears in the visible region and increases with the increasing of HAB. At 24, 28 mm HAB, the visible band becomes comparable to the UV emission and even higher at 32 mm HAB. From 36 to 90 mm HAB, the UV emission becomes very low compared to the visible one. At these heights, the form of spectra does not show any change indicating that there is no evolution of the fluorescent species. From 100 mm HAB, the LIF spectra shift much towards the visible regions and start broadening at 150 mm HAB.

4.1.4.2. Fluorescence induced by 532 nm excitation

The profile of LIF emission taken in the centerline of Jet A-1 flame and its corresponding spectra are shown in Figure 4.1.45. A bimodal profile is achieved, similarly to diesel flame case. The first peak of LIF signal is located at 60 mm HAB. After this height, the fluorescence emission decreases then increases again and reached the second peak at 120 mm HAB. The first peak starts very early in the flame and this might due to the fluorescence of petrogenic species in fuel. These species are then consumed during the combustion process to form pyrogenic species, leading to fluoresce the second peak of the profile. (Lemaire et al. 2007) also studied the emissions of PAH and soot particles in spray kerosene flame using LII and LIF techniques. However, the Vis-LIF profile obtained in their study only shows a mono-modal structure.

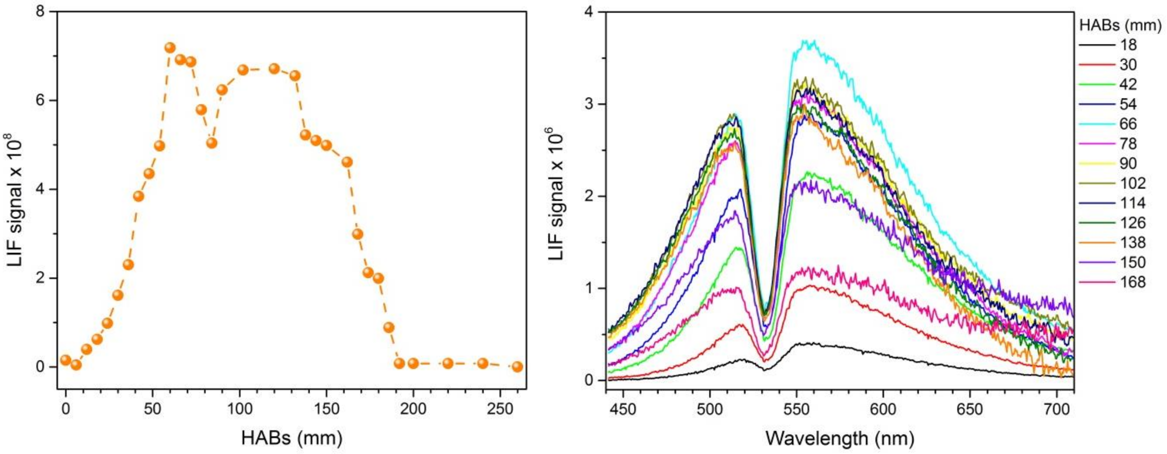

Figure 4.1.45. Left: LIF profile obtained at the centerline of Jet A-1 flame with 532 nm excitation. Right: LIF spectra with 532 nm excitation at different HABs in the Jet A-1 flame (obtained at the centerline). Laser fluence used is 5.8 mJ/cm2.

It is important to note that the study of (Lemaire et al. 2007) was carried on a modified McKenna burner. Their spray flame was ignited and stabilized with the aid of a methane flat flame. The use of the methane flame as a pilot flame creates high temperature zone near the tip of the nebulizer. Thus the petrogenic species are completely consumed due to the high temperature.

The LIF spectra obtained in Jet A-1 flame are normalized to the maximum intensity and shown in Figure 4.1.46. Both Stock and anti-Stock emissions are detected in this case. There is a noticeable evolution on LIF spectra from 18 – 78 mm HAB. These heights correspond to the zone of the first peak of the LIF profile. At higher HABs, the spectra do not show any change. This might indicate that there is an evolution of the fluorescent species in the zone 18 – 78 mm of the flame whereas the pool of excited and fluorescent species above this height seems to remain unchanged. It is to be noted that even for the measurement carried out with low laser fluence, we observe a slight increase of signal towards the end of obtained spectra at 150 and 168 mm HAB. This signal is attributed to LII emission coming from the soot particles, which may overestimate the LIF measurement at this height.

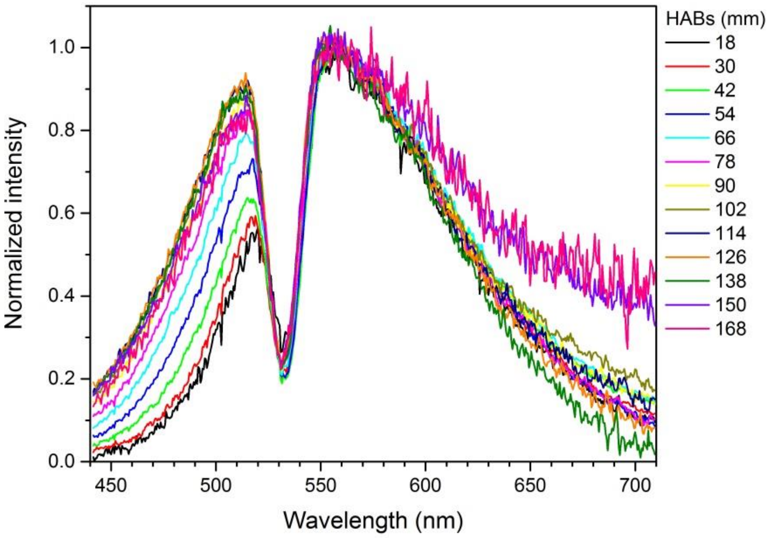

Figure 4.1.46. Normalized LIF spectra obtained at the centerline of Jet A-1 flame, with 532 nm excitation

4.1.4.3. *Incandescence induced by 532 nm excitation*

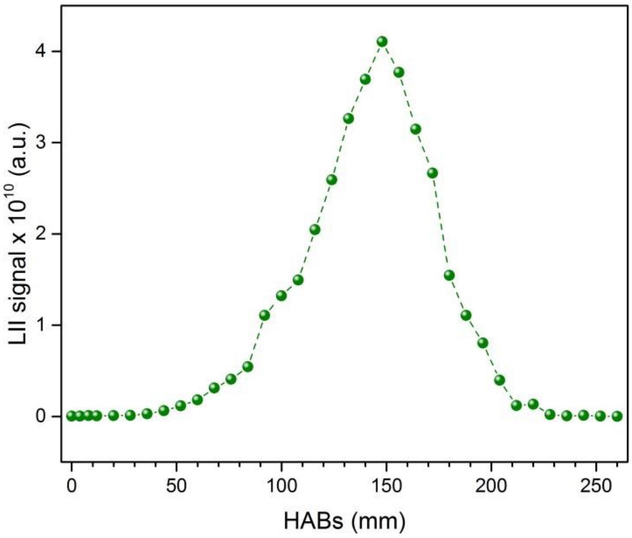

Figure 4.1.47. LII profile obtained at the centerline of the Jet A-1 flame with 532 nm excitation. The signal is integrated in the 750 – 883 nm spectral range. Laser fluence used is 183.1 mJ/cm^2.

The profile of the LII signal obtained at the centerline of the Jet A-1 flame with 532 nm excitation is presented in Figure 4.1.47. According to the figure, soot particles start forming at 60 mm HAB. The signal of incandescence from soot increases sharply until 150 mm HAB. Later, the incandescence emission decreases fast and completely disappears at 210 mm HAB. The start of soot formation is gain well correlated with the formation of the second peak in Vis-LIF, likely meaning that the formation of soot particles has a relation with pyrogenic fluorescence species, but not with petrogenic species.

With similar laser fluence, temporal LII profile taken in Jet A-1 flame is presented in Figure 4.1.48. The measurement is done along the height of the flame, from 86 to 216 mm HAB. The decay curves of other heights are not shown due to their low signal to noise. Generally, the time needed for incandescence signal to decay completely in this flame is 700 ns. For the visual ease, time constant is calculated with these time decay curves and shown in Figure 4.1.49. Time constant increases from 86 mm HAB and reaches its highest value at 166 mm HAB. This indicates the rise of soot particle size in this range of height. Afterwards, time constant decreases, ascribing that soot particles then reduce their size due to the oxidation in the combustion process.

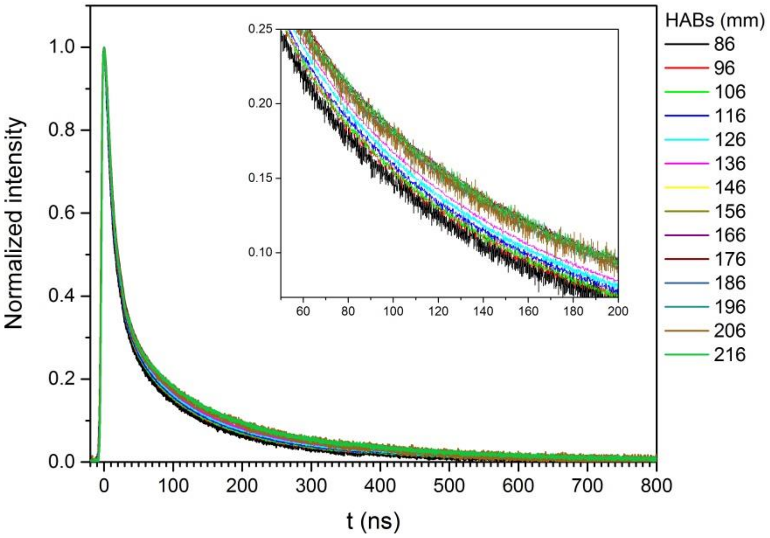

Figure 4.1.48. LII temporal profile obtained at different HABs in the Jet A-1 flame with 532 nm laser excitation. The decay curves are averaged over 1000 laser pulses.

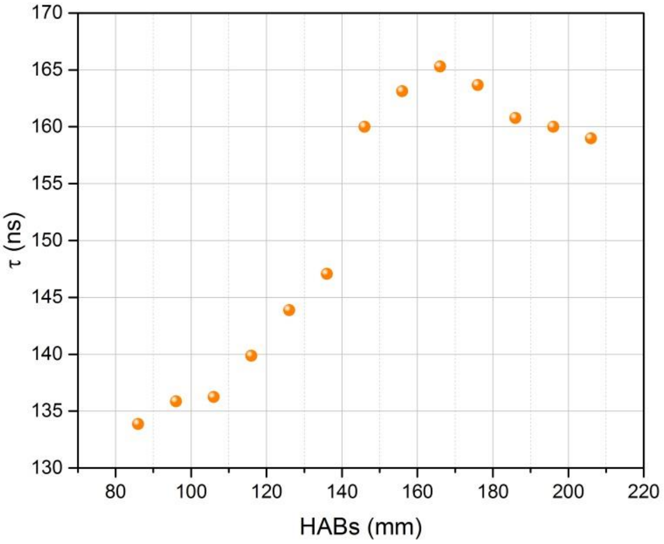

Figure 4.1.49. Time constant calculated from the decay curves in Figure 4.1.48

Figure 4.1.50 displays an overview of the detected classes of compounds in the centerline of the Jet A-1 flame.

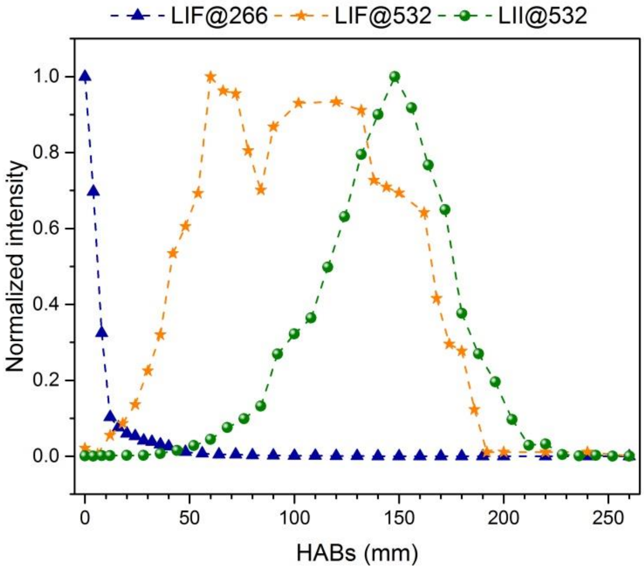

Figure 4.1.50. Variation of soot particles and their precursors in the centerline of the Jet A-1 flame.

The UV-LIF signal starts at 0 mm HAB due to the presence of petrogenic species in fuel and decreases sharply and completely fade out above 140 mm HAB. The consumption of fuel leads to the decrease of UV-LIF and increase of the fluorescence signal with visible excitation. The Vis-LIF species reach their first maximum at 60 mm HAB are then consumed along with the combustion process and re-increase in the flame to reach the second peak at 120 mm HAB. The soot particles form at 40 mm HAB. The maximum of LII signal 532 nm excitation is around 150 mm HAB. After this height, the signal decreases due to the oxidation process and disappears at 210 mm HAB.

4.1.5. SPK flame

SPK – Synthetic Paraffinic Kerosene – is widely known as one of the alternative fuels for aviation. SPK is mainly composed of alkane and cycloalkane, with or without a very small amount of aromatic compounds. With the absence of aromatic species in the fuel, it is expected to reduce the soot formation compared to conventional aviation fuels.

Applying LII and LIF techniques with various excitation wavelengths, 2D images of soot and soot precursors taken in the SPK flame are presented in Figure 4.1.51. As in previous flames, the signal of UV-LIF starts early in the flame due to the fluorescence ability of the fuel. The fuel is then consumed in the combustion process, leading to the strong reduction of UV-LIF signal at 10 mm HAB. After this height, Vis-LIF signal slightly started and getting intense at 150 mm HAB. The signal then decreases strongly and completely disappears after 220 mm HAB. Incandescence emissions from soot particles start at 110 mm HAB. The signal increases gradually until reaching its highest value at 165 mm HAB. After this height, the signal from soot decreases and fades out from 220 mm HAB.

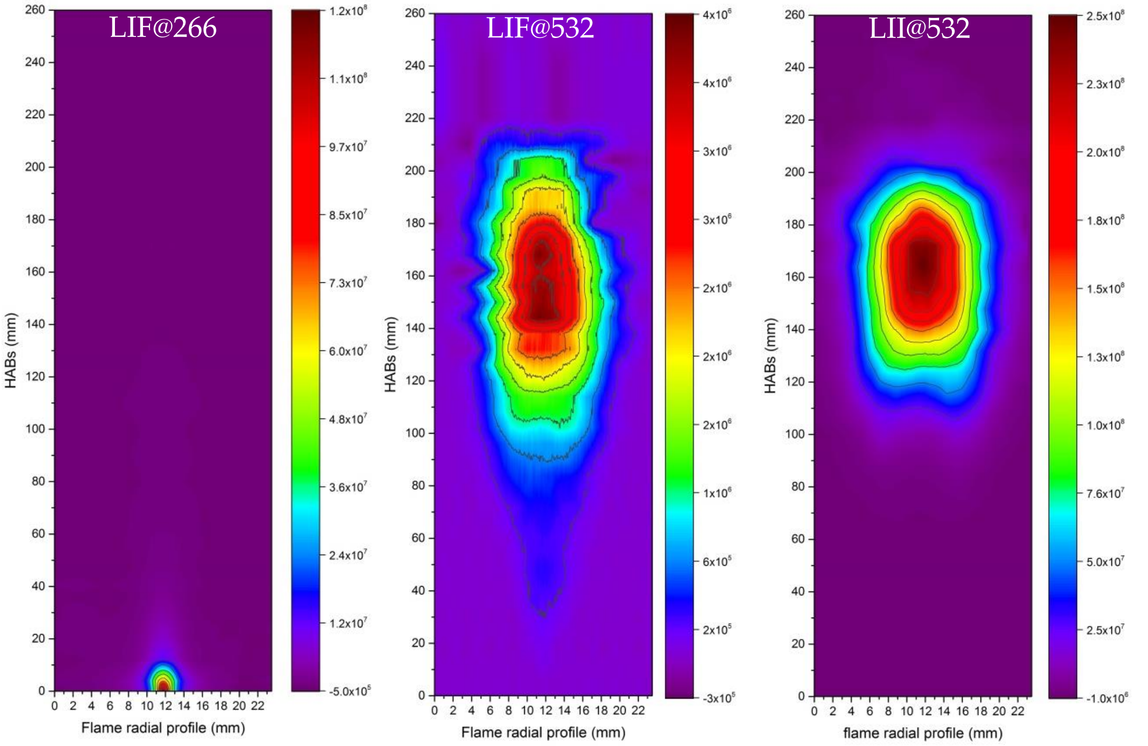

Figure 4.1.51. 2D plots of soot and soot precursors obtained by coupling of LII and LIF at 266 and 532 nm excitation taken in the SPK swirled jet flame.

4.1.5.1. Fluorescence induced by 266 nm excitation

UV-LIF measurements are carried out with 266 nm excitation. Figure 4.1.52 represents the UV profile taken at the centerline of the SPK flame and its corresponding spectra at different HABs.

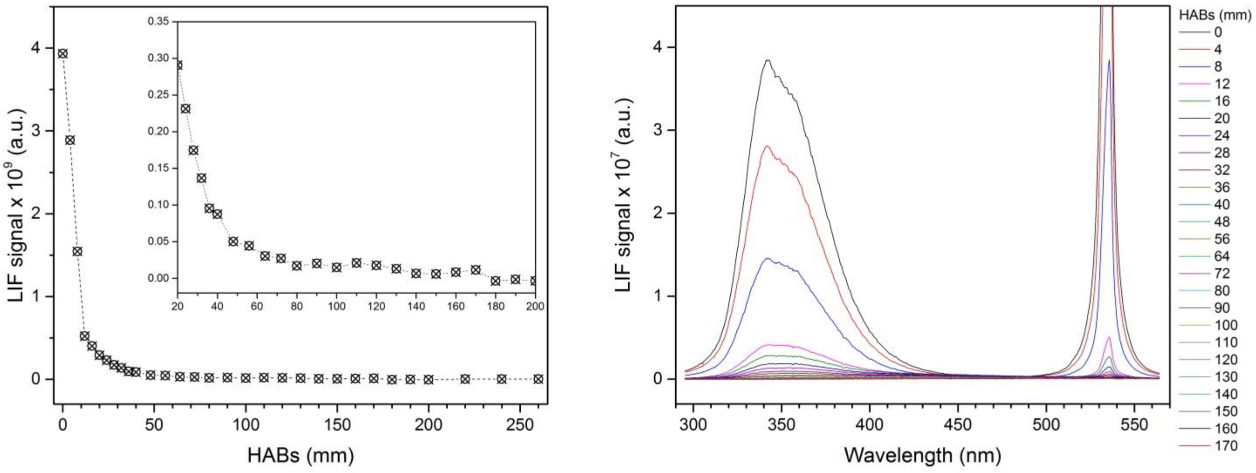

Figure 4.1.52. Left: LIF profile obtained at the centerline of the SPK flame with 266 nm excitation. Right: LIF spectra with 532 nm excitation at different HABs in the SPK flame (obtained at the centerline). Laser fluence used is 1.5 mJ/cm².

There is the presence of the second order scattering from laser excitation at 532 nm in the fluorescence spectra. Thus only light emissions in the range of 290 – 470 nm are integrated to plot the profile. The highest intensity of LIF signal is obtained at the outlet of the nebulizer, 0 mm HAB. By comparing the spectra of fluorescence emission at 0, 4 and 8 mm HAB with the LIF spectrum of cold fuel droplet as in Figure 4.1.53, it can be concluded that these three first fluorescence spectra are due to the unburned fuel components. This signal decreases sharply from 0 mm HAB to 16 mm HAB due to the consumption of the fuel during the combustion process.

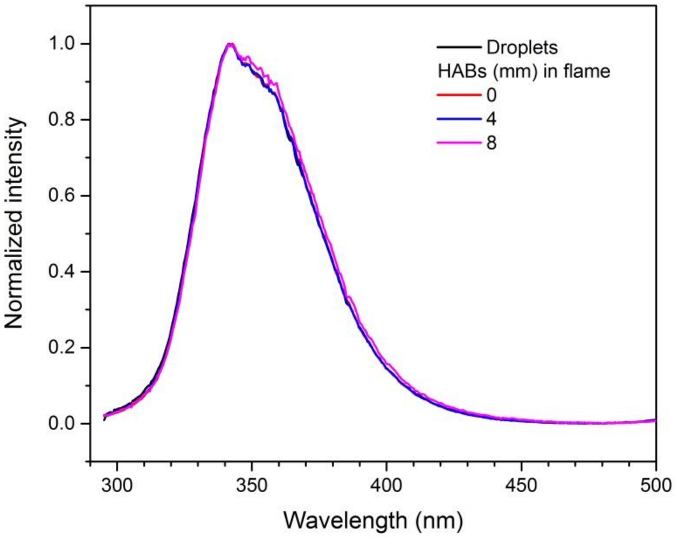

Figure 4.1.53. Comparison of LIF emission from several HABs in the SPK flame and from SPK droplets

After 16 mm HAB, the LIF emission keeps decreasing but more gradually until 170 mm HAB, the LIF signal at the centerline of the SPK flame completely fades out.

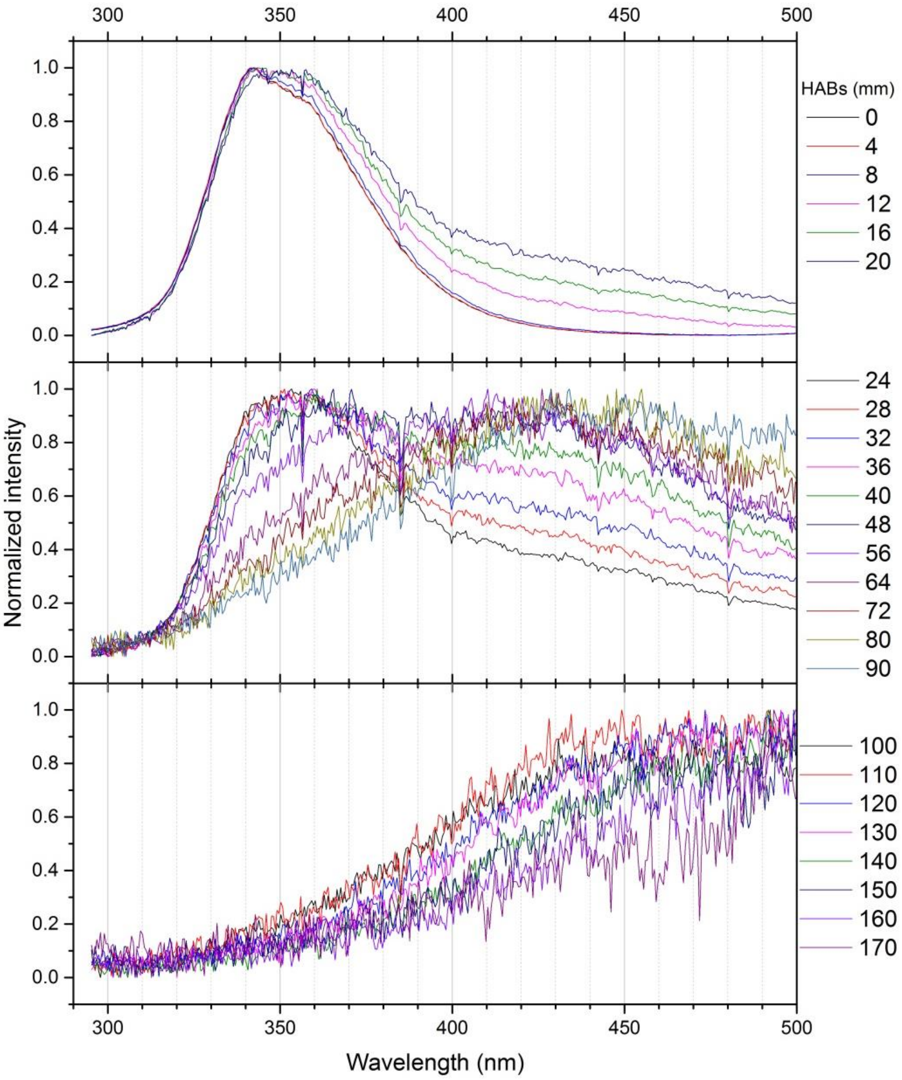

Figure 4.1.54. Normalized spectra of fluorescence emissions at different HABs in the SPK flame, obtained with 266 nm excitation.

Fluorescence spectra are normalized to their relative maximum intensity and presented in Figure 4.1.54. The first three spectra at 0, 4 and 8 mm HAB highlighting identical structure with highest intensity at 340 – 360 nm indicates that there is no or very minor change occurring to the fluorescence species at these heights. As discussed previously, these spectra are identical to the spectrum of cold fuel droplets. So at these heights, the light emission is dominated by the fluorescence of aromatic components in the SPK fuel. From 12 mm HAB, the relative intensity of the visible band, from 430 – 460 nm, increases comparably to the UV band. This indicates that there are new fluorescence components forming at higher HAB. The visible bands are getting more intense with higher HAB. Above 48 mm, the relative intensity of the UV band decreases and finally disappears at 100 mm HAB in the soot inception zone while the spectra are globally redshifted from 450 to 500 nm.

4.1.5.2. *Fluorescence induced by 532 nm excitation*

Figure 4.1.55 represents the profile of fluorescence emissions obtained at the centerline of the SPK flame and its corresponding spectra.

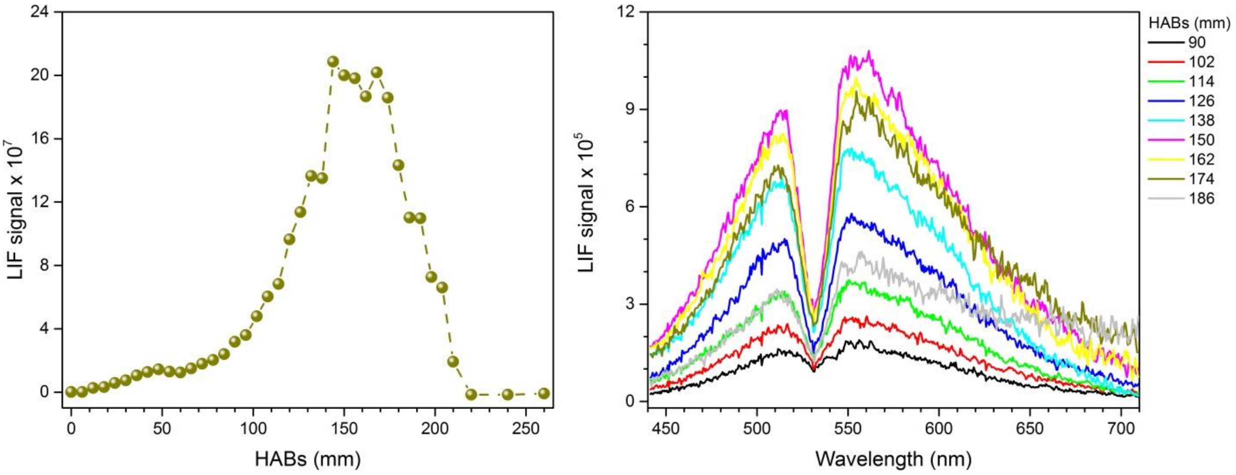

Figure 4.1.55. Left: LIF profile obtained at the centerline of the SPK flame with 532 nm excitation. Right: LIF spectra with 532 nm excitation at different HABs in the SPK flame (obtained at the centerline). Laser fluence used is 5.8 mJ/cm².

From the figure, the Vis-LIF signal starts early in the flame, at 12 mm HAB. Vis-LIF signal increases slightly and reaches a first peak at 50 mm HAB, then strongly rises until a second peak at 150 mm HAB. Above this height, the signal decreases dramatically and completely vanishes at 220 mm HAB. For a better interpretation, Vis-LIF spectra are normalized to their relative highest intensity and shown in Figure 4.1.56. Shapes of all spectra are identical. This suggests that there is no change in the pool of the Vis fluorescence species during the combustion process.

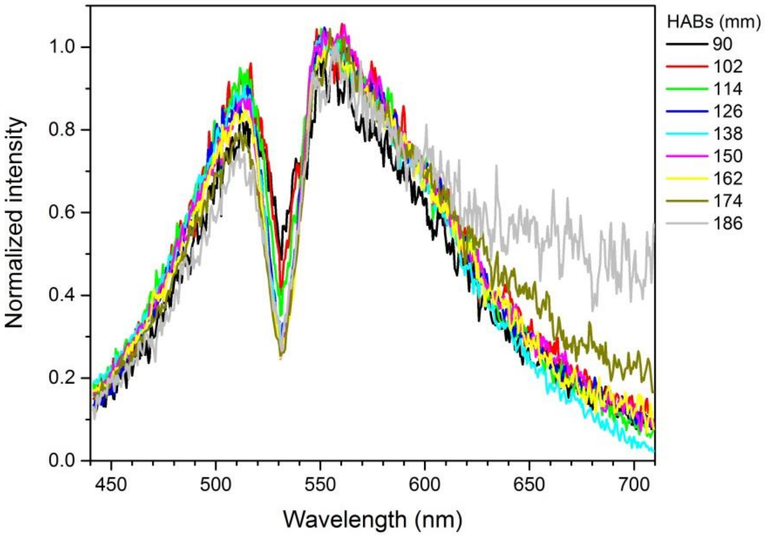

Figure 4.1.56. Normalized LIF spectra obtained at the centerline of the SPK flame with 532 nm excitation.

4.1.5.3. Incandescence induced by 532 nm excitation

The profile of incandescence signal obtained in the SPK flame is represented in Figure 4.1.57. Incandescence signal from soot particles starts at 90 mm HAB, that is close the peak of the profile of the fluorescence species at visible excitation. The LII signal increases strongly up to 165 mm HAB. It is then decreasing and disappears at 220 mm HAB.

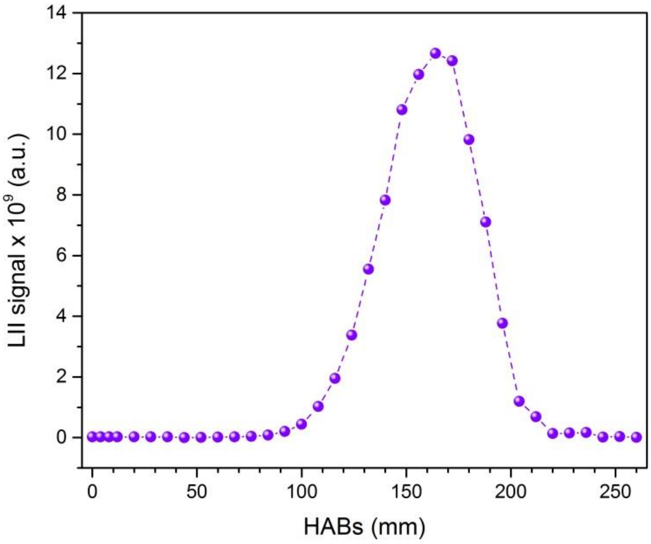

Figure 4.1.57. LII profile obtained at the centerline of the SPK flame with 532 nm excitation. Emitted light is collected in the range 750 - 883 nm.

A PMT is employed to measure the decay time of LII signal from soot particles in the SPK flame. LII decay curves, which are shown in Figure 4.1.58, are decreasing over 700 ns.

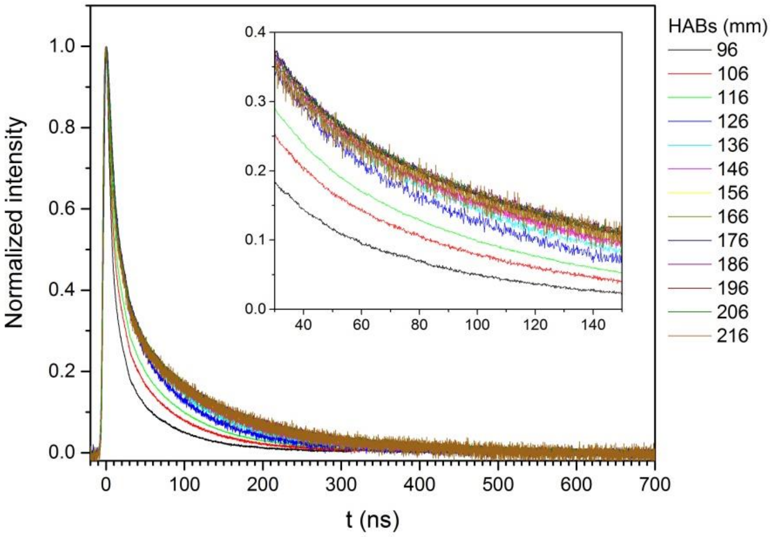

Figure 4.1.58. Decay curves of LII signal taken in the sooting zone of the SPK flame. Each curve is recorded with 1000 laser pulses.

There are noticeable differences in the decay curves measured from 96 mm to 136 mm HAB, indicating an increase of the particle size with increasing HAB. However, it is difficult to distinguish decay curves at other HABs. To ease the discrimination, time constant is calculated with the interval of 85 ns to 285 ns for each decay curve and shown in Figure 4.1.59. As it can be seen clearly from the figure, the time constant increases gradually from 96 mm to 186 mm HAB. This implies the increase of particle size in the combustion process. The soot particles then reach their largest size at 186 – 196 mm in the flame. After this height, the decreasing time constant indicates a reduction of the size of soot particles due to the oxidation process.

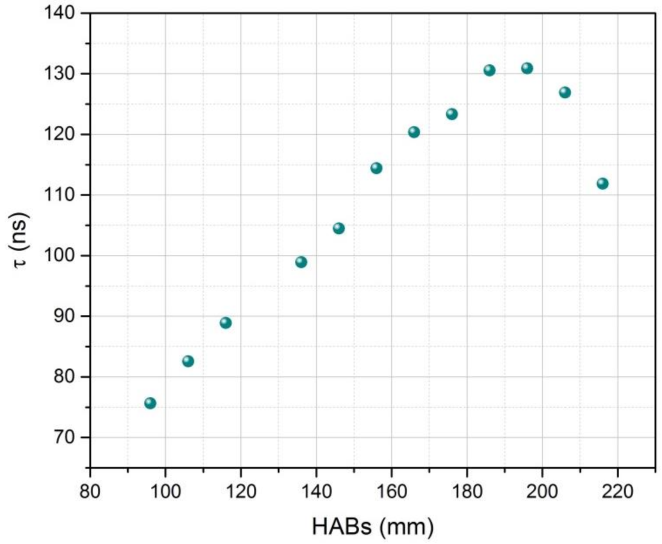

Figure 4.1.59. Time constant calculated from Figure 4.1.58

Figure 4.1.60 sums up the evolution of the profiles of soot particles and their precursors along the centerline of the SPK flame, detected by LII/LIF techniques at different wavelengths.

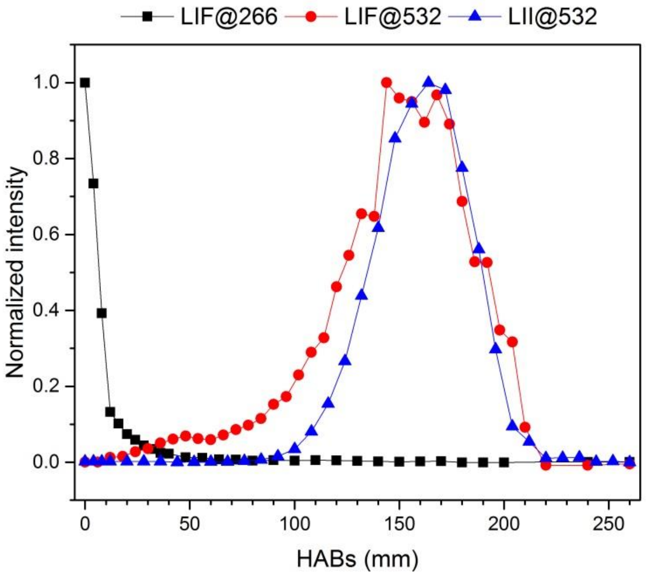

Figure 4.1.60. Variation of soot particles and their precursors detected from LII/LIF measurements in the centerline of the SPK flame.

The UV-LIF signal starts at the exit of the nebulizer due to the high ability to fluoresce of fuel components. The strong decrease of UV-LIF signal reveals a fast consumption of the fuel during the combustion process. Vis-LIF signal is activated near the end of the UV-LIF. The Vis-LIF signal is formed quickly and rised after the consumption of fuel with a first peak at 50 mm HAB. These species are then consumed contribute to the appearance of the second peak of Vis-LIF at 150 mm HAB. The Vis-LIF signal disappears completely at 220 mm HAB. The start of LII signal is around 90 mm HAB. The LII signal reaches its peak at 165 mm HAB and then decreases towards the upstream of the flame.

4.1.6. Absolute soot volume fraction measurement by LII calibration

4.1.6.1. LII temperature

The average temperature of the soot particles can be derived from the LII spectrum as below (all term present in the equation were introduced in subchapter 2.4.2):

$$ln\left(\frac{LII(t_0,\lambda)\lambda^6}{E(m)}\right) = -\frac{hc}{kT\lambda} + \ln(48\pi hc^2 f_v) \qquad \text{(eq.30)}$$

However, the $E_m(\lambda)$ can affect the shape of the LII emitted intensity, and the LII temperature deduced from the emission spectrum. Many studies claim that this absorption function is strongly dependent on the soot maturity (Migliorini, Thomson, and Smallwood 2011; Olofsson et al. 2015; Yon et al. 2015; Bescond et al. 2016; Michelsen 2017; Johansson et al. 2017; Kelesidis and Pratsinis 2019) and seems to be dependent on the type of fuel (S. Bejaoui et al. 2014; Yon et al. 2015). This can be explained by a dehydrogenation and solidification phenomenon that results in strong absorption when nanoparticles are annealing or by the presence of organic compounds reducing the absorption capacity at longer wavelengths, according to (Bescond et al. 2016). However, (Johansson et al. 2017) claimed that with the increase of soot maturity, the aromatic or aliphatic character might increase or vice versa. Up to now, there is still poor understanding of this optical property of soot due to the limitation of available measurement techniques. It is necessary to develop techniques that are able to provide measurements which are tied to particle maturity and optical properties (Michelsen 2017).

The average temperature calculated from the LII emitted signal is defined by the gate width. In this case, the measurement is taken over 50 ns at the beginning of laser pulse. The LII signal needs to be corrected by the transfer function (TF) before the calculation procedure. In this representation, the variation of the *E(m)* function is not taken account.

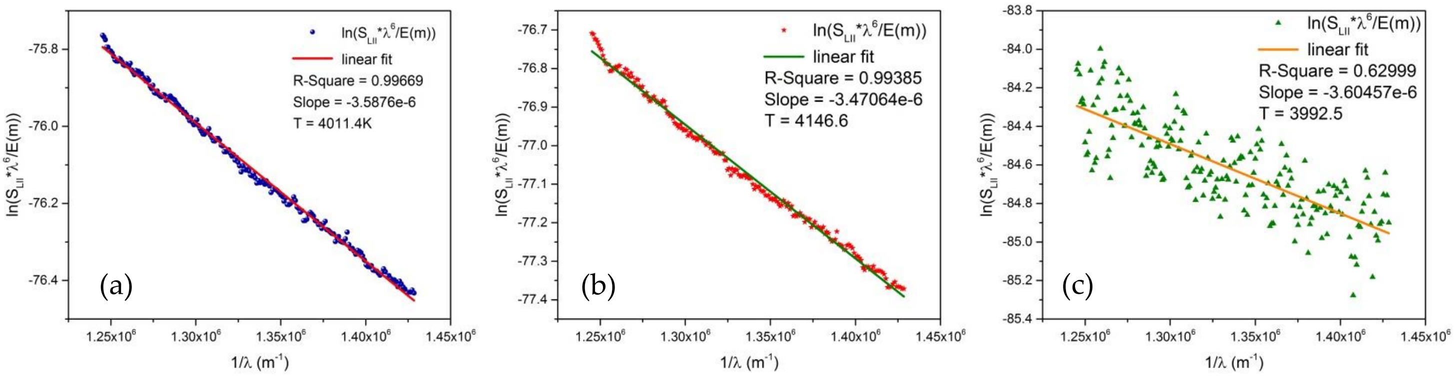

Figure 4.1.61. Representation of the slope of three LII spectra from (a) Diesel 156 mm HAB, (b) Mixture 172 mm HAB and (c) *N*-butanol 200 mm HAB. From the slope, the soot average temperature be deduced. The LII signal is obtained with 1064 nm excitation.

Some examples representative for average temperature deduced from LII signal obtained in Diesel flame at 156 mm HAB, Mixture flame at 172 mm HAB and *N*-butanol flame at 200 mm HAB are shown in Figure 4.1.61. Incandescence measurement is conducted with 1064 nm excitation. The signal is obtained during 50 ns after the LII peak with 800 laser pulses. The spectra obtained in the 700 – 800 nm range are used for the calculation. Good linear fits are obtained for diesel and mixture flame, whereas the R-Square achieved in *n*-butanol case is only 0.62. This can be explained by the weak LII signal from soot in the *n*-butanol flame. However, soot from all three flames was heated up to 3990 – 4150 K. The temperature reached by the particles in LII measurement is an essential data needed to calculate the soot volume fraction, which will be presented in the next subchapter.

4.1.6.2. *Soot volume fraction measurement*

As mentioned before, LII cannot be used alone to determine the soot volume, it must be coupled with other techniques. In other words, it needs to be calibrated. The calibration of the LII data can be done with indirect or direct approaches (Mansmann 2019). Indirect calibration methods consist of different measurement techniques as Laser extinction (Shaddix, Harrington, and Smyth 1994; Vander Wal and Jensen 1998; Delhay et al. 2009; Wiltafsky et al. 1996; Axelsson, Collin, and Bengtsson 2001; Huber, Altenhoff, and Will 2016), Gravimetric sampling (Vander Wal, Zhou, and Choi 1996), Transmission electron microscopy or Cavity ring down spectroscopy (Schoemaecker Moreau et al. 2004). Other particle sources whose volume fraction is known could also be used (Ni et al. 1995). The indirect approaches have the disadvantage that the calibrated aerosol properties tend to be uncertain (varying with process condition or time, for example), which can introduce significant uncertainty (Mansmann 2019). Also, the need of applying other measurement techniques makes these approaches heavy and complicated to realize.

The direct calibration approach was first introduced by (Snelling et al. 2005). This is also called two-color approach (Vander Wal 2009). In principle, a source of known radiance or irradiance is used to obtain the instrument relative sensitivity. The temperature of the soot particles heated by laser pulses can be obtained with two-color pyrometry. The absolute soot volume fraction can be then determined from the absolute LII signal intensity. Common light sources used with two-color approach are tungsten filament lamp, halogen lamp and integrating sphere (Mansmann 2019).

In this work, we propose a new direct method to calibrate the soot volume fraction from LII signal, which is obtained with an ICDD camera. An integration sphere from SphereOptics CSTM-LR-6-M is used. Light emitted from the sphere is a black body type radiation in the range of 360-1000 nm with an adjustable temperature. The temperature can be computed using an external power supply module by changing the power input (voltages). The spectral radiance of the sphere at 12V was calibrated by Labsphere, Inc., Optical Calibration Laboratory using a standard tungsten halogen lamp. The sensitivity of experiment set up of LII experiment can be determined since the sphere output was placed at the same position as the burner and using the same optical pathway by ratio between calibrated spectral radiance and the signal recorded by the ICCD camera from the sphere. The optical setup for absolute light intensity calibration is shown schematically in Figure 4.1.62. The LII absolute signal is then used to calculate the soot volume fraction with the knowledge of the soot temperature heated by laser pulses during the LII measurement. The demonstration of the calculation is presented as below.

4.1.6.3. Calibrated lamp signal

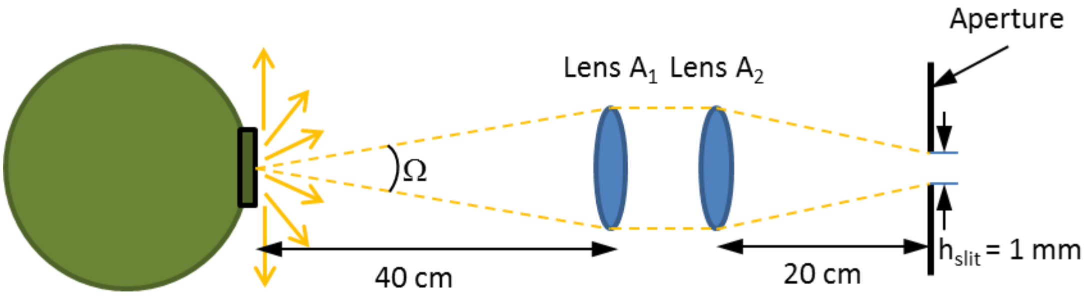

Figure 4.1.62. Schematic of the optical set up for the calibration with the sphere

The spectral radiance of the sphere, obtained at a unit of solid angle, integrated in a wavelength interval Δλ is:

$$R = \frac{2\pi hc^2}{\lambda^5} \cdot \frac{1}{exp\left(\frac{hc}{\lambda k T_{lamp}}\right) - 1} \cdot \frac{1}{2\pi} \cdot \Delta\lambda \qquad [W.m^{-2}.sr^{-1}] \qquad \text{(eq.31)}$$

where h is the Planck constant, c is the speed of light, k is the Boltzmann constant, T_{lamp} is the temperature of the calibration lamp. The value of the spectral radiance of the sphere is calibrated with equipment and methods traceable to the U.S. National Institute of Standards and Technology (NIST).

The radiance intensity [count] from the sphere obtained by the CCD camera at one pixel, in a wavelength interval Δλ [m] can be expressed as below

$$S_{CCD} = \frac{2\pi hc^2}{\lambda^5} \cdot \frac{1}{exp\left(\frac{hc}{\lambda k T_{lamp}}\right) - 1} \cdot \frac{1}{2\pi} \cdot \Delta\lambda \cdot S_{1\,pixel} \cdot \Omega \cdot \beta \qquad \text{(eq.32)}$$

where $S_{1\,pixel}$ [m^2] is the surface area of collected image in the space that is corresponding to one pixel in CCD camera, Ω [sr] is the collection solid angle from a photon emitted from sphere to the lens A$_1$, β [count.W^{-1}] is the transmission coefficient, which depends on the set up of the experiment and the detected wavelength range. From (eq.31 and eq.32), S_{CCD} can be rewritten as

$$S_{CCD} = R \cdot S_{1\,pixel} \cdot \Omega \cdot \beta \qquad \text{(eq.33)}$$

4.1.6.4. *LII signal intensity from soot particles*

The total (over 4π sr) power radiated at wavelength λ by N$_p$ particles with radius R$_p$, at temperature T can be expressed as follows:

$$E(T,\lambda) = Q_{em}(R_p,\lambda) \cdot \frac{2\pi hc^2}{\lambda^5} \cdot \frac{1}{exp\left(\frac{hc}{\lambda \kappa T}\right) - 1} \cdot 4\pi R_p^2 \cdot N_p \qquad \text{(eq.34)}$$

$Q_{em}(R_p,\lambda)$ is the emission coefficient of soot. Based on the theory RDG-FA (Rayleigh Debye Gans/Fractal Aggregate), the absorption coefficient of soot meeting the Rayleigh criteria $2\pi R_p \ll \lambda$, where λ is the wavelength of the electromagnetic wave considered, is:

$$Q_{abs} = \frac{8\pi R_p}{\lambda_{abs}} \cdot E(m) \qquad \text{(eq.35)}$$

with $E(m)$ the soot refractive index function. By using the Kirchhoff approximation of equalizing the emission coefficient with the absorption coefficient for the same temperature and wavelength, (eq.34) can become

$$E(T,\lambda) = \frac{8\pi R_p}{\lambda} \cdot E(m) \cdot \frac{2\pi hc^2}{\lambda^5} \cdot \frac{1}{exp\left(\frac{hc}{\lambda k T}\right) - 1} \cdot 4\pi R_p^2 \cdot N_p \qquad \text{(eq.36)}$$

Thus, the LII signal intensity obtained for the CCD camera at one steradian, for one pixel, in a wavelength interval Δλ can be expressed as:

$$S_{LII} = \frac{8\pi R_p}{\lambda} \cdot E(m) \cdot \frac{2\pi hc^2}{\lambda^5} \cdot \frac{1}{exp\left(\frac{hc}{\lambda k T}\right) - 1} \cdot 4\pi R_p^2 \cdot N_p \cdot \Delta\lambda \cdot V_m \cdot \frac{1}{4\pi} \cdot \Omega \cdot \beta \qquad \text{(eq.37)}$$

where V_m [m^3] is the total volume of particulate in the region of space which is imaged onto the camera. This volume is defined by the laser beam diameter and the width of the aperture slit. Ω [sr] is the collection solid angle from a photon emitted from the sphere to the lens A$_1$, β [count.W^{-1}] is the transmission coefficient as presented in (eq.32). Since the optical setups of the LII experiment and of the calibration sphere are the same, Ω and β values can be obtained from (eq.33). In addition, the soot volume fraction f_v is defined as

$$f_v = N_p \cdot \frac{4\pi R_p^3}{3} \qquad \text{(eq.38)}$$

By combining (eq.33), (eq.37) and (eq.38), the soot volume fraction can be obtained with

$$f_v = \frac{S_{LII} \cdot R}{S_{CDD} \cdot \Delta\lambda} \cdot \left[exp\left(\frac{hc}{\lambda kT}\right) - 1\right] \cdot \frac{S_{1\,pixel}}{V_m} \cdot \frac{\lambda^6}{12\pi hc^2 E(m)} \qquad \text{(eq.39)}$$

$S_{1\,pixel}$ can be obtained with $S_{1\,pixel} = 2 \times h_{slit} \times 2 \times l_{pixel}$ due to the presence of the achromatic lenses system as shown in Figure 4.1.62. V_m can be achieved with $V_m = 2 \times l_{pixel} \times \frac{\pi\phi_{laser}^2}{4}$. h_{slit} is 1 mm for all experiment. l_{pixel} equals to 23 µm. The diameter ϕ_{laser} of the 1064 nm excitation laser beam is 1.1 mm, as presented in subchapter 2.4.3, with top-hat profile. Most of the parameters are known, except T – temperature of heated soot, and *E(m)* – function of the soot refractive index. T can be deduced by exploiting the LII spectrum as presented in previous subchapter. Thus, only *E(m)* is unknown. In fact, *E(m)* is not constant with the wavelength range and strongly dependent on the maturity of the soot particles (Migliorini, Thomson, and Smallwood 2011; Olofsson et al. 2015; Yon et al. 2015; Bescond et al. 2016; Michelsen 2017; Johansson et al. 2017; Kelesidis and Pratsinis 2019) and seems to be dependent on the type of fuel (S. Bejaoui et al. 2014; Yon et al. 2015). In the study of (Irimiea 2017), the authors presented the function $E(m) = 1.143 - 0.00214\lambda + 1.362 \times 10^{-6}\lambda^2$ where λ is in nm. However, the authors did not take into account the variation of *E(m)* with the maturity of the soot particles. In this work, a mean value of *E(m)* of 0.3 is used for a wavelength centered at 755 nm, except for the *n*-butanol flame. As discussed in the subchapter 4.1.2, soot particles from this flame have properties as NSP found in "nucleation" flames of (Desgroux et al. 2017; Betrancourt et al. 2017; Mouton et al. 2013). In the PhD thesis of (Betrancourt 2017), the author indicated that in a "nucleation" flame, *E(m)* has a value of 0.25. Thus this value is used to calculate the f_v of soot in the *n*-butanol flame. The soot particles found in this flame did not change their size along the flame. Additionally their fluence curves showed a linear trend without any sublimation threshold detected.

Figure 4.1.63 presents the results of 2D resolved soot volume fraction in diesel, mixture and *n*-butanol flame with applying the direct calibration method on LII signal. As it can be seen from these figures, the diesel flame produced the highest amount of soot, with a maximum f_v at 2696 ppb, followed by the mixture flame with a maximum of f_v 976 ppb. The flame producing the least soot particles is the *n*-butanol flame with a maximum at 0.53 ppb. In other words, maximum f_v produced in diesel flame is 2.76 times higher than in the mixture flame and is more than 5000 times higher than in the *n*-butanol flame.

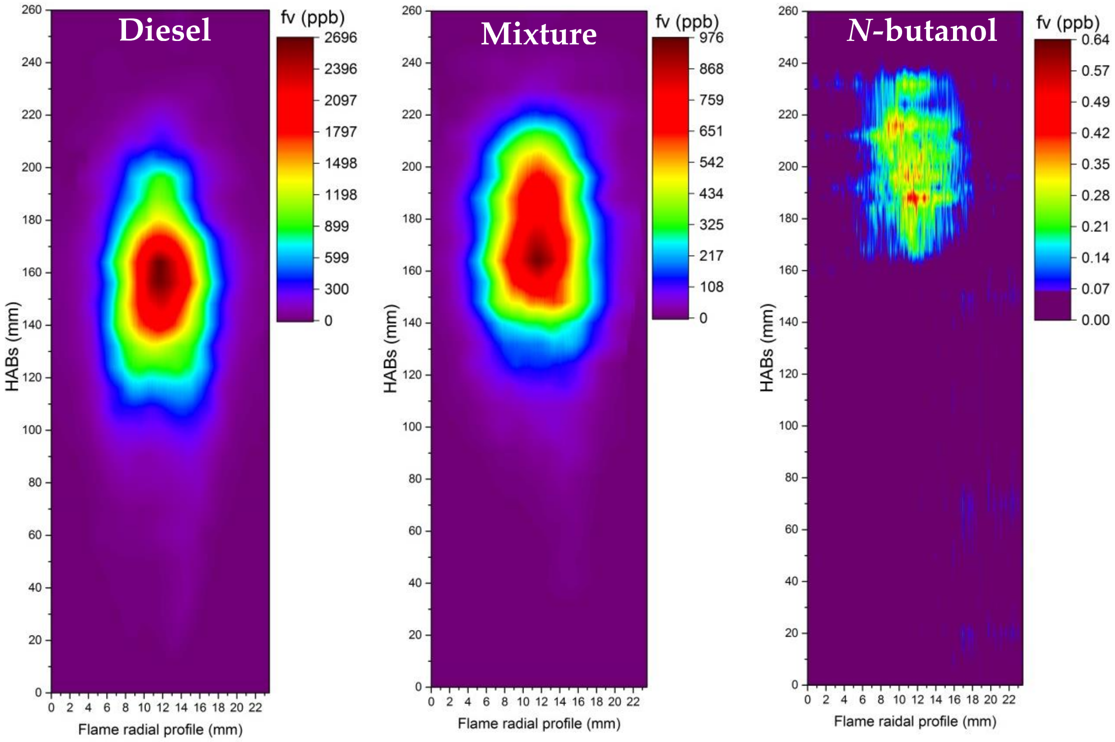

Figure 4.1.63. 2D profile of soot volume fraction in three flames: diesel, mixture and *n*-butanol

A similar approach is applied for the LII signal from the Jet A-1 and SPK swirled flames to deduce their soot volume fractions. The 2D profiles of f_v in these two flames are presented in Figure 4.1.64. We observe that the Jet A-1 flame produced higher amount of soot, with a maximum f_v at 1590 ppb, than the SPK flame, which has maximum f_v at 494 ppb. It can be said that the SPK emits approximately three times less soot particles than Jet A-1 (in the combustion conditions used in this work).

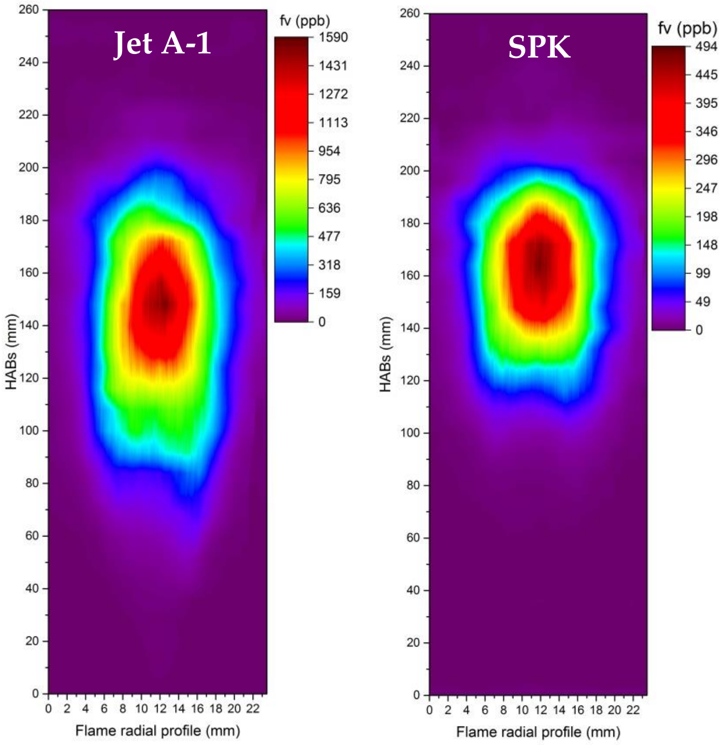

Figure 4.1.64. 2D profile of soot volume fraction in three flames: Jet A-1 and SPK

An average soot volume fraction is determined for the three flames by dividing the sum of f_v to the flame diameter. However, it is difficult to determine the flame diameter for a turbulent flame; the average f_v is obtained instead for a length corresponding to the slit of the apparatus. In this study the sum of f_v is divided by 23.5 mm. The result is shown in Figure 4.1.65. According to the study of (Bejaoui et al. 2015), *E(m,1064)* varies from 0.22 to 0.37 in a function of HABs in rich premixed flat methane flame. This variation is due to the variation of maturity of soot particles along the flame. Thus error bars are added into Figure 4.1.65 to represent the possibility of f_v change due to the maturity of soot particles.

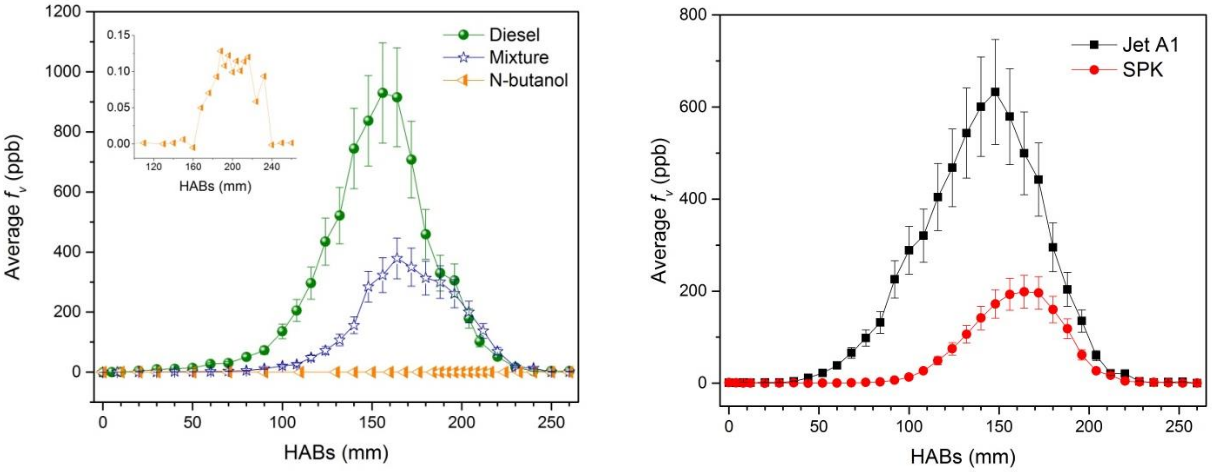

Figure 4.1.65. Average soot volume fraction of three automobile-fueled flames (left panel) and two aero-fueled flames (right panel). Error bars represent the variation of *E(m)* in function of the maturity of soot particles.

This new method of calibration extends the quantitative capability of the in-situ LII technique without using other sources of soot of a known volume fraction. However, different issues have to be solved to gain in accuracy. Firstly, as *E(m)* is strongly dependent on the temperature, soot maturity and nature of fuel, the assumption of *E(m)* based on earlier works is not valid for all kind of soot. Especially soot particles formed in the butanol flame which appear to share similar properties with NSP formed in the nucleation flame, certainly characterized by a different *E(m)* value in comparison with the mature soot measured in the diesel and mixture flames. The *n*-butanol flame f_v calculated here thus might be very overestimated or underestimated due to this big difference. Secondly, to valid this calibration method using the absolute LII signal, it is necessary to other known quantitative methods as Laser extinction or Cavity ring down to compare the results. This work might be realized in the future in a laminar diffusion flame for instance.

4.2. Mass spectrometry analyses of soot particles generated in swirled jet flames

In this subchapter, two-step laser mass spectrometry and secondary ion mass spectrometry techniques are used to study the chemical composition of soot particles and PAHs sampled from the three flames: diesel, *n*-butanol and mixture.

4.2.1. Diesel flame

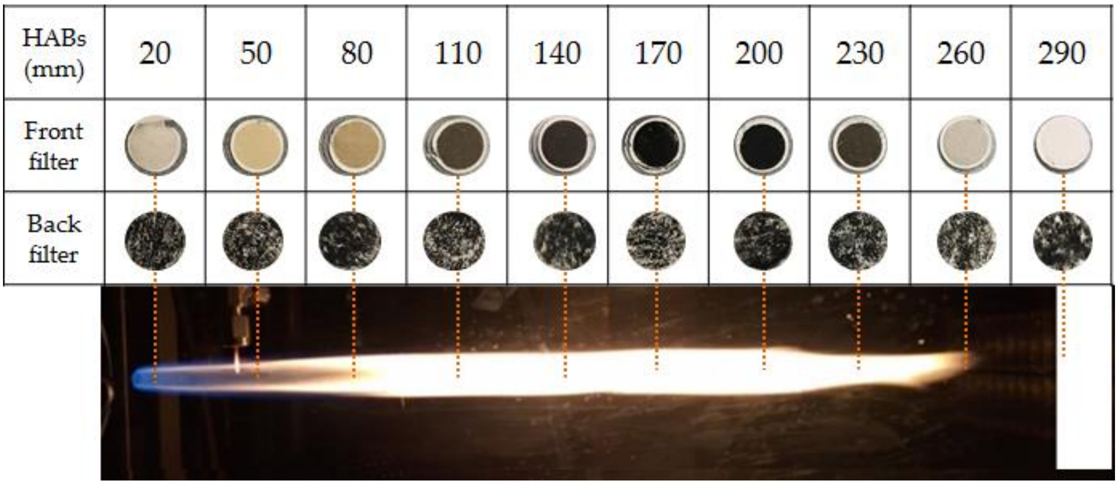

Figure 4.2.1. Photos of the diesel flame and Front and Back filters corresponding to different HABs. (The photo of flame is 90^o rotated to have better vision)

Combustion products from the diesel flame are sampled at different HABs using the two-filter technique as presented in subchapter 2.3. Particulate matter is collected on a neat ("front") glass fiber filter, while gas phase products are captured using a layer of activated black carbon deposited on the "back" glass fiber filter. The sampling time is 2 min for all samples. Photos of front and back samples collected from diesel flame are displayed in Figure 4.2.1.

By visual inspection, the evolution of combustion byproducts with the increase of HAB can be observed from the color of front filters. At 20 mm HAB, the filter is light yellow without the presence of particles. At 50 cm and 80 mm HAB, the filters are getting darker and the color shifts to more brown than yellow due to the condensation of higher-mass molecules on the filters. The front filter obtained at 110 mm HAB starts having the black shade even if it is not completely black, indicating the start of soot formation in the flame at this height. Higher than that, at 140 and 170 mm, the filters are completely black and seem to be loaded with carbonaceous particles. This zone is also detected as highest soot presence in LII profiles with 532 and 1064 nm excitations, that are presented in subchapter 4.1.1. The following front filters sampled at 200, 230 and 260 mm HAB in the diesel flame have different shades of gray color with less particles deposited due to the reduction of soot particles at these heights. A sample taken 30 mm above the flame tip, at 290 mm HAB, is also collected. This front filter does not show much change compared to the original with color of the filter. This indicates that not much soot is present above the flame tip. While the change of color in front filters provide an easy way to differentiate them, the back filters cannot be easily discriminated by visual inspection as they are all covered by the black carbon layer deposited to capture the gas phase.

4.2.1.1. L2MS mass spectra of diesel samples

These filters are analyzed using 532 nm wavelength (20.64 mJ/cm^2) for surface desorption and 266 nm wavelength (6.23 mJ/cm^2) for ionization. Each mass spectrum is averaged over 200 laser pulses with a delay of 100 µs between desorption and ionization laser pulses.

Raw baseline corrected mass spectra for ten front filters and ten back filters collected in diesel flame at ten different HABs are presented in Figure 4.2.2 and Figure 4.2.3 with their most abundant peak. In general, the mass spectra are rich in aromatic species from *m*/*z* 92 ($C_7H_8^+$ – toluene) up to *m*/*z* 472 ($C_{38}H_{16}^+$ – up to twelve aromatic rings – circumbiphenyl) and appear clustered in groups. The sequences of groups obtained usually show a distance of *m*/*z* 10, 12 or 14 to the closest neighbor. Each group appears with few strong peaks due to the more stable PAH ions occurring together with a number of satellites (Stein and Fahr 1985). The satellites on the left *m*/*z*-1, *m*/*z*-2 are usually due to the loss of one or two H from the parent molecule or to species containing 5-membered rings (Dobbins, Fletcher, and Chang 1998). Whereas the satellites on the right *m*/*z*+1, *m*/*z*+2 present due to the isotopologue ions, contributing by isotopes of carbons. Carbon has two stable isotopes, ^{12}C (98.9%) and ^{13}C (1.1%). The contribution of hydrogen's isotope is negligible. The probability $P(k)$ to get k of ^{13}C in a molecule containing n carbon atoms can be given by

$$P(k) = C_k^n \cdot (0.011)^k \cdot (0.989)^{n-k} \qquad \text{(eq.40)}$$

where C_k^n is a binomial coefficient (number of possible combination of k elements out of n). For instance, a C_{60} PAH has ~51.5% of probability of containing only ^{12}C, ~34.4% of containing one ^{13}C, and ~11.3% of containing two ^{13}C, and so on. Thus, in its mass spectrum, series of three peaks spaced by one unit mass having relative abundance 51-34-11. If in a mass spectrum, the relative intensity of *m*/*z*+2 does not match the relative abundance of predicted isotopic distributions, it is possible that peak *m*/*z*+2 corresponds to a PAH precursor ion. To deduce this, it is necessary to compare between obtained mass distributions with a calculated isotopic distributions predicting the peak sequence of a molecule (Faccinetto 2009).

Mass spectra of front filters contain higher mass species than those of back filters. The mass spectra are mainly dominated by $C_{16}H_{10}^{+}$ peak. At low HABs near the burner, 20 cm and 50 mm, mass spectra contain mainly high-hydrogen species. This might be due to the presence of unburned fuel surviving up to these heights. The dominance of hydrogen-rich species reduces with higher HABs. At higher HABs, from 80 mm up to 140 mm, mass spectra shift to higher mass and show higher overall signal.

Unlike front filters, mass spectra of back filters contain mostly species with mass not heavier than *m/z* 250. This is because only the gas phase of combustion byproducts is captured on these back filters. The lightest mass which can be found in these spectra is *m/z* 92 – $C_7H_8^{+}$ toluene. These mass spectra are mainly dominated by the peak *m/z* $C_{14}H_{10}^{+}$. There is no noticeable difference between the spectra obtained at different HABs. In contrast with the front filter, at 290 mm HAB, sequence of peaks is still observed in mass spectra. It can be said that unlike the particulate matter and condensable PAHs, the gas phase PAHs can survive throughout the oxidation process of the combustion and can even end up in the environment.

Beside the presence of pericondensed PAH peaks in the L2MS mass spectra, there is the involvement of different classes of aromatic hydrocarbon compounds which are rich in hydrogen. According to the recent study of (Adamson et al. 2018), there are four different classes of aromatic hydrocarbon compounds. The first three classes for C_xH_y with C/H ratio of ≥ 1 include: (i) pericondensed aromatic compounds, (ii) pericondensed aromatic compounds with a single short side-chain like $-CH_3$ or $-C_2H$ or five-membered ring structures, (iii) aliphatically bridged multicore aromatics. The fourth class is aliphatically substituted (or alkylated) aromatic rings, corresponds to $C_{x-1}H_{y+12}$ with C/H ratio < 1. All three classes of aromatic compounds with C/H ratio ≥ 1 are found in the forest of peaks in L2MS mass spectra in this case.

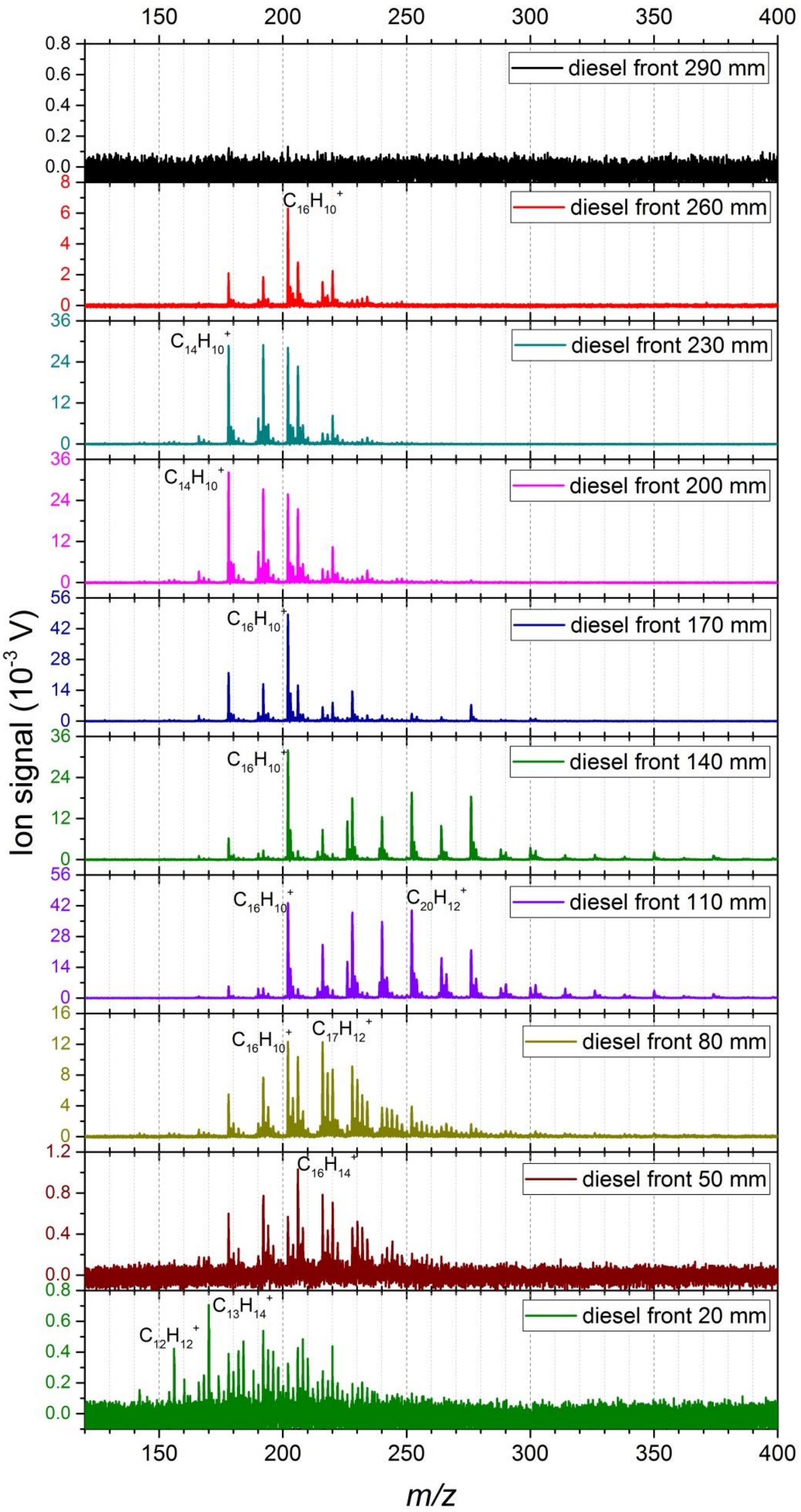

Figure 4.2.2. L2MS mass spectra of front diesel samples at different HABs. 266 nm is used for ionization.

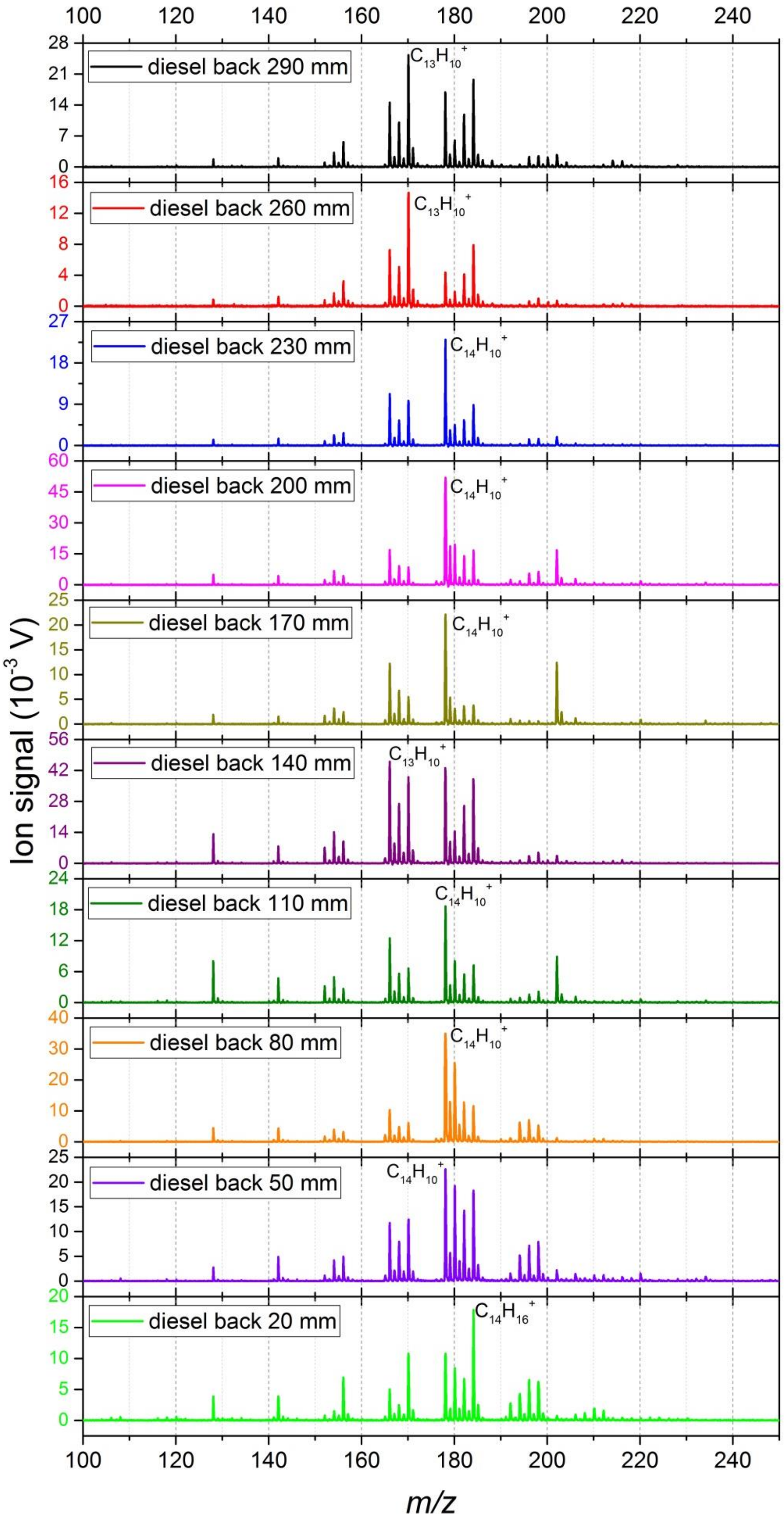

Figure 4.2.3. L2MS mass spectra of back diesel samples at different HABs. 266 nm is used for ionization.

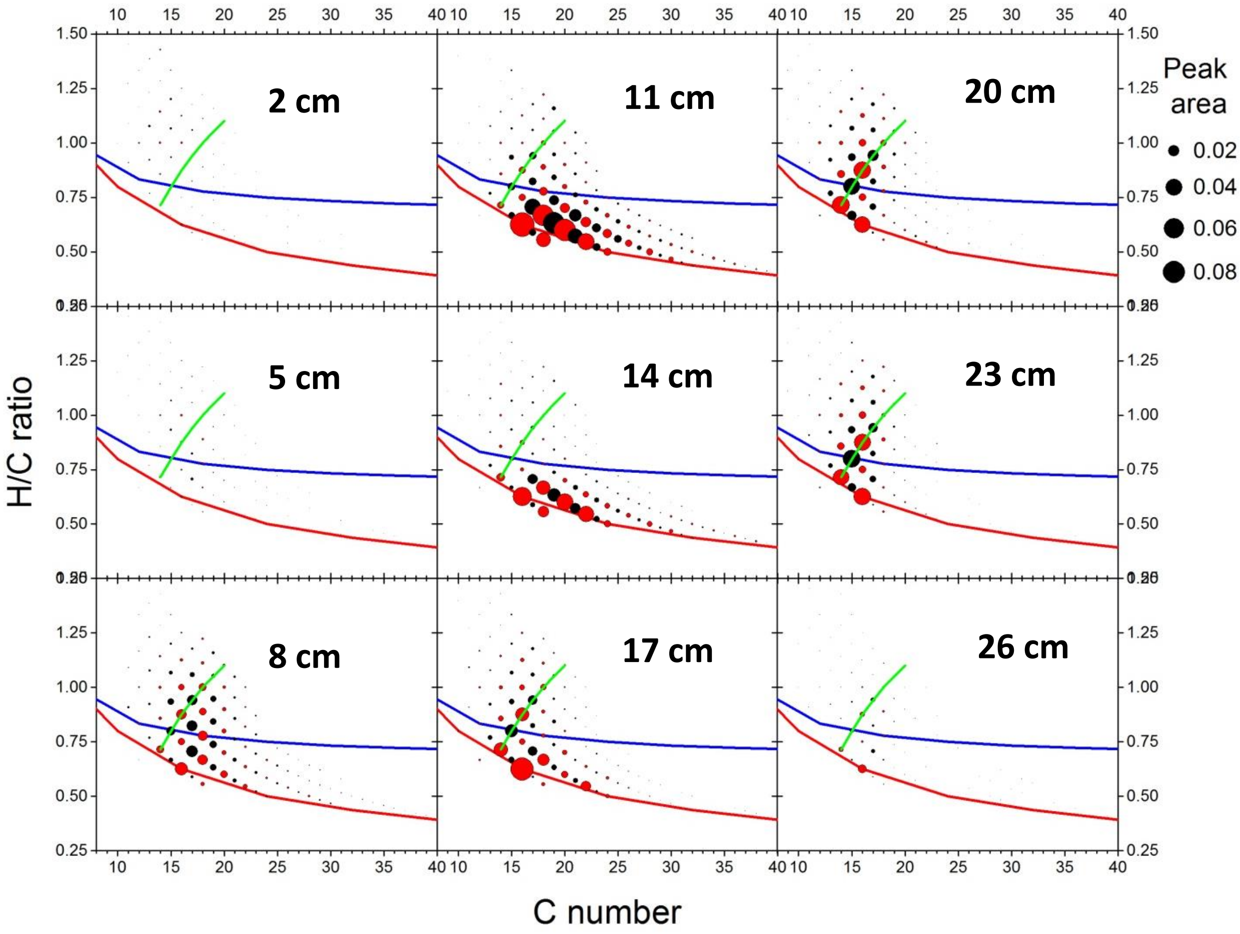

Figure 4.2.4. H/C diagram from L2MS mass spectra of the combustion products collected on Front filters at different HABs in the diesel flame. Black dots represent odd numbers of C, red dots represent even numbers of C. The blue lines represent the limits of benzene oligomers and the red lines represent pericondensed PAHs (D'Anna, Sirignano, and Kent 2010). The green lines represent alkyl-phenathrene series.

Figure 4.2.4 presents H/C diagrams of all mass detected in mass spectra of diesel front filters. Area of dots represents the integrated area of detected peaks in mass spectra of the sample set. The blue lines represent the limits of benzene oligomers and pericondensed PAHs adapted from (D'Anna, Sirignano, and Kent 2010). As it can be seen from the figure, at 2 cm and 5 cm HAB position near the burner, mass spectra contain major of hydrogen-rich species, which have high H/C ratio. However, the signal of these peaks is very weak. With the increase of HAB, at 8 cm, the hydrogen-rich species are reduced, and replaced by more condensed species with lower H/C ratio. The overall signal of the mass spectrum increases compared to lower HAB. At 11 cm, the sequence of mass is more consistent to the pericondensed PAHs line with larger C number with more intense signal. According to the LII profile in the diesel flame, 11 cm is the start of the incandescence emission. Higher than that, at 14 cm, the signal of pericondensed PAHs decreases. At 17 cm HAB, after the LII signal starts dropping, mass spectrum at this height shows the presence of species with lower C number and higher H/C ratio. This trend keeps going along the flame at higher HABs due to the oxidation process in the combustion. This figure shows good evidence that pericondensed PAHs play an important role in soot formation in diesel flame.

In the study of (Adamson et al. 2018), they claim that during the combustion process, aromatic species react with aliphatic hydrocarbons to form alkylated aromatic compounds. These compounds then react to form aliphatically bridged structures, which can get oxidized further to form pericondensed PAHs. As it can be seen in Figure 4.2.4, hydrogen-rich species, which might correspond to alkylated PAHs and aliphatically bridged PAHs, are present mainly at low HABs as 2, 5 and 8 cm. At higher HABs, from 11 cm, signal of these species decreases with an increase of the pericondensed PAHs. And from this height, LII signal starts rising, witnessing the formation of soot particles in the diesel flame.

To get better insight into the difference in chemical composition between diesel samples, PCA is applied to all L2MS mass spectra. 147 peaks are selected and integrated, before being normalized to the sum of 147 peak area for each mass spectrum. The data matrix is then scaled with Pareto method (as presented in subchapter 2.5.3) before applying the analysis. Figure 4.2.5 presents the score plots of this set of samples for the first three principal components, which represent more than 74% of the variance. The loadings corresponding to these principal components are displayed in Figure 4.2.6. The first principal component PC1 corresponds to large hydrocarbon species with $m/z \geq 190$ with positive coefficients and lower-mass hydrocarbon components ($m/z < 184$) with negative coefficients. Projection on PC1 separates remarkably the two main groups, front samples and back samples. Thus the most significant difference between these two groups is the mass of species. Front filters which collected particulate matter contain mostly high-mass PAHs, whereas back filters collected lighter species ($m/z < 250$), which pass through the front filters as described in chapter 3. PC2 is composed of high mass species and particularly the condensed species of 4 - 6 aromatic rings with formula C_xH_{12}, x in the range of 18 – 22, with positive loadings. The negative loadings of PC2 are composed mainly of alkyl-phenanthrene or alkyl-anthracene. The PC2 discriminates essentially front samples at immediate HABs (110 mm and 140 mm) and the other front samples. At lower HABs, the presence of these alkyl-PAHs is due to unburned fuel. Above 230 mm HAB, there might be some droplets that still survive probably transported at this height by the air shield surrounding the flame, causing the presence of these alkyl-PAHs. The higher order principal component PC3 also allows discrimination between samples at different HABs. Negative loadings of PC3 are composed of unsubstituted PAHs species as $C_{10}H_8^+$, $C_{14}H_{10}^+$, $C_{16}H_{10}^+$, $C_{22}H_{12}^+$, whereas other compounds, which are more hydrogenated species corresponding to alkyl PAHs, are responsible for positive coefficients of PC3. As it can be seen in the score plot, these condensed PAHs are present with higher proportion in their relative mass spectra at high HABs (higher than 110 mm).

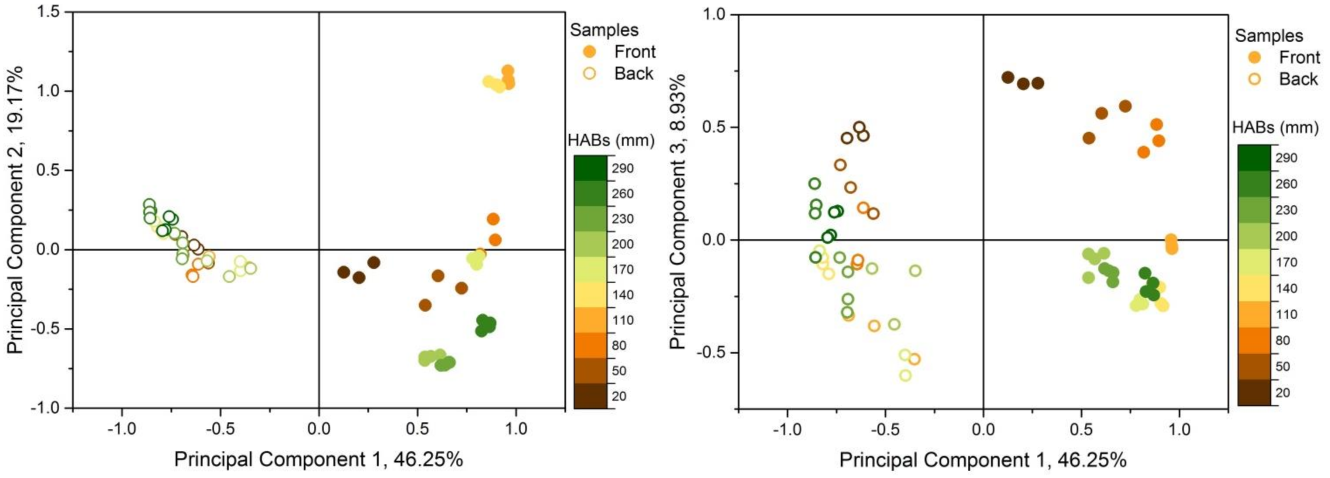

Figure 4.2.5. Score plots of PC1, PC2 and PC3 of PCA results obtained on L2MS mass spectra of diesel samples

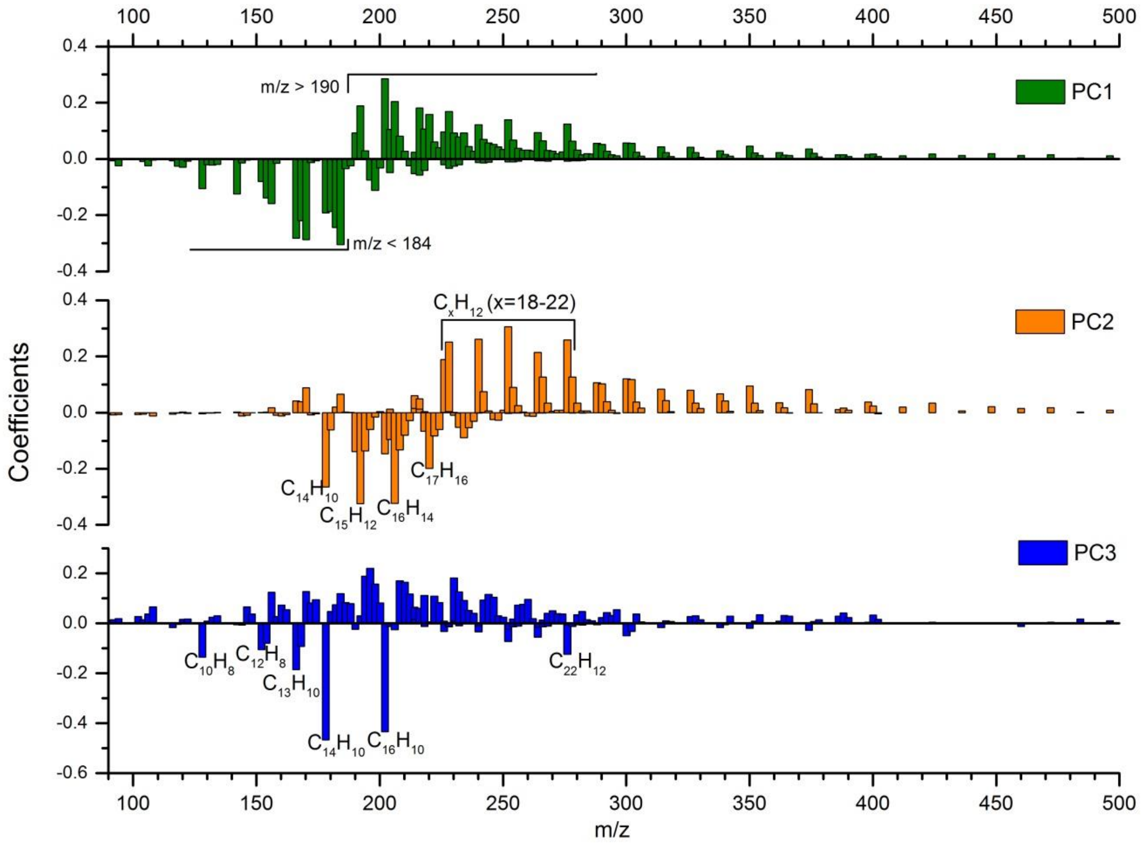

Figure 4.2.6. Loadings corresponding to PC1, PC2 and PC3 presented in Figure 4.2.5

4.2.1.2. SIMS mass spectra of diesel samples

To obtain more chemical information on the combustion by-products, Tof-SIMS is applied to further mass-analyze samples from the diesel flame and the spectra are presented in Figure 4.2.7 and Figure 4.2.8. SIMS mass spectra of diesel samples are composed of two main peak distributions: a first distribution with low mass $m/z \leq 180$ including mostly hydrocarbon fragments and inorganic ions originating from the GFF substrate, and a second distribution with high mass *m*/*z* > 180 mostly contributed with aromatic compounds. Positive polarity of SIMS mass spectra of diesel samples is shown in Figure 4.2.7 covering the mass range *m*/*z* 100 – 600. Mass spectra of back samples overlay the mass spectra of front samples at each HAB. In this range of mass, front sample mass spectra are mostly dominated by peaks attributed to PAHs. The highest peak in most cases is assigned to ion $C_{13}H_9^+$. In the mass spectra of samples collected at 80 mm, 110 mm and 190 mm HAB, the sequence of mass is particularly richer in PAHs. Some peaks at higher mass, for instance $C_{19}H_{11}^+$, $C_{24}H_{12}^+$ are dominant. Peaks attributed to PAHs with an odd number of carbon atoms are observed to lose also an odd number of hydrogen atoms. At 260 mm and 290 mm HAB, the sequence of PAH peaks from $C_{22}H_{12}^+$ and higher mass PAHs is almost absent. Compared to mass spectra of front samples, back samples spectra show significantly lower signal of PAHs. The results obtained with the ToF-SIMS technique is coherent to what was achieved in the L2MS analysis, except for low-mass PAHs. This is due to the different working temperatures of these two techniques. L2MS analyzes samples under low temperature condition (-100°C) that avoids the sublimation of volatile species.

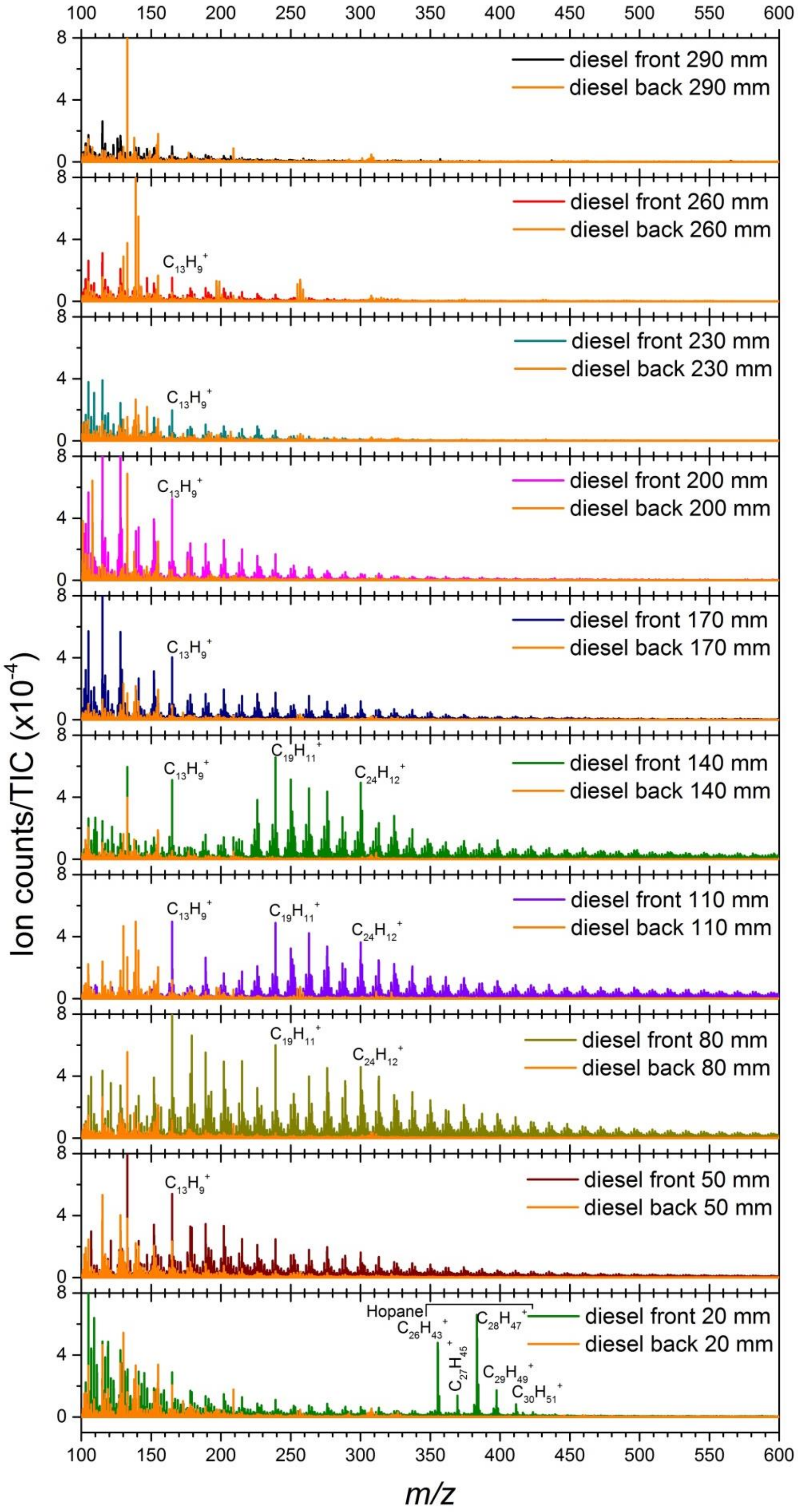

Figure 4.2.7. Positive SIMS mass spectra of diesel front and back samples. Data is normalized by the total ion count of each spectrum.

Additionally, there is presence of hopanes ($C_{27}H_{45}^+$, $C_{28}H_{47}^+$, $C_{29}H_{49}^+$, $C_{30}H_{51}^+$, etc.) (Siljeström et al. 2009) in SIMS spectra of diesel front sample at 20 mm HAB. These compounds are also called "biological markers" or "chemofossils" since they are always present in crude oils (Petrov 1987). Hopanes are produced during the long time of burial, when the biogenic molecules undergo chemical alteration under the effect of biodegradation, mineral catalysis, high pressure and temperature (Bryselbout, Henner, and Lichtfouse 1998). At 20 mm HAB, diesel fuel is not completely vaporized and gets into the sampling system, deposited on the collected samples. This leads to the presence of hopanes in only this sample. At higher HABs, these compounds involve in the combustion process and get consumed.

Negative SIMS spectra of diesel front samples are presented in Figure 4.2.8. The spectra are generally dominated by H^-, O^-, OH^-, CH^- and C_2H^- fragment ions. There is significant difference between mass spectra at different HABs. For samples at 20 mm to 110 mm, the mass spectra are dominated by C_nH^- fragment ions. Additionally, peaks corresponding to the hydrogenated carbon cluster C_nH^- of even number of carbons show more intense signal than the one with odd number of carbons at these heights in the flame. This feature becomes less obvious with the increase of HAB above 110 mm. At 140 mm, 170 mm and 200 mm, mass spectra still show the dominance of C_2H^- peak, however the signal of CH^- and C_2^- clusters increases. From 230 mm HAB, the dominance of carbon and hydrogenated carbon clusters is replaced by O^-, OH^- peaks.

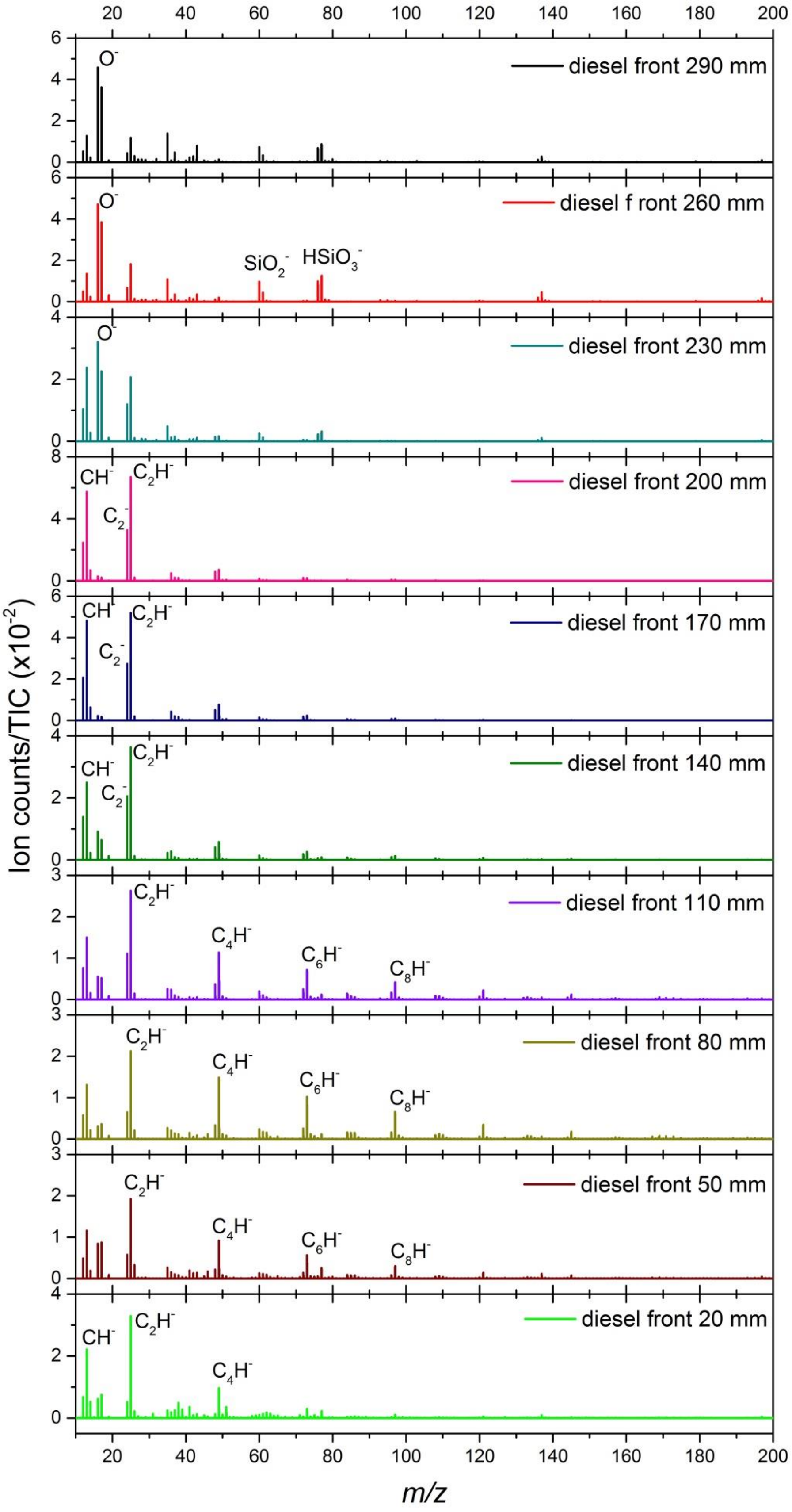

Figure 4.2.8. Negative SIMS mass spectra of diesel front samples. The spectra are normalized to the total ion count

Negative SIMS mass spectra of diesel back filters are presented in Figure 4.2.9. All mass spectra are dominated by H^-, O^-, OH^-, CH^-, C_2^-, Cl^-. There is no obvious trend or difference between these mass spectra.

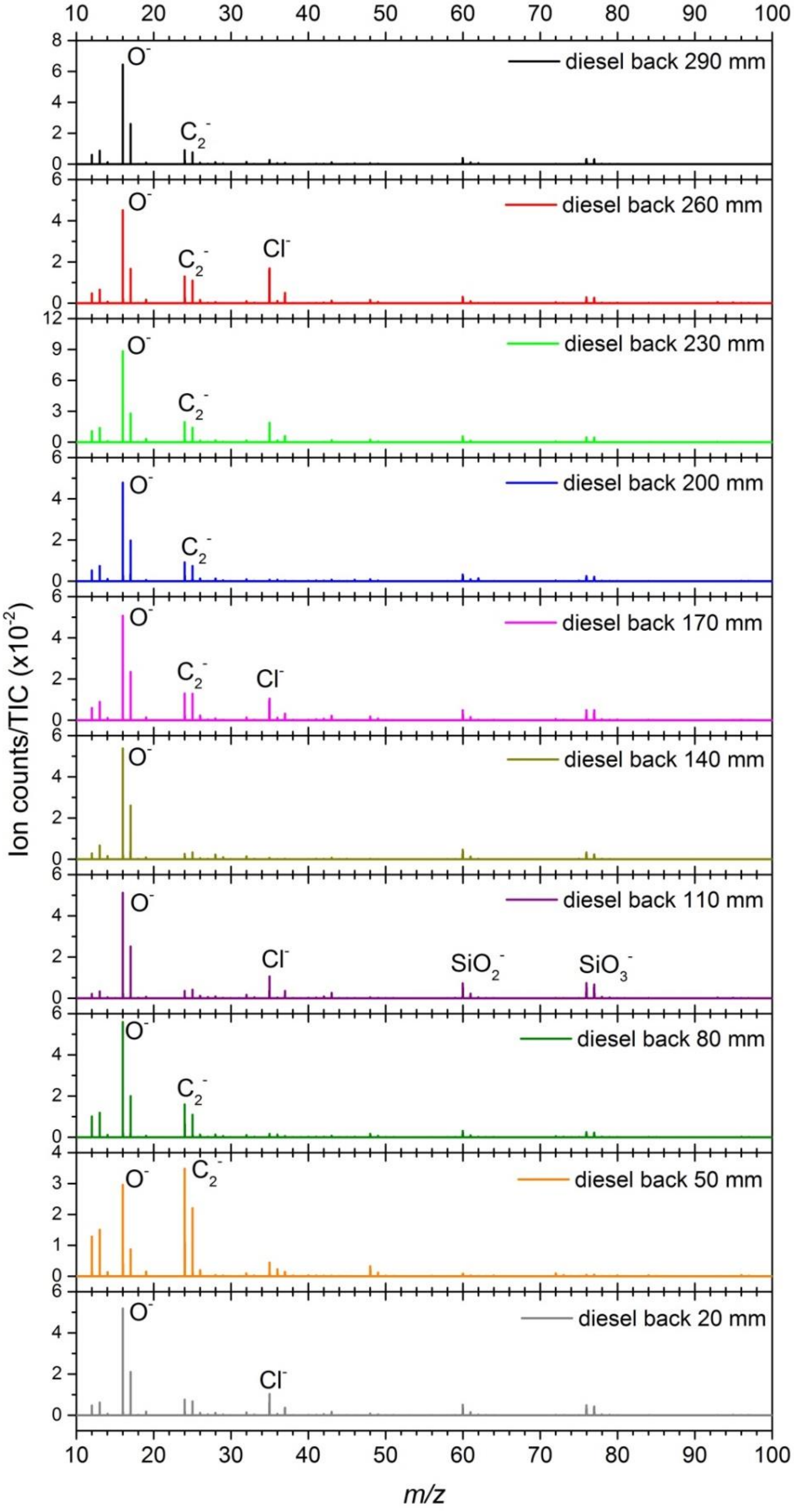

Figure 4.2.9. SIMS spectra (negative polarity) of diesel back samples

PCA analysis is performed separately for both positive and negative SIMS spectra of diesel samples. 270 and 223 mass peaks including organic and inorganic ions are chosen for the analysis of SIMS positive and negative spectra, respectively. Score plots of the various samples projected on the first two components representing most of the variance inside the sets of samples are presented in Figure 4.2.10 and Figure 4.2.12 for positive and negative polarity, respectively.

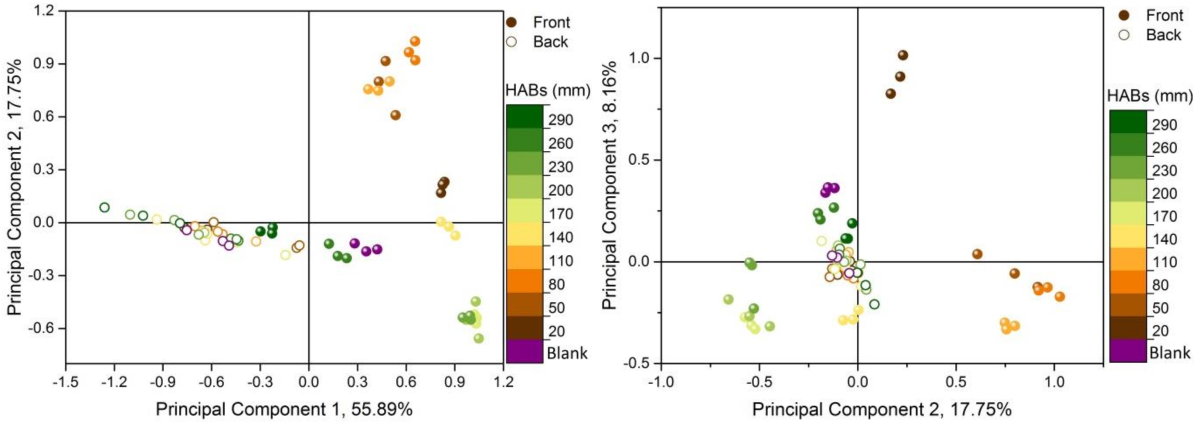

Figure 4.2.10. Score plots of PC1, PC2 and PC3 of PCA applied on SIMS mass spectra (positive polarity) of diesel samples

In the case of positive SIMS spectra, the first component PC1 (representing 55.89% of the variance) shows a remarkable discrimination between the front and back samples. These samples are separated from each other mainly by the positive coefficients of hydrocarbons fragments. They are also distinguished with the negative loadings, which are mainly associated to inorganic ion clusters. This can be explained by the important amount of PAHs which provide hydrocarbon fragments on front samples, whereas back samples contain less organic material. The inorganic ion clusters, which are dominant in back samples, come from the desorption of GFF substrate. The samples are separated by their level of material loadings on the sample. That means front samples (except the one at 29 cm HAB) contain much more combustion products than back samples and front sample at 29 cm.

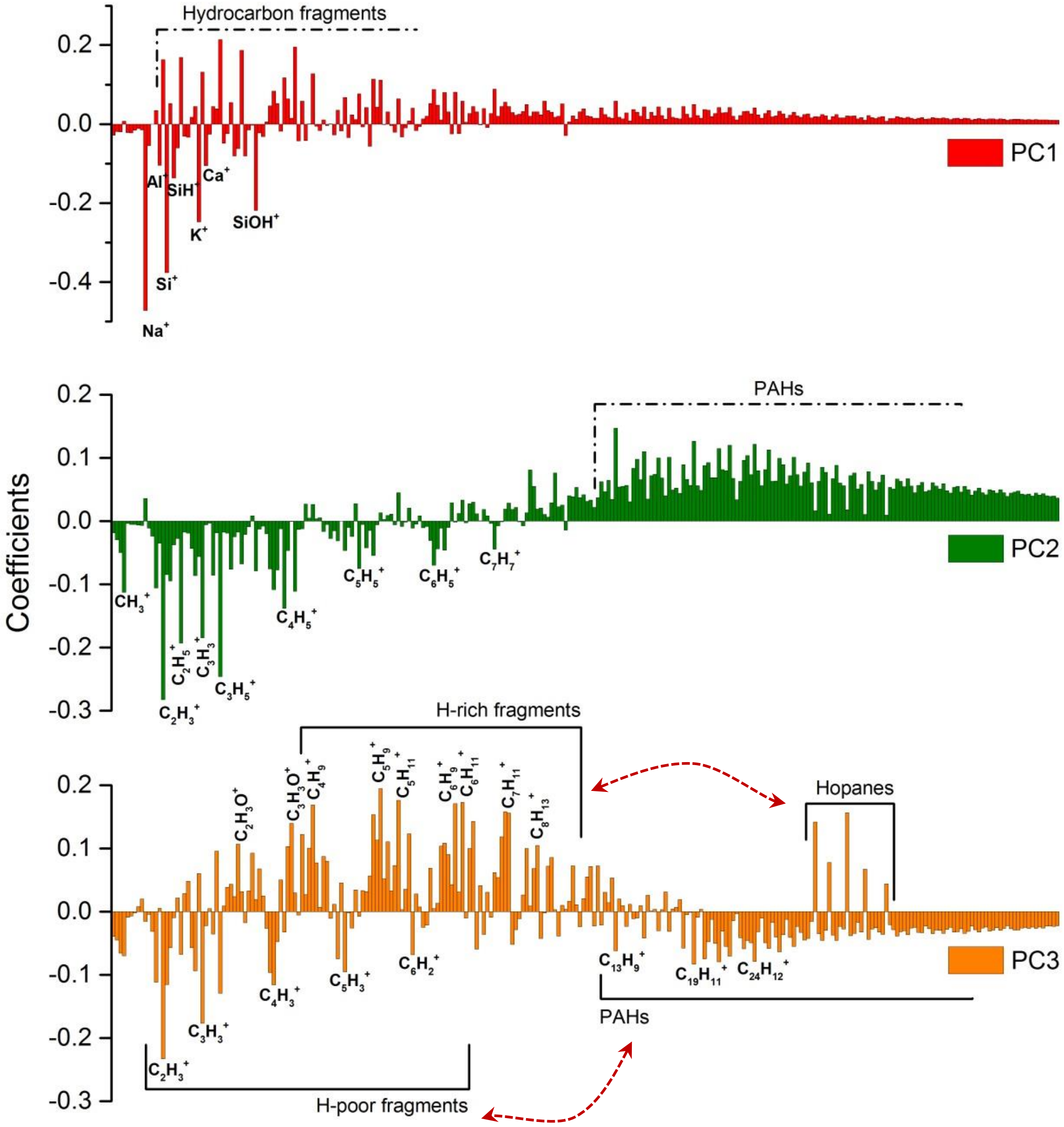

Figure 4.2.11. Loadings of PC1, PC2 and PC3 corresponding to Figure 4.2.10

The second component PC2, accounting for 17.5% of variance, allows the discrimination between front samples at different HABs. This component is composed of selected PAHs with positive loadings, and of fragments and small aromatic compounds with negative loadings. With this component, front samples at 5 cm, 8 cm and 11 cm are well separated to the others due to their high content of PAHs. Front samples at 17 cm, 20 cm and 23 cm are located on the negative side of the PC2. The discrimination of this component shows a good coherence with the results achieved in the L2MS analysis and also with the Vis-LIF measurement. Before the soot is formed at 11 cm HAB, the soot precursors accumulate at high concentration. After this height, the presence of soot precursors in flame reduces as they are consumed to form soot. At even higher in the flame, the leftover soot precursors are oxidized and only small aromatic compounds could survive at these heights. The third component PC3 only shows a small variance between the samples, 8.16%. This component mainly separates front sample at 2 cm to the rest of the sample set. PC3 is composed of derivate of hopanes and high-hydrogenated fragments with positive loadings, and of low-hydrogenated fragments and PAHs with negative loadings. This confirms the L2MS results that the front sample at 2 cm contains unburned diesel fuel.

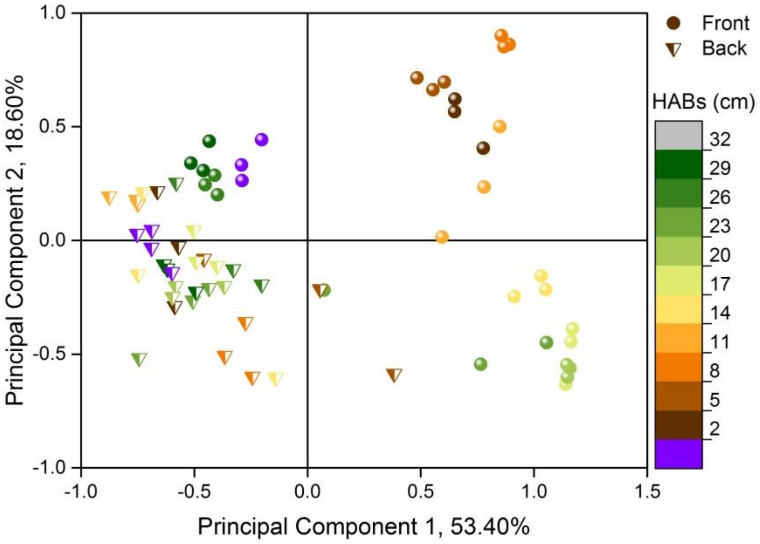

Figure 4.2.12. Score plot of PC1 and PC2 applied on negative SIMS spectra of diesel samples

For the negative polarity SIMS spectra (Figure 4.2.12 and Figure 4.2.13), the first component PC1, which represents 53.4% of the variance, discriminates the samples containing C_n^- and C_nH^- carbon cluster fragments from those containing higher signals of O^-, H^-, SiO_2^- and SiO_3^- which are corresponding to blank. The second component PC2 (accounting for 18.6% of the variance) separates between samples containing organic material and elemental carbons – mature soot. The positive loadings of this PC2 are associated to C_nH^- hydrogenated carbon clusters with n in the range of 4 – 10 with an even number of carbons. The negative coefficients are associated to carbon clusters as C^-, C_2^-, C_3^-, C_4^- and O^-. From this result, it can be said that front samples at 2 cm to 11 cm mainly contains organic material – soot precursors, whereas the ones collected at higher HABs until 23 cm contain soot. At the end of the flame, 26 cm and 29 cm, soot and soot precursors are almost completely oxidized, thus these samples are located with the blanks and back samples in the PCA score plot.

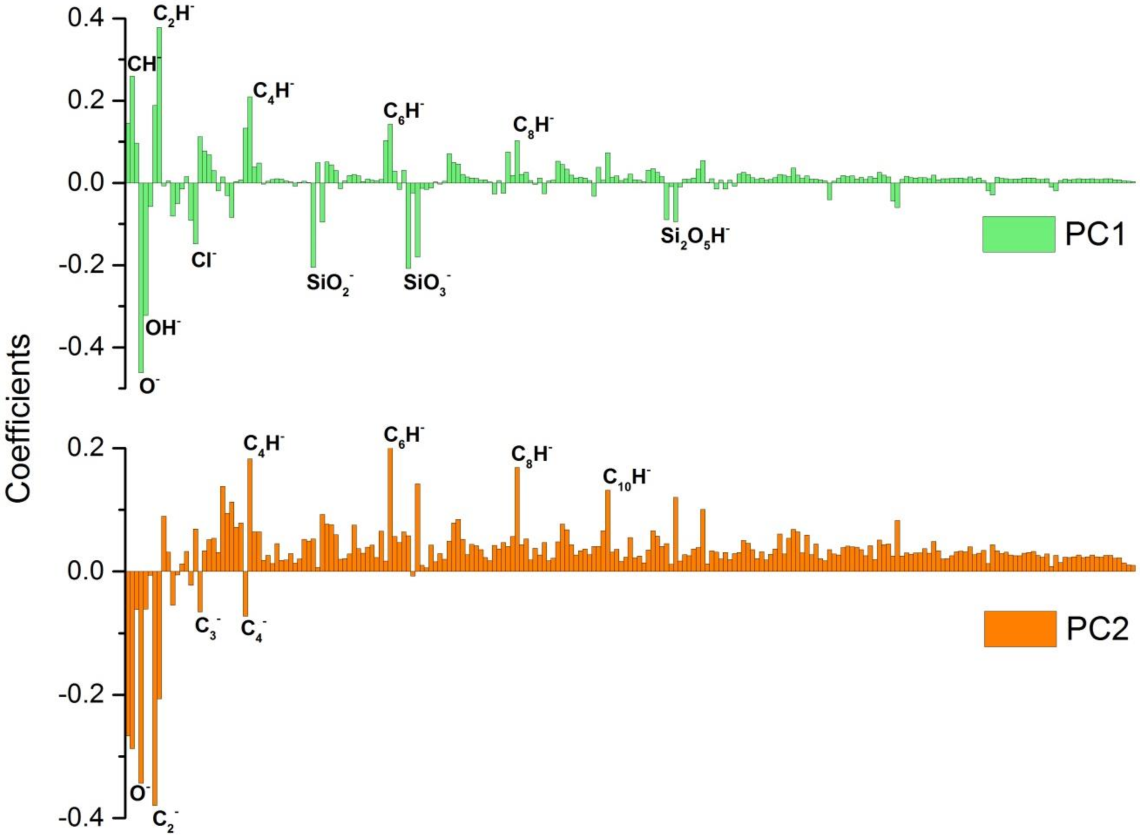

Figure 4.2.13. Loading plots corresponding to PC1 and PC2 shown in Figure 4.2.12

4.2.2. *N*-butanol flame

Similarly to diesel flame, *n*-butanol flame is also sampled at 10 HABs with the two-filter techniques. The front and back samples collected are shown in Figure 4.2.14.

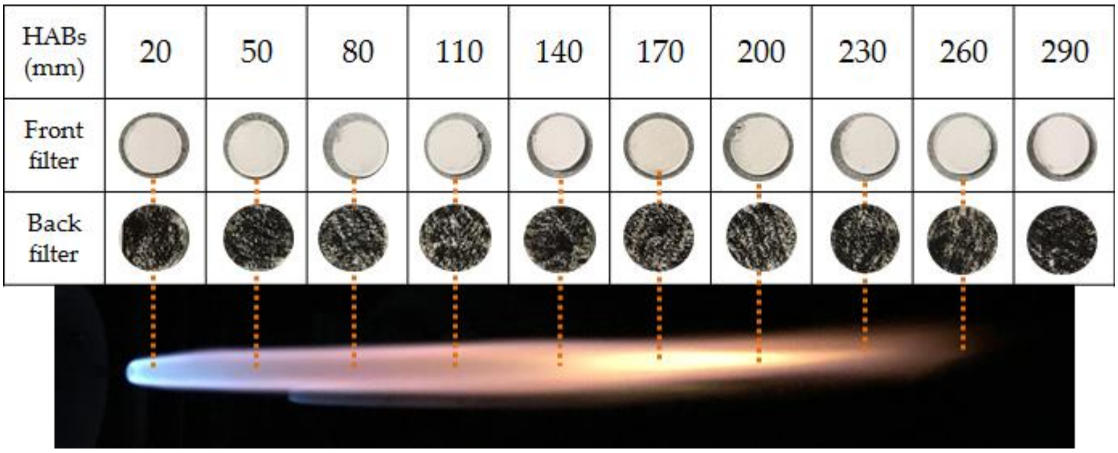

Figure 4.2.14. Photos of *n*-butanol flame and Front and Back filters corresponding to different HABs. (The photo of the flame is rotated 90° for better view)

When comparing with the front samples collected in the diesel flame, as shown in Figure 4.2.1, *n*-butanol front samples contain very small amount of deposited material. These front samples are all whitish. This confirms the result achieved in the LII measurement, i.e. the *n*-butanol flame generates much less particulate matter than the diesel one. Back samples have blackish color due to the deposition of black carbon on the glass fiber filter before the sampling procedure.

These samples are mass analyzed using the L2MS and ToF-SIMS techniques.

4.2.2.1. L2MS mass spectra of *n*-butanol samples

Samples collected from the *n*-butanol flame are analyzed with L2MS using 532 nm wavelength for laser desorption and 266 nm wavelength for laser ionization. The laser ionization fluence is similar to the one used in diesel samples analysis (5.7 mJ/cm^2). However, laser desorption to analyze front samples is used at higher fluence (65 mJ/cm^2) in order to desorb more efficiently since the front samples are whitish and do not contain much material. Each mass spectrum is averaged over 200 laser shots. Three to four mass spectra are recorded for each sample, corresponding to three to four zones on the sample. L2MS mass spectra of *n*-butanol front and back samples are presented in Figure 4.2.15 and Figure 4.2.16, respectively.

Mass spectra of *n*-butanol front samples show very low signal-to-noise. This is due to the extremely low loading of the samples. There are some peaks assignable in these mass spectra as $C_{16}H_{10}^+$ and $C_{14}H_{10}^+$ presenting at the samples from 110 mm to 230 mm. Exceptionally, the front samples at 170 mm show a higher mass peak, which is assigned to $C_{22}H_{12}^+$.

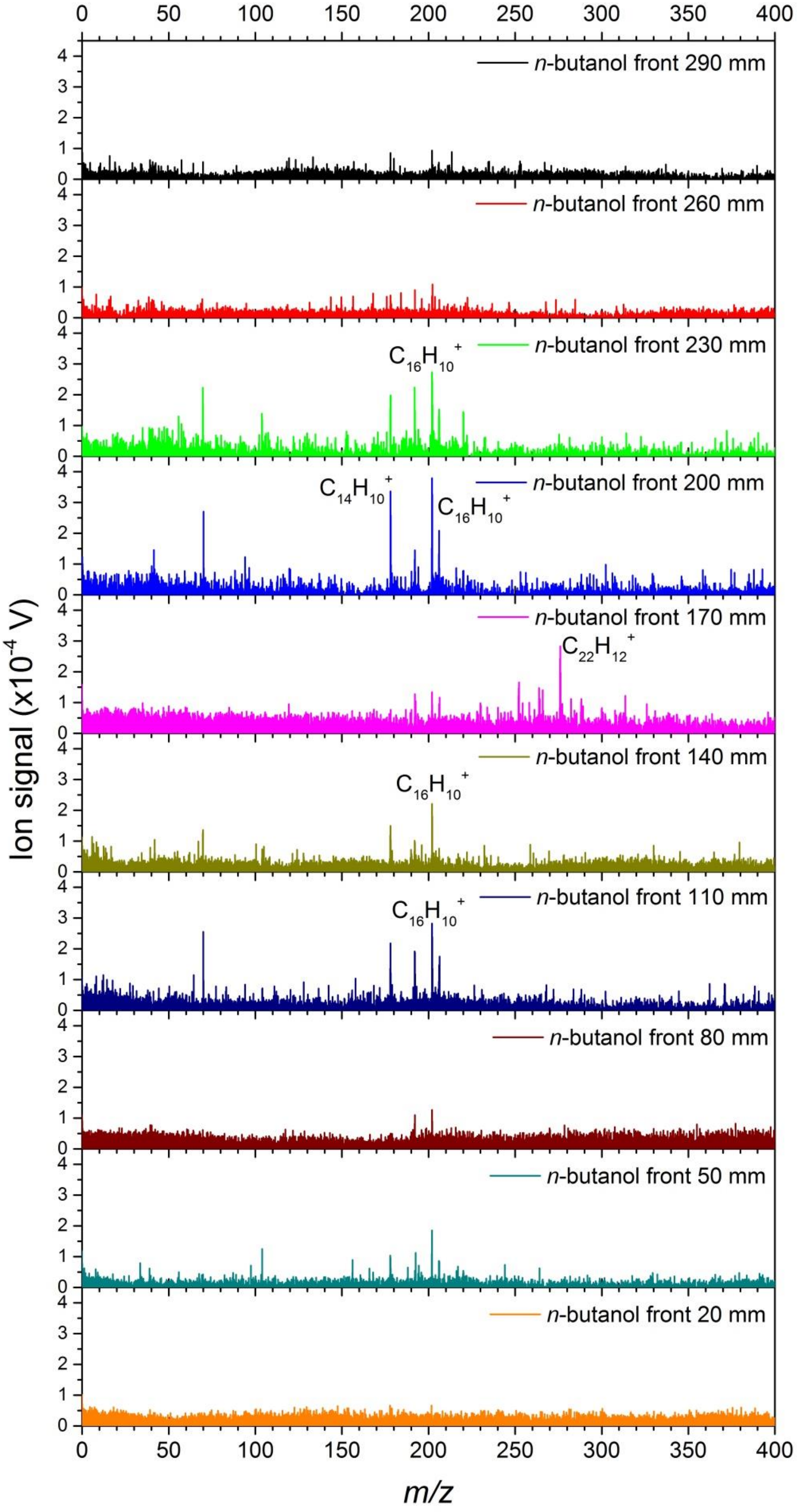

Figure 4.2.15. L2MS mass spectra of *n*-butanol front samples, obtained with 532 nm laser desorption and 266 nm laser ionization

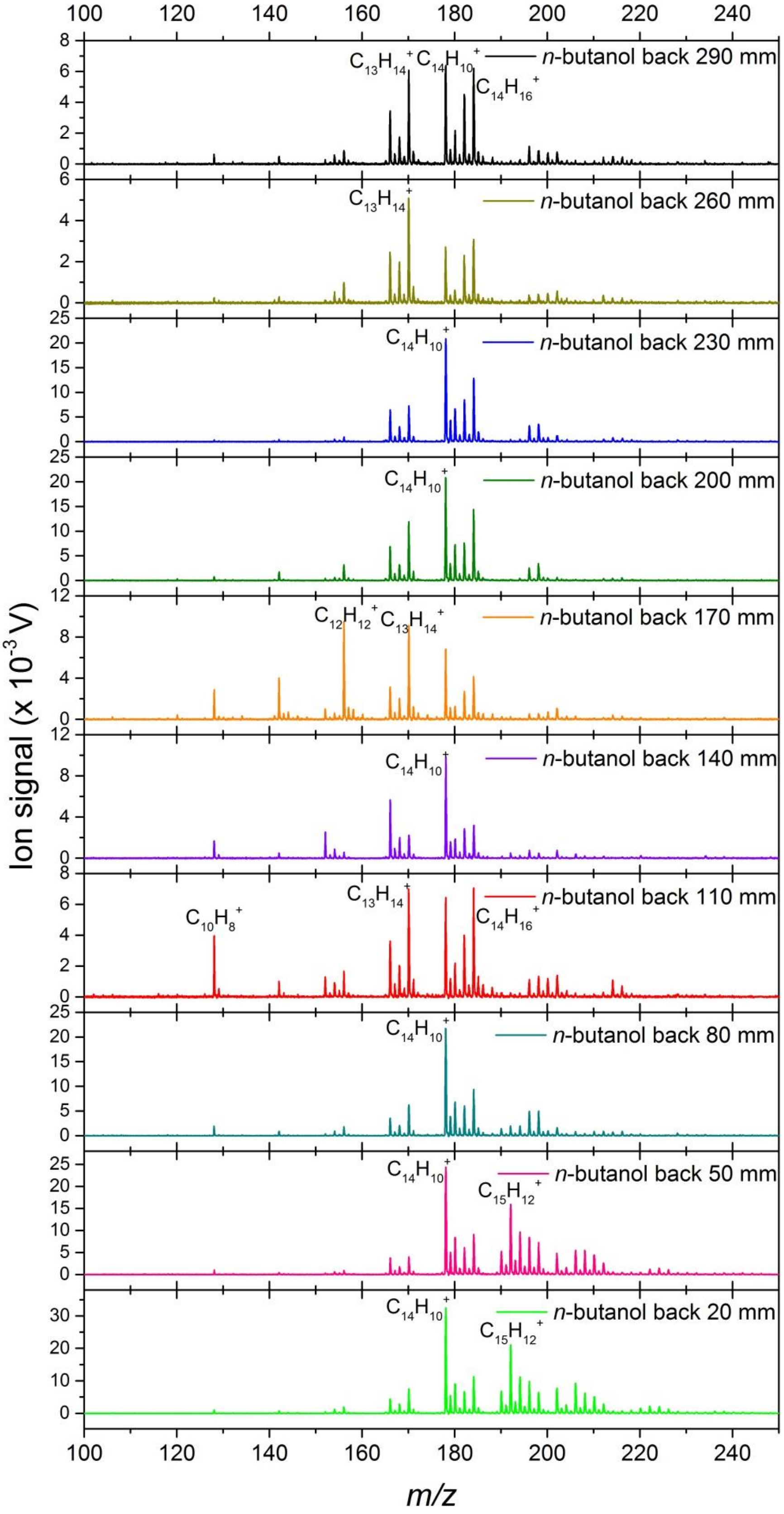

Figure 4.2.16. L2MS mass spectra of *n*-butanol back samples, obtained with 532 nm laser desorption and 266 nm laser ionization

Unlike front samples, mass spectra of *n*-butanol back samples – which are supposed to contain gas phase of combustion products – show good signal-to-noise. The mass spectra at 20 and 50 mm HAB are very similar to each other with most intense peaks assigned to $C_{14}H_{10}^{+}$ and $C_{15}H_{12}^{+}$. *m/z* $C_{14}H_{10}^{+}$ stays intense in all mass spectra at 10 different HABs. Alkyl-PAHs are present frequently along the flame. After 80 mm HAB, the mass distribution shifts to the lower value.

4.2.2.2. *SIMS mass spectra of n-butanol samples*

N-butanol front and back samples are analyzed using the ToF-SIMS technique. As described in subchapter 2.5.2, SIMS mass spectra have better mass resolution compared to L2MS ones with the price of having also fragmentation due to the high energy Bi_3^+ beam. Positive SIMS mass spectra of these samples are shown in Figure 4.2.17. SIMS mass spectra display two mass distributions. The low masses (*m/z* < 120) consists mostly of fragments. Higher masses are related to PAHs and other compounds. As it can be seen in the figure, mass spectra of back samples are similar to each other with the dominance of low masses at all HABs. The PAHs present on back samples are mainly volatile species. These compounds are present in L2MS but not in ToF-SIMS. It can be said that ToF-SIMS is less sensitive to the volatile PAHs than L2MS due to the lacking of cooling system.

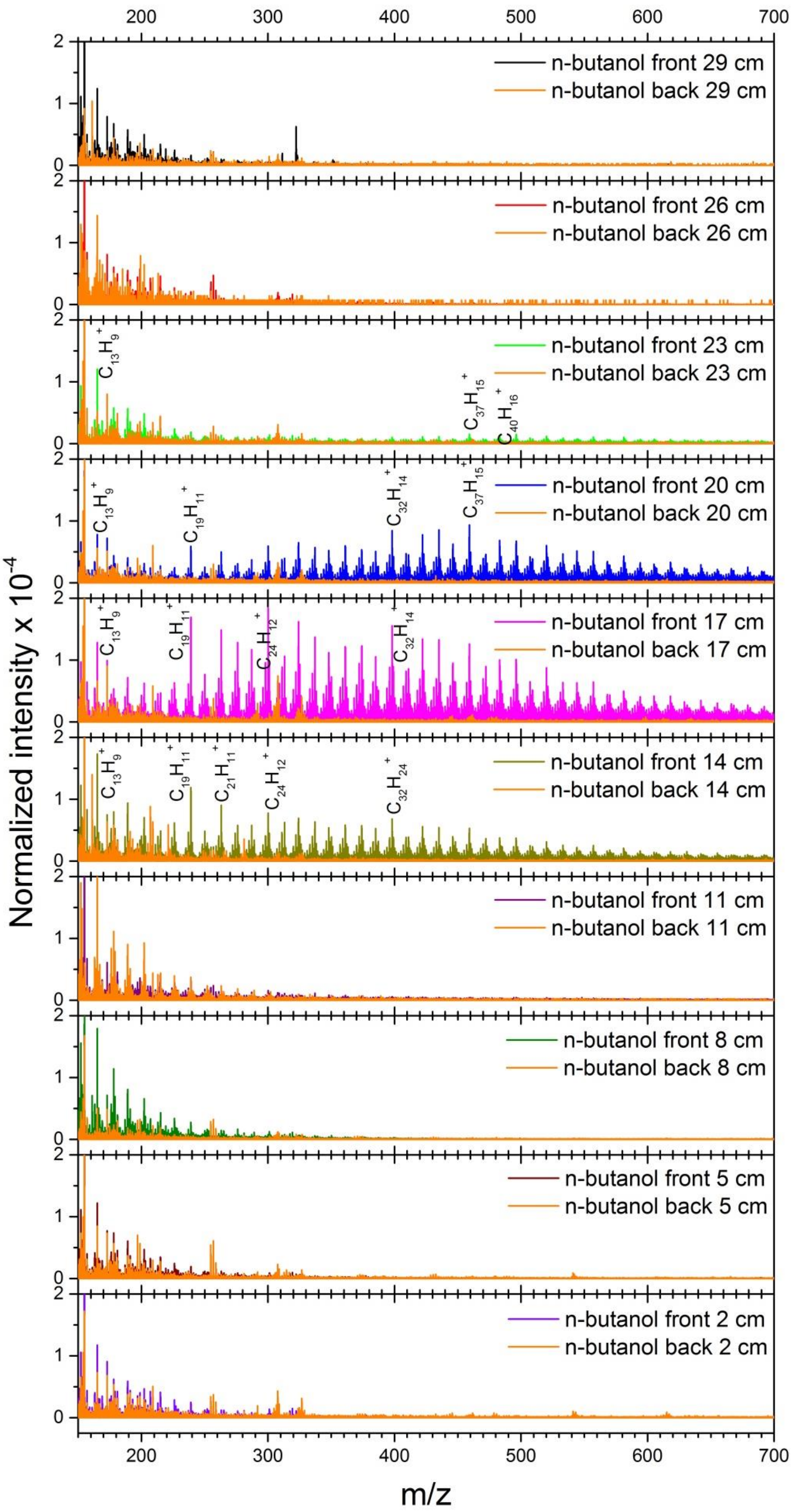

Figure 4.2.17. Positive SIMS spectra of *n*-butanol samples. Data is normalized to the total ion count for each spectrum.

Mass spectra of front filters from 20 mm to 110 mm HAB are very similar with the dominance of low masses. High mass peaks, which are assigned to PAH compounds, start appearing at 140 mm up to 230 mm HAB in the flame. These mass spectra are dominated by $C_{13}H_9^+$, $C_{19}H_{11}^+$, $C_{24}H_{12}^+$, $C_{32}H_{14}^+$, $C_{37}H_{15}^+$. With the increase of HAB, the sequence of PAHs shifts to higher masses. These PAHs cannot be detected in L2MS analysis with 532 nm laser desorption. After this height, high masses peaks disappear with the dominance of fragments.

To have better insight into the composition differences between the samples, PCA is applied to all positive mass spectra. 192 peaks associated with hydrocarbon fragments and compounds are considered for each mass spectrum. The 192 peaks integrated area are normalized to the corresponding Partial Ion Count (PIC, i.e. the sum of the 192 considered peaks integrated area), and then Pareto scaled to obtain a matrix with variables as peaks and observation as samples. Score plot of PC1 and PC2 with their corresponding loadings are presented in Figure 4.2.18 and Figure 4.2.19, respectively. The first two principal components represent more than 72% of the variance. The first component PC1 is composed of hydrocarbon fragments with number of carbon less than 5 with negative coefficients, and high-mass peaks associating to PAH compounds with positive coefficients. This principal component discriminates front samples and back samples. The second principal component discriminates mainly the front samples at from 140 mm to 230 mm HAB from the others. The positive loadings of this PC are composed of highly-hydrogenated hydrocarbon fragments and also a few peak associated to low-mass aromatic compounds as $C_{10}H_8^+$, $C_{12}H_8^+$ and $C_{13}H_9^+$. These peaks might be assigned to aliphatics or long-chain akyl-PAH compounds. PC2 is composed of low-hydrogenated fragments and high-mass PAH peaks.

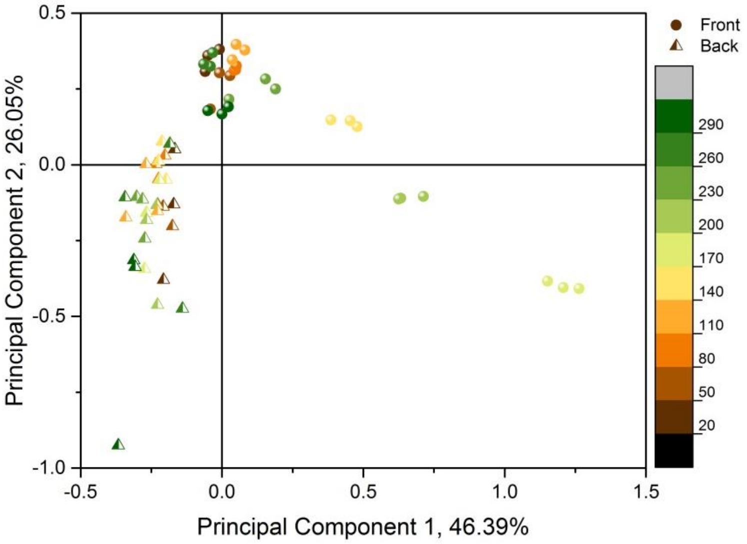

Figure 4.2.18. Score plot of PC1 and PC2 applied on positive SIMS mass spectra of *n*-butanol samples.

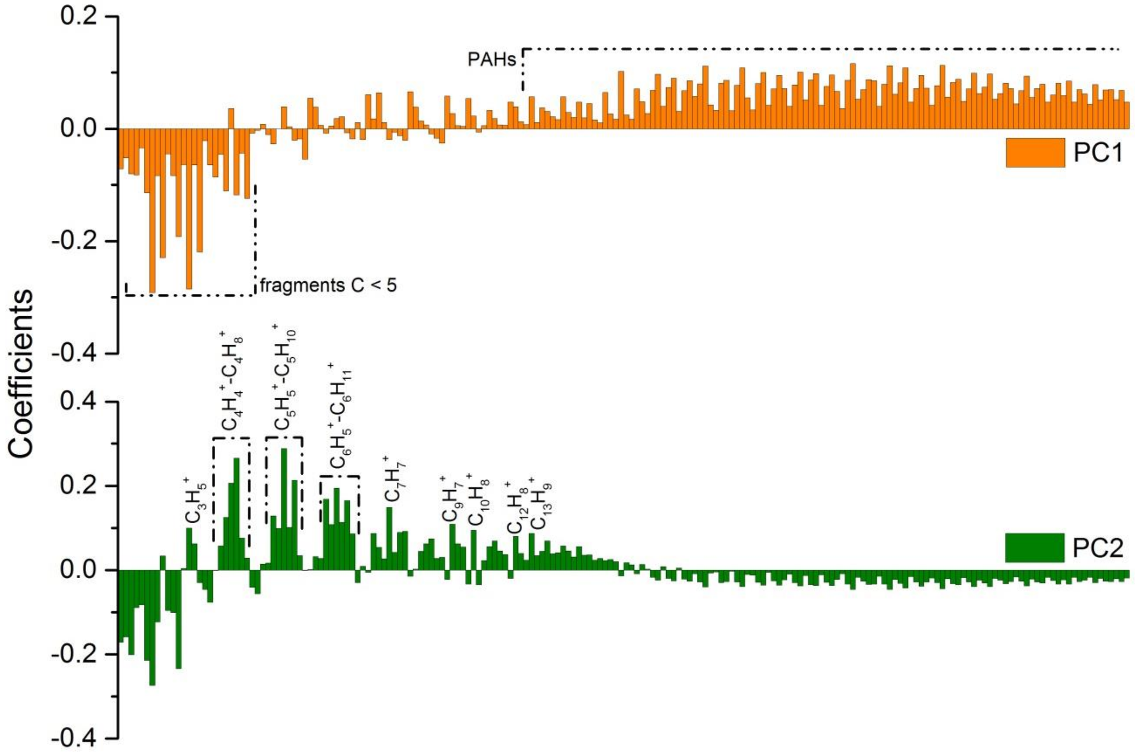

Figure 4.2.19. Loadings corresponding to PC1 and PC2 as presented in Figure 4.2.18

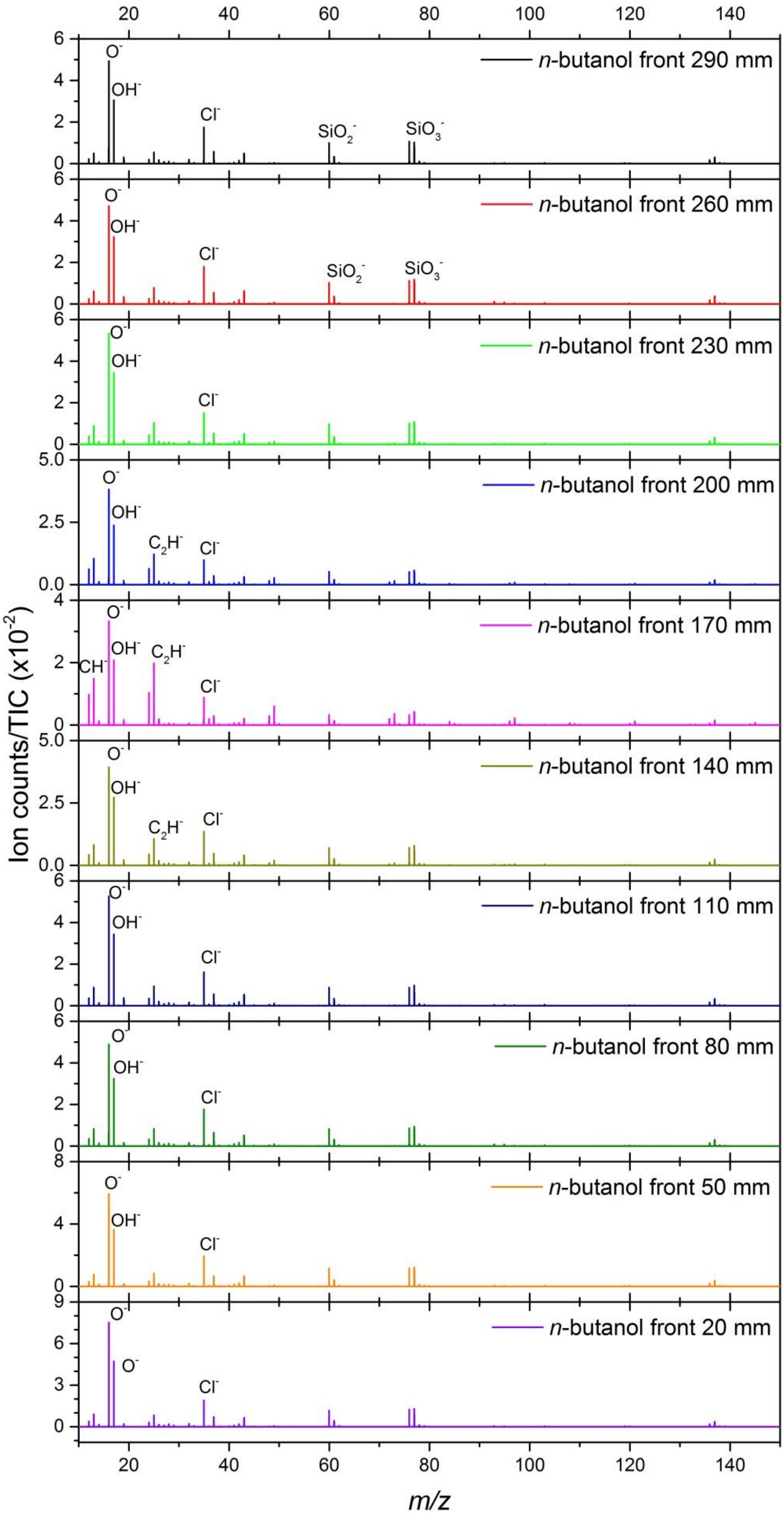

Figure 4.2.20. Negative SIMS spectra of *n*-butanol front samples

Negative SIMS mass spectra of *n*-butanol front samples are shown in Figure 4.2.20. All mass spectra are dominated by $\mathrm{H^-}$, $\mathrm{O^-}$, $\mathrm{OH^-}$. PCA is applied to negative SIMS mass spectra of all samples. A matrix of 164 peaks associated to organic fragments and compounds for each sample is used, after being normalized to PIC and Pareto scaled. The first two principal components represent 73% of variance. PC1 (representing 48.74% of the variance) is composed of carbon clusters C_n^- with negative coefficients, and other peaks with positive coefficients. This PC separates front samples and back samples. Since back samples are covered with a layer of black carbon before the sampling procedure, these carbon clusters are associated to the presence of this elemental carbon. There is almost no soot in *n*-butanol flame, thus these carbon clusters are less present in front samples.

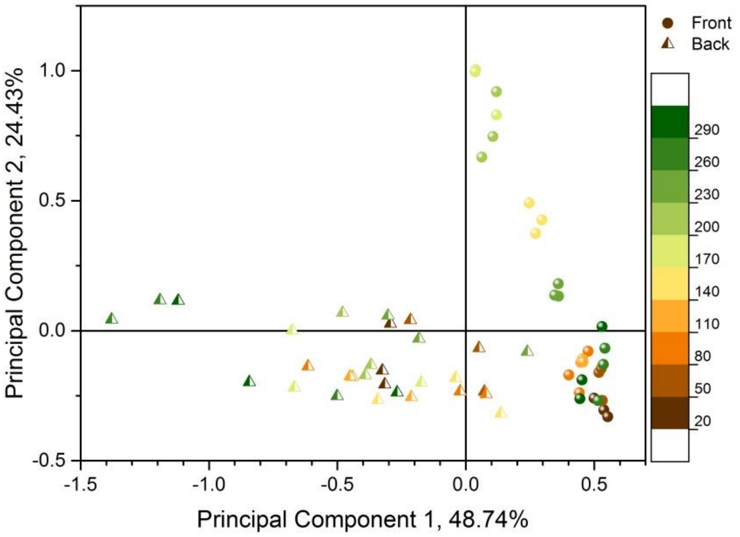

Figure 4.2.21. Score plot of PC1 and PC2 for negative SIMS mass spectra of *n*-butanol samples.

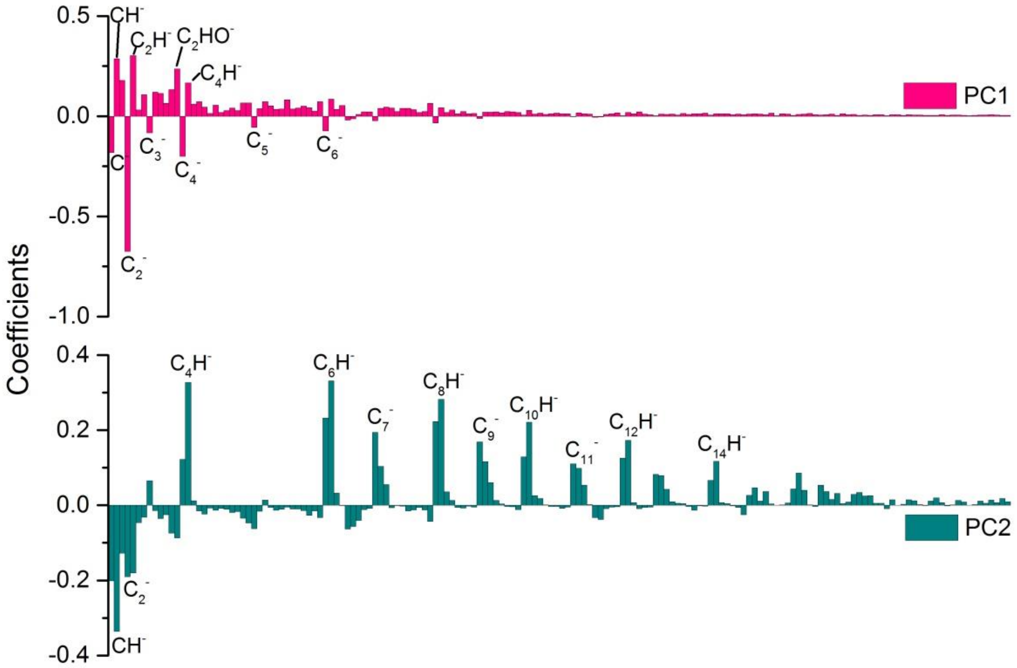

Figure 4.2.22. Loading plot corresponding to PC1 and PC2 represented in Figure 4.2.21

PC2 (representing 24.43% of variance) is composed of the sequence of $\mathrm{C}_n\mathrm{H}^-$ clusters with $n \geq 4$ with positive coefficients and C^-, C_2^-, CH^-, $\mathrm{C}_2\mathrm{H}^-$ with negative coefficients. This principal component separates front samples at 140 mm to 230 mm HAB from the others. Compared to the PCA of positive SIMS mass spectra from the same set of samples, $\mathrm{C}_n\mathrm{H}^-$ clusters with $n \geq 4$ seem to be linked to the PAHs on the sample.

4.2.3.Mixture flame

The mixture flame is sampled at 6 different HABs. The two-filter technique is also applied in this flame. Front and back samples collected are shown in Figure 4.2.23.

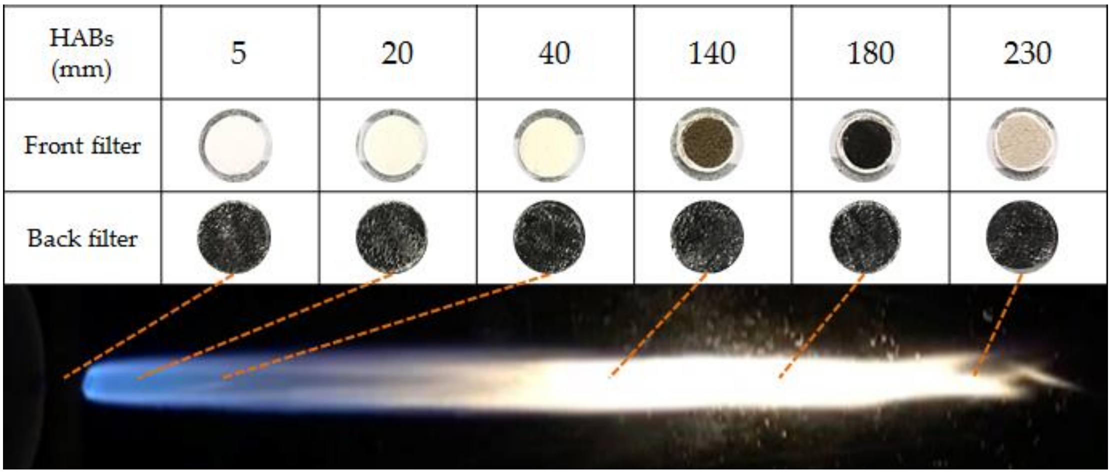

Figure 4.2.23. Photo of front and back samples collected at 6 HABs in the mixture flame.

The sampling heights are chosen according to the LII/LIF profile of this flame presented in subchapter 4.1.3. At 5 mm, the flame has not started yet. This height is also corresponding to the most intense signal of UV-LIF. 20 mm HAB is corresponding to the start of Vis-LIF signal. These first two front samples are whitish after sampling. 40 mm and 140 mm HABs are sampled since they correspond to the first and second peaks of Vis-LIF, respectively. The front samples at these heights show an evolution: yellowish at 40 mm and brown at 140 mm. At the peak of LII signal – 180 mm, soot is also collected, giving black sample. And lastly, samples are collected at 230 mm HAB since this is the end of the LII signal. The sample has light grey color at this HAB.

4.2.3.1. L2MS mass spectra of the mixture flame samples

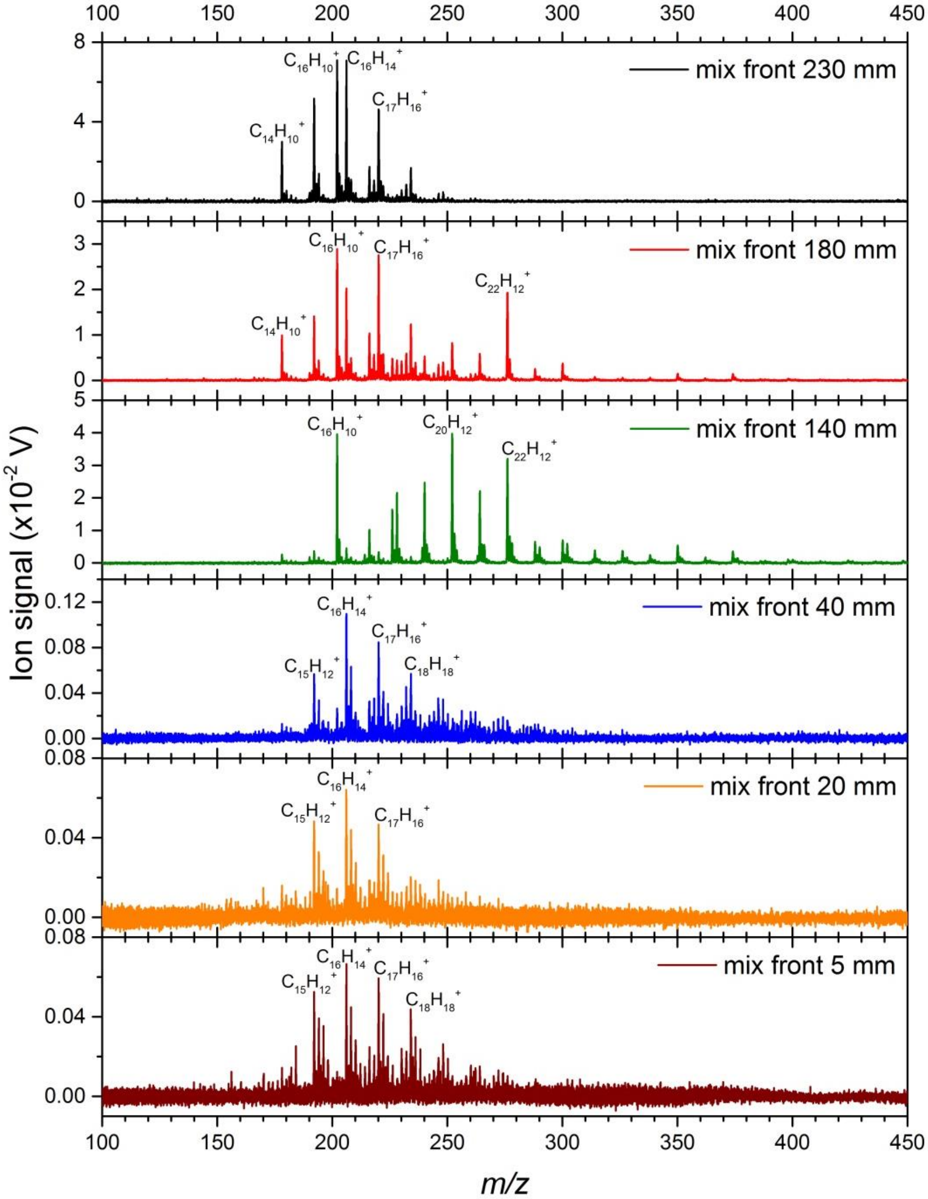

Figure 4.2.24. L2MS mass spectra of the mixture flame front samples

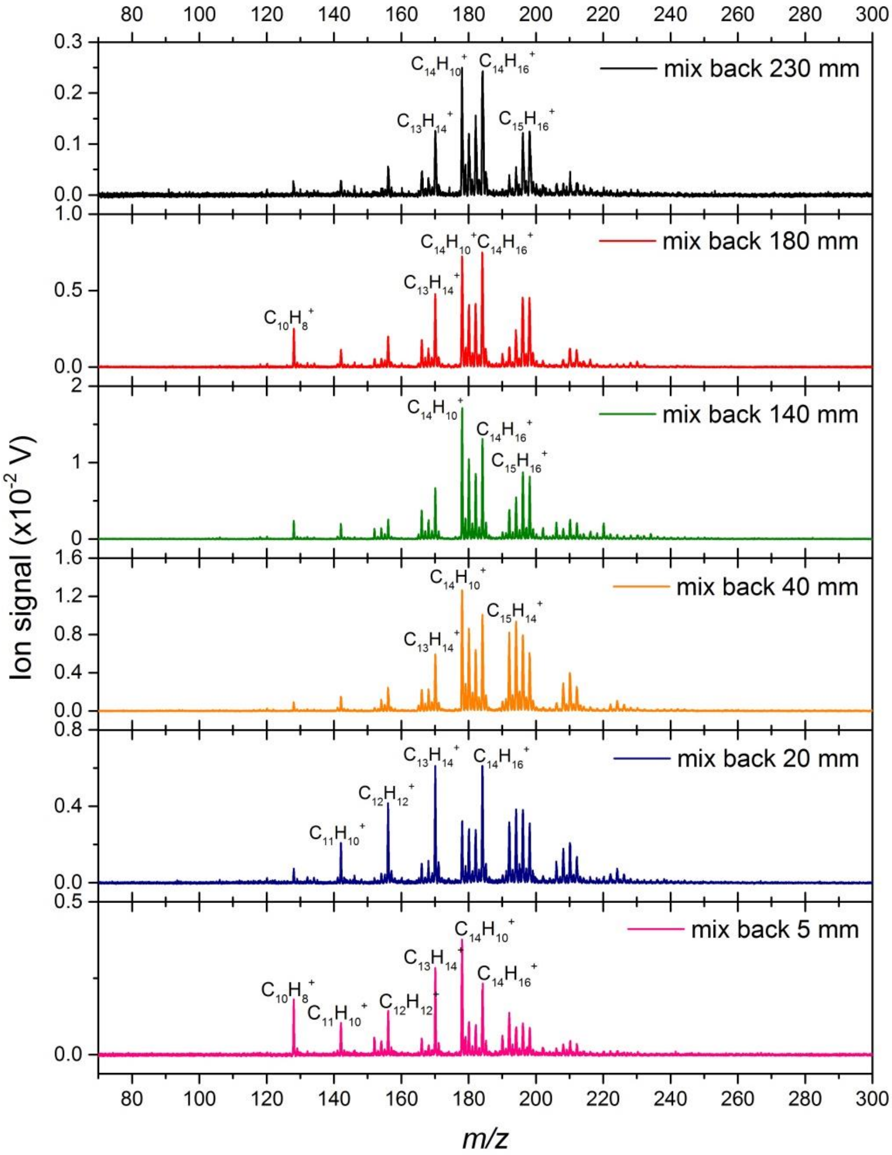

Figure 4.2.25. L2MS mass spectra of the mixture flame back samples

Front and back samples obtained in the mixture flame are L2MS analyzed. The result is shown in Figure 4.2.24 and Figure 4.2.25. For the first three front samples, at 5, 20, 40 mm HAB, mass spectra are rich in alkyl-PAHs as $C_{15}H_{12}^+$, $C_{16}H_{14}^+$, $C_{17}H_{16}^+$, $C_{18}H_{18}^+$, which might come from the unburned fuel. With the increase of HAB, the presence of alkyl PAHs in mass spectra is reduced. The front sample at 140 mm HAB is rich in PAHs as $C_{16}H_{10}^+$, $C_{20}H_{12}^+$, $C_{22}H_{12}^+$. At 180 and 230 mm HAB, the mass sequence shifts to the left, with lower mass peaks. Some alkyl-PAHs associated peaks reappear in this zone as $C_{16}H_{14}^+$, $C_{17}H_{16}^+$. L2MS mass spectra of back samples are rich in volatile PAHs and alkyl-PAHs as $C_{13}H_{14}^+$, $C_{14}H_{10}^+$, $C_{15}H_{16}^+$, etc. The mass sequence shifts to higher masses with the increase of HAB.

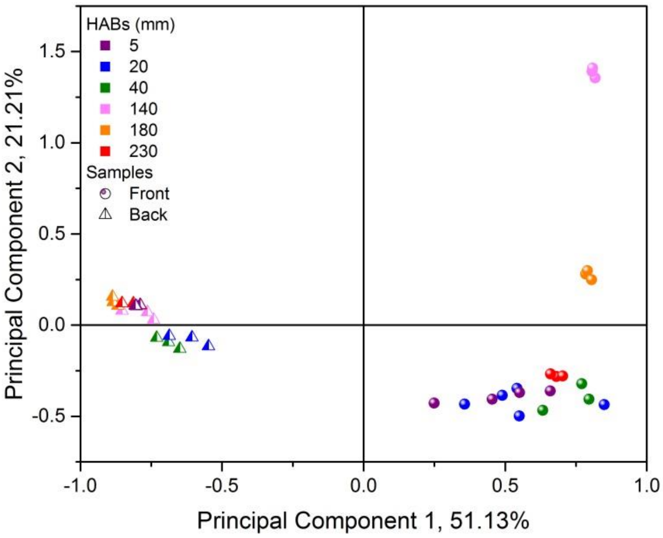

Figure 4.2.26. Score plot of PC1 and PC2 obtained from L2MS mass spectra of the mixture flame front and back samples.

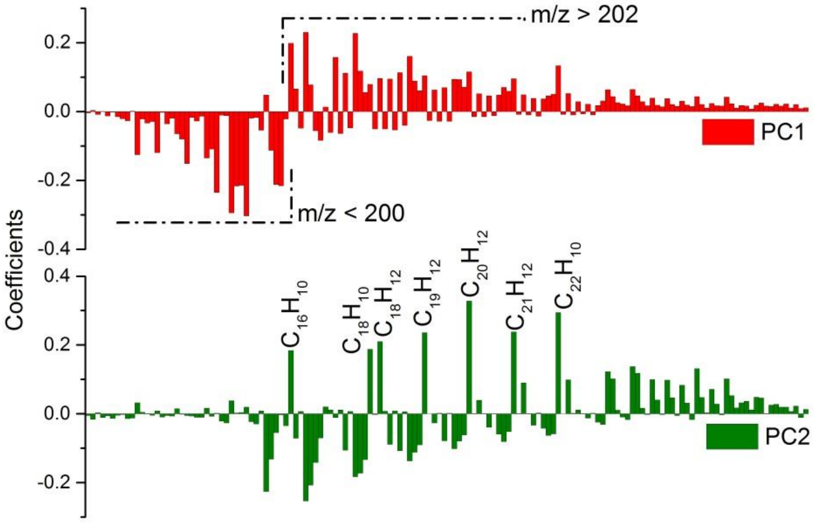

Figure 4.2.27. Loadings corresponding to PC1 and PC2 represented in Figure 4.2.26

PCA is applied to the mixture flame front and back samples with 146 selected peaks. The score plot and the loadings are displayed in Figure 4.2.26 and Figure 4.2.27, respectively. PC1 and PC2 represent 72% of the variance. The first principal component, PC1, is composed of peaks with *m*/*z* ≥ 202 with positive coefficients, and of peaks with *m*/*z* < 202 with negative coefficients. This principal component separates front and back samples due to the nature of the materials collected on the filters. Front samples contain dominantly non-volatile species whereas back samples captured volatile compounds with low masses thanks to the black carbon coating. PC2 represents 21.21% of the variance. The PC2 is composed mainly of pericondensed PAHs from $C_{16}H_{10}^{+}$ to $C_{22}H_{12}^{+}$ with positive coefficients and of alkyl-PAHs with negative coefficients. Front samples at 140 and 180 mm HAB are well separated from the others. This can be explained as at low HABs (5, 20, 40 mm), front samples also collect species from unburned fuels – which contains a lot of alkyl-PAH compounds (the diesel part of the mixture). At 230 mm HAB, there might be some droplets that still survive probably transported at this height by the air shield surrounding the flame, causing the presence of some alkyl-PAHs.

4.2.3.2. SIMS mass spectra of the mixture flame samples

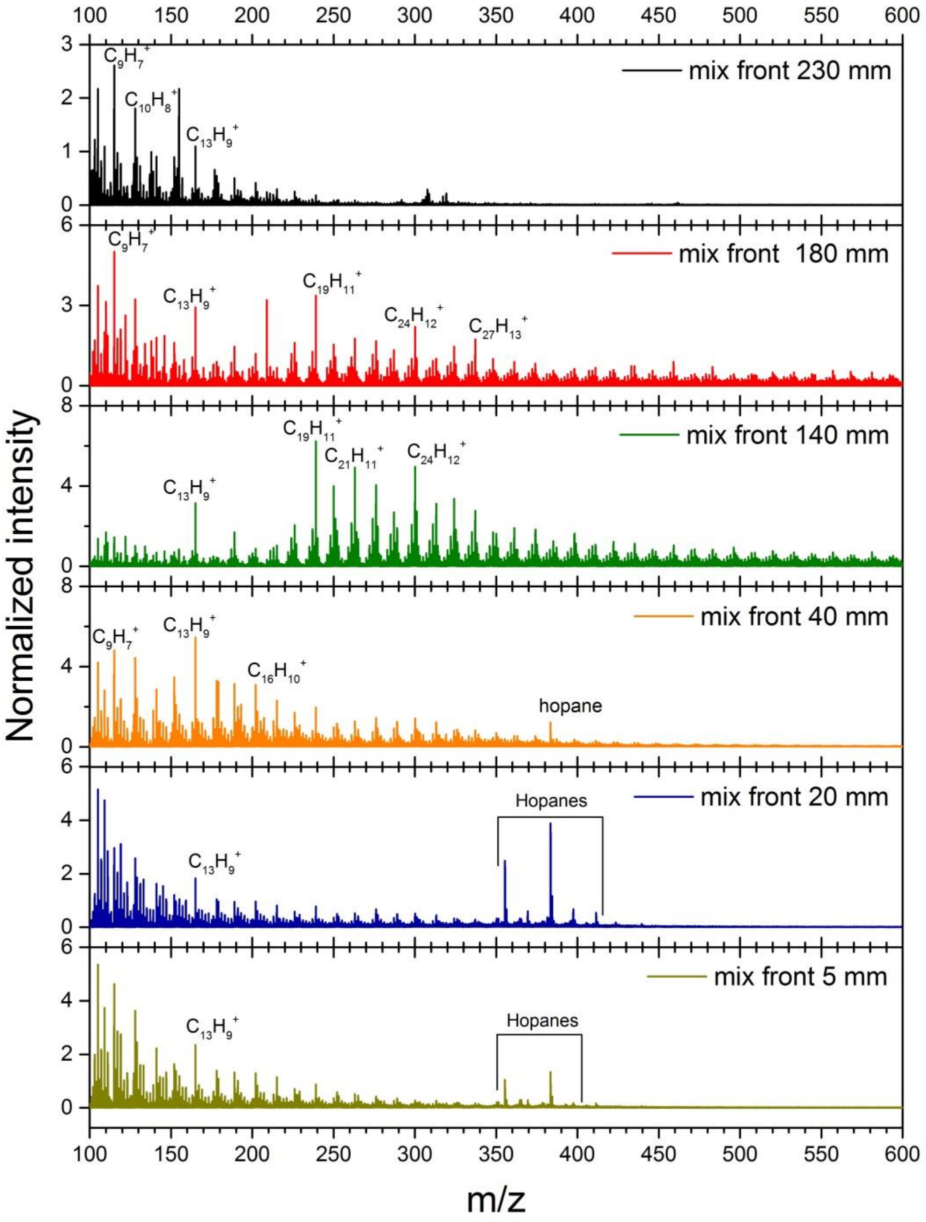

Figure 4.2.28. Positive SIMS spectra of the mixture flame front samples

Mixture flame samples are also mass-analyzed with the ToF-SIMS technique using a Bi_3^+ beam. Both positive and negative polarities of mass spectra are obtained. The positive SIMS spectra of front samples are displayed in Figure 4.2.28. At several low HABs, 5, 20, 40 mm, there is the presence of hopanes - "biological markers" or "chemofossils" presenting in crude oils (Petrov 1987). Since 50%v/v of mixture fuel is diesel, these hopanes compounds are found at low HABs when the fuel is not completely burned yet. At these heights, peaks associated to light PAHs are assigned as $C_9H_7^+$, $C_{13}H_9^+$, $C_{16}H_{10}^+$. Sequence of higher *m/z* peaks associated to PAHs are also present with low signals at these heights. At the height of maximum Vis-LIF signal – 140 mm HAB – the small PAHs reduce their intensities and heavy PAHs (*m/z* ≥ 239) appear more intensely. The most dominant peaks found in the mass spectra at this height are $C_{19}H_{11}^+$, $C_{21}H_{11}^+$, $C_{24}H_{12}^+$. At higher HAB, 180 mm, the presence of high mass PAHs decrease. Lastly, at 230 mm HAB – where LII and LIF signals are all faded out, the high mass PAHs signal disappears.

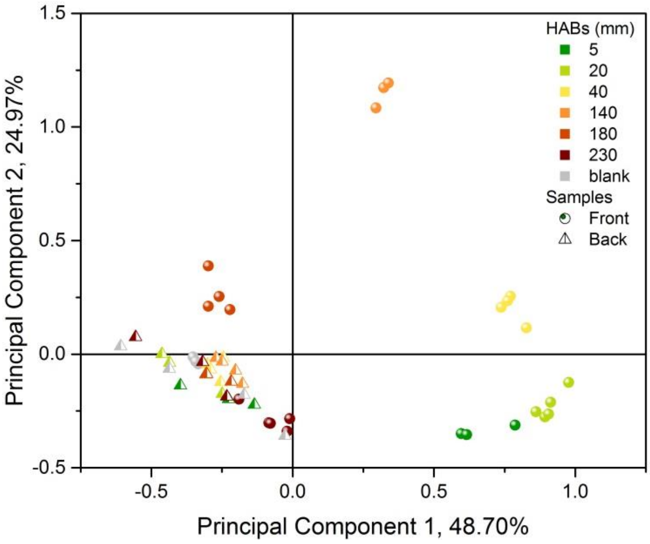

Figure 4.2.29. Score plot of the two first principal components in PCA applied on positive SIMS spectra of the mixture flame front and back samples.

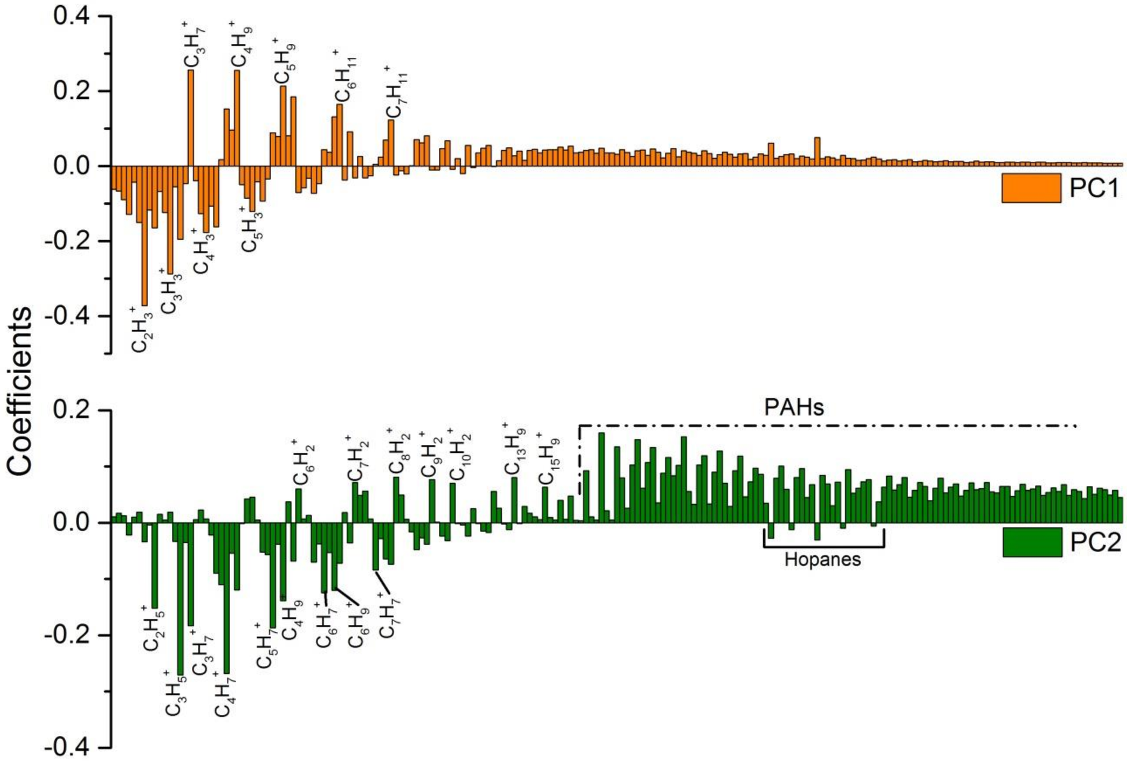

Figure 4.2.30. Loadings corresponding to PC1 and PC2 presented in Figure 4.2.29

PCA analyses on 197 attributed peaks from positive polarity show the separation of front and back samples and heights of sampling. The first two principal components represent 73% of the variance. PC1 shows the noticeable discrimination between samples containing unburned fuel (front samples at 5, 20 and 40 mm HAB) with others. This PC is composed of highly-hydrogenated fragments as $C_3H_7^+$, $C_4H_9^+$, $C_5H_9^+$, $C_6H_{11}^+$, $C_7H_{11}^+$ with positive coefficients, and of low-hydrogenated fragments with negative coefficients. The higher samples are extracted in the flame, the more their position shifts to the negative side of PC1. In other words, the higher samples are collected in the flame, the less unburned species from fuel are present on the filters. All back samples have negative PC1 values. PC2 separates samples with respect to their PAHs content. PC2 consists of low-hydrogenated fragments and PAHs with positive coefficients, while negative coefficients are associated with smaller fragments and hopanes. With the aid of PC2, it can be seen that the front sample at 140 mm HAB contains the highest proportion of PAHs in its mass spectrum, followed by 40 and 180 mm HAB front samples. Other front and back samples show a significant presence of fragments, which dominates the signal of PAHs, in their mass spectra. In other words, back samples and front samples at 5, 20, 230 mm HAB contain less soot precursors than front samples at 40, 140, 180 mm HAB.

Negative SIMS mass spectra of the mixture flame front samples are shown in Figure 4.2.31. Mass spectra are dominated by O^-, OH^-, CH^-, C_2H^-. At 40 and 140 mm HABs, there is a noticeable presence of C_nH^- with $n \geq 4$. To better understand the difference between mass spectra, PCA analyses are applied on 223 attributed peaks of negative mass spectra from mixture flame samples as displayed in Figure 4.2.32 and Figure 4.2.33.

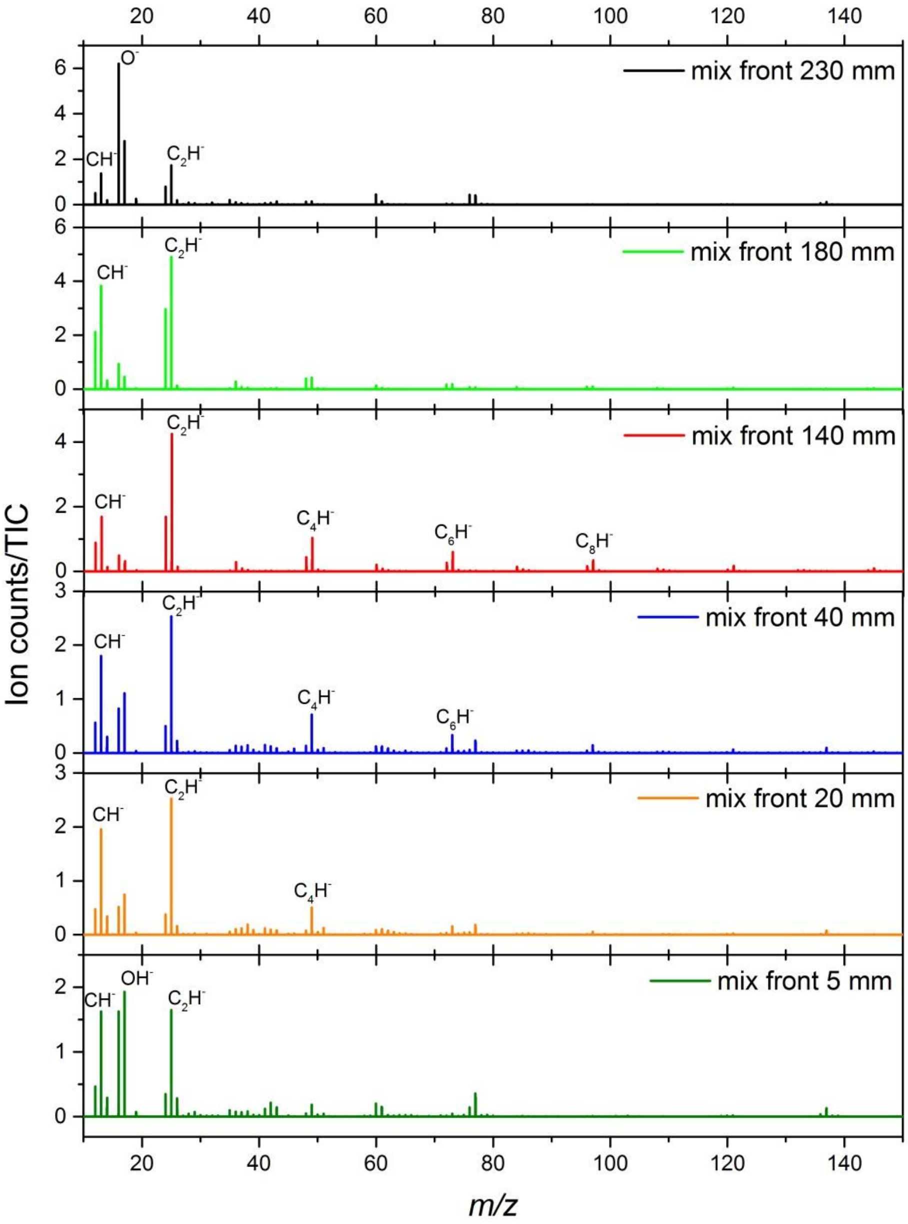

Figure 4.2.31. Negative SIMS mass spectra of the mixture flame front samples

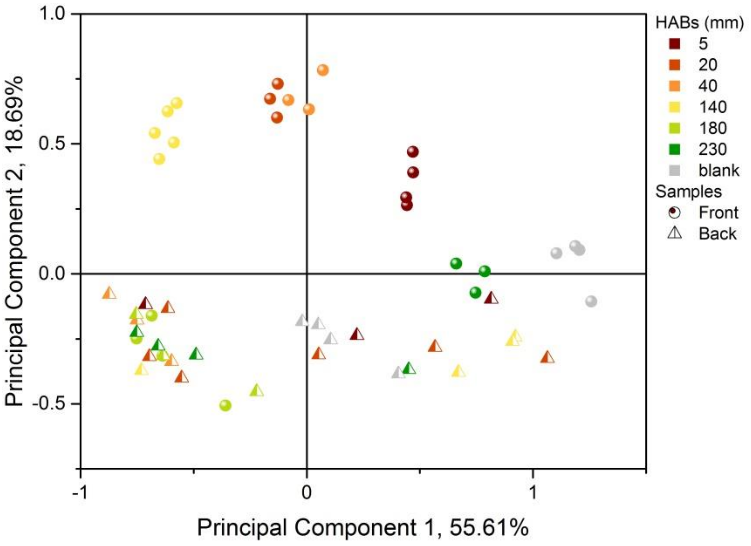

Figure 4.2.32. Score plot of PC1 and PC2 from PCA analysis applied on negative SIMS mass spectra of the mixture flame samples.

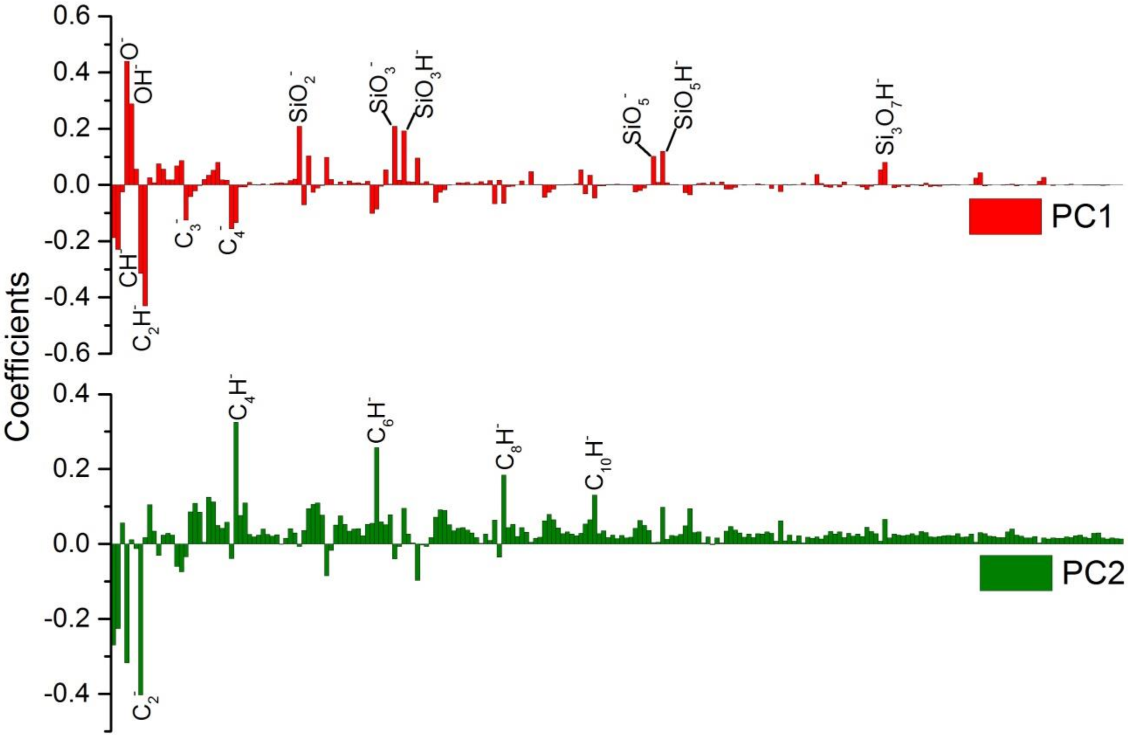

Figure 4.2.33. Loadings corresponding to PC1 and PC2 presented in Figure 4.2.32

PC1 (represents 55.61% of the variance) is composed of peaks associated mostly to the substrate as O^-, OH^-, SiO_2^-, SiO_3^-, etc. with positive coefficients, and others with negative coefficients. Thus the samples with low loadings are located mainly in the right side of the PC1 as blank, front samples at 5 mm and 230 mm and a part of back samples. PC2 shows a significant discrimination between front and back samples. This PC consists of C_nH^- clusters with $n \geq 4$ with positive coefficients, and with C_2^- cluster with negative coefficients. With the presence of black carbon on back samples, all of these samples are located on the negative side of PC2 whereas most of the front samples are located on the other side. There is an exception for the front sample at 180 mm HAB due to the high amount of soot on it. This HAB also corresponds to the maximum signal of LII in the in-situ measurement. In other words, PC2 separates samples in respect of elemental carbon content (black carbon and mature soot in this case) and organic carbon content (PAHs in this case).

4.3. Flame temperature measurement

The temperature is an important intensive parameter to follow or understand the combustion kinetics in the centerline of the flame. To this aim, the temperature at low HABs in the flame is measured using a thermocouple (K-type). However, this type of thermocouple can only be used in non-sooting zones of the flame. In the sooty zone, soot will deposit on the thermocouple, leading to the increase of its emissivity and thus increasing the radiation correction. The temperature measured by the thermocouple must be corrected for radiative losses with the method of (Hindasageri, Vedula, and Prabhu 2013). The temperature corrected for the radiative losses in the three flames is shown in Figure 4.3.1.

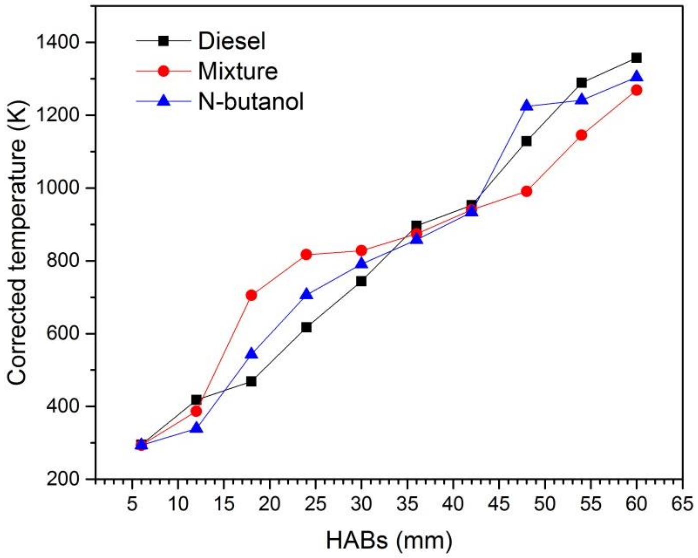

Figure 4.3.1. Temperature measured in the centerline of the three flames with a K-type thermocouple in non-sooting zone

The temperature measured is similar in the three flames in the range 5 mm to 60 mm HAB. Above this height, the measure range of the K-type thermocouple and the presence of soot particles limit the measurement. The temperature increases gradually from 300K to 1300K in this non-sooting zone for all flames. This zone also covers the first peak of the Vis-LIF profile obtained in diesel and mixture flames. In the study of (Pickett and Siebers 2003), they mentioned that the formation of soot could not occur in locations where the temperature is less than 1400K. This can explain why soot formation did not start with the first peak of Vis-LIF in the diesel and mixture flames. Thus the formation of soot particles in these flames is delayed until the temperature reaches higher value.

4.4. Discussion on the in-situ and ex-situ results

In-situ laser diagnostics as LII and LIF have been used for a long time to study the formation of soot and their precursors in flames (Bejaoui et al. 2015; Michelsen et al. 2007; Salma Bejaoui et al. 2014; Smallwood 2009; Axelsson, Collin, and Bengtsson 2001; Lemaire et al. 2007). Whereas ex-situ techniques as L2MS and ToF-SIMS have been used to investigate the chemical composition of combustion products and soot sample surface (Mihesan et al. 2006; Mihesan 2007; Faccinetto 2009; Faccinetto et al. 2011; Faccinetto et al. 2015; Irimiea 2017; Irimiea et al. 2019). In this subchapter, we propose a cross-analysis of the results obtained with these different techniques. One of the aims of this multiple-technique approach is to better delineate the chemical compounds responsible for the LII and LIF signals at different excitation wavelengths and to get a more precise insight into the chemical processes involved during soot inception.

4.4.1. Comparison between ex-situ L2MS results and in-situ LIF results

The PAH peak areas from L2MS mass spectra front sample of the diesel, the *n*-butanol and the mixture flames are integrated over the entire spectra and the total PAH signal is displayed in Figure 4.4.1. The L2MS is not a (directly) quantitative technique. However, the overall signal can give a semi-quantitative information about the PAH content of each sample. The signal is averaged over three mass spectra corresponding to three different areas on each sample and the error bars represent the standard deviation between them. Vis-LIF signal of the three flames is also plotted for comparison in the figure.

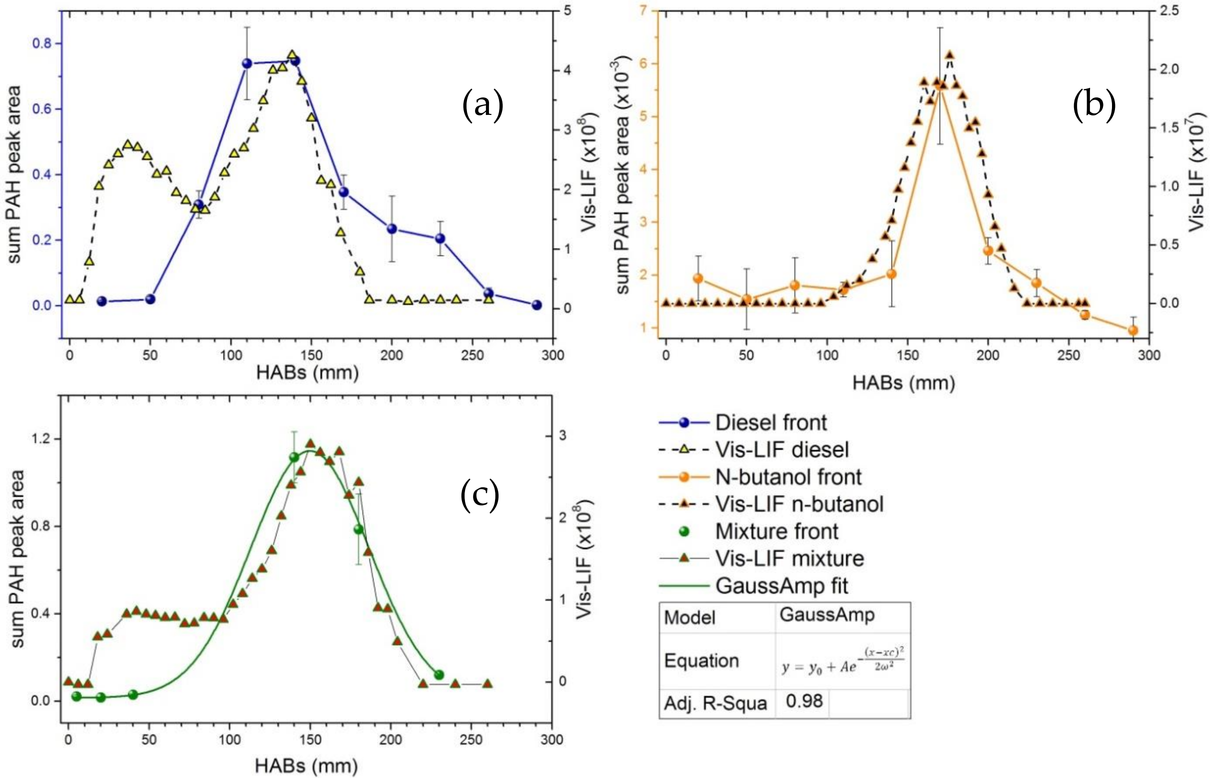

Figure 4.4.1. Comparison between the total PAH peak area obtained from L2MS mass spectra and the Vis-LIF signal of the three flames: (a) diesel, (b) *n*-butanol and (c) mixture. GaussAmp fit is applied for the mixture flame since there are only five HABs sampled for L2MS analysis.

We observe in the figure that there is good correlation between the total PAH signal detected by ex-situ L2MS and in-situ LIF by visible excitation. The fluorescence emission signal covers well the zone where the PAH content is the most important in the case of *n*-butanol. For the diesel and the mixture flames, the total PAH signal shows good agreement with the second peaks of Vis-LIF. As mentioned in subchapter 4.1, the first peak of the Vis-LIF profile from aromatic-content fuels might correspond to the petrogenic fluorescent species, which are formed quickly at the beginning of the flame. The second peak of the Vis-LIF profiles is attributed to the pyrogenic fluorescent species, which are formed later in the flame. Only *n*-butanol flame does not have bimodal Vis-LIF profile since there is no aromatic content as in the fossil fuel.

However, the results from L2MS do not show the correlation with the first peak of Vis-LIF attributed to petrogenic fluorescent species. This can be explained by the lack of carbonaceous matrix, which promotes more efficiently the desorption of adsorbed species thanks to the absorption of the laser beam and the induced thermal effect. Since L2MS uses 532 nm wavelength as laser desorption and the laser fluence is adjusted for a soft thermal desorption, it needs the presence of carbonaceous matrix to absorb the laser energy and transfer it into thermal energy, promoting the desorption of adsorbed species. At the region where petrogenic fluorescent species are present, soot particles have not been formed yet due to the low temperature (as presented in subchapter 4.3), thus L2MS is less sensitive.

4.4.2. Comparison between ex-situ SIMS results and in-situ LIF/LII results

4.4.2.1. Positive polarity of SIMS

A SIMS positive mass spectrum of soot sample usually contains a “forest” of hundreds to thousands of mass peaks including fragments and PAHs compounds as well as additional features due to the contamination or associated with the substrate. Thus it is challenging to extract the useful information from this “forest” of peaks. In this study, hierarchical clustering analysis (HCA) is applied to all peaks corresponding to hydrocarbon fragments and compounds in SIMS positive data of the three flames. The HCA is done based on Pearson correlation by using the Group Average method and the result is shown in Figure 4.4.2.

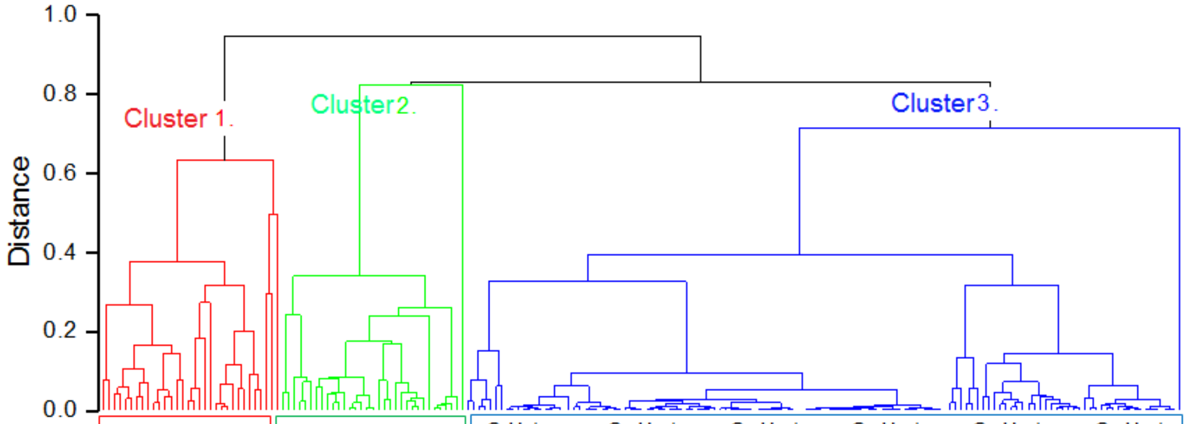

C_2H^+
C_4H^+
$C_2H_2^+$
C_3H^+
$C_3H_2^+$
$C_4H_2^+$
$C_2H_3^+$
$C_2H_4^+$
$C_3H_3^+$
$C_4H_3^+$
$C_4H_4^+$
$C_5H_3^+$
$C_5H_4^+$
$C_5H_2^+$
$C_6H_2^+$
$C_2H_5^+$
$C_3H_5^+$
$C_4H_5^+$
$C_3H_6^+$
$C_3H_4^+$
$C_5H_5^+$
$C_6H_5^+$
$C_6H_6^+$
$C_5H_6^+$
$C_7H_7^+$
$C_8H_7^+$
$C_6H_4^+$
$C_7H_5^+$
$C_8H_6^+$
C_5H^+
$C_6H_3^+$
C_7H^+

$C_3H_7^+$
$C_4H_7^+$
$C_4H_6^+$
$C_5H_7^+$
$C_6H_7^+$
$C_6H_8^+$
$C_4H_8^+$
$C_4H_9^+$
$C_5H_8^+$
$C_5H_9^+$
$C_6H_9^+$
$C_7H_9^+$
$C_5H_{11}^+$
$C_6H_{11}^+$
$C_6H_{13}^+$
$C_7H_{11}^+$
$C_8H_{13}^+$
$C_7H_8^+$
$C_8H_9^+$
$C_9H_9^+$
$C_8H_{11}^+$
$C_9H_{11}^+$
$C_{10}H_{13}^+$
$C_{11}H_{13}^+$
$C_{12}H_{15}^+$
$C_{11}H_{11}^+$
$C_5H_{10}^+$
$C_{26}H_{43}^+$
$C_{27}H_{45}^+$
$C_{28}H_{47}^+$
$C_{29}H_{49}^+$
$C_{30}H_{51}^+$
$C_6H_{14}^+$

$C_7H_2^+$
$C_8H_2^+$
$C_9H_2^+$
$C_{10}H_2^+$
$C_{12}H_2^+$
$C_7H_3^+$
$C_8H_3^+$
$C_{19}H_{11}^+$
$C_{21}H_{11}^+$
$C_{22}H_{12}^+$
$C_{23}H_{11}^+$
$C_{25}H_{11}^+$
$C_{24}H_{12}^+$
$C_{26}H_{12}^+$
$C_{21}H_9^+$
$C_{22}H_{10}^+$
$C_{23}H_9^+$
$C_{24}H_{10}^+$
$C_{20}H_{10}^+$
$C_{25}H_{13}^+$
$C_{27}H_{13}^+$
$C_{28}H_{14}^+$
$C_{31}H_{15}^+$
$C_{32}H_{16}^+$
$C_{34}H_{16}^+$
$C_{37}H_{17}^+$
$C_{35}H_{17}^+$
$C_{36}H_{18}^+$
$C_{26}H_{10}^+$
$C_{27}H_{11}^+$
$C_{28}H_{10}^+$
$C_{29}H_{11}^+$
$C_{28}H_{12}^+$
$C_{29}H_{13}^+$
$C_{30}H_{12}^+$
$C_{31}H_{13}^+$
$C_{30}H_{14}^+$
$C_{33}H_{15}^+$
$C_{36}H_{16}^+$
$C_{31}H_{11}^+$
$C_{33}H_{11}^+$
$C_{32}H_{12}^+$
$C_{33}H_{13}^+$
$C_{32}H_{14}^+$
$C_{38}H_{16}^+$
$C_{38}H_{18}^+$
$C_{41}H_{19}^+$
$C_{39}H_{17}^+$
$C_{40}H_{18}^+$
$C_{46}H_{20}^+$
$C_{43}H_{19}^+$
$C_{45}H_{19}^+$
$C_{41}H_{17}^+$
$C_{44}H_{18}^+$
$C_{50}H_{20}^+$
$C_{42}H_{18}^+$
$C_{47}H_{19}^+$
$C_{46}H_{18}^+$
$C_{49}H_{19}^+$
$C_{34}H_{12}^+$
$C_{36}H_{12}^+$
$C_{37}H_{13}^+$
$C_{35}H_{13}^+$
$C_{38}H_{14}^+$
$C_{39}H_{13}^+$
$C_{40}H_{14}^+$
$C_{42}H_{14}^+$
$C_{43}H_{15}^+$
$C_{41}H_{13}^+$
$C_{41}H_{15}^+$
$C_{43}H_{17}^+$
$C_{34}H_{14}^+$
$C_{36}H_{14}^+$
$C_{35}H_{15}^+$
$C_{37}H_{15}^+$
$C_{39}H_{15}^+$
$C_{42}H_{16}^+$
$C_{40}H_{16}^+$
$C_{44}H_{14}^+$
$C_{46}H_{16}^+$
$C_{48}H_{18}^+$
$C_{44}H_{16}^+$
$C_{45}H_{17}^+$
$C_{47}H_{17}^+$
$C_{49}H_{17}^+$
$C_{50}H_{18}^+$
$C_9H_7^+$
$C_{10}H_8^+$
$C_{11}H_9^+$
$C_{11}H_7^+$
$C_{12}H_8^+$
$C_{14}H_8^+$
$C_{12}H_{11}^+$
$C_{13}H_{13}^+$
$C_{13}H_9^+$
$C_{15}H_9^+$
$C_{16}H_{10}^+$
$C_{17}H_{11}^+$
$C_{19}H_{13}^+$
$C_{18}H_{13}^+$
$C_{14}H_{10}^+$
$C_{15}H_{11}^+$
$C_{14}H_{11}^+$
$C_{14}H_{13}^+$
$C_{15}H_{13}^+$
$C_{16}H_{13}^+$
$C_{18}H_{15}^+$
$C_{17}H_{15}^+$
$C_{17}H_{13}^+$
$C_{19}H_{15}^+$
$C_{18}H_{10}^+$
$C_{20}H_{12}^+$
$C_{21}H_{13}^+$
$C_{20}H_{15}^+$
$C_{24}H_{17}^+$
$C_{26}H_{17}^+$
$C_{22}H_{15}^+$
$C_{25}H_{15}^+$
$C_{27}H_{15}^+$
$C_{28}H_{17}^+$
$C_{31}H_{17}^+$
$C_{23}H_{13}^+$
$C_{24}H_{14}^+$
$C_{26}H_{14}^+$
$C_{29}H_{15}^+$
$C_{30}H_{16}^+$
$C_{33}H_{17}^+$
$C_{11}H^+$

Figure 4.4.2. Clustering dendrogram obtained for 193 peaks assigned for hydrocarbon fragments and compounds from SIMS positive spectra of diesel, *n*-butanol and mixture flame samples. Three clusters are divided within 193 peaks. The peak lists of three clusters are presented in three tables in the figure.

As it can be seen from the figure, HCA divides all the hydrocarbon peaks into three clusters. Cluster 1 includes small hydrogen fragments. Cluster 2 includes hydrogen-rich fragments and 5 peaks of hopane compounds. Cluster 3 includes hydrogen-poor fragments and most of the large aromatic compounds. All peaks among cluster 3 are integrated and then normalized to the sum of ion counts obtained for the three clusters (partial ion counts – PIC) detected in SIMS spectra. The result is presented in Figure 4.4.3. The Vis-LIF profiles of the three flames are also shown in the figure.

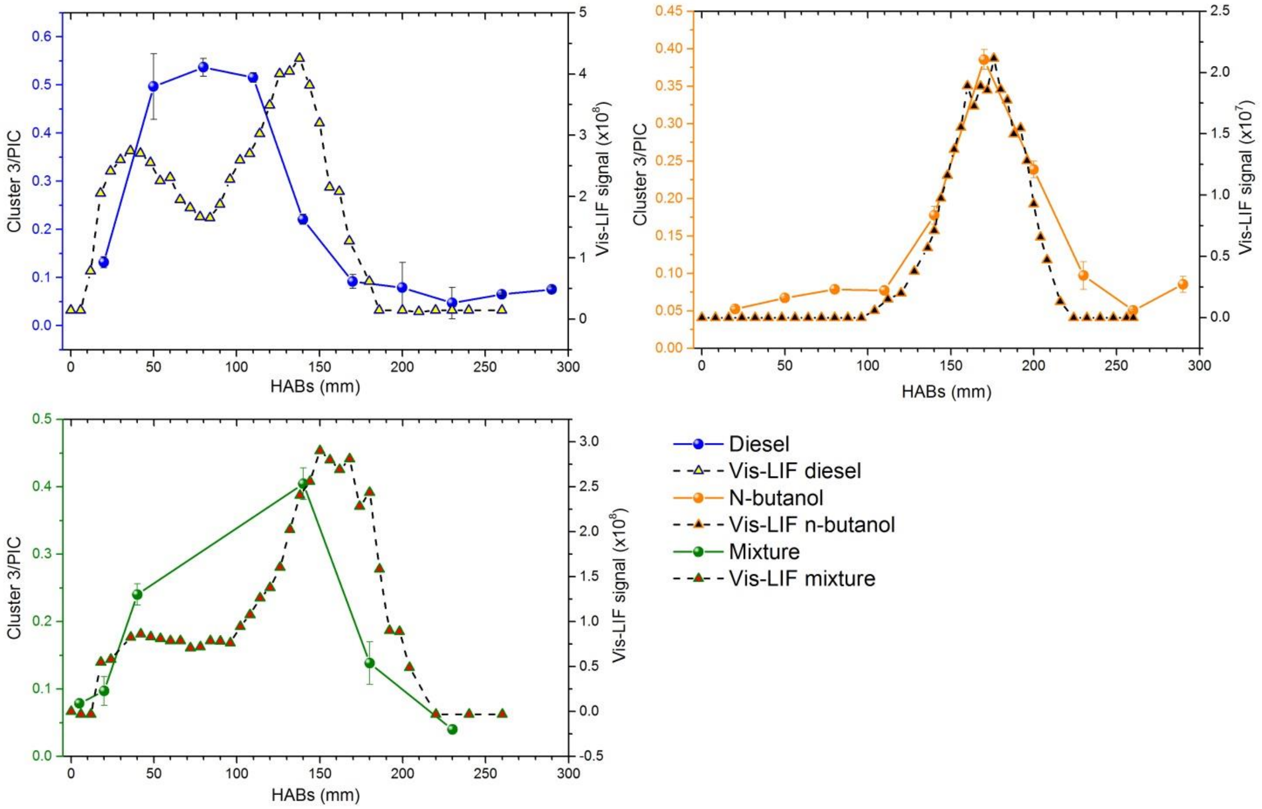

Figure 4.4.3. Comparison between the sum of Cluster 3 peak areas normalized to PIC obtained from SIMS positive mass spectra and Vis-LIF signal of the three flames: diesel, *n*-butanol and mixture

In the case of *n*-butanol, similarly to what was observed for the total PAH content in L2MS spectra, the sum of Cluster 3/PIC obtained from SIMS positive spectra shows strong correlation with the Vis-LIF signal. However, in the cases of the diesel and the mixture flames, the sum of Cluster 3/PIC covers both first and second peaks of Vis-LIF profile, unlike the result achieved with L2MS. This might be due to the high energy of primary ion beam in ToF-SIMS technique. The strong Bi_3^+ ion beam at 25 keV is able to cause strong collision with the molecules on the solid surface of samples and eject them more efficiently than with a visible laser beam when soot particles are still not present or in a very low amount. Thus, SIMS analysis technique is able to detect soot precursors collected on the samples whether carbonaceous matrix is present or not.

4.4.2.2. *Negative polarity of SIMS*

For negative polarity of SIMS mass spectra, there is presence of C_n^- and $\mathrm{C}_n\mathrm{H}^-$ clusters ($n = 1 - 16$). In some studies, C_n^- and $\mathrm{C}_n\mathrm{H}^-$ are used as markers for the elemental carbon present in samples. (Pagels et al. 2013) claimed that the sum of $\mathrm{C}_2\mathrm{H}^-$, $\mathrm{C}_3\mathrm{H}^-$ and $\mathrm{C}_4\mathrm{H}^-$ is a marker for EC, whereas (Kirchner et al. 2003) supposed that C_5^-, C_6^- and C_7^- are associated to the fragment of soot core. Ewinger, Goschnick, and Ache (1991) and Le Roy et al. (2015) and Ngo et al. (2019) had the same ideas when proposing $\mathrm{C}_n\mathrm{H}^-$ fragments are related to organic compounds. C_n^- clusters with n = 2 – 4 are found as markers for EC (Popovicheva et al. 2017; Ngo et al. 2019), whereas C_n^- clusters with $n \geq 5$ are markers for organic carbon. The summary of studies on this issue is shown in Table 4.4.1.

Studies	
Pagels et al. 2013	C_2H^-, C_3H^-, C_4H^-: EC markers
Kirchner et al. 2003	C_5^-, C_6^-, C_7^-: soot core fragments
Ewinger, Goschnick, and Ache 1991	C_nH^-: organic compounds
Le Roy et al. 2015	C_nH^-: related to PAHs
Popovicheva et al. 2017	C_2^-, C_3^-, C_4^-: EC markers
Ngo et al. 2019	C_1^-, C_2^-, C_3^-, C_4^- : EC markers C_n^- ($n \geq 5$), C_nH^- : OC markers

Table 4.4.1. Literature on C_n^- and C_nH^- as indicators for EC and OC

A correlation coefficient analysis is applied for carbon, hydrogenated carbon clusters from SIMS mass spectra as well as LII/LIF signal obtained in diesel flame at all HABs. The result is shown in Figure 4.4.4 in the form of a heat map.

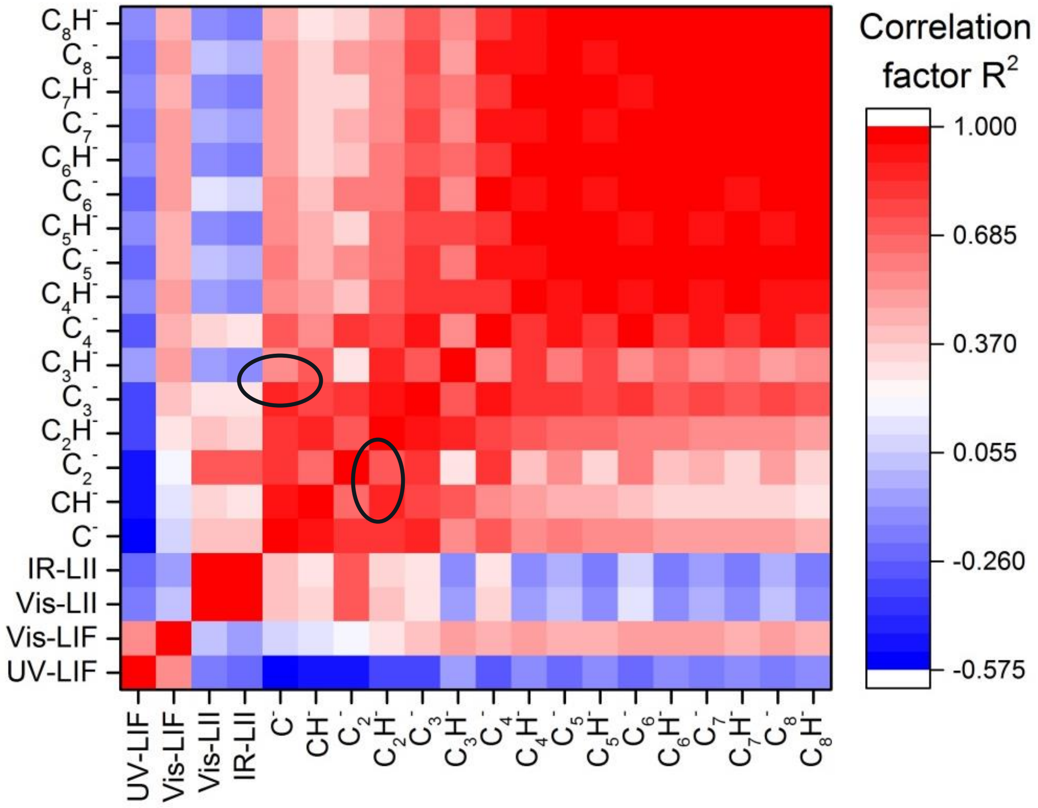

Figure 4.4.4. Correlation coefficients between in-situ LII/LIF signal recorded for the diesel flame and the C_n^-, C_nH^- ions defected by SIMS from the diesel flame front samples

As pointed out in the figure, there is a good correlation ($R^2 \approx 0.7$) between the LII signals (IR and Vis) and the C_2^- cluster signal, and to a lesser extent with C^-, C_3^- and C_4^-. The figure evidences also a strong correlation between all the C_n^- and C_nH^- (with n in the range of 4 – 8). These links outlines a common origin of these latter fragments. These peaks are present with significant ion counts in the mass spectra of diesel and mixture flame samples at certain HABs as shown in Figure 4.2.8 and Figure 4.2.31.

From the Figure 4.4.4, a question arises "is C_2^- in SIMS mass spectra an indicator of the same component as the LII signal obtained in the flame?". The evolution of the C_2^- peak normalized to total ion count in SIMS mass spectra of diesel and mixture flames is plotted in Figure 4.4.5, with the LII signal obtained with IR excitation in same flames.

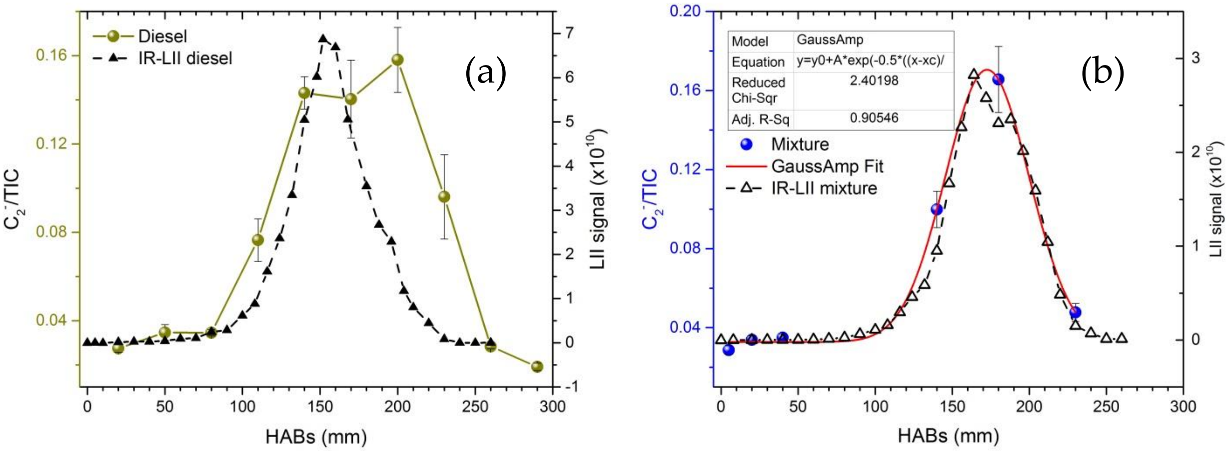

Figure 4.4.5. Evolution of C_2^- peak area normalized to TIC from SIMS negative mass spectra, in comparison with IR-LII of (a) diesel and (b) mixture flames

As it can be seen, the C_2^- signal shows a good correlation with the LII signal obtained in diesel and mixture flames. Although the match is not perfect for the diesel flame, the link found between LII and the C_2^- signal in SIMS should trigger further studies on this topic.

However, the variation of C_2^- signal in *n*-butanol flame does not give any good correlation with the LII signal of the flame due to a negligible LII signal in this flame and is not shown here. Correlation coefficient analysis is again applied on C_n^- and C_nH^- clusters for *n*-butanol SIMS mass spectra, as well as the profile of LII and LIF of this flame. The heat map of correlation factors is shown in Figure 4.4.6.

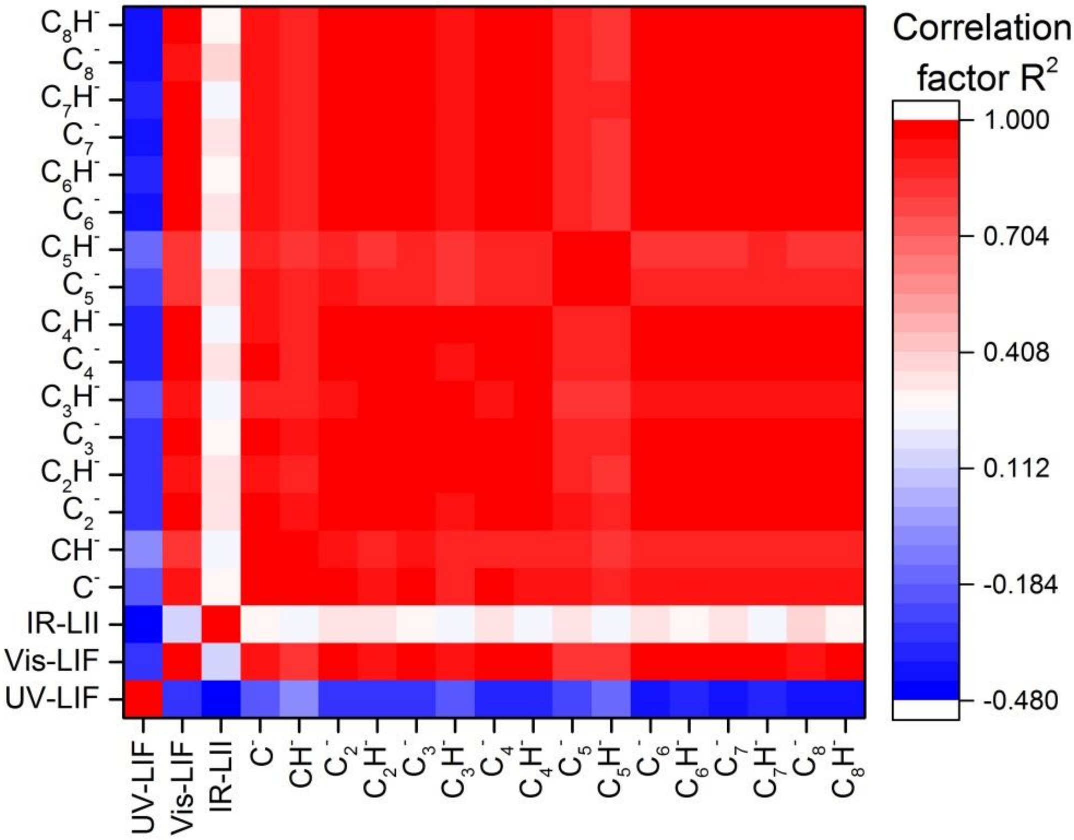

Figure 4.4.6. Correlation coefficients between in-situ **LII/LIF signal and C_n^-, C_nH^- obtained in negative polarity of SIMS mass spectra from *n*-butanol front samples**

Unlike the case of diesel and mixture flames, for *n*-butanol flame, there is no correlation between IR-LII signal and any peaks of negative SIMS mass spectra. All C_n^- and C_nH^- clusters have good correlation with the Vis-LIF signal. This can be explained with the very low amount of soot formed in *n*-butanol flame. The small amount of nascent soot collected on the filters is not sufficient to dominate carbon clusters derived from soot precursors.

With good correlation between C_4H^-, C_6H^- and C_8H^- in negative mass spectra, the sum of these ion peaks after normalization to TIC from SIMS mass spectra of the three flames are tracked and presented in Figure 4.4.7. There is also good correlation between the carbon clusters from C_4^- to C_8^- and the hydrogenated ones from C_4H^- to C_8H^-also but the series of C_4H^-, C_6H^- and C_8H^- are chosen as these peaks show significant influence to PCA results shown in Figure 4.2.13, Figure 4.2.22 and Figure 4.2.33.

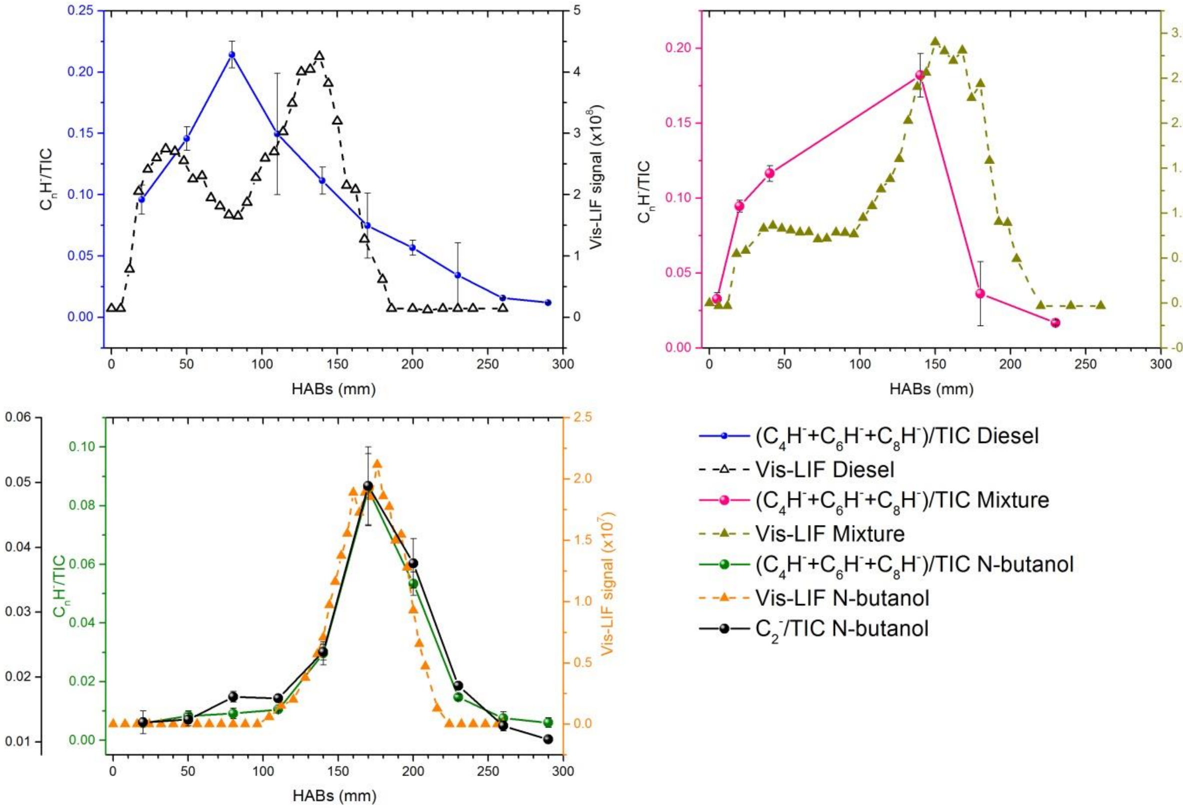

Figure 4.4.7. Evolution of the sum of C_4H^-, C_6H^- and C_8H^- normalized to TIC from SIMS negative mass spectra, in comparison with Vis-LIF signal from the three flames. The evolution of C_2^-/TIC in SIMS mass spectra of *n*-butanol is also presented.

Similar to the results achieved in SIMS positive mass spectra, the sum of normalized C_4H^-, C_6H^- and C_8H^- clusters covers both first and second peaks of Vis-LIF profiles of diesel and mixture flames. As presented, the high energy of primary ion beam in SIMS could be the main cause. Evolution of C_2^- cluster in *n*-butanol SIMS mass spectra is also presented in the figure. Strong agreement is shown between C_2^-, C_nH^- and Vis-LIF signal in this flame, which confirms the hypothesis proposed earlier that in *n*-butanol SIMS spectra C_2^- is mainly derived from soot precursors rather than nascent soot particles.

Briefly, this subchapter compares the results obtained from in-situ LIF/LII and ex-situ L2MS/SIMS. The results show that L2MS is a powerful technique to detect soot precursors, and it shows good coherence with the presence of pyrogenic fluorescent species – which are detected with Vis-LIF technique in the flame. However, L2MS with desorption at 532 nm is less effective in the flame zone where petrogenic compounds are observed because of the lack of carbonaceous matrix on the samples, reducing the efficiency of laser-induced thermal desorption in the analysis process. On the other hand, in the present case, the ex-situ SIMS technique is less impacted by the absence of carbon matrix, as an energetic ion beam is used. The total PAH content normalized to TIC/PIC and the sum of C_nH^- clusters (with n in the range of 4-8) show good correlations together and with the Vis-LIF signal and cover both petrogenic and pyrogenic peaks in LIF bimodal profile. The C_2^- cluster in SIMS spectra can be used as a soot particle carbon matrix (EC) indicator as its evolution in diesel and mixture flame fits well with the LII profile. However, care must be paid when using C_2^- since in the case of *n*-butanol flame – which produces very little amount of nascent soot - C_2^- is derived mostly from the soot precursors. Thus, it is necessary to exploit the correlation in the "forest" of peaks for data mining and be flexible in different cases.

4.4.3. Discussion and proposition on the species detected with in-situ and ex-situ techniques in this study

With the results obtained from in-situ LII/LIF and ex-situ L2MS/SIMS with the diesel flame, we observe that there are at least five different classes of species present. We presume them as class A, class B, class C, class D and soot particles which corresponds to the different signals detected with different excitation wavelengths. The four classes are defined as below according to the UV- and Vis-LIF spectra obtained in the diesel flame.

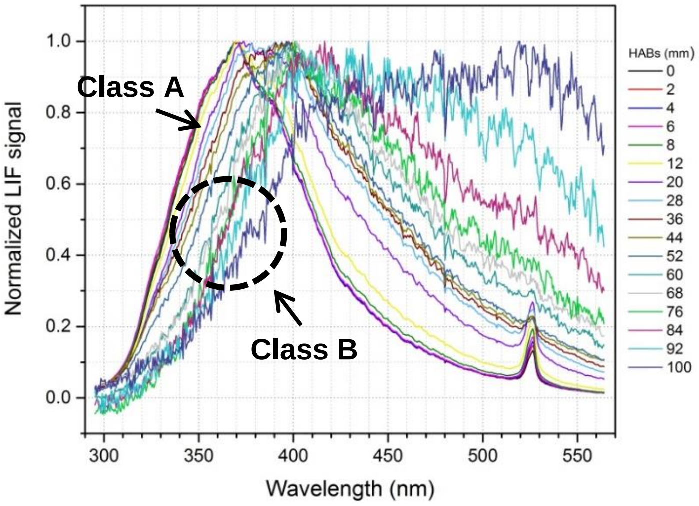

Figure 4.4.8. Class A and B species defined according to the normalized UV-LIF spectra obtained at the centerline of the diesel flame

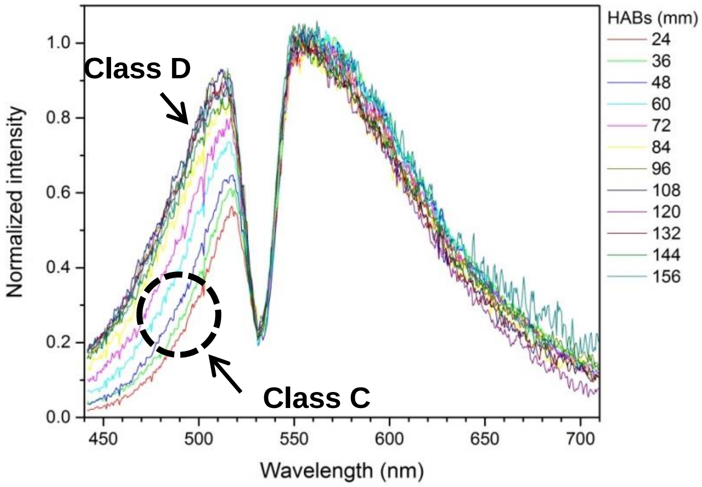

Figure 4.4.9. Class C and D species defined according to the normalized Vis-LIF spectra obtained at the centerline of the diesel flame

The definition of the four classes of species are presented in Table 4.4.2

Class	Characteristics
A	Species which are present in the fuel and fluorescent with 266 nm excitation. Their LIF spectra are similar to the pure fuel spectrum.
B	Pyrogenic species that are formed from class A and fluorescent with 266 nm excitation with an evolution observed in their UV-LIF spectra.
C	Pyrogenic species that correspond to the first peak of Vis-LIF profile with an evolution observed in their Vis-LIF spectra.
D	Pyrogenic species that correspond to the second peak of Vis-LIF profile with identical form of Vis-LIF spectra
Soot	Nano particles which are detected by the LII measurement

Table 4.4.2. Characteristics of four classes of species detected in the diesel flame

These species coexist along the height of the flame as illustrated in Figure 4.4.10. The figure is derived from the variation of the LII and LIF signals in the centerline of the diesel flame.

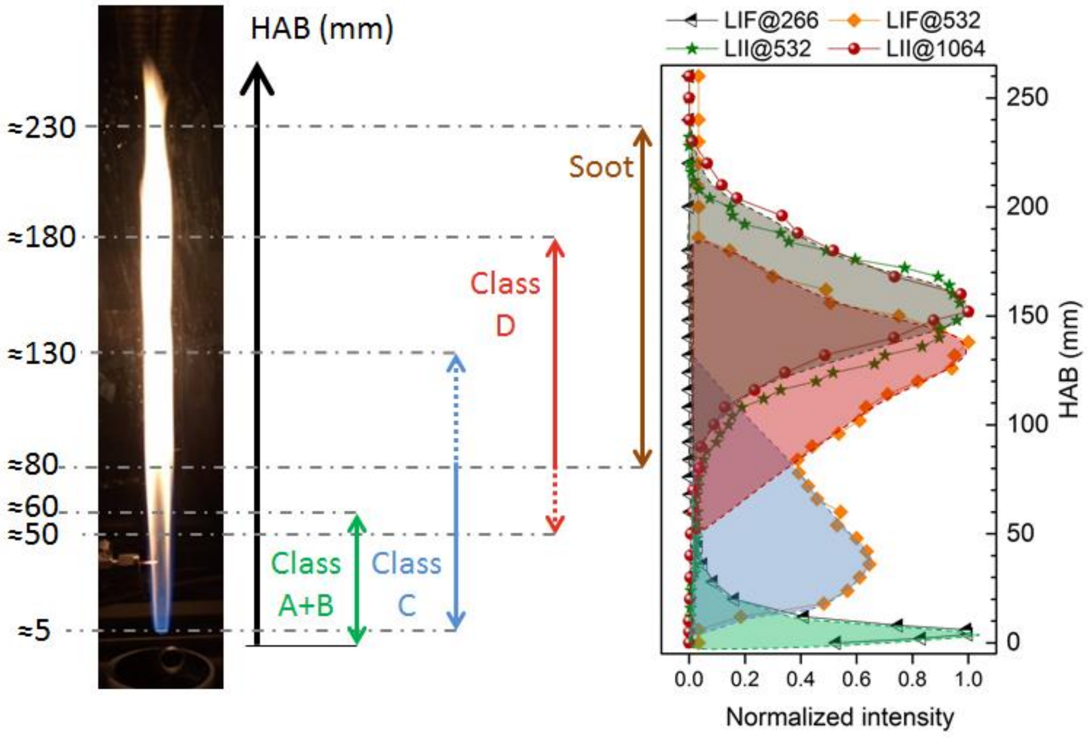

Figure 4.4.10. Positions of the five classes detected in the diesel flame. The red and blue dot lines are presumed and extended from the Vis-LIF profile.

The decrease of UV-LIF signal with HAB in the diesel is contributed from the competition of two main processes: (i) the consumption of species existing in fuel – class A and (ii) the production of pyrogenic species – class B. The presence of class A is confirmed by the identical LIF spectra of several HABs with the diesel droplets at 0 mm HAB as shown in Figure 4.4.8. The change of the UV-LIF spectral shape at higher HABs shows the evidence of the class B formation.

Class C and D are named for the species contributing to the first and second peak of the Vis-LIF profile obtained in the diesel flame, respectively. The difference between these species can be noticed from the normalized Vis-LIF spectra shown in Figure 4.4.9. These species are fluorescent with 532 nm excitation wavelength. Regarding the recent study of (Mercier et al. 2019), no mono-PAH is able to fluoresce at this wavelength. They proposed "dimers of moderated sized PAHs" being responsible for the fluorescence signal obtained with this visible excitation. However, with L2MS and SIMS technique, we could not detect these species, which might be destroyed due to the laser desorption (L2MS) or the primary ion beam (SIMS).

It is possible that both class C and D species are precursors of soot since the soot starts being formed in the zone with their coexistence. However, the class-D species likely cohabite with the soot particles more than the class C as shown in Figure 4.4.10. Additionally, the sum of PAH content detected in the L2MS fits well with the position of this class D (in Figure 4.4.3).

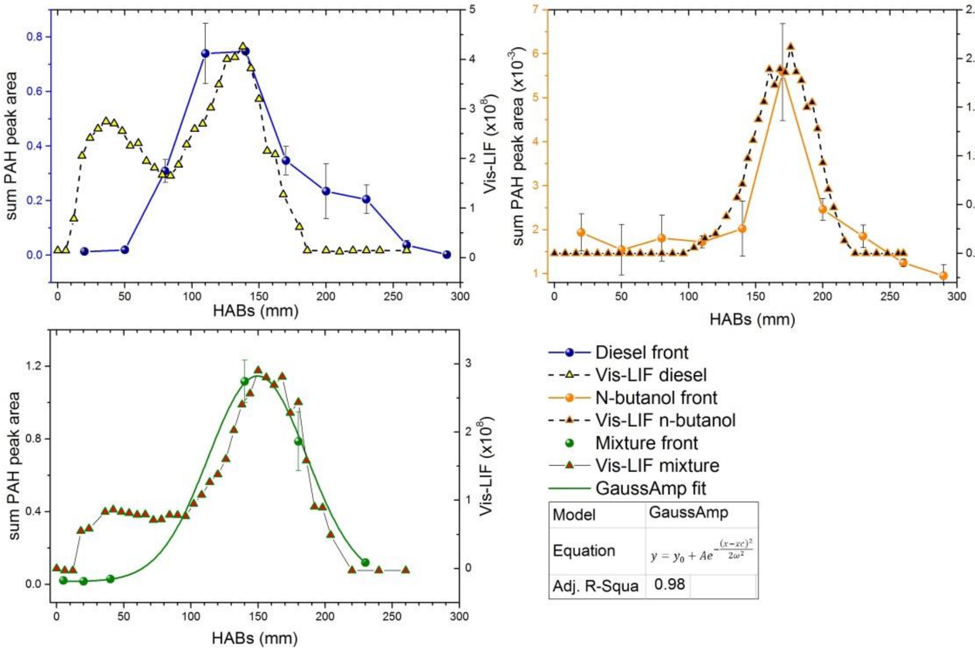

Table 4.4.3. Comparison between the total PAH peak area obtained from L2MS mass spectra and the Vis-LIF signal of the three flames: (a) diesel, (b) *n*-butanol and (c) mixture. GaussAmp fit is applied for the mixture flame since there are only five HABs sampled for L2MS analysis.

This leads to few possibilities of the class D content as following:

(i) Coating of the soot particles. The second-peak Vis-LIF signal observed in the diesel flame might come from the coating of the soot particles. In the study of (Ngo et al. 2019), they were able to see the fluorescence signal coming from the organic coating of soot particles collected from the CAST device with the continuous laser irradiance of 5.4 kW/cm^2 in the Raman measurement. This irradiance is lower to the one we used for the Vis-LIF measurement in the diesel flame (laser irradiance of 1 MW/cm^2

corresponding to the laser fluence of 6 mJ/cm^2 with 6ns FWHM). Thus during the LIF measurement, the coating can be desorbed and detected.

(ii) Class D might contain gas phase complexes which coexist around the soot particles. These complexes could include:
  a. Dimers of aromatic compounds formed by van der Waals forces (Giordana, Maranzana, and Tonachini 2011; Sabbah et al. 2010; Chakarova and Schröder 2005)
  b. Aliphatically bridged PAHs (Adamson et al. 2018)
  c. PAH complexes formed by covalent σ bound created between two carbon atoms of two aromatic compounds by covering two electrons available from π molecular orbitals.

Nonetheless, to answer all questions posed above, it is necessary to carry out further works. Within the results we found in this work, we propose a pathway of soot formation including the four classes of species presented above as below:

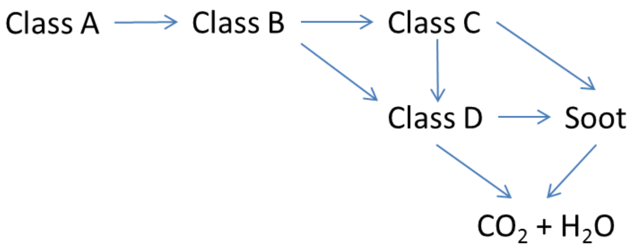

Figure 4.4.11. Proposing kinetic pathway of the soot formation in the diesel flame

In the proposing pathway, the fuel (class A) is consumed to formed bigger species (class B). The reduction of class A and production of class B both associate to UV-LIF signal. The class B forms the class C and the class D in parallel. These species fluoresce with the visible excitation, leading to the appearance of the first and second peak in Vis-LIF profile. The class C is responsible to the formation of the class D and soot particles in the flame, whereas these particles are partly produced by the class D species. Both of them (class D and soot) go further in the combustion and get oxidized. However, the class D is oxidized faster and disappeared before the disappearance of LII signal.

The proposition of different classes of species is also applied in the n-butanol flame and illustrated in Figure 4.4.12.

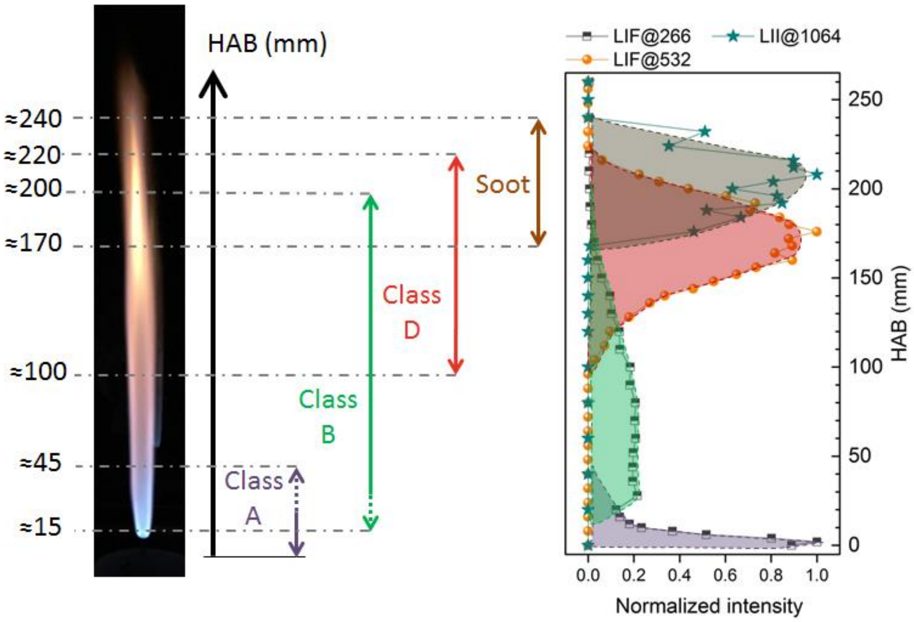

Figure 4.4.12. Positions and characteristics of the classes of species detected in the *n*-butanol flame

Zones of class A and B are discriminated more obviously in this flame. These two classes can be shown in Figure 4.4.13.

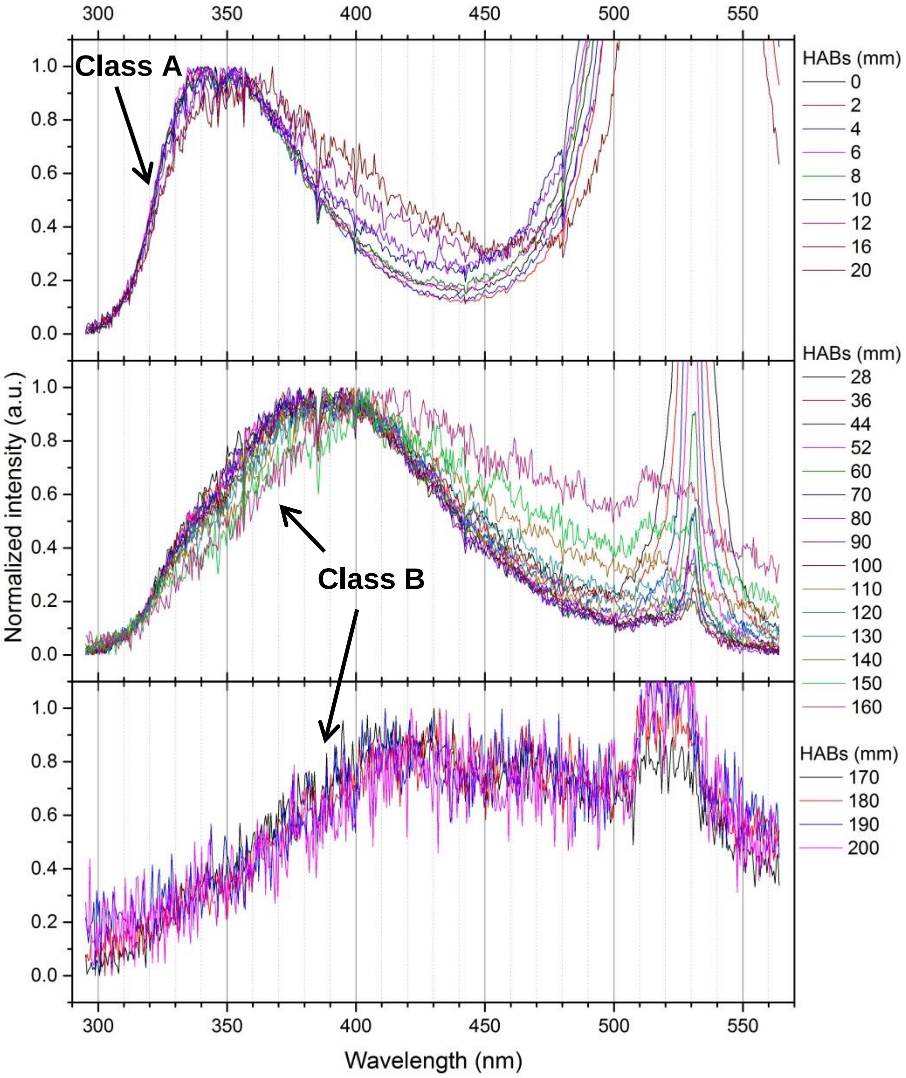

Figure 4.4.13. Class A and B species defined according to the normalized UV-LIF spectra obtained at the centerline of the n-butanol flame

The class C is not present in the n-butanol flame due to two reasons (i) the Vis-LIF signal obtained in the flame shows only mono-modal profile, (ii) there is no evolution of normalized Vis-LIF spectra as presented in Figure 4.4.14. This is probably due to the absence of petrogenic aromatic compounds in the *n*-butanol fuel. The species corresponding to Vis-LIF signal detected in this flame are classified as class D since the spectra are identical to which observed in the diesel flame.

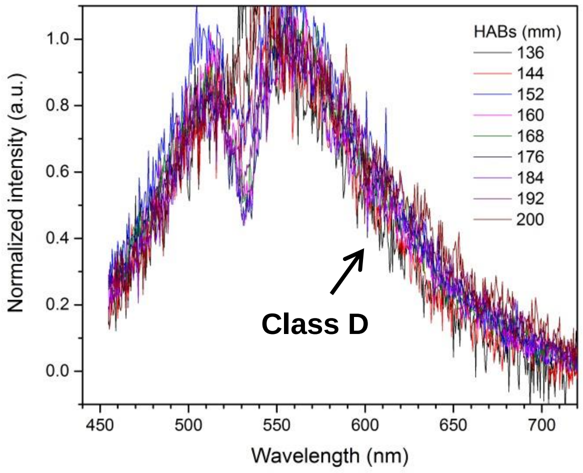

Figure 4.4.14. Normalized LIF spectra obtained at the centerline of the *n*-butanol flame with 532 nm excitation

Due to the lacking of the presence of the class C in the n-butanol flame, soot formation pathway can be described as below:

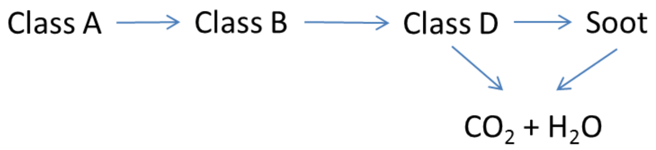

Figure 4.4.15. Proposing kinetic pathway of the soot formation in the *n*-butanol flame

The fuel (class A) is consumed to produce the class B species. The fluorescence signal obtained with 266 nm excitation in this flame is contributed by both of these classes. Then the class D is formed, followed by the formation of soot particles. Both class D and soot are oxidized. Although the class C is not present in the n-butanol flame, the soot particles are still formed. In other words, class D species are important precursors of soot.

4.5. Comparison inter-fuels

4.5.1. Compare three automobile fuels

Soot precursors are the key factor leading to the soot formation. Indeed, the amount of soot produced in the three flames and deduced from LII measurements varies in the same proportion as the Vis-LIF signal detected, as presented in Figure 4.5.1. Thus with the same heating value produced by three flames, *n*-butanol is able to diminish around 5000 times of soot particles. By blending 50% of volume of *n*-butanol in diesel fuel, the soot amount formed is reduced by a factor ≈2.

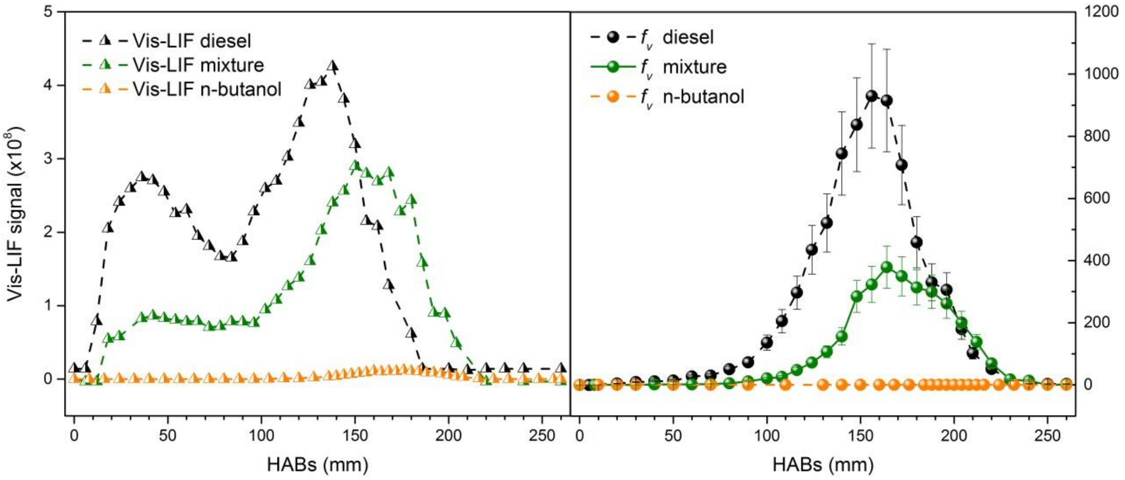

Figure 4.5.1. Comparison of Vis-LIF signal and average soot volume fraction (calculated from the LII signal) for the three flames: diesel, mixture and *n*-butanol.

There are many hypotheses proposed in the literature to explain the reduction of soot formation in the combustion of *n*-butanol compared to conventional diesel fuel. Some of them are related to the presence of O atom in *n*-butanol chemical structure. The intramolecular oxygen content in *n*-butanol is considered as a "trap" that restrains the nucleation process of soot particles (Geng et al. 2019), consumes soot precursors, thus reducing soot formation and promoting soot oxidation (Wei, Cheung, and Huang 2014; Zhang et al. 2019). Some other authors claimed that the C-O bond in *n*-butanol is the decisive reason as C-O bond is more difficult to break compared to other C-C bonds in the molecule. The dissociation energies of each bond in the *n*-butanol molecule are presented in Figure 4.5.2.

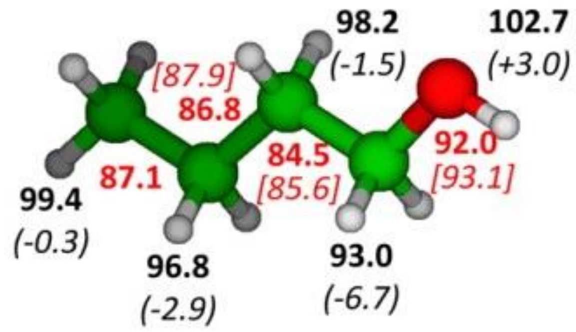

Figure 4.5.2. C-H or O-H (black) and C-C or C-O (red) bond dissociation energies (BDEs) (kcal mol^{-1}) for *n*-butanol. Numbers in parentheses ( ) represent the difference in BDEs with respect to a primary C-H bond. Numbers in brackets [ ] are experimental values (Pelucchi et al. 2016).

This C-O bond is then able to survive the fuel-rich ignition, the carbon atom bonded to O atom cannot make contribution to the soot formation (Wei, Cheung, and Huang 2014; Westbrook, Pitz, and Curran 2006; Boot et al. 2009). Additionally, *n*-butanol only has one β-carbon atom in the molecule due to the presence of –OH, resulting in lower mole fraction of important radicals to form precursors of soot (M. Li et al. 2019). It is to note that α-carbon atom is the first carbon atom that attaches to the functional group (in this case, functional group is –OH), Thus β-carbon atom is defined as the second carbon atom.

The higher concentration of ·OH and ·HO_2 radicals in *n*-butanol combustion is also the reason leading to the reduction of soot (Geng et al. 2019). These radicals promote the oxidation of carbon to CO and CO_2, leading to a depletion of carbon atoms to form soot precursors (Cheng, Dibble, and Buchholz 2002). Furthermore, ·OH can converse active hydrogen to molecular hydrogen which can slow down the formation of soot (Xinling Li et al. 2019).

From the point of view of fuel properties, (Pan et al. 2019; Geng et al. 2019; Zhang et al. 2019) suggested that higher volatility, lower boiling temperature and lower viscosity of *n*-butanol compared to diesel fuel also contribute to soot lowering. These properties of *n*-butanol lead to a better spray quality, a better evaporative atomization. They can improve gas phase fuel-air mixing which can reduce the formation of soot.

Besides the chemistry of the combustion process and the fuel properties, the temperature in the flame also has important influence to the soot formation. Soot formation cannot occur in locations where the temperature is less than 1400 – 1600K (McEnally and Pfefferle 2000; Glassman 1989; Pickett and Siebers 2003). Thus it is important to determine the temperature in the diesel flame and the *n*-butanol flame in the zone where LII signal is present. As mentioned in subchapter 4.3, it is impossible to measure the temperature in the sooting zone with a K-type thermocouple, but it can be deduced from the luminous emission of the flame. The temperature in the sooting zone of these flames will be measured in a future scheduled campaign.

Above all, *n*-butanol does not contain any aromatic compound as in diesel or mixture fuels. The lack of these aromatic compounds might be the main reason explaining why *n*-butanol and its mixture produce less soot than diesel. This is evidenced by the comparison of the soot volume fraction between the three fuels in Figure 4.5.1 (right panel). By mixing 50%v/v of *n*-butanol in diesel, the Vis-LIF signal and soot volume fraction are reduced by nearly a factor of two. This conclusion is coherent with the studies of Liu et al. (2018); Chen et al. (2017). They indicated that the diminution of aromatic compounds (in this case toluene) in the blend is the dominant factor for the lowering of soot.

4.5.2. Comparison of the two aeronautic fuels

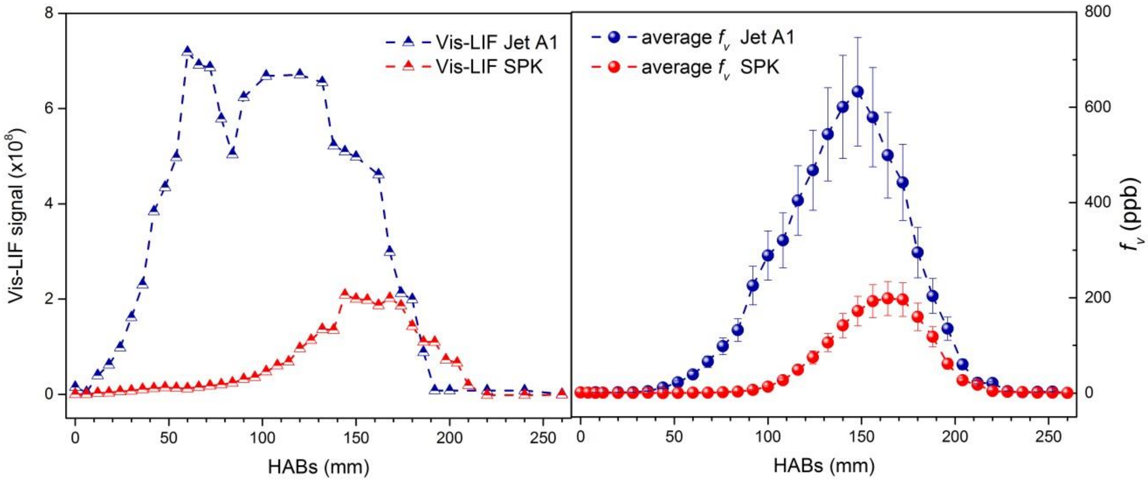

Figure 4.5.3. Comparison of Vis-LIF signal and average soot volume fraction (calculated from LII signal) for the Jet A-1 and SPK flames.

Similar to the three automobile flames, a comparison between the Vis-LIF profiles and the soot volume fractions calculated from the LII signal of the two aviation fuels is shown in Figure 4.5.3. The Vis-LIF signal obtained from the Jet A-1 flame is approximately three times higher than the one of the SPK flame. A similar trend is observed for the f_v of these two flames.

The difference between the soot amount formed in the Jet A-1 and SPK flames can be explained with the reduction of aromatic compounds in the SPK fuel (Saffaripour et al. 2011; Bester and Yates 2009; Xue et al. 2017; Braun-Unkhoff et al. 2017; Zheng et al. 2018; Chan et al. 2015; Corporan et al. 2012; Chalmers et al. 2012) as presented in Table 5.1.1. The proportion of aromatics in SPK is only 1.4% whereas for standard conventional jet fuel, this number varies from 15 to 23%. The decrease of aromatic content increases the hydrogen-to-carbon (H/C) ratio, which is directly related to the heat capacity of the combustion products and impacts the soot formation (Hileman and Stratton 2014; Braun-Unkhoff et al. 2017; Chalmers et al. 2012). Besides, the proportion of iso-paraffins, n-paraffins and cyclo-paraffins in fuels also have important influence to the soot production. Sooting tendency varies with different classes of compounds as n-paraffins < iso-paraffins < cyclo-paraffins < aromatics (Lobo et al. 2015). In other words, with the same H/C ratio, n-paraffins produce less soot than iso-paraffins (Lobo et al. 2015; Corporan et al. 2011; Corporan et al. 2012). Some physical properties of fuels might also influence the formation of soot. As having higher fraction of paraffins than Jet A-1 fuel, SPK has higher vapor pressure (Lobo et al. 2015), leading to a better mixing with air during the atomization, resulting in a more complete combustion (Braun-Unkhoff et al. 2017).

4.5.3. Discussion on the Vis-LIF spectra of the five studied flames

As presented in several subchapters as 4.1.1.2, 4.1.3.2 and 4.1.4.2 for the Vis-LIF signal from three different flames (diesel, mixture and Jet A-1), we observed that there is always a shift of the overall structure of the Vis-LIF spectrum from red to blue in the first peak of the Vis-LIF profile. After this zone, the Vis-LIF spectra do not change in the form, marking that the pool of fluorescent species does not evolve anymore. The Vis-LIF spectra obtained at the second peak of the diesel, mixture, Jet A-1 flames as well as at the (only) peak of the n-butanol and SPK flames are shown in Figure 4.5.4. The spectra are normalized to their maximum intensity.

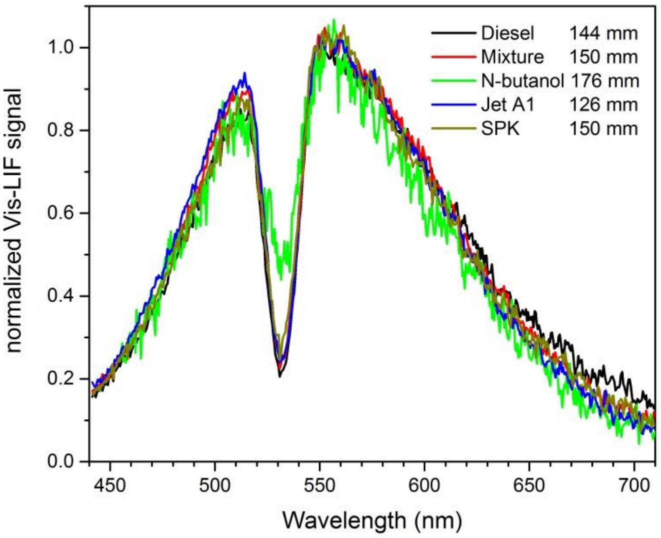

Figure 4.5.4. Vis-LIF spectra of five flames: diesel, mixture, n-butanol, Jet A-1 and SPK. The spectra are normalized to their maximum intensity.

From the figure, we observe that the Vis-LIF spectra from five different flames are identical in form, indicating that the composition of these soot precursors – class D species – is mostly identical for different fuels. As presented in previous subchapter 4.4.3, class D species here might include multitude of bridged-PAHs, dimers of PAHs, coating of soot particles, gas phase complexes etc. which fluoresce globally in the same way with 532 nm excitation wavelength. The soot precursors – the key of soot formation procedure – are still poorly understood. However, until now, we can conclude that the nature of fuel has no or very minor influence to the nature of these class D species.

4.6. Conclusion

This chapter is dedicated to the characterization of soot precursors and soot particles using in-situ and ex-situ techniques in five different swirled jet flames: diesel, n-butanol, mixture, Jet A-1 and SPK.

UV-LIF is able to detect the light or heavy molecules present in the combustion process. The spectra of UV-LIF are red-shifted with the increase of HABs, indicating the evolution of the fluorescent species. However, UV-LIF signal of swirled jet flames is dominated by the intense signal coming from fuel-related (petrogenic) fluorescent species.

Vis-LIF allows detecting the soot precursors – which play the key role in soot formation. For the first time, a bimodal profile (versus HAB) of Vis-LIF is obtained in jet flames of (only) aromatic-containing fuels. The first peak of the Vis-LIF profile might be related to an unknown class C species, whereas the second peak might be contributed by class D species, which include multitude of soot coating, bridged-PAHs, dimers of PAHs, etc. There is an evolution detected of the class C species, leading to the change in form of spectra in the first peak of Vis-LIF profile. The second-peak Vis-LIF spectra are identical for all five fuels, thus the nature of these fuels does not influence to the nature of the species.

Vis-LII and IR-LII show good coherence and repeatability in detecting and localizing the soot particles along the flame. The LII signal can be used to deduce the absolute soot volume fraction with a new direct mode of using a known light source as the Sphere. The soot volume fraction in the n-butanol flame is approximately 5000 times less than in the diesel flame. The characteristics of soot particles in n-butanol flame show similarity to nascent soot particles. SPK fuel is able to diminish the soot formation by three times compared to Jet A-1 fuel.

The total PAH signal detected by the ex-situ L2MS technique shows good correlation with the Vis-LIF signal of pyrogenic fluorescent species. The total PAH signal recorded by ex-situ SIMS and the sum of $\mathrm{C}_n\mathrm{H}^-$ mass peaks (with n = 4, 6, 8) have good correlation with the Vis-LIF signal of both petrogenic and pyrogenic fluorescent species. The C_2^- carbon cluster from SIMS mass spectra can be used as soot marker as it fits well with the LII signal. However, the C_2^- can only be used in sooting flames, but not for special flames as the n-butanol one – which produces nascent soot particles.

Chapter 5.

Study of particulate emissions from aeronautic fuels with a customized miniCAST burner

5. Study of particulate emissions from aeronautic fuels with a customized miniCAST burner

The experiment carried out with the "liquid CAST" in PC2A and PhLAM laboratories is in the framework of the ROC project (Réponse Optique des émissions de CAST alimenté en carburants alternatifs) – which was financed by the GDR Suie. A part of this project was carried out in ONERA laboratory (D. Delhaye, I. K. Ortega), which also developed and provided the liquid CAST instrument. Only results regarding the campaign carried out in PC2A and PhLAM will be presented in this chapter.

5.1. Experimental set up

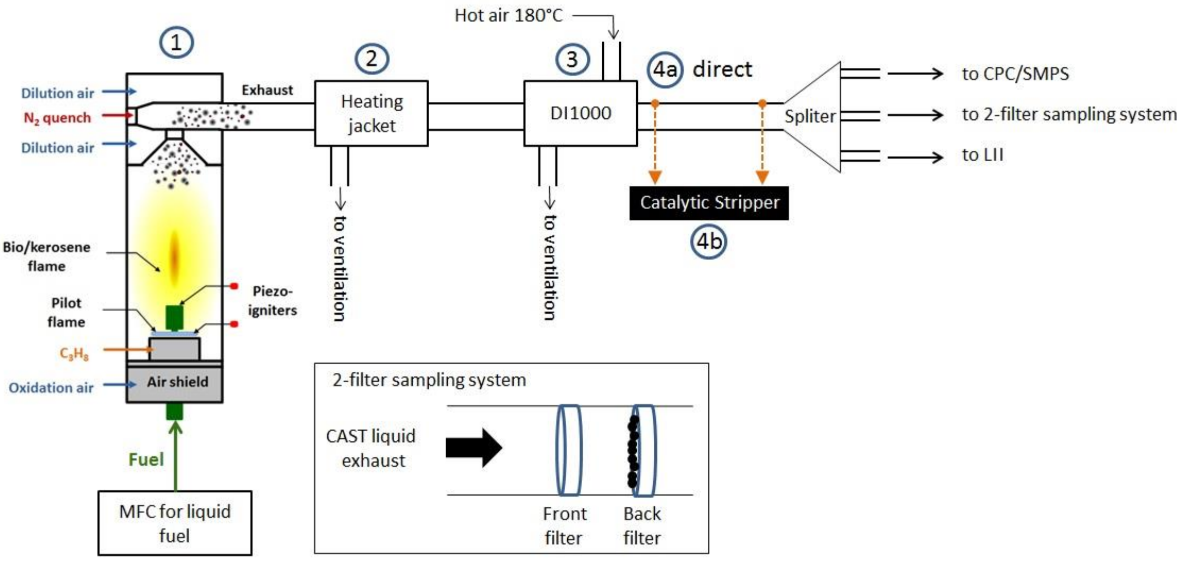

Figure 5.1.1. Schematic of the experiment on liquid CAST and sampling line used for the analysis of emissions produced after the combustion of standard and alternative jet fuels

The sampling line used to collect and characterize the liquid CAST exhaust is shown in Figure 5.1.1. The liquid CAST instrument is described in detail in subchapter 2.1.3. The fuels used during the campaign are Jet A-1, SPK from Hydroprocessed Esters and Fatty Acids (HEFA) and a mixture of 50% Jet A-1 and 50% SPK in mass (labeled S50 as following). The properties of these fuels are presented in Table 5.1.1. The emissions of the CAST are first passing through a set of metallic joints heated at 150°C and connected at atmospheric pressure in order to stabilize the flame. Then the flow is diluted by a first DEKATI stage (DI1000) with air heated up to 180°C. The exhaust is analyzed directly (4a) or after passing through a Catalytic Stripper (CS) (4b). The CS is supplied by Catalytic Instruments (model CS10 Catalytic Stripper). This device is a heated catalytic element used to remove semi-volatile material by oxidation. The working temperature of this CS in our case is 300°C to avoid the desorption of Si from the sampling lines. The flow is then split into three equal sub-flows. The first sub-flow is diluted by a second stage (VKL box) for the CPC and SMPS. The second sub-flow is sent to a Teflon tube with inner diameter of 4 mm, in a quartz window chimney to a custom LII system. The third one is directed through our two-filter system for further mass spectrometry analysis. The 4-mm-diamter flow of smoke is measured by the LII system using the second generated harmonic (532 nm) of a pulsed Nd:YAG laser (Quantel Brilliant B, 6 ns pulse width, 10 Hz) as excitation. The fluence curves for each set point of the CAST were obtained at variable laser fluences. As described in subchapter 4.1, a fluence curve shows the variation of the incandescence signal with the increase of the laser fluence. The configuration of the optical setup for LII measurements is reported in subchapter 4.1.

Property	**Jet A-1**	**SPK**
Density at 15°C, kg/m^3	780-820	759
Distillation temperature, °C		
10% boiling point	155-201	169.6
Final boiling point	235-285	243.9
Net heat of combustion, MJ/kg	42.86-43.50	-
Aromatics	15-23%v/v	1.4%w/w
Naphthalenes, %v/v	1.0-3.5	-
Cycloparaffins, %w/w	-	10.3
Paraffins, %w/w	-	86.3
Smoke point, mm	20-28	-
Hydrogen, %w/w	13.4-14.3	-
Sulphur	< 0.3%w/w	< 3 mg/kg
Kinematic viscosity at -20°C, mm^2/s	2.5-6.5	-

Table 5.1.1. Properties of Jet A-1 and SPK used in the experiment

In parallel, particulate matter from the exhaust is collected on the filters with our two-filter system for further mass spectrometry analysis. The aim of this sampling scheme is to discriminate the PAHs in gas phase from those condensed on PM. The two-filter system is described in detail in subchapter 2.3.

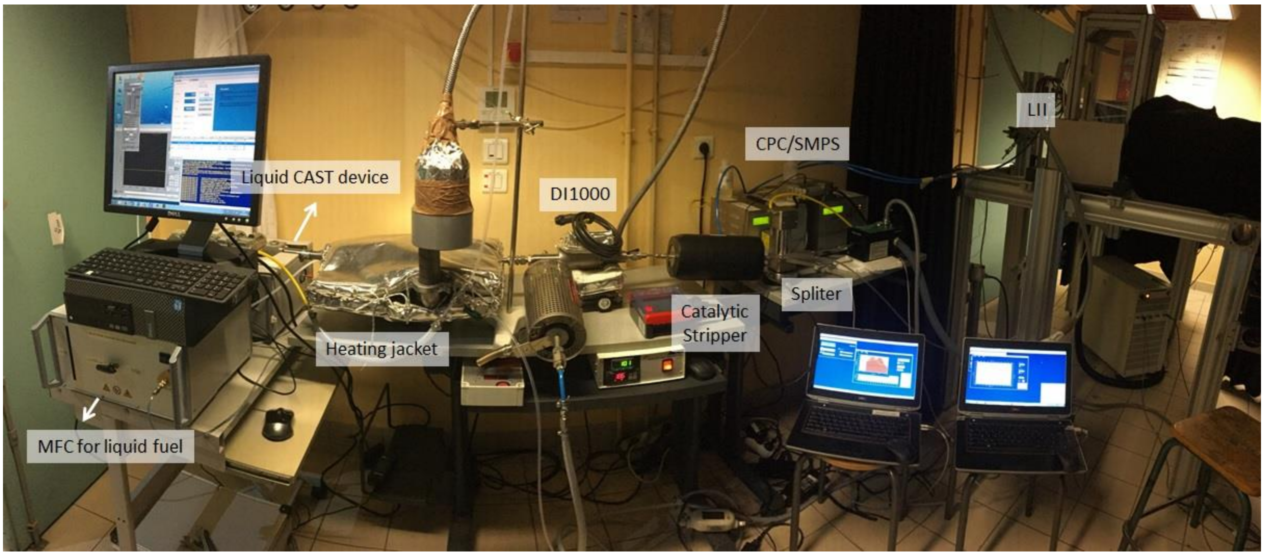

Figure 5.1.2. Photo of the experimental set up

5.2. Fluence curves

The emitted incandescence signal is broadband collected over a spectral doman of 200 nm in the 606 – 806 nm range. The optical configuration used in this experiment is similar to the one described in subchapter 2.4. The only different parameter used in this case is the laser beam profile. The total diameter of the laser beam is 8.5 mm. A top hat profile is formed by centering the laser beam with the exhaust system (4 mm). The edge of the laser beam has higher diameter than the exhaust stream, therefore only the volume corresponding to the exhaust from Teflon tube is analyzed. The combustion exhaust is directed into a quartz window chimney. The incandescence signal is recorded perpendicularly with respect to the CCD camera. The LII signal corresponding to 750-800 nm domain is integrated for the fluence curves. At these wavelengths, there is no fluorescence emission occurring in the spectra. At first, the LII signal increases with the rise of the laser fluence. At a certain threshold and when sufficient energy is injected into soot particles, they start sublimating and the incandescence signal then decreases. By comparing the fluence curves obtained at different working points, it is possible to obtain ideas of the maturity of soot. The comparison must be made on the left side of the sublimation threshold for each fluence curve, since the right side is difficult to estimate after the sublimation of particles by overheating.

The variation of the LII signal with the laser fluence obtained for Jet A-1 and SPK fuel burned with different oxidation air flows is shown in Figure 5.2.1. From the left panel of the figure, we observe that SPK produces significantly a lower soot volume fraction than Jet A-1 fuel. The soot is reduced noticeably with the increase of the oxidation air flow. This is due to their maturity which changing from 2 to 3 L/min oxidation air flow. The LII signal is normalized to the value where it reaches the sublimation point and shown in the right panel. There is no signal detected in the case of SPK fuel burned with 3L/min of oxidation air flow. The shift between the peaks of each curve is dictated by the oxidation flow and by the type of fuel. With the increase of oxidation air flow, the sublimation point shifts to higher laser fluence. This could be related to the organic content of these different types of soot but also to their bulk properties (Michelsen 2017). A higher laser fluence is required to bring young soot to similar LII signal levels than mature soot (Irimiea 2017). In other words, the shift to higher laser fluence indicates that soot particles are less mature. Soot particles produced with SPK fuel are less mature than the ones from Jet A-1 fuel. The maturity of particles in this case decreases with the increase of oxidation air flow while the soot volume fraction (which is assumed to be proportional with the LII signal at a given fluence value) decreases significantly with the increase of the oxidation air flow.

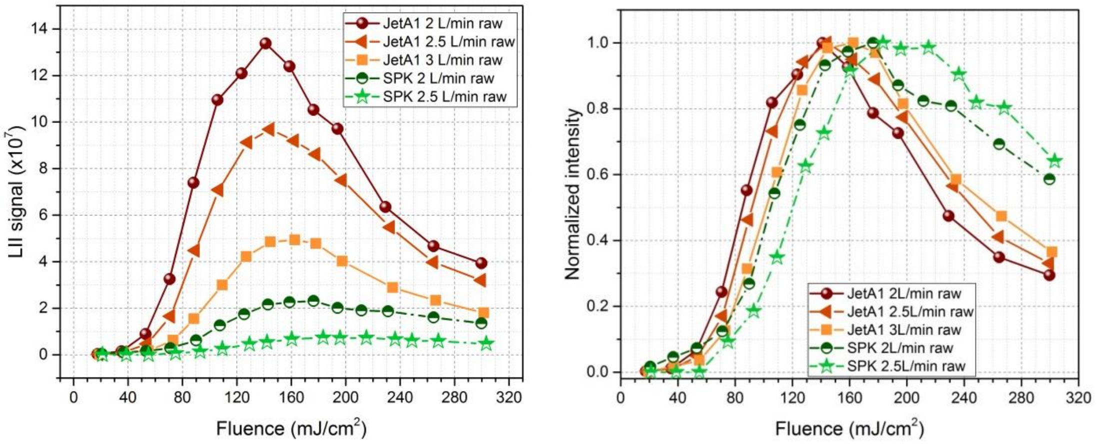

Figure 5.2.1. Fluence curves obtained for 105 µL min-1 Jet A-1 fuel and 105 µL min-1 SPK fuel burned with 2, 2.5 and 3 L/min oxidation air flow. The fluence curves are obtained in the exhaust of the CAST without CS. Left panel shows the original fluence curves whereas right panel shows the fluence curves normalized to the maximum point of each curve.

The fluence curves corresponding to the exhaust of the CAST with Jet A-1 and SPK with and without CS treatment are showed in Figure 5.2.2. We observe that in the case of Jet A-1 fuel, the CS is able to remove a fraction of the particulate matter from the exhaust which is due to the losses over the CS and the fraction removed after the catalysis process. However, the diminution of soot by CS is not as efficient as the increase of the oxidation air flow and this may be due to the inefficiency of the CS in conditions where high content of volatile and semi-volatile particulate matter is present in the exhaust. A similar trend is observed for SPK fuel with 2 L/min oxidation air flow, but not for 2.5 L/min of air.

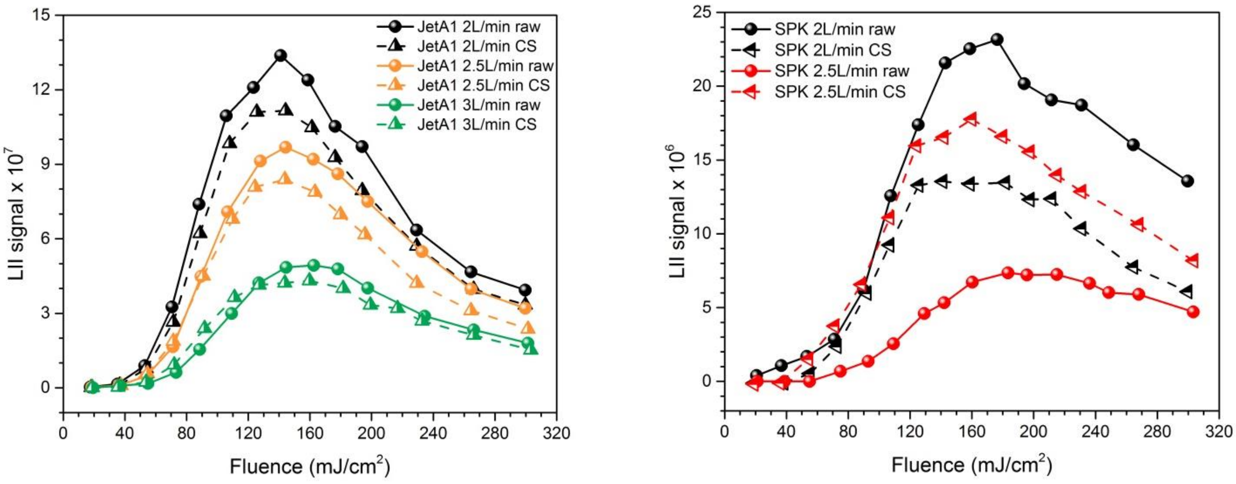

Figure 5.2.2. Comparison of the fluence curves obtained with and without CS treatment from Jet A-1 and SPK fuels.

Figure 5.2.3 shows the fluence curves obtained for the exhaust of the CAST with Jet A-1 fuel with and without the use of the CS in the sampling line. Each graph corresponds to one setting of the oxidation flow. A small shift is observed in the sublimation peak detected for soot from Jet A-1 with and without being treated with CS for 3 L/min oxidation air flow. This is an indicator that the bulk properties of these particles are playing a role on the absorption and emission of radiation.

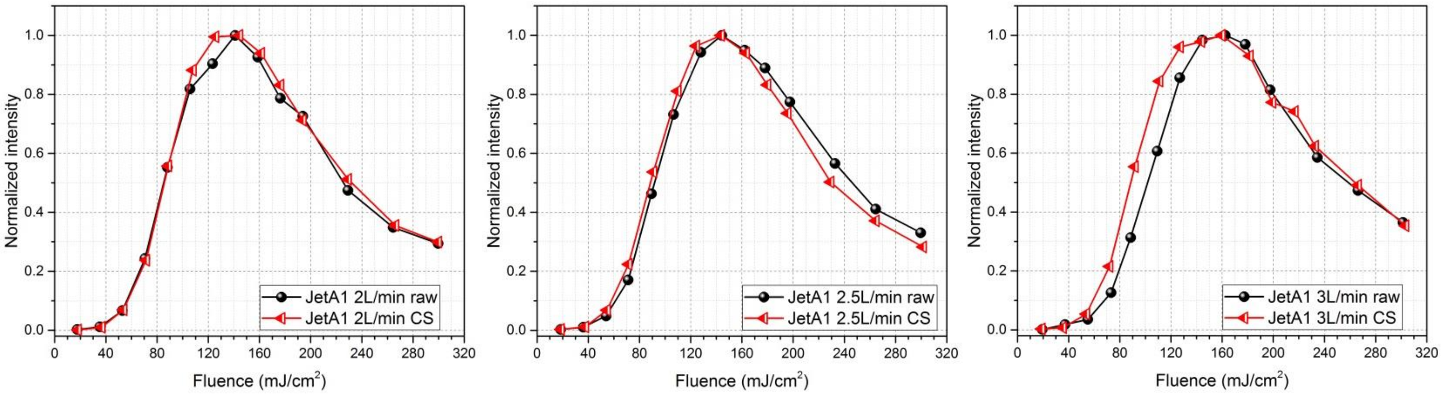

Figure 5.2.3. Fluence curves obtained for 105 µL min-¹ Jet A-1 fuel burned with 2, 2.5, 3 L/min oxidation air flow. Each graph corresponds to one setting of the oxidation flow. Black and red line-scatters represent results obtained in the exhaust of CAST without CS and with CS, respectively.

In the case of SPK soot, a different trend is observed. The shift between sublimation threshold of direct and CS mode becomes broadened with the increase of oxidation air flow. CS might "clean" the soot surface by removing the volatile/semi-volatile species, leading to the increase of absorption cross section of soot particles. More work is needed to better understand the changes of absorption cross section of the particles with the variation of the temperature. Optical effects of coatings or morphology could have a considerable impact on to the evolution of LII signals (Irimiea 2017; Lefevre et al. 2019).

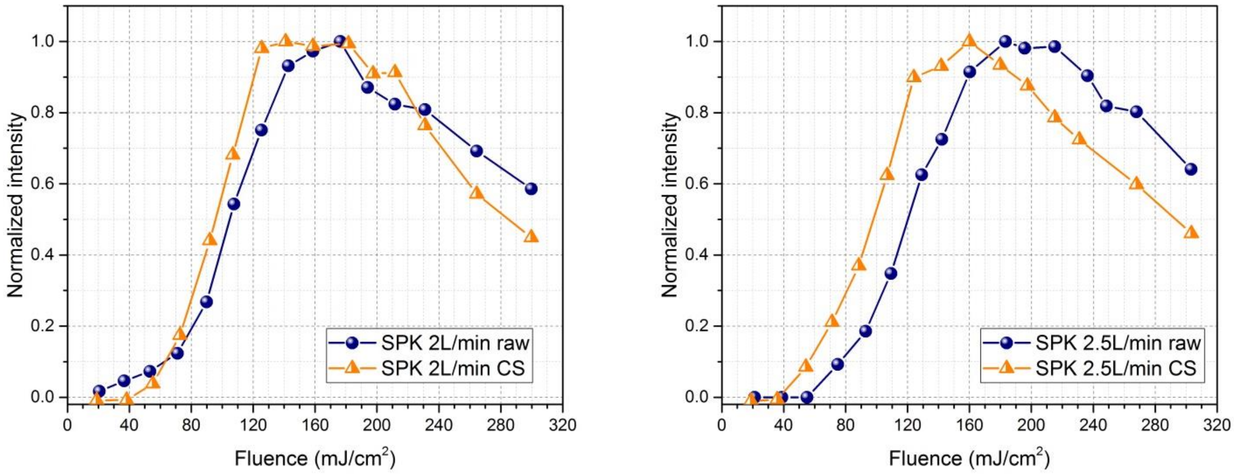

Figure 5.2.4. Fluence curves obtained for 105 µL min-¹ SPK fuel burned with 2, 2.5, 3 L/min oxidation air flow. Each graph corresponds to one setting of the oxidation flow. Blue and orange line-scatters represent results obtained in the exhaust of CAST without CS and with CS, respectively.

5.3. Chemical characterization of particulate emissions

Photos of front samples collected at different working points are shown in Figure 5.3.1. All samples are collected during 5 minutes with a flow rate of 0.6 L/min. Back samples are not shown here since they are all black due to the presence of black carbon on the filters. The color of front samples varies from yellowish, yellow to brown or black depending on the fuel nature and the oxidation air flow. In general, Jet A-1 samples are mostly black, except the 3L/min sampling point. The higher the oxidation air flow is, the lighter the color of the sample is. SPK and S50 samples are yellow and brown in general.

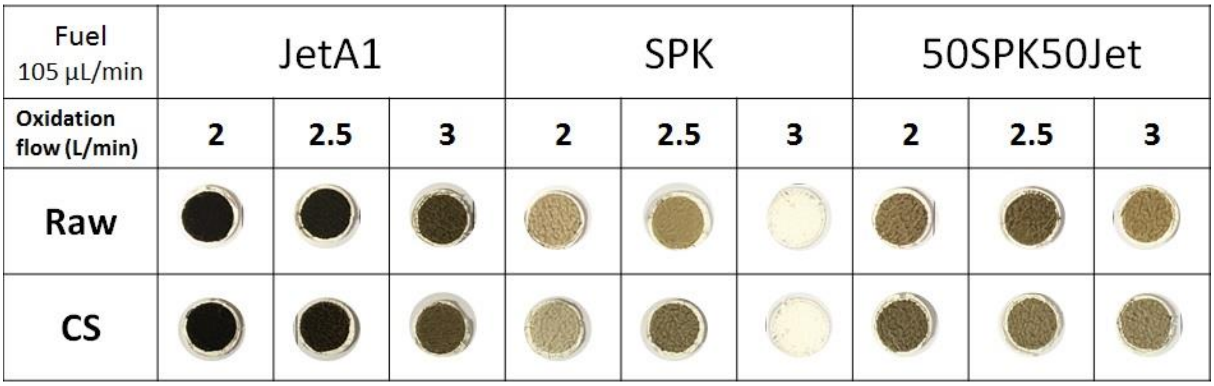

Figure 5.3.1. Photos of front and back samples collected at different set points with the "liquid" CAST

Front and back samples collected at the exhaust of the liquid CAST are mass-analyzed using the L2MS and SIMS techniques. The chemical composition of the condensed and the condensable gas phase is then determined separately. The effect of the CS treatment on the partitioning of the aromatic species between the two filters is also discussed.

5.3.1.1. L2MS mass spectra

Figure 5.3.2 displays the L2MS mass spectra of Jet A-1 front samples obtained at different oxidation air flows with and without CS. Spectra of Jet A-1 raw samples are rich in PAHs with *m/z* in 128 – 600 range. In general, the total signal obtained increases with the oxidation air flow in the order 3 L/min, 2 L/min, 2.5 L/min. The heaviest mass detected is *m/z* 632 for Jet A-1 2 and 2.5 L/min and *m/z* 572 for 3 L/min. The average *m/z* in mass spectra (which can be determined as $\bar{M} = \frac{\sum M \cdot I}{\sum I}$, with M molecular mass assigned to peaks and I ion signal) shifts to lower values with the increase of oxidation air flow (as in Figure 5.3.5).

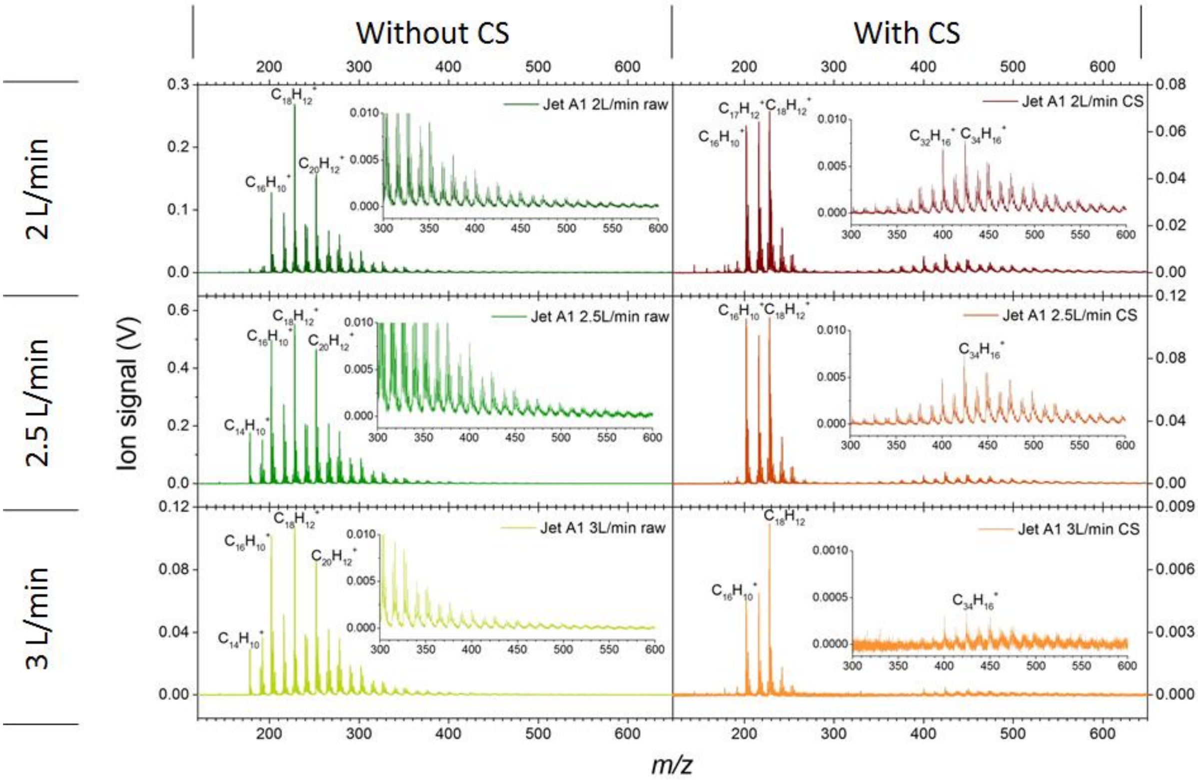

Figure 5.3.2. L2MS mass spectra of front samples collected in the CAST exhaust using Jet A-1 as fuel with three different oxidation air flow rates (upper panels: 2 L/min; middle panels: 2.5 L/min; lower panels: 3 L/min). The exhaust is treated with CS (right panels) or without CS (raw – left panels).

The total mass signal obtained from Jet A-1 CS samples is significantly weaker than the raw ones at the same oxidation air flow. Remarkably, the PAH distribution in these mass spectra is cut off in the range *m*/*z* 250 – 380, resulting into two noticeable PAH ranges on all CS mass spectra. The heaviest mass detected in CS mass spectra is higher compared to raw samples with *m*/*z* 718 for 2 L/min sample and *m*/*z* 632 for 2.5 L/min sample. The opposite behavior is obtained for the 3 L/min sample where the heaviest *m*/*z* is 548. The average *m*/*z* obtained with CS sample spectra is higher compared to raw samples, but they still have a similar trend: the average *m*/*z* decreases with the increase of the oxidation air flow. The total signal obtained for CS samples shows a reduction by a factor of 20 compared to raw sample at 3 L/min, whereas at other oxidation flows, the reduction factor obtained is 5.

According to the mass spectra, the CS is efficient in removing PAH from the soot particles. But this efficiency seems to be specific to the *m*/*z* rang 250 – 380 in which PAHs are classified as nvPM.

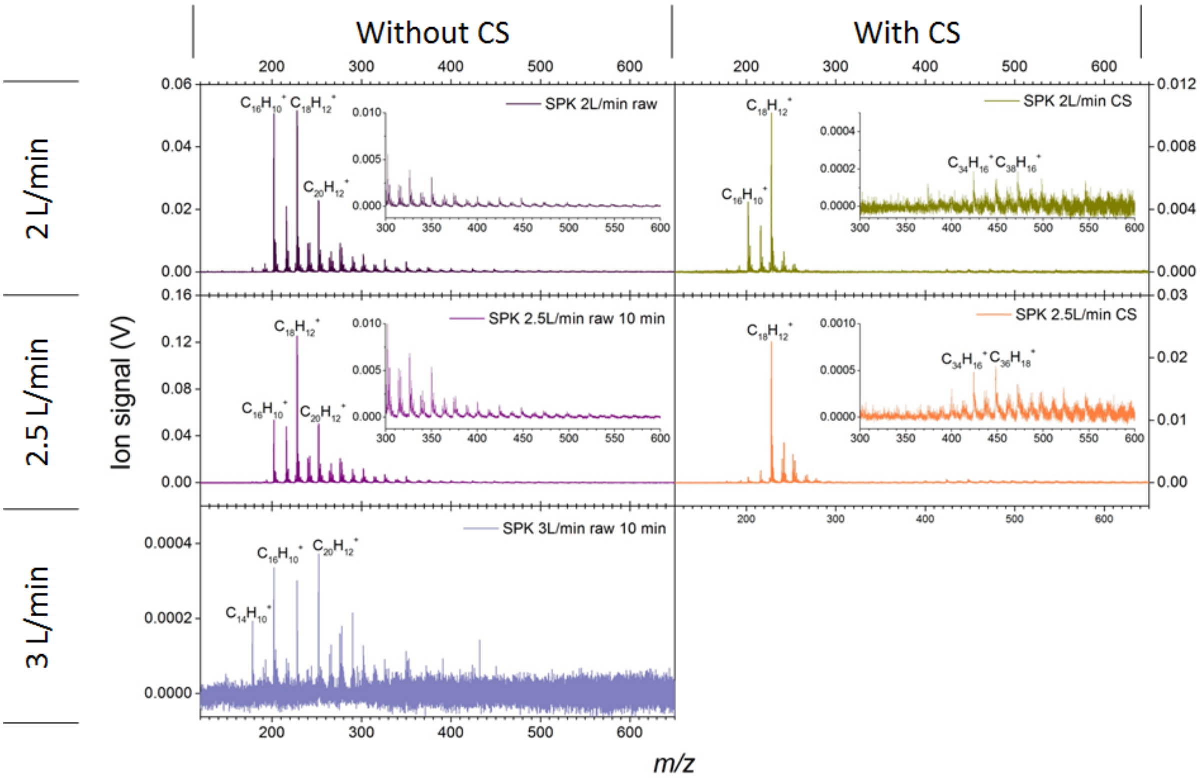

Figure 5.3.3. L2MS mass spectra of front samples collected in the CAST exhaust using SPK as fuel with three different oxidation air flow rates (upper panels: 2 L/min; middle panels: 2.5 L/min; lower panels: 3 L/min). The exhaust is treated with CS (right panels) or without CS (raw – left panels).

L2MS mass spectra obtained from SPK front samples at different oxidation air flows are showed in Figure 5.3.3. Significantly, SPK mass spectra show a lower signal than the ones obtained for Jet A-1 samples at the same conditions. However, raw samples obtained at 2 and 2.5L/min still have a high content of PAH, while the one at 3L/min shows very low signal. All mass spectra are dominated by *m/z* 228 peak, except SPK 3 L/min raw sample. Mass spectra of CS samples show lower PAH content compared to raw ones. However, the bimodal distribution is still present as in the case of Jet A-1 samples.

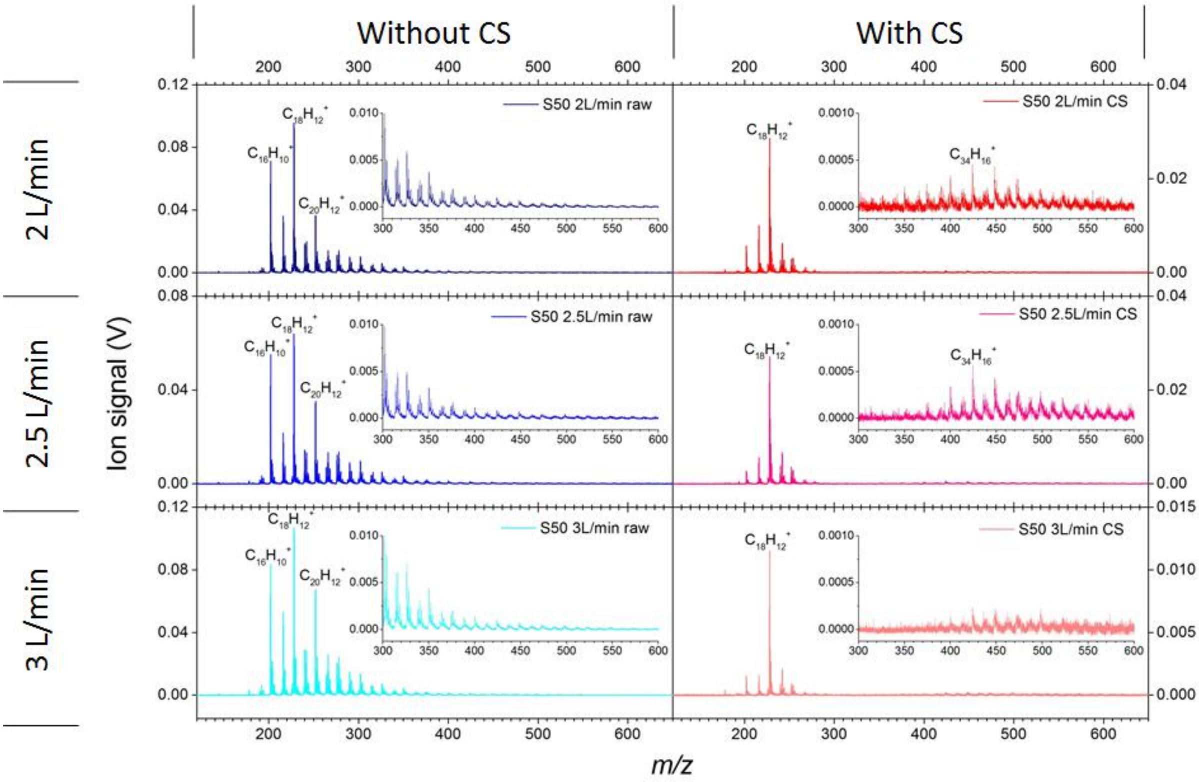

Figure 5.3.4. L2MS mass spectra of front samples collected in the CAST exhaust using S50 as fuel with three different oxidation air flow rates (upper panels: 2 L/min; middle panels: 2.5 L/min; lower panels: 3 L/min). The exhaust is treated with CS (right panels) or without CS (raw – left panels).

L2MS mass spectra obtained with S50 raw and CS samples are shown in Figure 5.3.4. Overall, the mass signal of these samples shows an intermediate behavior between Jet A-1 and SPK, as the fuel if 50%w/w Jet A-1 - 50%w/w SPK. The mass spectra of all samples are dominated by *m/z* 228. The CS samples also show a bimodal distribution of PAHs, similar to the other two (neat) fuels. The average masses detected in S50 CS mass spectra is higher than one from raw spectra.

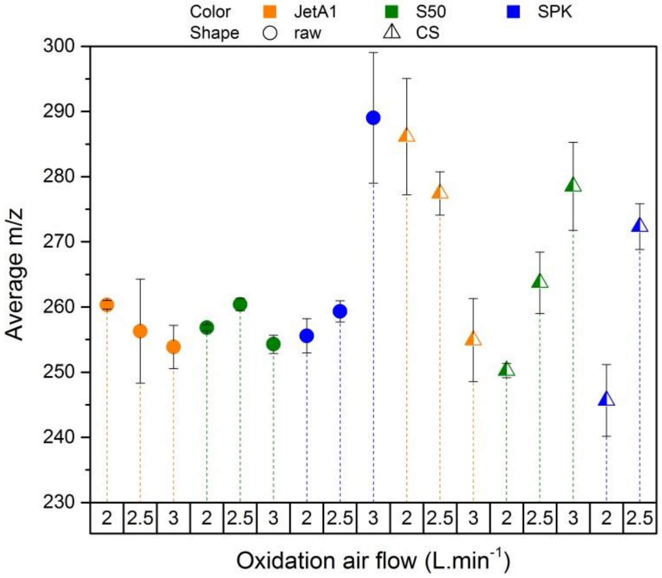

Figure 5.3.5. Average *m*/*z* detected in L2MS mass spectra of liquid CAST front samples

HCA analysis is applied on L2MS mass spectra of all front samples with 183 peaks taken into account. The clustering is calculated on the furthest distance method with Euclidian distance between the observations (samples). From the clustering dendrogram, it is deduced that the samples can be imparted into three main clusters at a distance of 1.5. The first cluster (red color) is represented by all front raw samples, whereas the second (green color) and third clusters (blue color) are representative of CS samples.

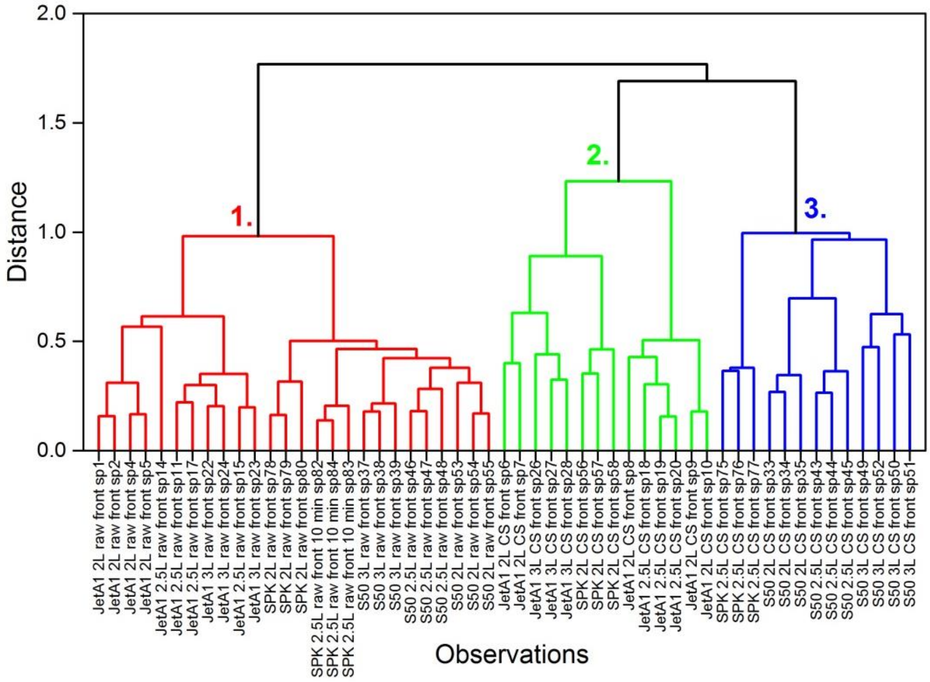

Figure 5.3.6. Clustering dendrogram obtained with L2MS mass spectra of liquid CAST front samples

A similar result is achieved with PCA analysis applied on the same sample set as presented in Figure 5.3.7. PC1 (representing 44.9% of variance) discriminates between samples with and without CS treatment. The positive coefficients of this principal component are mainly associated to PAHs in the range *m/z* 252-396 and some light species with *m/z* < 202, whereas negative coefficients are composed of larger species with *m/z* > 396 and intermediate-size aromatic species with 16-19 carbon atoms. This might be due to the performance of the CS which is more optimum in this mass range. PC2 separates mainly Jet A-1 CS samples and SPK CS samples. The positive loadings of PC2 are associated with PAHs with 16-17 carbon atoms, whereas PAHs with 18-21 carbon atoms compose its negative loadings. The CS samples obtained from SPK are more complex since they are on both sides of the PC2 axis.

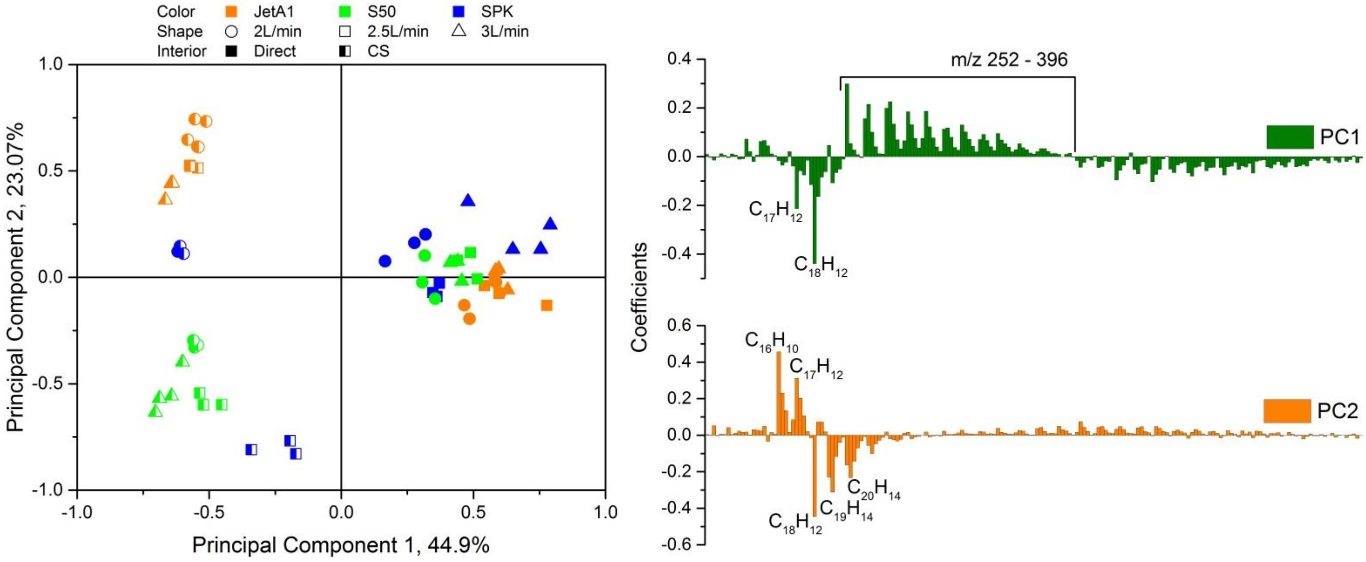

Figure 5.3.7. PCA score plot (left panel) obtained from L2MS mass spectra of liquid CAST front samples and loadings (right panel) of first two principal components

The PCA is also applied on the raw front sample set. The PC1 separates the samples function of the nature of the fuel. PC1, representing 49.8% of the total variance, is composed of pericondensed PAHs with negative loadings and alkylated derivatives with positive loadings. As shown in Figure 5.3.9, at the same oxidation air flow, the sum of alkylated PAHs decreases in the order Jet A-1 < S50 < SPK. This might be explained by the chemical properties of the fuel used. As SPK contains mostly alkane and cycloalkane, these species are easier to be fragmented into small radicals during the pyrolysis step and form pericondensed PAHs in following steps. Jet A-1 contains PAHs and alkyl-PAHs. The rings likely have better resistance than the chain during the pyrolysis process. They have the chance to react with other radicals in the process to form more alkyl PAHs than the SPK fuel.

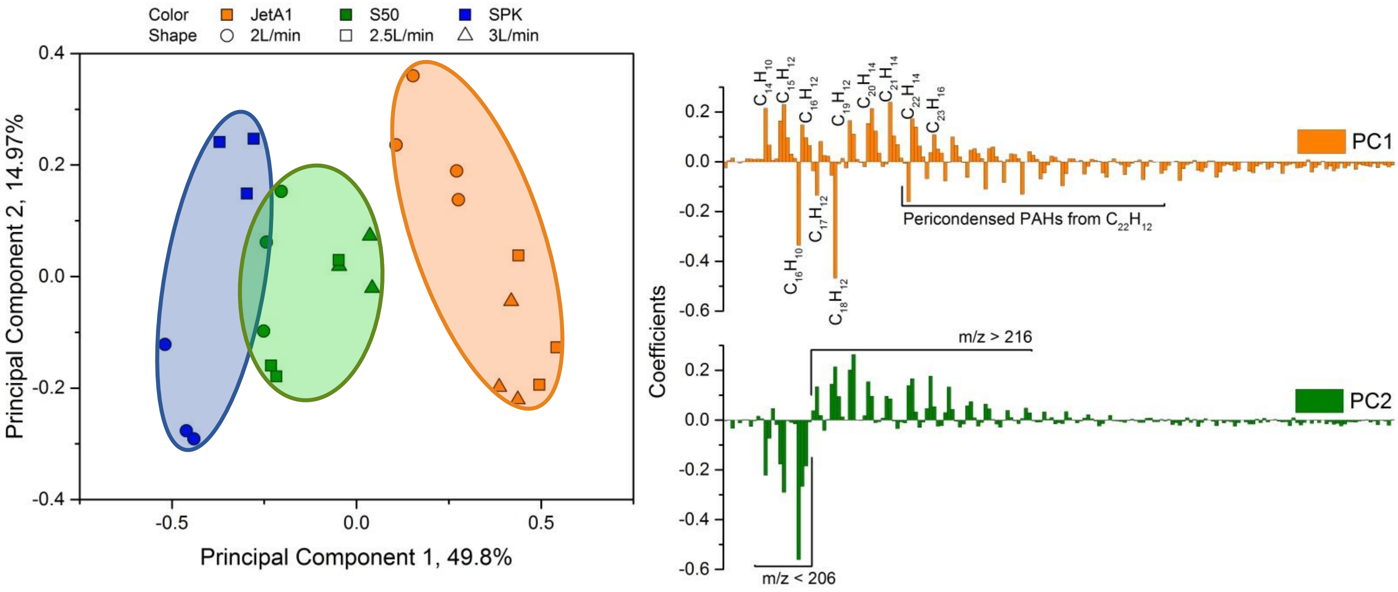

Figure 5.3.8. Score and loading plots of PCA applied on L2MS mass spectra of liquid CAST front raw samples

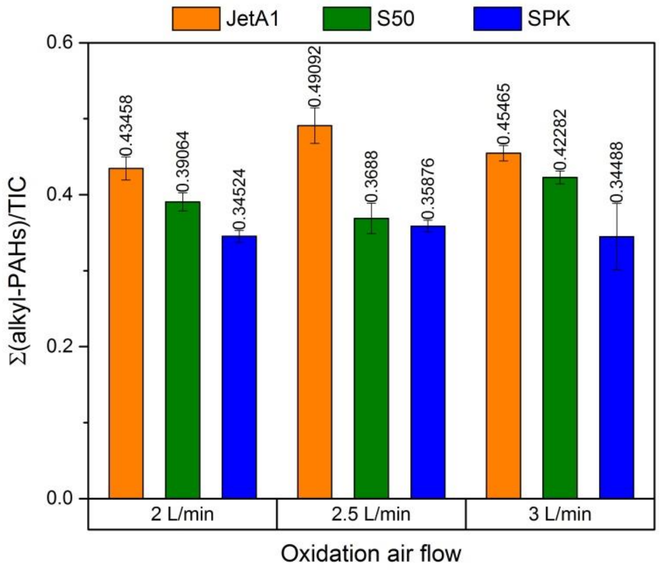

Figure 5.3.9. Variation of alkyl-PAHs sum, normalized to TIC, detected in L2MS spectra of liquid CAST front raw samples

To sum up, the use of SPK fuel can reduce the emissions of condensed matter in the exhaust, compared to Jet A-1 fuel. The S50 exhaust shows an intermediate behavior between Jet A-1 and SPK. Untreated exhaust of Jet A-1 fuel contains more alkyl-PAHs than the ones of SPK and S50. CS shows a good performance in reducing the PAH emissions from the exhaust of the CAST. CS also shows its optimum efficiency on removing PAHs in the range *m/z* 250 – 380.

L2MS results obtained on the back samples are displayed in Figure 5.3.10, Figure 5.3.11, Figure 5.3.12 for Jet A-1, SPK and S50, respectively. Gas phase species that are carried along the exhaust flow are lighter than *m/z* 250, which correspond to svPM and vPM. There is not much noticeable difference between the samples of the three fuels at different oxidation air flows. However, the difference between raw and CS treated samples is remarkable. In all cases, heavier *m/z* are detected in CS samples, compared with raw one. This leads to the idea that CS might induce some chemical reaction affecting the gas phase species.

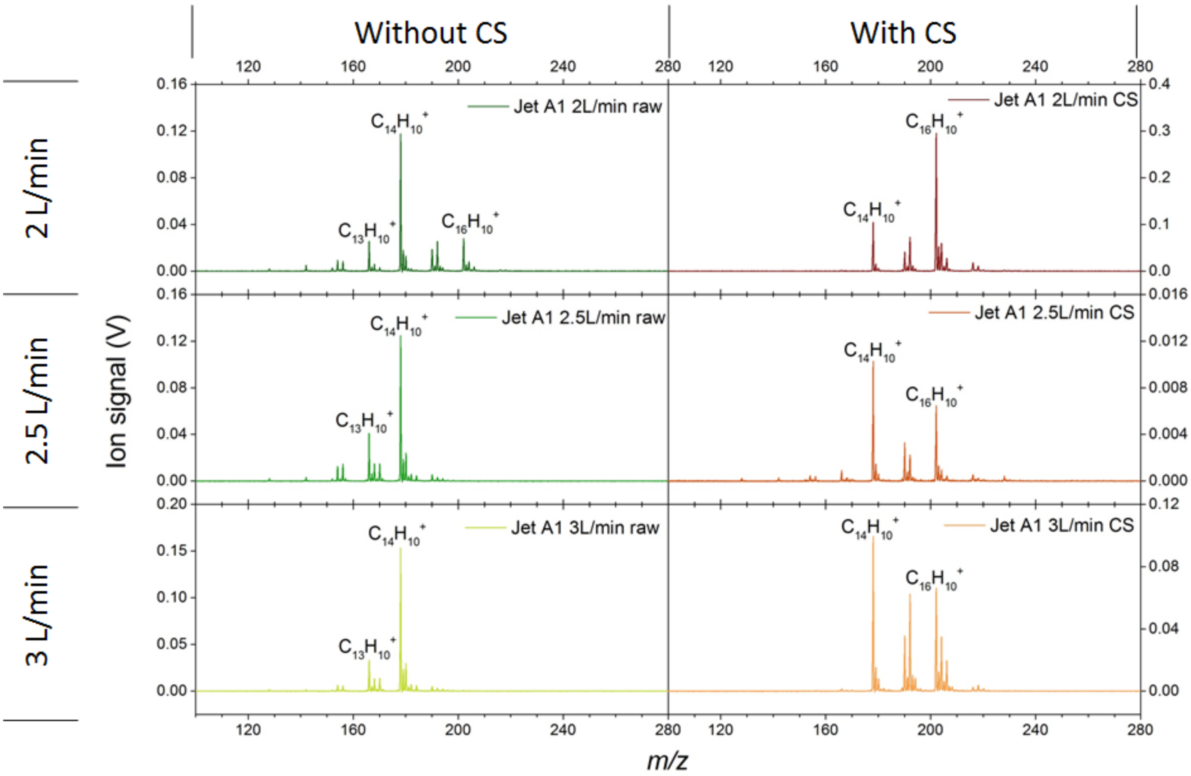

Figure 5.3.10. L2MS mass spectra of back samples collected in the CAST exhaust using Jet A-1 as fuel with three different oxidation air flow rates (upper panels: 2 L/min; middle panels: 2.5 L/min; lower panels: 3 L/min). The exhaust is treated with CS (right panels) or without CS (raw – left panels).

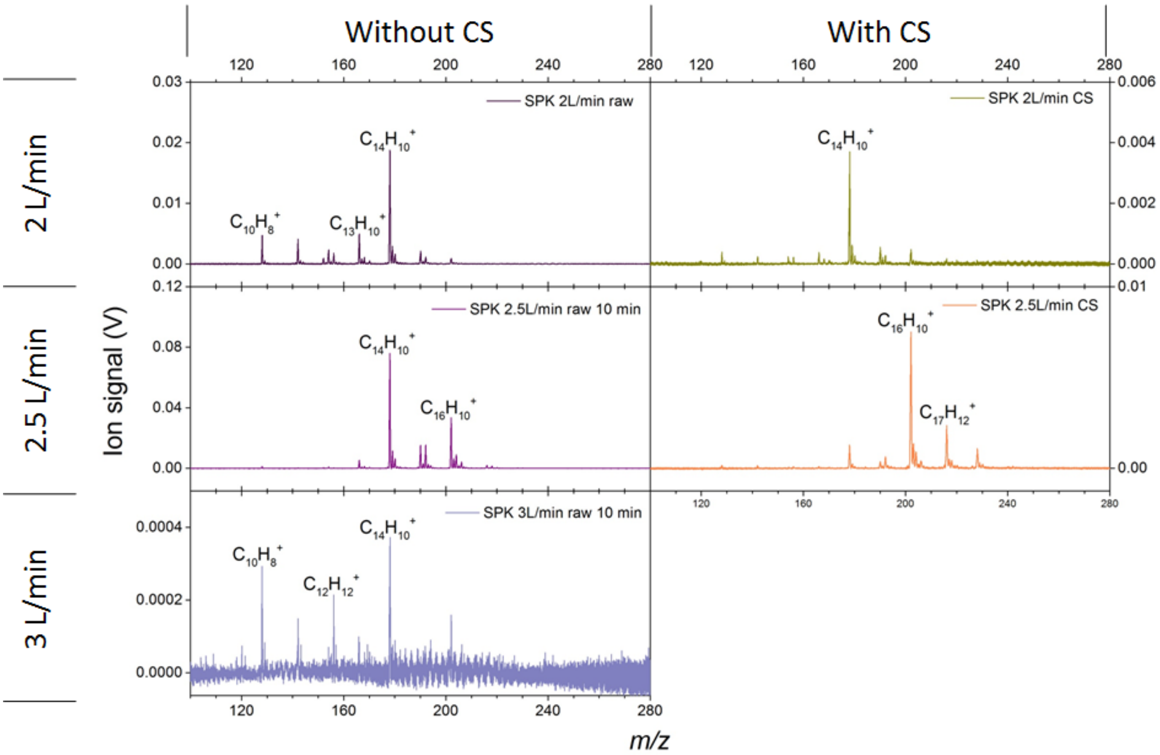

Figure 5.3.11. L2MS mass spectra of back samples collected in the CAST exhaust using SPK as fuel with three different oxidation air flow rates (upper panels: 2 L/min; middle panels: 2.5 L/min; lower panels: 3 L/min). The exhaust is treated with CS (right panels) or without CS (raw – left panels).

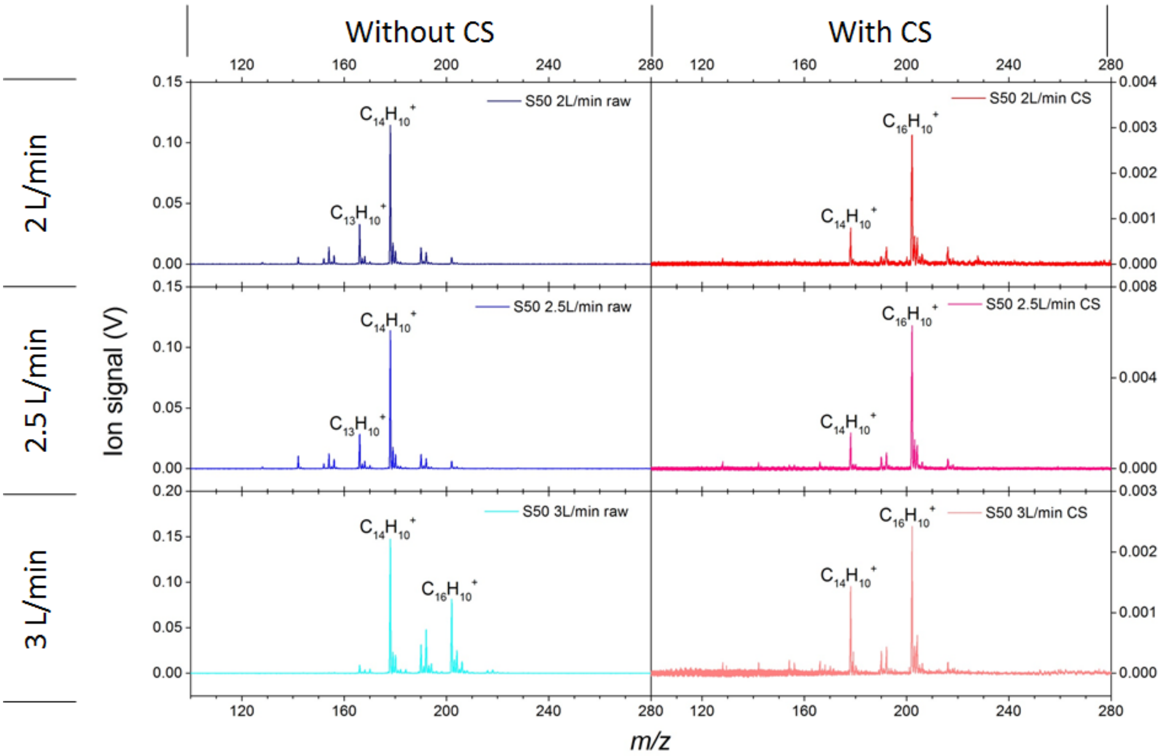

Figure 5.3.12. L2MS mass spectra of back samples collected in the CAST exhaust using SPK as fuel with three different oxidation air flow rates (upper panels: 2 L/min; middle panels: 2.5 L/min; lower panels: 3 L/min). The exhaust is treated with CS (right panels) or without CS (raw – left panels).

5.3.1.2. *SIMS mass spectra*

As shown in the L2MS result, there is not much difference between samples at different oxidation air flow rates. Thus samples obtained from liquid CAST at 2.5 L/min oxidation air flow were selected to be analyzed using ToF-SIMS because they show intermediate properties among the sample set in L2MS characterization. SIMS spectra in positive and negative polarities are shown in Figure 5.3.13 and Figure 5.3.14. As mentioned before, positive SIMS spectra include two main groups: fragments with $m/z < 150$ and PAHs and other compounds with $m/z > 150$. SIMS mass spectra of front samples are rich in PAHs. Raw samples mass spectra are dominated by $C_{22}H_{12}^+$. CS samples spectra show a bimodal PAH distribution, similar to the L2MS results. The first distribution is dominated by $C_{16}H_{10}^+$ and $C_{18}H_{12}^+$ peak, whereas the second distribution is characterized by peaks in the range $398 < m/z < 496$. Mass spectra of back samples are dominated by fragmentation and peaks associated to light PAHs as $C_{10}H_8^+$, $C_{11}H_9^+$, $C_{12}H_8^+$, etc. Positive SIMS spectra seem to be in good agreement with what achieved with L2MS technique.

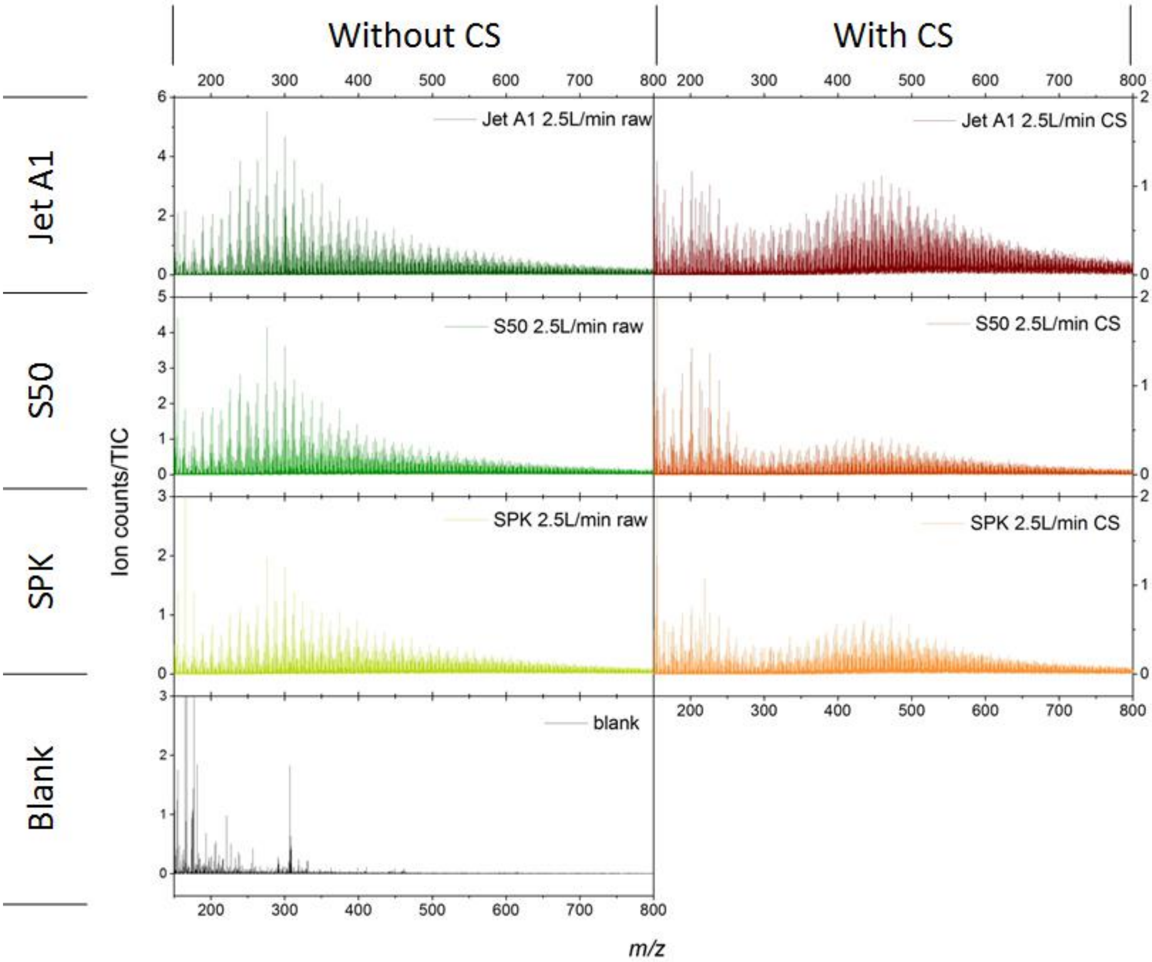

Figure 5.3.13. Positive SIMS mass spectra of front samples collected in the CAST exhaust using Jet A-1, SPK and S50 as fuel with 2.5 L/min oxidation air flow rate.

Negative SIMS mass spectra of front samples are mainly dominated by H^-, O^-, OH^-, C_n^- and C_nH^- clusters. Additional strong features correspond to C_nH^- clusters with $n \geq 4$ where n is an even number of carbons presenting. Strong signal of peaks associated to substrate (quartz fiber filter) is present in some samples. On the other hand, back samples are dominated by H^-, O^-, OH^- and C_2^-. The series of C_nH^- is not detected in this set of samples.

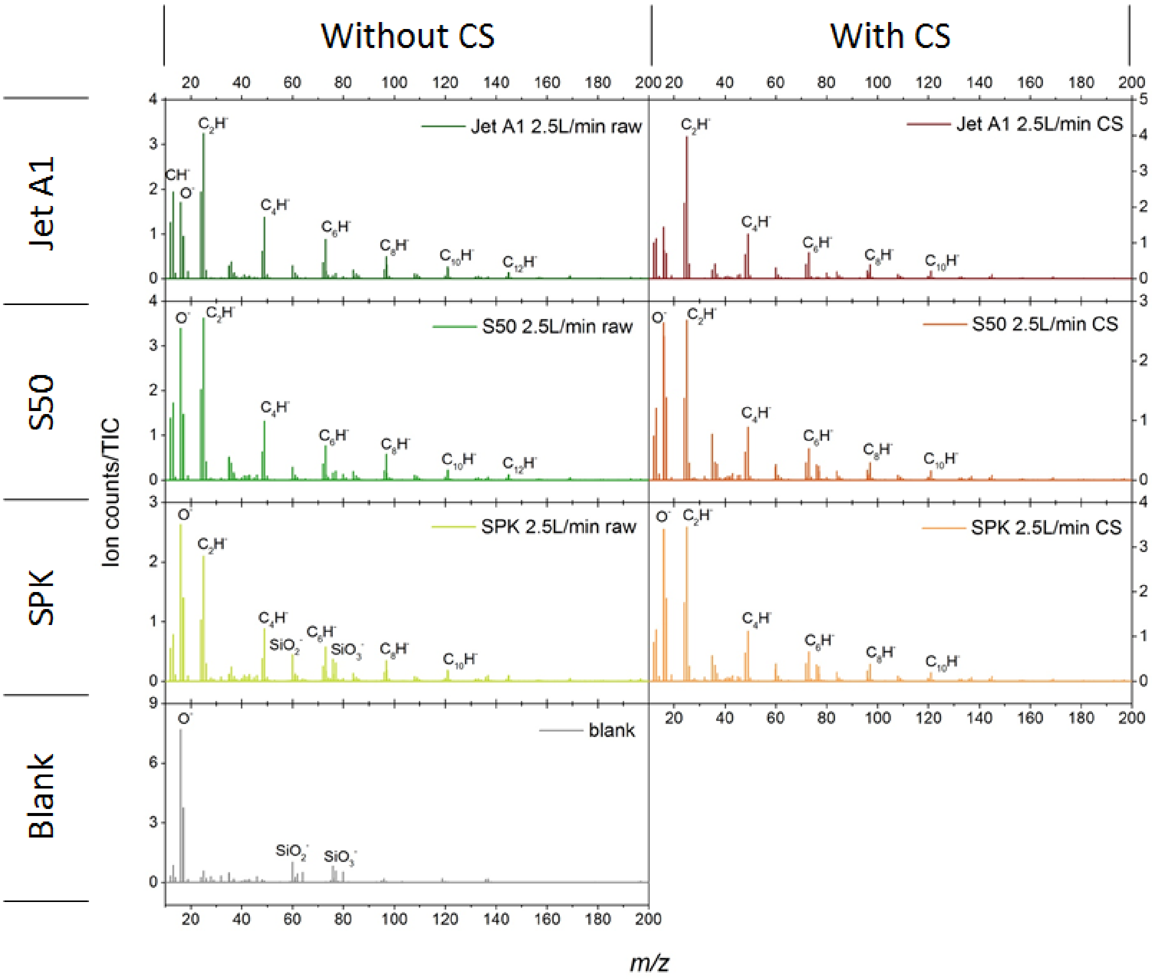

Figure 5.3.14. Negative SIMS mass spectra of front samples collected in the CAST exhaust using Jet A-1, SPK and S50 as fuel with 2.5 L/min oxidation air flow rate.

To better discriminate these samples, PCA is applied to both positive and negative SIMS mass spectra. A list of 153 peaks associated to hydrocarbon fragments and PAHs are chosen for PCA for the positive polarity SIMS spectra. The score plot of the first two principal components is displayed in Figure 5.3.15 and their corresponding coefficients are shown in Figure 5.3.16. As it can be seen in the figure, the first two principal components (representing 66% of the variance) separate well front and back samples as well as raw and CS samples. PC1 is composed of PAHs and series of $C_nH_2^+$ peaks with positive loadings, and fragments with negative loadings. In other words, this principal component distinguishes samples due to the proportion of PAHs in their mass spectra. Regarding PC1, raw front samples contain the highest content of PAHs, followed by CS front samples and raw back samples. CS back samples contain the lowest content of PAHs among the sample set. The second principal component discriminates mostly raw back samples from the others. PC2 is represented by low-hydrogenated fragments and a few light PAHs with positive coefficients, and of highly-hydrogenated fragments and heavy PAHs with negative coefficients.

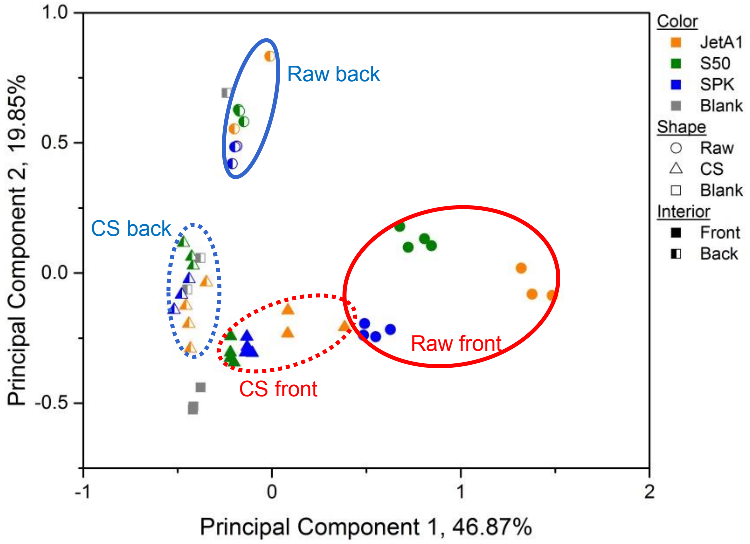

Figure 5.3.15. Score plot of PCA applied on positive SIMS mass spectra of liquid CAST samples

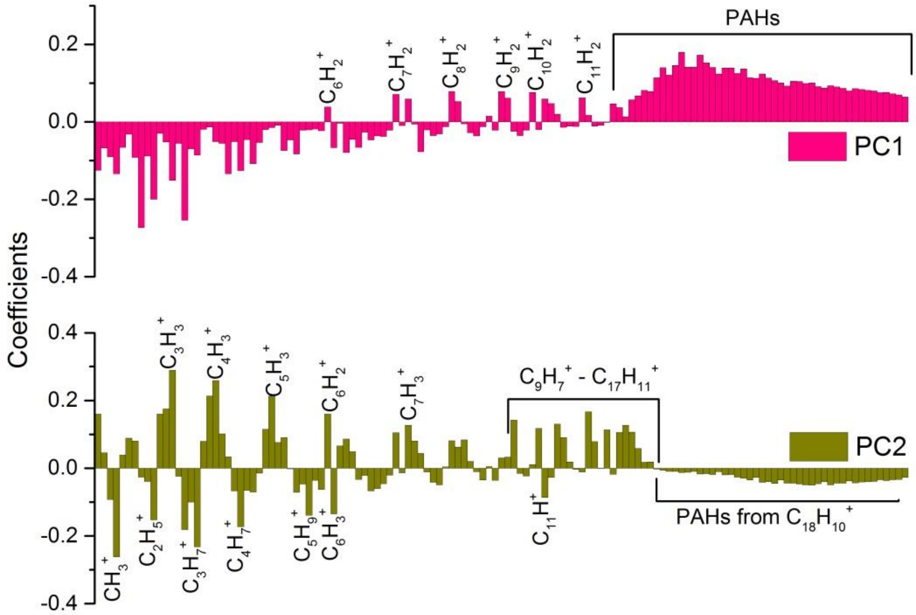

Figure 5.3.16. Loadings corresponding to PC1 and PC2 displayed in Figure 5.3.15

The result of PCA analysis applied on 223 detected peaks in negative SIMS mass spectra is presented in Figure 5.3.17 and Figure 5.3.18. The first two principal components represent more than 70% of the total variance obtained for this set of samples. PC1 is composed of peaks associated to the substrate as O^-, OH^-, SiO_2^-, SiO_3^-, etc. with its positive coefficients, and of peaks associated to the combustion byproducts deposited on filters as C_n^- and C_nH^- clusters. Regarding the discrimination given by PC1, Jet A-1 sample contains the highest quantity of combustion byproducts, followed by S50 samples and SPK samples. CS and raw back samples are also separated by PC1. PC2 is composed of mainly C_2^- with negative coefficients, and C_nH^- clusters with n even and ≥ 4 with positive coefficients. The PC2 separates remarkably front and back samples. The result is in good agreement with chapter 4, C_2^- is found as the indicator of elemental carbon as black carbon is deposited on back samples; and C_nH^- is found as marker for organic carbon. There is no noticeable separation among the back samples given by PC2.

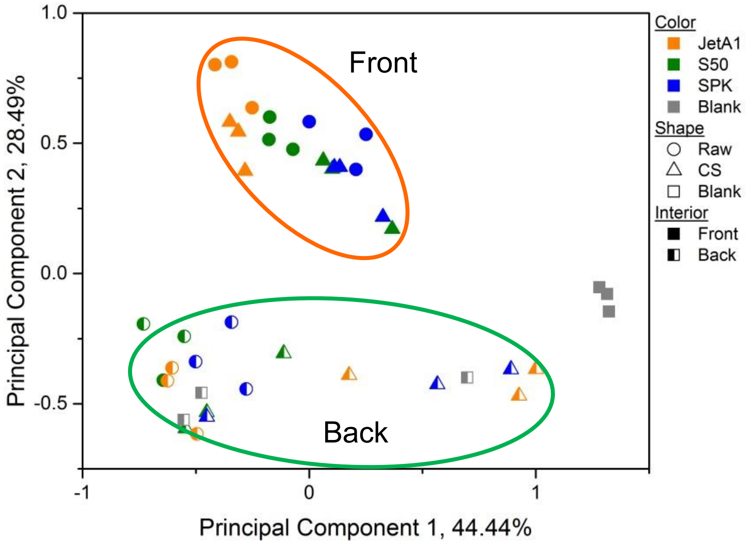

Figure 5.3.17. PCA applied on negative SIMS spectra of liquid CAST samples

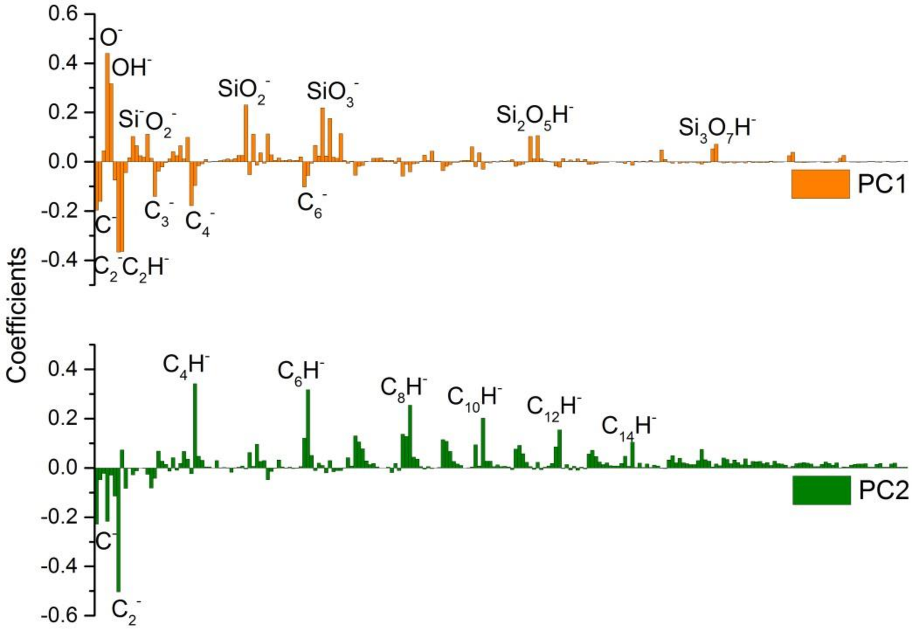

Figure 5.3.18. Coefficients corresponding to PC1 and PC2 presented in Figure 5.3.17

Regarding PCA results obtained with positive and negative SIMS mass spectra, the variation of total PAHs and $\mathrm{C}_n\mathrm{H}^-$ clusters in their respective mass spectra is calculated and presented in Figure 5.3.19. Positive mass spectra are normalized to partial ion counts – which include all hydrogenated fragments and peaks associated to PAH compounds. Negative SIMS mass spectra are normalized to their corresponding total ion counts before the calculation. Only $\mathrm{C}_n\mathrm{H}^-$ with n = 4, 6, 8 are chosen for the calculation. The same trend is obtained between two front and back sample sets as front samples show a higher total PAH content and total $\mathrm{C}_n\mathrm{H}^-$ than back samples. Additionally, with the same fuel, CS samples always show an inferior value of PAHs and $\mathrm{C}_n\mathrm{H}^-$ than raw ones, for both front and back samples, proving the good performance of the CS in removing the organic content from the exhaust emissions. With the same condition of combustion, the total PAH signal and $\mathrm{C}_n\mathrm{H}^-$ decrease in the order Jet A-1 > S50 > SPK, indicating that the use of alternative fuel, compared to conventional fossil fuel, is able to reduce to the aromatic fraction in the particulate-phase.

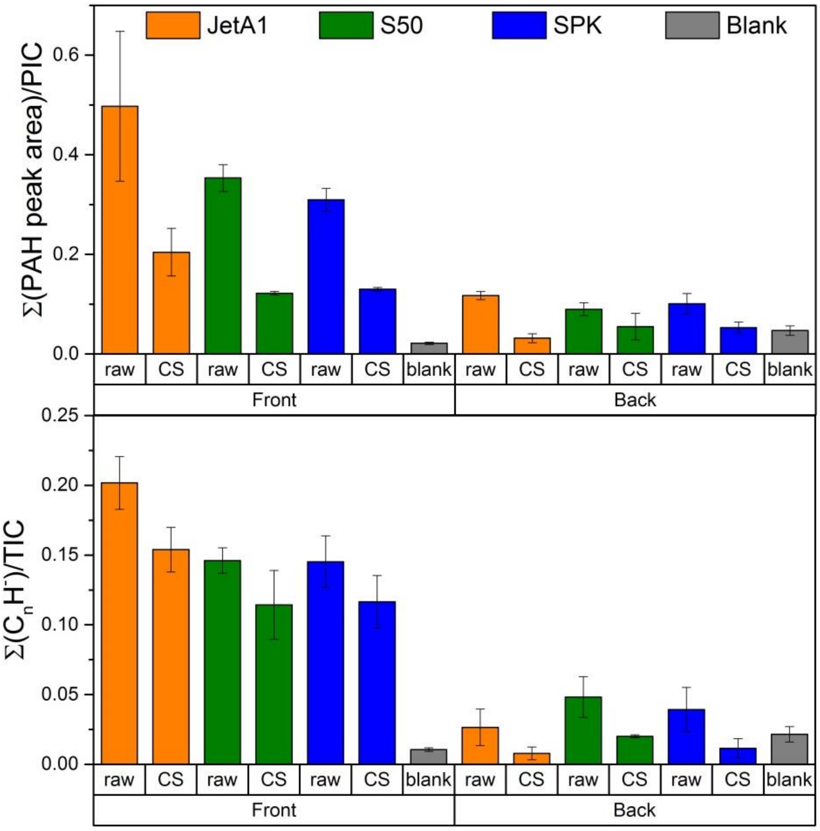

Figure 5.3.19. Variation of total PAH peaks area in positive SIMS mass spectra and total CnH- peak area in negative SIMS mass spectra obtained with Jet A-1, S50 and SPK burned with 2.5L/min oxidation flow.

5.4. Conclusions

By using conventional fossil fuel for aviation, Jet A-1, and an alternative fuel, SPK, we conclude that SPK, with high content of alkanes and cycloalkanes, is able to reduce the soot volume fraction and also the PAH content found at their surface from the exhaust. A catalytic stripper used in the exhaust sampling line shows good performance in removing (organic) species condensed on the particle surface with optimum efficiency in a mass range of aromatic species

(250 < *m*/*z* < 380). The performance of CS on the gas phase exhaust is complex. CS seems to interfere and allow some chemical reactions, leading to a slight shift of the PAH distribution to higher-mass aromatic species in the gas phase.

Chapter 6.

Conclusions & perspectives

6. Conclusions and perspectives

The main purpose of this PhD work was the study of the influence of different alternative fuels to the formation of soot and their precursors and their chemical composition. The work was conducted with two combustors: a swirled jet flame and a CAST instrument.

Different fuels were investigated: diesel, *n*-butanol, blend of diesel and *n*-butanol, Jet A-1 and SPK. N-butanol and a blend of 50%v/v n-butanol in diesel were studied as highly promising alternative fuels for diesel, whereas Synthetic Paraffinic Kerosene was investigated as an alternative aviation fuel to replace the conventional Jet A-1 fuel.

The analysis methods consist of in-situ techniques, as Laser Induced Incandescence and Laser Induced Fluorescence; and ex-situ techniques as Two-step Laser Mass Spectrometry and Time-of-Flight Secondary Ion Mass Spectrometry. LII and LIF have been using to study soot particles and their precursors for long time at PC2A laboratory (Desgroux et al. 1995; Schoemaecker Moreau et al. 2004; Mercier et al. 2005; Therssen et al. 2007; Desgroux et al. 2008; Lemaire 2008; Bejaoui 2012; Irimiea 2017; Mercier et al. 2019; etc.). L2MS has been implanted and developed by ANATRAC group for more than 15 years to study the chemical composition of particle surface (Mihesan et al. 2006; Bouvier et al. 2007; Thomson et al. 2007; Faccinetto et al. 2008; Ziskind et al. 2009; Faccinetto et al. 2011; Faccinetto et al. 2015; Irimiea 2017)

This work at first focused on the method development for a new technique to separate gas phase and particulate-bound polycyclic aromatic hydrocarbons using a two-filter system. To this purpose, the miniCAST instrument, which was provided by CORIA laboratory, was used as soot generator. The front filters collected particulate matter whereas the back filters collected the gas phase of the exhaust from the miniCAST. Four different set points were taken for different exhaust properties. The samples collected were mass analyzed with L2MS and ToF-SIMS. Upon the classification proposed by Bari et al. (2010), non-volatile PAHs, which have more than 4 benzene rings, mostly stay with particulate phase on front samples. Volatile PAHs, which have 1-2 aromatic rings, were only detected in the gas phase – which was captured on back filters. Semi-volatile PAHs (3-4 aromatic rings) appeared on both particulate matter and gas phase of the CAST exhaust. On the other hand, the total PAH content and $\mathrm{C}_n\mathrm{H}^-$ signal detected by SIMS shows good coherence with the organic carbon content; whereas C_2^- signal is found in line with the elemental carbon content found in previous works of (Yon, Bescond, and Ouf 2015; Bescond et al. 2016). Thus the two-filter system has good performance in the separation of two phases found in the exhaust of a combustor. This system was then applied for further work in this study.

The second part of the thesis has been dedicated to the soot and soot precursors formation in our home-made swirled jet burner with five different fuels: diesel, *n*-butanol, mixture, Jet A-1 and SPK. The swirled burner showed good stability and repeatability to burn these five liquid fuels directly without the involvement of any other pilot flames. Three excitation wavelengths at UV (266 nm), visible (532 nm) and infrared (1064 nm) were applied for the LII and LIF measurements. The LIF measurements were carried out with the UV and Vis excitations.

(i) Components of five fuels fluoresce strongly with the UV light, even for *n*-butanol, thus the UV-LIF signal was the most intense at the outlet of the nebulizer. The UV-LIF signal disappeared quickly at higher HABs due to the consumption of fuels for the combustion process. However, with this excitation, the emission spectra were red shifted with the HAB, indicating that the pool of fluorescent species changes along the flame.

(ii) For the first time, fluorescence signal obtained with visible excitation wavelength in the diesel, mixture and Jet A-1 flames showed a bimodal profile. The bimodal only appeared in the flames of fuels containing aromatic species. The first peak of the bimodal Vis-LIF appeared with the decrease of UV-LIF. There was a blue shift in the LIF spectra of the first peak zone, implying the evolution of the pool of these fluorescent species. Soot particles have not formed at this zone yet because the temperature, measured by a K-type thermocouple, was not high enough for the formation of soot. The second peak of Vis-LIF profile starts with the decrease of the first peak. Fluorescence emission spectra in this zone are identical even for different fuels, indicating that the composition of soot precursors are mostly identical for different fuels and the nature of fuels does not influence or influence very little the nature of these species.

(iii) LII signals obtained from the Vis and the IR excitations showed good coherence. By using a calibrated radiance source as the integrating Sphere, the absolute soot volume fraction was determined with the LII signals observed from the ICCD camera. The advantage of this direct calibration method is that no other additional methods or a standard flame needs to be used.

(iv) Combination in-siu and ex-situ results, five different classes are proposed for the species present in these flames. Class A corresponds to the species present in fuels. Class B species is proposed for the pyrogenic species which fluoresce with 266 nm excitation. The UV-LIF signal is attributed by the presence of class A and class B in the flame. The fluorescent species which attribute to the first peak of Vis-LIF are classified as class C. This class of species is not monomer of PAH. The nature of these species is still unknown and need more investigation. Class D is presumed to be responsible for the second peak of Vis-LIF signal. It might include multitude of different species as gas phase complexes, soot coating, dimers of PAHs, etc. Both class C and class D are precursors of soot particles and they cohabitate in the flame.

Three flames burning conventional and alternative automobile fuels were sampled with the two-filter system. The analyzes of the combustion by-product samples with L2MS and SIMS showed an evolution of the surface chemical composition of soot particles sampled at different HABs. The total PAHs signal detected with L2MS showed good coherence with the second peak of the Vis-LIF signal, whereas the total PAH signal and the sum of $\mathrm{C}_n\mathrm{H}^-$ (n = 4, 6, 8) observed from SIMS covered both pyrogenic and petrogenic zones of the Vis-LIF. C_2^- carbon cluster observed from negative SIMS showed a good consistence with the LII signal in the diesel and mixture sooting flames, but not in the n-butanol flame.

N-butanol produced approximately 5000 times less soot than diesel in swirled jet flames of the same heating value. By blending 50%v/v of *n*-butanol in diesel, the amount of soot produced diminished only with a factor of 2. The characteristics of soot particles formed in the *n*-butanol flame showed a similarity with nascent soot particles produced in nucleation flames, i.e. they did not change their size with HABs and their LII fluence curves showed linear trend. For aeronautic fuels, SPK produced ≈3 times less soot than Jet A-1. The soot volume fraction varies proportionally with pyrogenic Vis-LIF signal for five flames, indicating that soot precursors, which are detected by Vis-LIF, play an essential role in the formation of soot.

The third part of this PhD work involved the characterization campaign with liquid CAST device, which was developed by ONERA laboratory. This device is able to burn different types of liquid fuel with a help of a pilot flame. Jet A-1, SPK and a mixture of them were used as fuels in CAST. The exhaust of CAST was characterized with the LII technique and was sampled with the two-filter system. These samples were later analyzed using L2MS and SIMS. The exhaust flow was characterized with and without Catalytic Stripper treatment. The results showed that with the same condition SPK produced less soot and PAHs in exhaust emissions than the Jet A-1 fuel. CS showed a good performance in removing species condensed on the particulate matter; especially it was more efficient in removing aromatic species in the range *m/z* 250 – 380. The performance of CS on the gas phase exhaust is complex. CS seems to interfere and allow some chemical reactions, leading to a slight shift of the PAH distribution to higher-mass aromatic species in the gas phase.

This work brings new research opportunities:

- *N*-butanol is an interesting fuel that needs to be investigated more in the future. A study with a scanning mobility particle sizer to get an insight on the size of nascent soot particles in this flame can be carried out in the future.
- As mentioned earlier, temperature is an important factor in soot formation. Measuring temperature in "sooting" zone of diesel and *n*-butanol can help to understand why this biofuel does not produce much PM.
- The new direct calibration method to derive absolute volume fraction from LII signal obtained with ICCD camera needs to be validated. The validation can be carried out on a laminar diffusion flame with other classic methods as Laser extinction or Cavity ring down to compare the results.
- It is necessary to investigate the chemical nature of class C and class D species proposing in this work as they play an important role in the soot formation.

References

Abdel-Shafy, Hussein I., and Mona S.M. Mansour
2016 A Review on Polycyclic Aromatic Hydrocarbons: Source, Environmental Impact, Effect on Human Health and Remediation. Egyptian Journal of Petroleum 25(1): 107–123.

Abrahamson, Joseph P., Joseph Zelina, M. Gurhan Andac, and Randy L. Vander Wal
2016 Predictive Model Development for Aviation Black Carbon Mass Emissions from Alternative and Conventional Fuels at Ground and Cruise. Environmental Science & Technology 50(21): 12048–12055.

Adamson, B. D., S. A. Skeen, M. Ahmed, and N. Hansen
2018 Detection of Aliphatically Bridged Multi-Core Polycyclic Aromatic Hydrocarbons in Sooting Flames with Atmospheric-Sampling High-Resolution Tandem Mass Spectrometry. The Journal of Physical Chemistry A 122(48): 9338–9349.

Allouis, C., B. Apicella, R. Barbella, et al.
2003 Monitoring of Fuel Consumption and Aromatics Formation in a Kerosene Spray Flame as Characterized by Fluorescence Spectroscopy. Chemosphere 51(10): 1097–1102.

An, Yan-zhao, Sheng-ping Teng, Yi-qiang Pei, et al.
2016 An Experimental Study of Polycyclic Aromatic Hydrocarbons and Soot Emissions from a GDI Engine Fueled with Commercial Gasoline. Fuel 164: 160–171.

Axelsson, B., R. Collin, and P.E. Bengtsson
2001 Laser-Induced Incandescence for Soot Particle Size and Volume Fraction Measurements Using on-Line Extinction Calibration: Applied Physics B 72(3): 367–372.

Baena-Zambrana, S., S.L. Repetto, C.P. Lawson, and J.K.-W. Lam
2013 Behaviour of Water in Jet Fuel—A Literature Review. Progress in Aerospace Sciences 60: 35–44.

Balthasar, Michael
2000 Detailed Soot Modeling in Laminar and Turbulent Reacting Flows. Lund, Sweden.

Bari, Md. Aynul, Günter Baumbach, Bertram Kuch, and Günter Scheffknecht
2010 Particle-Phase Concentrations of Polycyclic Aromatic Hydrocarbons in Ambient Air of Rural Residential Areas in Southern Germany. Air Quality, Atmosphere & Health 3(2): 103–116.

Bejaoui, S., R. Lemaire, P. Desgroux, and E. Therssen
2014 Experimental Study of the E(m, λ)/E(m, 1064) Ratio as a Function of Wavelength, Fuel Type, Height above the Burner and Temperature. Applied Physics B 116(2): 313–323.

Bejaoui, Salma
2012 Etude spectroscopie des suies et de leurs précurseurs par Incandescence et Fluorescence Induite par laser. Université Lille Sciences et Technologies.

Bejaoui, Salma, Sébastien Batut, Eric Therssen, et al.
2015 Measurements and Modeling of Laser-Induced Incandescence of Soot at Different Heights in a Flat Premixed Flame. Applied Physics B 118(3): 449–469.

Bejaoui, Salma, Xavier Mercier, Pascale Desgroux, and Eric Therssen
2014 Laser Induced Fluorescence Spectroscopy of Aromatic Species Produced in Atmospheric Sooting Flames Using UV and Visible Excitation Wavelengths. Combustion and Flame 161(10): 2479–2491.

van den Berg, Robert A., Huub CJ Hoefsloot, Johan A Westerhuis, Age K Smilde, and Mariët J van der Werf
2006 Centering, Scaling, and Transformations: Improving the Biological Information Content of Metabolomics Data. BMC Genomics 7(142). http://www/biomedcentral.com/1471/2164/7/142.

Bescond, A., J. Yon, F.-X. Ouf, et al.
2016 Soot Optical Properties Determined by Analyzing Extinction Spectra in the Visible Near-UV: Toward an Optical Speciation According to Constituents and Structure. Journal of Aerosol Science 101: 118–132.

Bester, Nigel, and Andy Yates
2009 Assessment of the Operational Performance of Fischer-Tropsch Synthetic-Paraffinic Kerosene in a T63 Gas Turbine Compared to Conventional Jet A-1 Fuel. *In* Volume 2: Combustion, Fuels and Emissions Pp. 1063–1077. Orlando, Florida, USA: ASME. http://proceedings.asmedigitalcollection.asme.org/proceeding.aspx?articleid=1646803, accessed August 1, 2019.

Betrancourt, Christopher
2017 Experimental Study of Soot Formation in Laminar Premixed Flames of Fuels of Interest for Automobile and Aeronautics: A Focus on the Soot Nucleation Process. Université Lille Sciences et Technologies.

Betrancourt, Christopher, Fengshan Liu, Pascale Desgroux, et al.
2017 Investigation of the Size of the Incandescent Incipient Soot Particles in Premixed Sooting and Nucleation Flames of *n* -Butane Using LII, HIM, and 1 Nm-SMPS. Aerosol Science and Technology 51(8): 916–935.

Blin, J., C. Brunschwig, A. Chapuis, et al.
2013 Characteristics of Vegetable Oils for Use as Fuel in Stationary Diesel Engines—Towards Specifications for a Standard in West Africa. Renewable and Sustainable Energy Reviews 22: 580–597.

Boot, Michael, Peter Frijters, Carlo Luijten, et al.
2009 Cyclic Oxygenates: A New Class of Second-Generation Biofuels for Diesel Engines? †. Energy & Fuels 23(4): 1808–1817.

Bouvier, Y., C. Mihesan, M. Ziskind, et al.

2007 Molecular Species Adsorbed on Soot Particles Issued from Low Sooting Methane and Acetylene Laminar Flames: A Laser-Based Experiment. Proceedings of the Combustion Institute 31(1): 841–849.

Braun-Unkhoff, M., N. Hansen, T. Methling, K. Moshammer, and B. Yang
2017 The Influence of i -Butanol Addition to the Chemistry of Premixed 1,3-Butadiene Flames. Proceedings of the Combustion Institute 36(1): 1311–1319.

Bravo-Sánchez, Micael G., Gustavo A. Iglesias-Silva, Alejandro Estrada-Baltazar, and Kenneth R. Hall
2010 Densities and Viscosities of Binary Mixtures of *n* -Butanol with 2-Butanol, Isobutanol, and *Tert* -Butanol from (303.15 to 343.15) K. Journal of Chemical & Engineering Data 55(6): 2310–2315.

Bryselbout, Carine, Pascale Henner, and Éric Lichtfouse
1998 Fossil Fuel Biomarkers in Plant Waxes as Pollution Parameters. Science of The Total Environment 222(3): 201–204.

Bünger, J., J. Krahl, K. Baum, et al.
2000 Cytotoxic and Mutagenic Effects, Particle Size and Concentration Analysis of Diesel Engine Emissions Using Biodiesel and Petrol Diesel as Fuel. Archives of Toxicology 74(8): 490–498.

Bünger, Jürgen, Jürgen Krahl, Axel Munack, et al.
2007 Strong Mutagenic Effects of Diesel Engine Emissions Using Vegetable Oil as Fuel. Archives of Toxicology 81(8): 599–603.

Cadrazco, Marlon, John R. Agudelo, Luz Y. Orozco, and Verónica Estrada
2017 Genotoxicity of Diesel Particulate Matter Emitted by Port-Injection of Hydrous Ethanol and n-Butanol. Journal of Energy Resources Technology 139(4): 042207.

Carpentier, Yvain, Thomas Pino, and Philippe Bréchignac
2013 R2PI Spectroscopy of Aromatic Molecules Produced in an Ethylene-Rich Flame. The Journal of Physical Chemistry A 117(39): 10092–10104.

Chakarova, Svetla D., and Elsebeth Schröder
2005 Van Der Waals Interactions of the Benzene Dimer: Towards Treatment of Polycyclic Aromatic Hydrocarbon Dimers. Materials Science and Engineering: C 25(5–8): 787–792.

Chalmers, Jennifer L. Y., Craig R. Davison, Wajid Ali Chishty, et al.
2012 Evaluation of the Impact of Alternative Fuel Use on the Emissions and Performance of a Service-Exposed T56 Engine. *In* Volume 1: Aircraft Engine; Ceramics; Coal, Biomass and Alternative Fuels; Controls, Diagnostics and Instrumentation P. 425. Copenhagen, Denmark: ASME. http://proceedings.asmedigitalcollection.asme.org/proceeding.aspx?doi=10.1115/GT2012-69978, accessed August 1, 2019.

Chan, Tak W., Wajid Chishty, Craig Davison, and David Buote

2015 Characterization of the Ultrafine and Black Carbon Emissions from Different Aviation Alternative Fuels. SAE International Journal of Fuels and Lubricants 8(3): 515–526.

Chen, Beiling, Xinlei Liu, Haifeng Liu, et al.
2017 Soot Reduction Effects of the Addition of Four Butanol Isomers on Partially Premixed Flames of Diesel Surrogates. Combustion and Flame 177: 123–136.

Chen, Zheng, Zhenkuo Wu, Jingping Liu, and Chiafon Lee
2014 Combustion and Emissions Characteristics of High N-Butanol/Diesel Ratio Blend in a Heavy-Duty Diesel Engine and EGR Impact. Energy Conversion and Management 78: 787–795.

Cheng, A. S., Robert W. Dibble, and Bruce A. Buchholz
2002 The Effect of Oxygenates on Diesel Engine Particulate Matter. *In* Pp. 2002-01–1705. https://www.sae.org/content/2002-01-1705/, accessed July 9, 2019.

Choi, Byungchul, and Xiaolong Jiang
2015 Individual Hydrocarbons and Particulate Matter Emission from a Turbocharged CRDI Diesel Engine Fueled with n -Butanol/Diesel Blends. Fuel 154: 188–195.

Christie, Simon, Prem Lobo, David Lee, and David Raper
2017 Gas Turbine Engine Nonvolatile Particulate Matter Mass Emissions: Correlation with Smoke Number for Conventional and Alternative Fuel Blends. Environmental Science & Technology 51(2): 988–996.

Ciajolo, A., B. Apicella, R. Barbella, et al.
2001 Depletion of Fuel Aromatic Components and Formation of Aromatic Species in a Spray Flame as Characterized by Fluorescence Spectroscopy. Energy & Fuels 15(4): 987–995.

Corporan, Edwin, Matthew J. DeWitt, Christopher D. Klingshirn, et al.
2012 Comparisons of Emissions Characteristics of Several Turbine Engines Burning Fischer-Tropsch and Hydroprocessed Esters and Fatty Acids Alternative Jet Fuels. *In* Volume 2: Combustion, Fuels and Emissions, Parts A and B P. 425. Copenhagen, Denmark: ASME. http://proceedings.asmedigitalcollection.asme.org/proceeding.aspx?doi=10.1115/GT2012-68656, accessed June 17, 2019.

Corporan, Edwin, Tim Edwards, Linda Shafer, et al.
2011 Chemical, Thermal Stability, Seal Swell, and Emissions Studies of Alternative Jet Fuels. Energy & Fuels 25(3): 955–966.

Cushman, Cody, Julia Zakel, Landon S. Fisher, et al.
2018 Sample Charging in ToF-SIMS: How It Affects the Data That Are Collected and How to Reduce It. Vacuum Technology & Coating.

Damyanov, Aleksandar
2019 Alcoholic Fuels in Diesel Engines. Methanol, Ethanol and Butanol. *In* Zukünftige Kraftstoffe. Wolfgang Maus, ed. Pp. 850–862. Berlin, Heidelberg: Springer Berlin Heidelberg. http://link.springer.com/10.1007/978-3-662-58006-6_33, accessed June 12, 2019.

D'Anna, Andrea, Mariano Sirignano, and John Kent
2010 A Model of Particle Nucleation in Premixed Ethylene Flames. Combustion and Flame 157(11): 2106–2115.

Delhay, J., P. Desgroux, E. Therssen, et al.
2009 Soot Volume Fraction Measurements in Aero-Engine Exhausts Using Extinction-Calibrated Backward Laser-Induced Incandescence. Applied Physics B 95(4): 825–838.

de_Richter, Renaud, and Sylvain Caillol
2011 Fighting Global Warming: The Potential of Photocatalysis against CO2, CH4, N2O, CFCs, Tropospheric O3, BC and Other Major Contributors to Climate Change. Journal of Photochemistry and Photobiology C: Photochemistry Reviews 12(1): 1–19.

Desgroux, P., L. Gasnot, J. F. Pauwels, and L. R. Sochet
1995 Correction of LIF Temperature Measurements for Laser Absorption and Fluorescence Trapping in a Flame: Application to the Thermal Perturbation Study Induced by a Sampling Probe. Applied Physics B Laser and Optics 61(4): 401–407.

Desgroux, P., X. Mercier, B. Lefort, et al.
2008 Soot Volume Fraction Measurement in Low-Pressure Methane Flames by Combining Laser-Induced Incandescence and Cavity Ring-down Spectroscopy: Effect of Pressure on Soot Formation. Combustion and Flame 155(1–2): 289–301.

Desgroux, Pascale, Alessandro Faccinetto, Xavier Mercier, et al.
2017 Comparative Study of the Soot Formation Process in a "Nucleation" and a "Sooting" Low Pressure Premixed Methane Flame. Combustion and Flame 184: 153–166.

Desgroux, Pascale, Xavier Mercier, and Kevin A. Thomson
2013 Study of the Formation of Soot and Its Precursors in Flames Using Optical Diagnostics. Proceedings of the Combustion Institute 34(1): 1713–1738.

Dobbins, R.A., R.A. Fletcher, and H.-C. Chang
1998 The Evolution of Soot Precursor Particles in a Diffusion Flame. Combustion and Flame 115(3): 285–298.

Doğan, Oğuzhan
2011 The Influence of N-Butanol/Diesel Fuel Blends Utilization on a Small Diesel Engine Performance and Emissions. Fuel 90(7): 2467–2472.

Dorado, M
2003 Exhaust Emissions from a Diesel Engine Fueled with Transesterified Waste Olive Oil⋆. Fuel 82(11): 1311–1315.

Elghawi, U.M., A. Mayouf, A. Tsolakis, and M.L. Wyszynski
2010 Vapour-Phase and Particulate-Bound PAHs Profile Generated by a (SI/HCCI) Engine from a Winter Grade Commercial Gasoline Fuel. Fuel 89(8): 2019–2025.

Esteban, Bernat, Jordi-Roger Riba, Grau Baquero, Antoni Rius, and Rita Puig
2012 Temperature Dependence of Density and Viscosity of Vegetable Oils. Biomass and Bioenergy 42: 164–171.

European Aviation Environmental Report
2019. European Union Aviation Safety Agency.

Ewinger, H. -P., J. Goschnick, and H. J. Ache
1991 Analysis of Organic Compounds with SNMS. Fresenius' Journal of Analytical Chemistry 341(1–2): 17–19.

Faccinetto, A., K. Thomson, M. Ziskind, and C. Focsa
2008 Coupling of Desorption and Photoionization Processes in Two-Step Laser Mass Spectrometry of Polycyclic Aromatic Hydrocarbons. Applied Physics A 92(4): 969–974.

Faccinetto, Alessandro
2009 High Sensitivity Detection of Polycyclic Aromatic Hydrocarbons Desorbed from Soot Particles Using Laser Desorption/Laser Ionization/Time-of-Flight Mass Spectrometry. An Approach for Studying the Soot Grwoth Process in Flames. Lille 1.

Faccinetto, Alessandro, Pascale Desgroux, Michael Ziskind, Eric Therssen, and Cristian Focsa
2011 High-Sensitivity Detection of Polycyclic Aromatic Hydrocarbons Adsorbed onto Soot Particles Using Laser Desorption/Laser Ionization/Time-of-Flight Mass Spectrometry: An Approach to Studying the Soot Inception Process in Low-Pressure Flames. Combustion and Flame 158(2): 227–239.

Faccinetto, Alessandro, Cristian Focsa, Pascale Desgroux, and Michael Ziskind
2015 Progress toward the Quantitative Analysis of PAHs Adsorbed on Soot by Laser Desorption/Laser Ionization/Time-of-Flight Mass Spectrometry. Environmental Science & Technology 49(17): 10510–10520.

Frenklach, Michael
2002 Reaction Mechanism of Soot Formation in Flames. Physical Chemistry Chemical Physics 4(11): 2028–2037.

Frenklach, Michael, and Hai Wang
1991 Detailed Modeling of Soot Particle Nucleation and Growth. Symposium (International) on Combustion 23(1): 1559–1566.

Geng, Limin, Yang Chen, Xubo Chen, and Chia-fon F. Lee
2019 Study on Combustion Characteristics and Particulate Emissions of a Common-Rail Diesel Engine Fueled with n-Butanol and Waste Cooking Oil Blends. Journal of the Energy Institute 92(3): 438–449.

Geng, Peng, Erming Cao, Qinming Tan, and Lijiang Wei

2017 Effects of Alternative Fuels on the Combustion Characteristics and Emission Products from Diesel Engines: A Review. Renewable and Sustainable Energy Reviews 71: 523–534.

van Gessel, A F H, B Hrycak, M Jasiński, et al.
2013 Temperature and NO Density Measurements by LIF and OES on an Atmospheric Pressure Plasma Jet. Journal of Physics D: Applied Physics 46(9): 095201.

Geyer, S. M., M. J. Jacobus, and S. S. Lestz
1984 Comparison of Diesel Engine Performance and Emissions from Neat and Transesterified Vegetable Oils. Transactions of the ASAE 27(2): 375–381.

Giordana, Anna, Andrea Maranzana, and Glauco Tonachini
2011 Carbonaceous Nanoparticle Molecular Inception from Radical Addition and van Der Waals Coagulation of Polycyclic Aromatic Hydrocarbon-Based Systems. A Theoretical Study. The Journal of Physical Chemistry C 115(35): 17237–17251.

Glassman, Irvin
1989 Soot Formation in Combustion Processes. Symposium (International) on Combustion 22(1): 295–311.

Goulay, Fabien, Paul E. Schrader, Xerxes López-Yglesias, and Hope A. Michelsen
2013 A Data Set for Validation of Models of Laser-Induced Incandescence from Soot: Temporal Profiles of LII Signal and Particle Temperature. Applied Physics B 112(3): 287–306.

Graham, Dan
2013 The Complexities of the Basics of PCA (Part I). Paper presented at the the SIIMS XIX meeting, Jeju, South Korea. https://www.nb.uw.edu/mvsa/complexities-basics-pca-i.

Graham, Daniel J., and David G. Castner
2012 Multivariate Analysis of ToF-SIMS Data from Multicomponent Systems: The Why, When, and How. Biointerphases 7(1): 49.

Greenhouse Gases Reviewer
2018. European Environment Agency.

Gutiérrez-Antonio, C., F.I. Gómez-Castro, J.A. de Lira-Flores, and S. Hernández
2017 A Review on the Production Processes of Renewable Jet Fuel. Renewable and Sustainable Energy Reviews 79: 709–729.

Hileman, J.I., and R.W. Stratton
2014 Alternative Jet Fuel Feasibility. Transport Policy 34: 52–62.

Hindasageri, V., R. P. Vedula, and S. V. Prabhu
2013 Thermocouple Error Correction for Measuring the Flame Temperature with Determination of Emissivity and Heat Transfer Coefficient. Review of Scientific Instruments 84(2): 024902.

Homann, Klaus-Heinrich
1998 Fullerenes and Soot Formation— New Pathways to Large Particles in Flames. Angewandte Chemie International Edition 37(18): 2434–2451.

Huang, Di, Xin Hua, Guang-Li Xiu, et al.
2017 Secondary Ion Mass Spectrometry: The Application in the Analysis of Atmospheric Particulate Matter. Analytica Chimica Acta 989: 1–14.

Huang, Haozhong, Zhongju Li, Wenwen Teng, et al.
2019 Influence of N-Butanol-Diesel-PODE3-4 Fuels Coupled Pilot Injection Strategy on Combustion and Emission Characteristics of Diesel Engine. Fuel 236: 313–324.

Huang, Haozhong, Zhaojun Zhu, Jizhen Zhu, et al.
2019 Experimental and Numerical Study of Pre-Injection Effects on Diesel-n-Butanol Blends Combustion. Applied Energy 249: 377–391.

Huber, Franz J. T., Michael Altenhoff, and Stefan Will
2016 A Mobile System for a Comprehensive Online-Characterization of Nanoparticle Aggregates Based on Wide-Angle Light Scattering and Laser-Induced Incandescence. Review of Scientific Instruments 87(5): 053102.

ICAO Environmental Report 2016 - Aviation and Climate Change
2017. the Environment Branch of the International Civil Aviation Organization. https://www.icao.int/environmental-protection/Documents/ICAO%20Environmental%20Report%202016.pdf.

Irimiea, Cornelia
2017 Characterization of Soot Particles and Their Precursors by Coupling Laser-Based Techniques. Université Lille Sciences et Technologies.

Irimiea, Cornelia, Alessandro Faccinetto, Yvain Carpentier, et al.
2018 A Comprehensive Protocol for Chemical Analysis of Flame Combustion Emissions by Secondary Ion Mass Spectrometry. Rapid Communications in Mass Spectrometry 32(13): 1015–1025.

Irimiea, Cornelia, Alessandro Faccinetto, Xavier Mercier, et al.
2019 Unveiling Trends in Soot Nucleation and Growth: When Secondary Ion Mass Spectrometry Meets Statistical Analysis. Carbon 144: 815–830.

Jacobson, Mark Z.
2001 Strong Radiative Heating Value Due to the Mixing State of Black Carbon in Atmospheric Aerosols. Nature(409): 695–697.

Jaramillo, Isabel C., Anne Sturrock, Hossein Ghiassi, et al.
2018 Effects of Fuel Components and Combustion Particle Physicochemical Properties on

Toxicological Responses of Lung Cells. Journal of Environmental Science and Health, Part A 53(4): 295–309.

Jia, Guorui, Mingfa Yao, Haifeng Liu, et al.
2015 PAHs Formation Simulation in the Premixed Laminar Flames of TRF with Alcohol Addition Using a Semi-Detailed Combustion Mechanism. Fuel 155: 44–54.

Johansson, K. O., F. El Gabaly, P. E. Schrader, M. F. Campbell, and H. A. Michelsen
2017 Evolution of Maturity Levels of the Particle Surface and Bulk during Soot Growth and Oxidation in a Flame. Aerosol Science and Technology 51(12): 1333–1344.

Kanaveli, Ioanna-Panagiota, Maria Atzemi, and Evripidis Lois
2017 Predicting the Viscosity of Diesel/Biodiesel Blends. Fuel 199: 248–263.

Karcher, W., R. J. Fordham, J. J. Dubois, P. G. J. M. Glaude, and M. Ligthart
1985 Spectral Atlas of Polycyclic Aromatic Compounds.

Kasha, Michael
1950 Characterization of Electronic Transitions in Complex Molecules. Discussions of the Faraday Society 9: 14.

Kelesidis, Georgios A., and Sotiris E. Pratsinis
2019 Soot Light Absorption and Refractive Index during Agglomeration and Surface Growth. Proceedings of the Combustion Institute 37(1): 1177–1184.

Kim, Ki-Hyun, Shamin Ara Jahan, Ehsanul Kabir, and Richard J.C. Brown
2013 A Review of Airborne Polycyclic Aromatic Hydrocarbons (PAHs) and Their Human Health Effects. Environment International 60: 71–80.

Kirchner, U, R Vogt, C Natzeck, and J Goschnick
2003 Single Particle MS, SNMS, SIMS, XPS, and FTIR Spectroscopic Analysis of Soot Particles during the AIDA Campaign. Journal of Aerosol Science 34(10): 1323–1346.

Kooter, Ingeborg M., Marcel A.T.M. van Vugt, Aleksandra D. Jedynska, et al.
2011 Toxicological Characterization of Diesel Engine Emissions Using Biodiesel and a Closed Soot Filter. Atmospheric Environment 45(8): 1574–1580.

Krahl, J., K. Baum, U. Hackbarth, et al.
2001 GASEOUS COMPOUNDS, OZONE PRECURSORS, PARTICLE NUMBER AND PARTICLE SIZE DISTRIBUTIONS, AND MUTAGENIC EFFECTS DUE TO BIODIESEL. Transactions of the ASAE 44(2). http://elibrary.asabe.org/abstract.asp??JID=3&AID=4675&CID=t2001&v=44&i=2&T=1, accessed June 7, 2019.

Krahl, Jürgen, Jürgen Bünger, Olaf Schröder, Axel Munack, and Gerhard Knothe
2002 Exhaust Emissions and Health Effects of Particulate Matter from Agricultural Tractors

Operating on Rapeseed Oil Methyl Ester. Journal of the American Oil Chemists' Society 79(7): 717–724.

Kumar, Vasu, Dhruv Gupta, Mohd Waqar Naseer Siddiquee, Aksh Nagpal, and Naveen Kumar
2015 Performance and Emission Characteristics of N-Butanol and Iso-Butanol Diesel Blend Comparison. *In* Pp. 2015-01–2819. https://www.sae.org/content/2015-01-2819/, accessed June 12, 2019.

Lapuerta, Magín, Juan José Hernández, David Fernández-Rodríguez, and Alexis Cova-Bonillo
2017 Autoignition of Blends of n -Butanol and Ethanol with Diesel or Biodiesel Fuels in a Constant-Volume Combustion Chamber. Energy 118: 613–621.

Lapuerta, Magín, Jesús Sánchez-Valdepeñas, Javier Barba, et al.
2019 Analysis of Soot from the Use of Butanol Blends in a Euro 6 Diesel Engine. Energy & Fuels 33(3): 2265–2277.

Le Roy, Léna, Anais Bardyn, Christelle Briois, et al.
2015 COSIMA Calibration for the Detection and Characterization of the Cometary Solid Organic Matter. Planetary and Space Science 105: 1–25.

Lefevre, Guillaume, Jérôme Yon, Maxime Bouvier, Fengshan Liu, and Alexis Coppalle
2019 Impact of Organic Coating on Soot Angular and Spectral Scattering Properties. Environmental Science & Technology 53(11): 6383–6391.

Lemaire, R.
2008 Etude de l'impact de la combustion de différents types de carburants sur les caractéristiques physico-chimiques des particules de suie par couplage de l'Incadescence et de la Fluorescence Induite par Laser. Université Lille Sciences et Technologies.

Lemaire, R., E. Therssen, J. F. Pauwels, and P. Desgroux
2007 Experimental Comparison of Soot Formation in Turbulent Flames of Kerosene and Surrogate Model Fuels. *In* Combustion Generated Fine Carbonaceous Particles Pp. 619–636. KIT Scientific Publishing. http://espace2.etsmtl.ca/id/eprint/12886.

Li, M., G. Xu, Y. Zhao, G. Li, and Z. Wang
2019 Influence of N-Butanol Addition on C3H3 Formation in n-Butane Combustion. Kinetics and Catalysis 60(1): 8–20.

Li, Xinling, Chun Guan, Ke Yang, Chun Shun Cheung, and Zhen Huang
2019 Impact of Lower and Higher Alcohol Additions to Diesel on the Combustion and Emissions of a Direct-Injection Diesel Engine. Environmental Science and Pollution Research. http://link.springer.com/10.1007/s11356-019-05275-y, accessed June 12, 2019.

Li, Xue, Edmund Mupondwa, and Lope Tabil
2018 Technoeconomic Analysis of Biojet Fuel Production from Camelina at Commercial Scale: Case of Canadian Prairies. Bioresource Technology 249: 196–205.

Liati, A., D. Schreiber, P.A. Alpert, et al.
2019 Aircraft Soot from Conventional Fuels and Biofuels during Ground Idle and Climb-out Conditions: Electron Microscopy and X-Ray Micro-Spectroscopy. Environmental Pollution 247: 658–667.

Libalova, Helena, Pavel Rossner, Kristyna Vrbova, et al.
2016 Comparative Analysis of Toxic Responses of Organic Extracts from Diesel and Selected Alternative Fuels Engine Emissions in Human Lung BEAS-2B Cells. International Journal of Molecular Sciences 17(11): 1833.

Lindsley, W. G.
2016 Filter Pore Size and Aerosol Sample Collection. NIOSH Manual of Analytical Methods (NMAM) 5th: 1–14.

Liu, Fushui, Yang Hua, Han Wu, Chia-fon Lee, and Yikai Li
2018 Experimental Investigation of Polycyclic Aromatic Hydrocarbons Growth Characteristics of Gasoline Mixed with Methanol, Ethanol, or *n* -Butanol in Laminar Diffusion Flames. Energy & Fuels 32(6): 6823–6833.

Liu, Haifeng, Peng Zhang, Xinlei Liu, et al.
2018 Laser Diagnostics and Chemical Kinetic Analysis of PAHs and Soot in Co-Flow Partially Premixed Flames Using Diesel Surrogate and Oxygenated Additives of n-Butanol and DMF. Combustion and Flame 188: 129–141.

Lobo, Prem, Simon Christie, Bhupendra Khandelwal, Simon G. Blakey, and David W. Raper
2015 Evaluation of Non-Volatile Particulate Matter Emission Characteristics of an Aircraft Auxiliary Power Unit with Varying Alternative Jet Fuel Blend Ratios. Energy & Fuels 29(11): 7705–7711.

Malmborg, Vilhelm B., Axel C. Eriksson, Sandra Török, et al.
2019 Relating Aerosol Mass Spectra to Composition and Nanostructure of Soot Particles. Carbon 142: 535–546.

Mansmann, Raphael Andreas
2019 Multi-Color Time-Resolved Laser-Induced Incandescence for the Measurement of Soot and Nanoparticle Aerosols. DuEPublico: Duisburg-Essen Publications online, University of Duisburg-Essen, Germany. https://duepublico2.uni-due.de/receive/duepublico_mods_00070080, accessed June 24, 2019.

Mayama, Norihito, Yusuke Miura, Kentaro Misawa, et al.
2013 Characterization of Black Carbon in Fine Aerosol Particles Using High Lateral Resolution TOF-SIMS. Analytical Sciences: The International Journal of the Japan Society for Analytical Chemistry 29(4): 479–482.

McCoy, B.J., and C.Y. Cha

1974 Transport Phenomena in the Rarefied Gas Transition Regime. Chemical Engineering Science 29(2): 381–388.

McEnally, Charles S., and Lisa D. Pfefferle
2000 Experimental Study of Nonfuel Hydrocarbons and Soot in Coflowing Partially Premixed Ethylene/Air Flames. Combustion and Flame 121(4): 575–592.

McLafferty, Fred W., and František Tureček
1993 Interpretation of Mass Spectra. 4th ed. Mill Valley, Calif: University Science Books.

Mehta, Pramod S., and K. Anand
2009 Estimation of a Lower Heating Value of Vegetable Oil and Biodiesel Fuel. Energy & Fuels 23(8): 3893–3898.

Mercier, X., E. Therssen, J.F. Pauwels, and P. Desgroux
2005 Measurements of Absolute Concentration Profiles of C2 in Non-Sooting and Sooting Diffusion Flames by Coupling Cavity Ring-down Spectroscopy and Laser Induced Fluorescence. Proceedings of the Combustion Institute 30(1): 1655–1663.

Mercier, Xavier, Olivier Carrivain, Cornelia Irimiea, Alessandro Faccinetto, and Eric Therssen
2019 Dimers of PAHs: The Missing Pieces in the Soot Formation Process. Physical Chemistry Chemical Physics.

Michelsen, H.A.
2017 Probing Soot Formation, Chemical and Physical Evolution, and Oxidation: A Review of in Situ Diagnostic Techniques and Needs. Proceedings of the Combustion Institute 36(1): 717–735.

Michelsen, H.A., F. Liu, B.F. Kock, et al.
2007 Modeling Laser-Induced Incandescence of Soot: A Summary and Comparison of LII Models. Applied Physics B 87(3): 503–521.

Michelsen, H.A., C. Schulz, G.J. Smallwood, and S. Will
2015 Laser-Induced Incandescence: Particulate Diagnostics for Combustion, Atmospheric, and Industrial Applications. Progress in Energy and Combustion Science 51: 2–48.

Migliorini, F., K. A. Thomson, and G. J. Smallwood
2011 Investigation of Optical Properties of Aging Soot. Applied Physics B 104(2): 273–283.

Mihesan, C., M. Ziskind, E. Therssen, P. Desgroux, and C. Focsa
2006 IR Laser Resonant Desorption of Polycyclic Aromatic Hydrocarbons. Chemical Physics Letters 423(4–6): 407–412.

Mihesan, Maria Claudia
2007 Mise En Oeuvre et Caractérisation d’une Technique de Désorption Laser Couplée à La Spectrométrie de Masse Pour l’analyse d’hydrocarbures Aromatiques Polycycliques Adsorbés à La Surface de Particules de Suies. Lille 1.

Miller, Joshua, and Lingzhi Jin
2018 Global Progress toward Soot-Free Diesel Vehicels in 2018. The international council of clean transportation. https://www.theicct.org/publications/global-progress-toward-soot-free-diesel-vehicles-2018.

Minjares, R, D Wagner, and S Akbar
2014 Reducing Black Carbon Emissions from Diesel Vehicles: Impacts, Control Strategies, and Cost-Benefit Analysis. The World Bank. http://documents.worldbank.org/curated/en/329901468151500078/pdf/864850WP00PUBL0l0report002April2014.pdf.

Moore, Richard H., Kenneth L. Thornhill, Bernadett Weinzierl, et al.
2017 Biofuel Blending Reduces Particle Emissions from Aircraft Engines at Cruise Conditions. Nature 543(7645): 411–415.

Mouton, Thomas
2014 Analyse Des Processus de Nucléation et de Croissance Des Particules de Suie Dans Des Flammes Par Flourescence Induite Par Laser En Jet Froid Appliquée Aux Hydrocarbures Aromatiques Polycycliques et Par Incandescence Induite Par Laser. Lille 1.

Mouton, Thomas, Xavier Mercier, Maxime Wartel, Nathalie Lamoureux, and Pascale Desgroux
2013 Laser-Induced Incandescence Technique to Identify Soot Nucleation and Very Small Particles in Low-Pressure Methane Flames. Applied Physics B 112(3): 369–379.

Ngo, Linh Dan, Dumitru Duca, Jennifer A. Noble, Raouf Ikhenazene, and Marin Vojkovic
2019 Chemical Discrimination of the Particulate and Gas Phases of MiniCAST Exhausts Using a Two-Filter Collection Method. Aerosol Measurement Techniques.

Nguyen, Q.V., R.W. Dibble, C.D. Carter, G.J. Fiechtner, and R.S. Barlow
1996 Raman-LIF Measurements of Temperature, Major Species, OH, and NO in a Methane-Air Bunsen Flame. Combustion and Flame 105(4): 499–510.

Ni, T., J. A. Pinson, S. Gupta, and R. J. Santoro
1995 Two-Dimensional Imaging of Soot Volume Fraction by the Use of Laser-Induced Incandescence. Applied Optics 34(30): 7083.

Nigam, Poonam Singh, and Anoop Singh
2011 Production of Liquid Biofuels from Renewable Resources. Progress in Energy and Combustion Science 37(1): 52–68.

Olofsson, Nils-Erik, Johan Simonsson, Sandra Török, Henrik Bladh, and Per-Erik Bengtsson
2015 Evolution of Properties for Aging Soot in Premixed Flat Flames Studied by Laser-Induced Incandescence and Elastic Light Scattering. Applied Physics B 119(4): 669–683.

Orain, M., P. Baranger, C. Ledier, J. Apeloig, and F. Grisch
2014 Fluorescence Spectroscopy of Kerosene Vapour at High Temperatures and Pressures: Potential for Gas Turbines Measurements. Applied Physics B 116(3): 729–745.

Pagels, Joakim, Dabrina D. Dutcher, Mark R. Stolzenburg, et al.
2013 Fine-Particle Emissions from Solid Biofuel Combustion Studied with Single-Particle Mass Spectrometry: Identification of Markers for Organics, Soot, and Ash Components: CHEMISTRY OF BIOMASS COMBUSTION AEROSOLS. Journal of Geophysical Research: Atmospheres 118(2): 859–870.

Pan, Mingzhang, Rong Huang, Jinyang Liao, et al.
2019 Experimental Study of the Spray, Combustion, and Emission Performance of a Diesel Engine with High n-Pentanol Blending Ratios. Energy Conversion and Management 194: 1–10.

Pavlenko, Nikita, Stephanie Searle, and Adam Christensen
2019 The Cost of Supporting Alternative Jet Fuels in European Union. The international council on clean transportation.

Pearlson, Matthew, Christoph Wollersheim, and James Hileman
2013 A Techno-Economic Review of Hydroprocessed Renewable Esters and Fatty Acids for Jet Fuel Production. Biofuels, Bioproducts and Biorefining 7(1): 89–96.

Pei, Lei, Guilin Jiang, Bonnie J. Tyler, Larry L. Baxter, and Matthew R. Linford
2008 Time-of-Flight Secondary Ion Mass Spectrometry of a Range of Coal Samples: A Chemometrics (PCA, Cluster, and PLS) Analysis. Energy & Fuels 22(2): 1059–1072.

Pelucchi, Matteo, Carlo Cavallotti, Eliseo Ranzi, Alessio Frassoldati, and Tiziano Faravelli
2016 Relative Reactivity of Oxygenated Fuels: Alcohols, Aldehydes, Ketones, and Methyl Esters. Energy & Fuels 30(10): 8665–8679.

Petarca, Luigi, and Francesco Marconi
1989 Fluorescence Spectra and Polycyclic Aromatic Species in a N-Heptane Diffusion Flame. Combustion and Flame 78(3–4): 308–325.

Petrov, Aleksandr A
1987 Petroleum Hydrocarbons. Berlin, Heidelberg: Springer Berlin Heidelberg. http://public.eblib.com/choice/publicfullrecord.aspx?p=3091357, accessed April 11, 2019.

Pickett, Lyle M., and Dennis L. Siebers
2003 Fuel Effects on Soot Processes of Fuel Jets at DI Diesel Conditions. *In* . http://papers.sae.org/2003-01-3080/, accessed February 15, 2017.

Popovicheva, Olga B., Natalia K. Shonija, Jaroslav Schwarz, et al.
2017 Chemical Composition of Diesel/Biodiesel Particulate Exhaust by FTIR Spectroscopy and Mass Spectrometry: Impact of Fuel and Driving Cycle. Aerosol and Air Quality Research 17(7): 1717–1734.

Rajesh Kumar, B., and S. Saravanan
2016 Use of Higher Alcohol Biofuels in Diesel Engines: A Review. Renewable and Sustainable Energy Reviews 60: 84–115.

Rakopoulos, D.C., C.D. Rakopoulos, E.G. Giakoumis, A.M. Dimaratos, and D.C. Kyritsis
2010 Effects of Butanol–Diesel Fuel Blends on the Performance and Emissions of a High-Speed DI Diesel Engine. Energy Conversion and Management 51(10): 1989–1997.

Rakopoulos, D.C., C.D. Rakopoulos, R.G. Papagiannakis, and D.C. Kyritsis
2011 Combustion Heat Release Analysis of Ethanol or N-Butanol Diesel Fuel Blends in Heavy-Duty DI Diesel Engine. Fuel 90(5): 1855–1867.

Ramanathan, V., and G. Carmichael
2008 Global and Regional Climate Changes Due to Black Carbon. Nature Geoscience 1(4): 221–227.

Richter, H, and J.B Howard
2000 Formation of Polycyclic Aromatic Hydrocarbons and Their Growth to Soot—a Review of Chemical Reaction Pathways. Progress in Energy and Combustion Science 26(4–6): 565–608.

Sabbah, Hassan, Ludovic Biennier, Stephen J. Klippenstein, Ian R. Sims, and Bertrand R. Rowe
2010 Exploring the Role of PAHs in the Formation of Soot: Pyrene Dimerization. The Journal of Physical Chemistry Letters 1(19): 2962–2967.

Saffaripour, Meghdad, Parham Zabeti, Mohammadreza Kholghy, and Murray J. Thomson
2011 An Experimental Comparison of the Sooting Behavior of Synthetic Jet Fuels. Energy & Fuels 25(12): 5584–5593.

Saxena, Mohit Raj, and Rakesh Kumar Maurya
2016 Effect of Butanol Blends on Nano Particle Emissions from a Stationary Conventional Diesel Engine. Aerosol and Air Quality Research 16(9): 2255–2266.

Schoemaecker Moreau, C., E. Therssen, X. Mercier, J.F. Pauwels, and P. Desgroux
2004 Two-Color Laser-Induced Incandescence and Cavity Ring-down Spectroscopy for Sensitive and Quantitative Imaging of Soot and PAHs in Flames. Applied Physics B 78(3–4): 485–492.

Schumacher, L.G., S.C. Borgelt, D. Fosseen, W. Goetz, and W.G. Hires
1996 Heavy-Duty Engine Exhaust Emission Tests Using Methyl Ester Soybean Oil/Diesel Fuel Blends. Bioresource Technology 57(1): 31–36.

Shaddix, Christopher R., Joel E. Harrington, and Kermit C. Smyth
1994 Quantitative Measurements of Enhanced Soot Production in a Flickering Methane/Air Diffusion Flame. Combustion and Flame 99(3–4): 723–732.

Shah, A., S. S. Thipse, A. Tyagi, et al.
2011 Literature Review and Simulation of Dual Fuel Diesel-CNG Engines. *In* Pp. 2011-26–0001. https://www.sae.org/content/2011-26-0001/, accessed August 21, 2019.

Shiraiwa, Manabu, Kathrin Selzle, and Ulrich Pöschl

2012 Hazardous Components and Health Effects of Atmospheric Aerosol Particles: Reactive Oxygen Species, Soot, Polycyclic Aromatic Compounds and Allergenic Proteins. Free Radical Research 46(8): 927–939.

Siljeström, Sandra, Tomas Hode, Jukka Lausmaa, et al.
2009 Detection of Organic Biomarkers in Crude Oils Using ToF-SIMS. Organic Geochemistry 40(1): 135–143.

Smallwood, G. J.
2009 A Critique of Laser-Induced Incandescence for the Measurement of Soot. Cranfield University. https://dspace.lib.cranfield.ac.uk/bitstream/handle/1826/5407/Gregory_J_Smallwood_Thesis_2009.pdf?sequence=1.

Smyth, K
1997 Aspects of Soot Dynamics as Revealed by Measurements of Broadband Fluorescence and Flame Luminosity in Flickering Diffusion Flames. Combustion and Flame 111(3): 185–194.

Snelling, David R., Gregory J. Smallwood, Fengshan Liu, Ömer L. Gülder, and William D. Bachalo
2005 A Calibration-Independent Laser-Induced Incandescence Technique for Soot Measurement by Detecting Absolute Light Intensity. Applied Optics 44(31): 6773.

Starck, Laurie, Ludivine Pidol, Nicolas Jeuland, et al.
2016 Production of Hydroprocessed Esters and Fatty Acids (HEFA) – Optimisation of Process Yield. Oil & Gas Science and Technology – Revue d'IFP Energies Nouvelles 71(1): 10.

Status of Technical Certification of Aviation Alternative Fuels
2017. Conference on aviation and alternative fuels.

Stein, Stephen E., and A. Fahr
1985 High-Temperature Stabilities of Hydrocarbons. The Journal of Physical Chemistry 89(17): 3714–3725.

Sun, Ping, Pierrette Blanchard, Kenneth A. Brice, and Ronald A. Hites
2006 Trends in Polycyclic Aromatic Hydrocarbon Concentrations in the Great Lakes Atmosphere. Environmental Science & Technology 40(20): 6221–6227.

Sundararaj, Ramraj H., Roshan Dinesh Kumar, Anoop Kumar Raut, et al.
2019 Combustion and Emission Characteristics from Biojet Fuel Blends in a Gas Turbine Combustor. Energy: S0360544219311892.

Tanaka, Yukata
1988 Sensitivity Analysis in Principal Component Analysis:Influence on the Subspace Spanned by Principal Components. Communications in Statistics - Theory and Methods 17(9): 3157–3175.

Therssen, E., Y. Bouvier, C. Schoemaecker-Moreau, et al.

2007 Determination of the Ratio of Soot Refractive Index Function E(m) at the Two Wavelengths 532 and 1064 Nm by Laser Induced Incandescence. Applied Physics B 89(2–3): 417–427.

Thomson, K., M. Ziskind, C. Mihesan, et al.
2007 Influence of the Photoionization Process on the Fragmentation of Laser Desorbed Polycyclic Aromatic Hydrocarbons. Applied Surface Science 253(15): 6435–6441.

Tissot, Bernard
2003 Sources d'énergie primaires et effet de serre. Comptes Rendus Geoscience 335(6–7): 597–601.

Todts, William
2018 CO2 Emissions from Cars: The Facts. Transport & Environment. Transport & Environment.

Topinka, Jan, Alena Milcova, Jana Schmuczerova, et al.
2012 Genotoxic Potential of Organic Extracts from Particle Emissions of Diesel and Rapeseed Oil Powered Engines. Toxicology Letters 212(1): 11–17.

Tran, L. S.
2013 Etude de la formation de polluants lors de la combustion de carburants oxygénés. Université de Lorraine.

Trindade, Wagner Roberto da Silva, and Rogério Gonçalves dos Santos
2017 Review on the Characteristics of Butanol, Its Production and Use as Fuel in Internal Combustion Engines. Renewable and Sustainable Energy Reviews 69: 642–651.

Turrio-Baldassarri, Luigi, Chiara L Battistelli, Luigi Conti, et al.
2004 Emission Comparison of Urban Bus Engine Fueled with Diesel Oil and 'Biodiesel' Blend. Science of The Total Environment 327(1–3): 147–162.

Valentino, Gerardo, Felice E. Corcione, Stefano E. Iannuzzi, and Simone Serra
2012 Experimental Study on Performance and Emissions of a High Speed Diesel Engine Fuelled with N-Butanol Diesel Blends under Premixed Low Temperature Combustion. Fuel 92(1): 295–307.

Valeur, Bernard
2005 Invitation à La Fluorescence Moléculaire. Bruxelles: De Boeck.

Vander Wal, Randall L., and Kirk A. Jensen
1998 Laser-Induced Incandescence: Excitation Intensity. Applied Optics 37(9): 1607.

Vander Wal, R.L., Z. Zhou, and M.Y. Choi
1996 Laser-Induced Incandescence Calibration via Gravimetric Sampling. Combustion and Flame 105(4): 462–470.

Vander Wal, R. L.
2009 Laser-Induced Incandescence: Excitation and Detection Conditions, Material Transformations and Calibration. Applied Physics B 96(4): 601–611.

Verma, Puneet, Mohammad Jafari, Yi Guo, et al.
2019 Experimental Analysis of the Morphology and Nanostructure of Soot Particles for Butanol/Diesel Blends at Different Engine Operating Modes. Energy & Fuels: acs.energyfuels.9b00368.

Viteri, F., S. Gracia, á. Millera, R. Bilbao, and M.U. Alzueta
2017 Polycyclic Aromatic Hydrocarbons (PAHs) and Soot Formation in the Pyrolysis of the Butanol Isomers. Fuel 197: 348–358.

Vozka, Petr, Pavel Šimáček, and Gozdem Kilaz
2018 Impact of HEFA Feedstocks on Fuel Composition and Properties in Blends with Jet A. Energy & Fuels 32(11): 11595–11606.

Vozka, Petr, Dan Vrtiška, Pavel Šimáček, and Gozdem Kilaz
2019 Impact of Alternative Fuel Blending Components on Fuel Composition and Properties in Blends with Jet A. Energy & Fuels 33(4): 3275–3289.

Wartel, Maxime
2011 Développement de La Méthode Fluorescence Induite Par Laser En Jet Froid Pour La Quantification d'espèces Aromatiques Impliquées Dans La Formation Des Particules de Suie Dans Les Flammes. Lille 1.

Wei, Liangjie, C.S. Cheung, and Zuohua Huang
2014 Effect of N-Pentanol Addition on the Combustion, Performance and Emission Characteristics of a Direct-Injection Diesel Engine. Energy 70: 172–180.

Wei, Lijiang, and Peng Geng
2016 A Review on Natural Gas/Diesel Dual Fuel Combustion, Emissions and Performance. Fuel Processing Technology 142: 264–278.

Westbrook, Charles K., William J. Pitz, and Henry J. Curran
2006 Chemical Kinetic Modeling Study of the Effects of Oxygenated Hydrocarbons on Soot Emissions from Diesel Engines †. The Journal of Physical Chemistry A 110(21): 6912–6922.

Wiltafsky, Georg, Wolfgang Stolz, Jürgen Köhler, and Christoph Espey
1996 The Quantification of Laser-Induced Incandescence (LII) for Planar Time Resolved Measurements of the Soot Volume Fraction in a Combusting Diesel Jet. *In* P. 961200. https://www.sae.org/content/961200/, accessed June 24, 2019.

Xu, H, T Zhu, AM Shi, and ED Gu
2018 Study of 1-butanol absorption and fluorescence spectra induced by UV-light. Guang Pu Xue Yu Guang Pu Fen Xi: 178–182.

Xue, Xin, Xin Hui, Pradeep Singh, and Chih-Jen Sung
2017 Soot Formation in Non-Premixed Counterflow Flames of Conventional and Alternative Jet Fuels. Fuel 210: 343–351.

Yan, Fangqin, Xiaobei Cheng, Liang Qiu, et al.
2017 Spray Flame Soot Sampling and Morphology Analysis of Butanol–Diesel Blends. Journal of the Energy Institute 90(6): 855–863.

Yao, Mingfa, Hu Wang, Zunqing Zheng, and Yan Yue
2010 Experimental Study of N-Butanol Additive and Multi-Injection on HD Diesel Engine Performance and Emissions. Fuel 89(9): 2191–2201.

Yilmaz, Nadir, and Stephen M. Davis
2016 Polycyclic Aromatic Hydrocarbon (PAH) Formation in a Diesel Engine Fueled with Diesel, Biodiesel and Biodiesel/n-Butanol Blends. Fuel 181: 729–740.

Ying, Yaoyao, and Dong Liu
2017 Effects of Butanol Isomers Additions on Soot Nanostructure and Reactivity in Normal and Inverse Ethylene Diffusion Flames. Fuel 205: 109–129.

Yon, J., A. Bescond, and F.-X. Ouf
2015 A Simple Semi-Empirical Model for Effective Density Measurements of Fractal Aggregates. Journal of Aerosol Science 87: 28–37.

Yon, J., E. Therssen, F. Liu, S. Bejaoui, and D. Hebert
2015 Influence of Soot Aggregate Size and Internal Multiple Scattering on LII Signal and the Absorption Function Variation with Wavelength Determined by the TEW-LII Method. Applied Physics B 119(4): 643–655.

Zhang, Tankai, Mats Andersson, Karin Munch, and Ingemar Denbratt
2019 Optical Diagnostics of Spray Characteristics and Soot Volume Fractions of *n* -Butanol, *n* -Octanol, Diesel, and Hydrotreated Vegetable Oil Blends in a Constant Volume Combustion Chamber. *In* Pp. 2019-01–0019. https://www.sae.org/content/2019-01-0019/, accessed June 12, 2019.

Zhang, Zhi-Hui, and Rajasekhar Balasubramanian
2017 Effects of Cerium Oxide and Ferrocene Nanoparticles Addition As Fuel-Borne Catalysts on Diesel Engine Particulate Emissions: Environmental and Health Implications. Environmental Science & Technology 51(8): 4248–4258.

Zheng, Lukai, Chenxing Ling, Emamode A. Ubogu, et al.
2018 Effects of Alternative Fuel Properties on Particulate Matter Produced in a Gas Turbine Combustor. Energy & Fuels 32(9): 9883–9897.

Zíková, N., J. Ondráček, and V. Ždímal

2015 Size-Resolved Penetration Through High-Efficiency Filter Media Typically Used for Aerosol Sampling. Aerosol Science and Technology 49(4): 239–249.

Ziskind, M., A. Faccinetto, P. Desgroux, E. Therssen, and C. Focsa
2009 Analysis of Polycyclic Aromatic Hydrocarbons Adsorbed on Soot Surface by Laser Desorption, Laser Ionization and Mass Spectrometry. *In* Polycyclic Aromatic Hydrocarbons: Pollution, Health Effects and Chemistry Pp. 231–248. Nova Science Publishers, Inc.